Radiative Acceleration in the Jets of SS433

by

Iain Moray Anderson

Thesis
submitted to the
University of Glasgow
for the degree
of Ph.D.

Department of Physics and Astronomy,
The University,
Glasgow G12 8QQ.

July 1993.

To those that cared, helped and supported me: I thank you all.

Summary

First catalogued as entry number 433 in an objective prism survey of strong Hα emission line objects by Stephenson and Sanduleak in 1977, SS433 rose rapidly to fame in 1978 following the observation of moving hydrogen and helium lines in its optical spectrum. It has since proved to be an enduring astronomical puzzle. SS433 is a galactic object at a distance of some 5kpc and is located very near the centre of the supernova remnant W50 with which it is believed to be interacting. The consensus on the SS433 system itself is that it consists of a binary system comprising an OB star undergoing Roche-lobe overflow onto a supercritically accreting compact object, most probably a neutron star though possibly a black hole, leading to the formation of a geometrically thick accretion disc. Emergent from the narrow funnels of this thick disc are two oppositely aligned and highly collimated jets which move at a remarkably constant speed of 0.26c.

The purpose of this thesis is to investigate the suitability of radiative acceleration as a mechanism for accelerating the jets to a speed of 0.26c and to determine whether such a mechanism can satisfy the stringent constraints on the constancy of the jets' speed imposed by observations.

In the overview of the SS433 detailed in chapter 1, an historical account of the object is given as well as a summary of the observations and the many theotetical models that it has inspired. Though this review is by no means comprehensive, its length reflects the complexity of the object and the vast amount of work that has been published on it.

Chapter 2 acts as a theoretical prelude to the remaining research chapters. In the first part of this chapter some common terms and definitions encountered in special relativity and radiative transfer are elucidated and some useful Lorentz invariants and Lorentz transformations are introduced. In the latter part of this chapter the general vector equation of motion of a spherical jet fragment moving within the time independent radiation field of a blackbody emitter is derived.

Solutions to the general vector equation of motion for a spherical jet fragment, or 'bullet', moving within the radiation field of both infinite planar and infinite conical, isothermal blackbody radiators are sought in chapter 3. Terminal speeds which are dependent on the geometry of the radiator are found to exist. The degree to which radiation pressure can aid in the process of jet collimation is also assessed.

Continuing the analysis of chapter 3, the first topic considered in chapter 4 is the motion of a bullet above an infinite, planar radiator for which the emergent, frequency integrated specific intensity is given by a generalisation to the Eddington limb darkening approximation. This is followed by an investigation of the motion of a bullet moving along the symmmetry axis of an infinite, conical radiator for which the surface temperature decays exponentially with

increasing distance from the funnel apex. Applicability of this ad hoc temperature profile to SS433 is achieved by ensuring that the e-folding distance of the temperature profile is consistent with the observations. Brief sections on axial motion above a finite, isothermal, planar radiator and radial motion above an isotropic, spherical radiator then ensue. The concluding research of chapter 4 comprises an analysis of the axial equation of motion of a bullet moving within a finite accretion funnel. The funnel is modeled first as an isothermal, conical radiator and then as a conical radiator for which the run of temperature with distance from the funnel apex is given by that of a polytropic gas with an index appropriate for a radiation dominated regime. The results of the former model are found to be in surprisingly good agreement with the observations of SS433.

Finally, in chapter 5 topics related to the work contained in this thesis and which could be considered in any further investigation are presented. These include suggestions for improving the 'bullet' model of chapters 2,3 and 4 and the possible inclusion of a phenomenon which has been termed the 'Compton rocket' effect.

Alhough a small proportion of the research contained in this thesis, principally part of chapter 3, consists of material which has previously been published by Icke (1989), the work presented here was undertaken independently and completed prior to the publication of Icke's results.

Contents

Chapter 1

SS433 : An Overview

§1.1 Introduction

The purpose of this chapter is to provide the reader with a broad understanding of the SS433 system. It is not intended to be a comprehensive review. In his anecdotal account of the 'discovery' of SS433, Clark (1984) noted that there were 2 papers published on the object in 1978, 28 in 1979, 73 in 1980 and 122 in 1981. This exponential increase in the publication rate has, thankfully, not been maintained to the present and has in fact become a decline in recent years. Even so, a recent literature search on the 'Simbad' data base revealed 506 citations relating to SS433. The sheer volume of published work on the system clearly makes a comprehensive review an impossible task. For a detailed review of the first 6 years of observations the reader should consult Margon (1984) and for a more recent perspective those of Katz (1986), Cherepashchuk (1988) (particularly for photometry) and Zwitter et al. (1989) are recommended.

I will begin with a resumé of the early history of SS433 and the observations that prompted the development of the kinematic model. This is followed by a summary of the observations at all wavelengths and the many theories that have been propounded. I will conclude with a discussion of the possible evolutionary path followed by SS433 and its suitability as an analogue for extragalactic jets.

§1.2 The Rise to Prominence

The enigmatic object SS433 was first catalogued in an objective prism spectral survey of strong Hα emission line objects by Stephenson and Sanduleak (1977) as entry number 433. The region had previously been associated with prominent radio emission (Clark, Green and Caswell, 1975) and recorded as an X-ray source in the Ariel 5 survey, catalogue entry A1909+04, (Seward et al., 1976) and in the Uhuru satellite observatory survey (Forman et al., 1976). It was again cited as an X-ray source in the fourth Uhuru catalogue as entry 4U1908+04 (Forman et al., 1978) though no identification with the radio and optical observations was made due largely to the poor accuracy with which the X-ray and radio sources could be localised. However, in 1978 the association of these distinct observations with the optical source SS433 was made independently by Clark and Murdin (1978) and Seaquist et al. (1979) with the former group and Ryle et al. (1978) proposing a possible link with the supernova remnant W50. Confirmation of the common

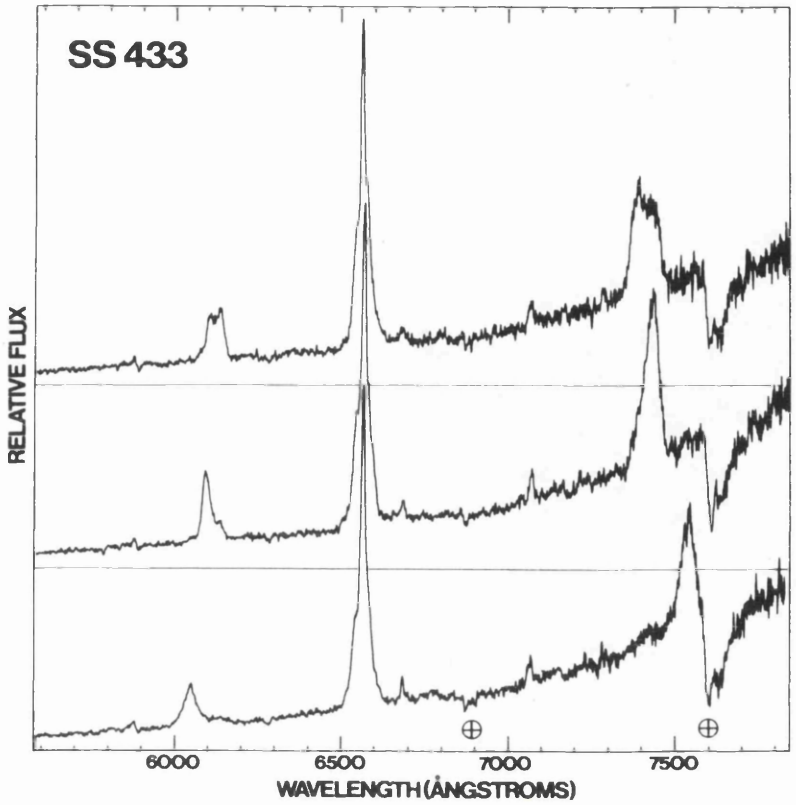

Fig. 1.1. The red/infrared spectrum of SS433 on three of four consecutive nights, obtained with 10Å resolution on the Lick 0.6m reflector. The dramatic changes in both the wavelength and profile of the two unidentified emission features flanking H_α are well illustrated. HeI λ5876, 6678, 7065 emission is visible, as are the unresolved interstellar NaD lines and the λ6284 band. The upper, centre and lower panels were observed in 1978 on October 23, 24 and 26 respectively (from Margon et al. 1979a).

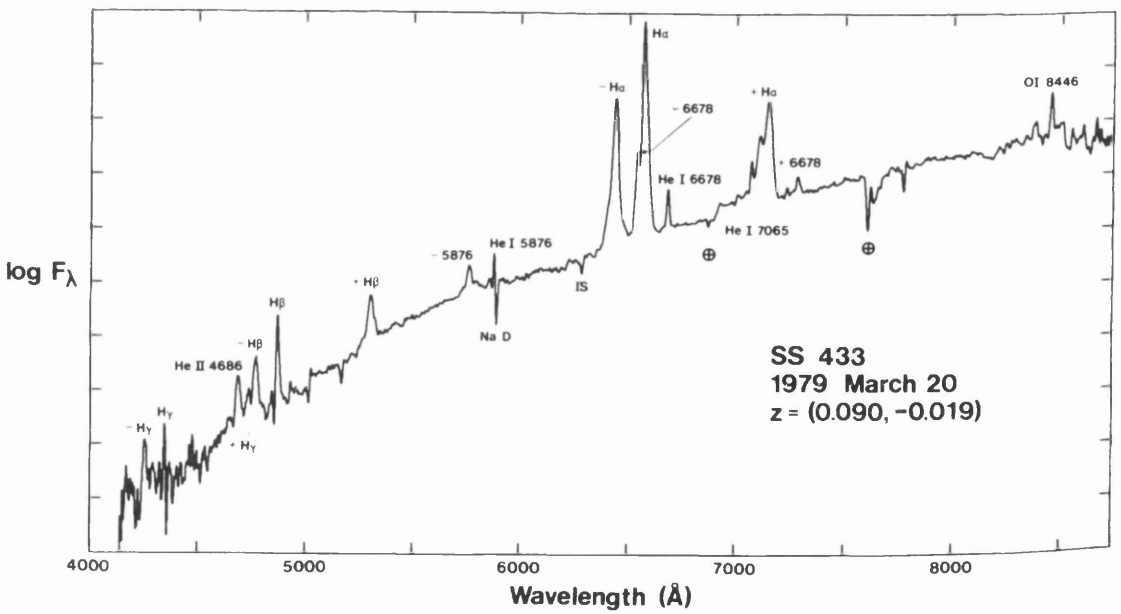

Fig. 1.2. The spectrum of SS433 obtained on March 20, 1979 with the Lick Observatory 3m Shane reflector. The principle emission features are identified with the prefixes '+' and '-' denoting lines in the redshifted and blueshifted systems respectively. Each division on the ordinate corresponds to 0.83 mag (from Margon et al. 1979b).

origin of the X-ray, optical and radio emissions was provided by an accurate determination of the location of the X-ray source (Seaquist, 1981a). The first moderate-resolution spectral data published (Clark and Murdin, 1978) showed a complex red continuum, resulting from strong interstellar reddening, dominated by strong broad emission lines, including the Balmer series (Hα, Hβ, Hγ, Hδ), lines from neutral helium and higher excitation features. The spectrum bore similarities to that of the eccentric orbit X-ray binary Circinus X-1 (Clark, Parkinson and Caswell, 1975) which was itself associated with a supernova remnant (G321.9-0.3) leading Clark and Murdin (1978) to tentatively suggest that they were members of the same class of object. In December 1978 at the Texas Symposium, Bruce Margon reported the presence of moving hydrogen and helium lines in the optical spectrum; an event which marked the begining of SS433's ascension to its present status as an object of great astrophysical significance. The spectroscopic observations of Margon et al. (1979a; Fig. 1.1) and Mammano et al. (1980) revealed unidentified emission features flanking the stationary hydrogen and neutral helium lines that drifted periodically, shifting smoothly by up to $\pm$1 000 Å through the spectrum showing conclusively that Circinus X-1 and SS433 were different objects with SS433 being by far the more exotic. Mammano et al. (1980) attributed the anomalous emission features to Zeeman splitting whilst Margon et al. (1979a) considered the possibility, though seemingly implausible on account of the enormous velocities and change in velocities implied, that they were due to Doppler shifted satellites of the stationary Balmer and neutral helium lines. Further observations by Margon et al. (1979b; Fig. 1.2) and Liebert et al. (1979) showed unambiguously that the moving spectral features were indeed Doppler-shifted Balmer and HeI emissions with Liebert et al. (1979) ruling out a magnetic interpretation for the features on the basis of polarimetric measurements. Margon et al. (1979b) reported the velocity variations to be cyclical and roughly sinusoidal with a period of 164$\pm$3 days and maximum positive and negative radial velocities of +50 000 km/s and -35 000 km/s respectively symmetric about a red-shift of z=0.04. Detailed analysis of the 'stationary' lines spectra by Crampton, Cowley and Hutchings (1980) revealed a 13.1 day periodic variation with an amplitude of K = 73 km/s which they interpreted as representing orbital motion. The appearance and width of the profiles was similar to those originating in the accretion disc of cataclysmic variables prompting Crampton, Cowley and Hutchings (1980) to interpret the observations as representing a low mass binary system not unlike Cyg X-2 (Cowley, Crampton and Hutchings 1979). An explanation and theoretical model for these unprecedented spectral features was necessary.

§1.3 The Kinematic Model

§1.3.1 The Simple Kinematic Model

One of the earliest theoretical papers on the system was that of Milgrom (1979) in which he proposed that the Hα emission comes from two regions, symmetrically situated about a central object with velocities of equal constant magnitude and opposite sign. Longitudinal

and transverse Doppler effects are responsible for the wavelength shift with the variation in wavelength resulting from changes in the angle between the velocity vectors and the line of sight due to a rotation of the line connecting the two regions. Milgrom (1979) discussed the schematic configurations which satisfied these constraints: The line emission comes from

i) the illuminated regions of a disc the matter of which moves in a circular Keplerian orbit about a central object that emits radiation in oppositely directed pencil beams.

ii) two opposite conical sections within which matter is free falling radially onto the central object.

iii) two opposite conical sections within which matter is moving radially away from the central object.

Milgrom (1979a) noted that configuration iii) is at an advantage over the other two possible configurations, requiring a central object only of stellar mass. Katz (1980) pointed out the difficulty with configuration iii) in finding a central, compact object with a 164 day rotation period that would not be spun-up (or spun-down) in a fraction of its period by accretion torques. Fabian and Rees (1979) attributed the features on either side of the Balmer lines to cool gas trapped within approaching and receding jets emanating from a central object which, they suggested, arose from the formation of shocks within a jet of variable beam-speed. Amitae-Milchgrub, Piran and Shaham (1979) suggested that the features originated in a ring of matter orbiting round a massive black hole $\sim 10^6 M_\odot$ formed by the capture of a normal solar type star with the periodicity arising from precession of the ring about the central black hole.

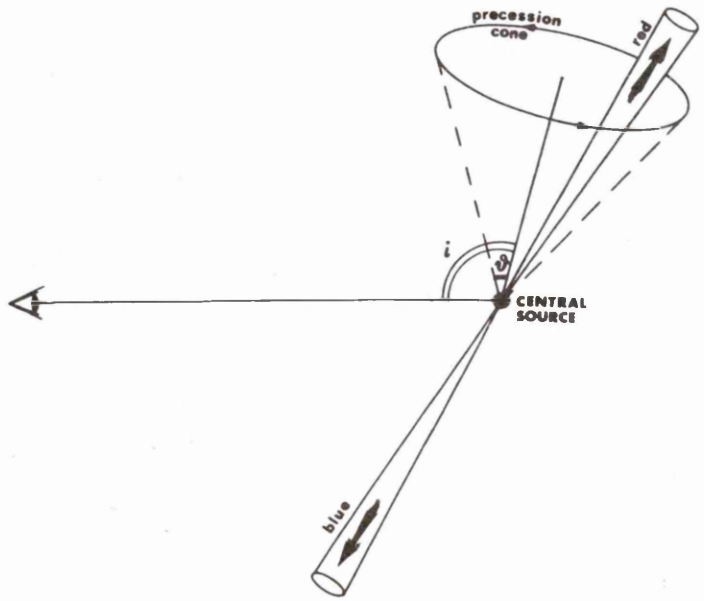

Fig. 1.3. A schematic representation of the kinematic model (from Zhi, Ruffini and Stella, 1981).

With the benefits of additional data not available to Milgrom, Abell and Margon (1979) were able to elaborate on schematic configuration iii) proposed by Milgrom (1979a) to formulate the 'kinematic' model. The model conjectures that matter is ejected from a central source in two collimated, closely aligned opposing jets which rotate on a cone about some axis (Fig. 1.3).

The emission lines in the jet directed towards earth are observed to be blue shifted whilst those in its receding counterpart are red shifted. The simple kinematic model, in which the rotation rate is constant, is specified by seven free parameters:

- β the speed of the jets in units of c
- θ the semi-angle of the cone formed by the precession of the jets about the rotation cone axis
- i the inclination of the rotation cone axis to the line of sight
- P_0 the rotation period
- t_0 a time at which the rotation phase is zero
- χ the position angle of the cone axis projected onto the plane of the sky
- $s_{\rm rot}$ the sense of the jet rotation; +1 for clock-wise and -1 for anti-clockwise.

All but the last two of the model parameters can be derived from the moving emission line data and for this reason it is also known as the 5-parameter model. A complete model parameter fit and the removal of the degeneracy in the angles θ and i inherent in any deductions made solely from the optical data is possible with additional radio observations. Abell and Margon (1979) provided accurate solutions to five of the model free parameters and predicted the cross-over of the moving features from the red to the blue and vice versa. This prediction was later verified by observation (Bedogni et al., 1980; Margon, Grandi and Downes, 1980). From the widths of the Doppler-shifted emission lines Milgrom, Anderson and Margon (1982) concluded that the velocity of the jet material was very constant. Further confirmation of the validity of the 'kinematic' model was provided by both radio (Gilmore et al., 1981; Hjellming and Johnston, 1981 (a) and (b)) and X-ray (Seward et al., 1980; Watson et al., 1983) observations.

Quoting the best-fit model parameters for the Doppler shifts of Margon and Anderson (1989) and the best-fit parameters for the VLA data of Hjellming and Johnston (1981b), the seven model parameters are:

- β(units of c) 0.2602
- θ(degrees) 19.85
- i(degrees) 78.83
- P_0(days) 162.50
- t_0(JD) 2 443 562.37
- χ(degrees) 100
- $s_{\rm rot}$ -1 .

The VLBI observations of Spencer (1979) and Walker et al. (1981) also indicate a mean position angle χ of 100°. It should be noted in passing that all seven model parameters can in principal

be determined from radio data; however the five model parameters derived from the optical data are adopted on the basis of their greater accuracy.

Adopting the phase convention of Abell and Margon (1979) and Margon et al. (1979b), the Doppler shift of either jet is given by

$$z \equiv \frac{\lambda_{\rm obs} - \lambda_{\rm line}}{\lambda_{\rm line}} = (\gamma - 1) - \gamma\beta\,(\sin\theta \sin i \cos(2\pi\psi) + \cos\theta \cos i)\, s_{\rm jet} \qquad (1.1)$$

where $s_{\rm jet} = +1$ for the approaching jet, -1 for the receding jet, the Lorentz factor $\gamma \simeq 1.036$ and the precessional phase ψ is defined as

$$\psi(t) = \psi_0 + \frac{(t - t_0)}{P_0} \qquad \text{with} \qquad \psi_0 = \frac{1}{2\pi} \arccos\left(-\cot i \cot\theta\right) . \qquad (1.2a, b)$$

The phase convention was chosen to be similar to standard spectroscopic binary notation. The jets are perpendicular to the line of sight twice in one rotation period. This happens when the Doppler shift of either jet is identically equal to the transverse Doppler red-shift which, by Eq. (1.1), occurs at phase values 0 and 0.342. It is evident from Eq. (1.1) that the Doppler shift of either jet is biased by the $(\gamma - 1)$ term thus accounting for the symmetry observed in the Doppler shifts about z=0.04 (Margon et al., 1979b). This is simply a manifestation of the transverse Doppler effect and for the Hα line, wavelength 6562.8 Å, corresponds to a shift of $\sim$ 234 Å into the red.

§1.3.2 Kinematic Deviations and Embellishments

General theoretical arguments indicate that the jet acceleration takes place in a rotating accretion disc suggesting precession of the accretion disc (see §1.6.3) as the logical origin of the 164 day rotation period (Katz, 1980, 1981; van den Heuvel, 1980). Simple stellar rotation locked to the beams as the underlying system clock had been ruled out (Abell and Margon, 1979; Katz, 1980) on the grounds that the inferred kinetic energy of the jets is far greater than the total rotational energy of a feasible compact object with a 164 day period. The precession hypothesis gained further credibility with the observations of Crampton and Hutchings (1981) who found that the Hβ emission profile, the intensity of the HeI emission and the HeI and FeII absorption lines varied in a manner consistent with origin in a precessing accretion disc. Comparison with other X-ray binaries suggested the possible existence of a substantial accretion disc as an additional component of the SS433 system.

It is evident from the data (Fig. 1.4) that the observed moving lines do not adhere rigorously to the predictions of the simple kinematic model. In fact the observations typically lie within a strip of width $\sim$ 100 Å about their predicted value (Mammano et al., 1983). To date at least three types of deviation have been detected.

The first form is manifest as two short-term periods (Katz et al., 1982; Mammano et al., 1983; Newsom and Collins, 1981) superposed on the 164 day periodic motion of the moving

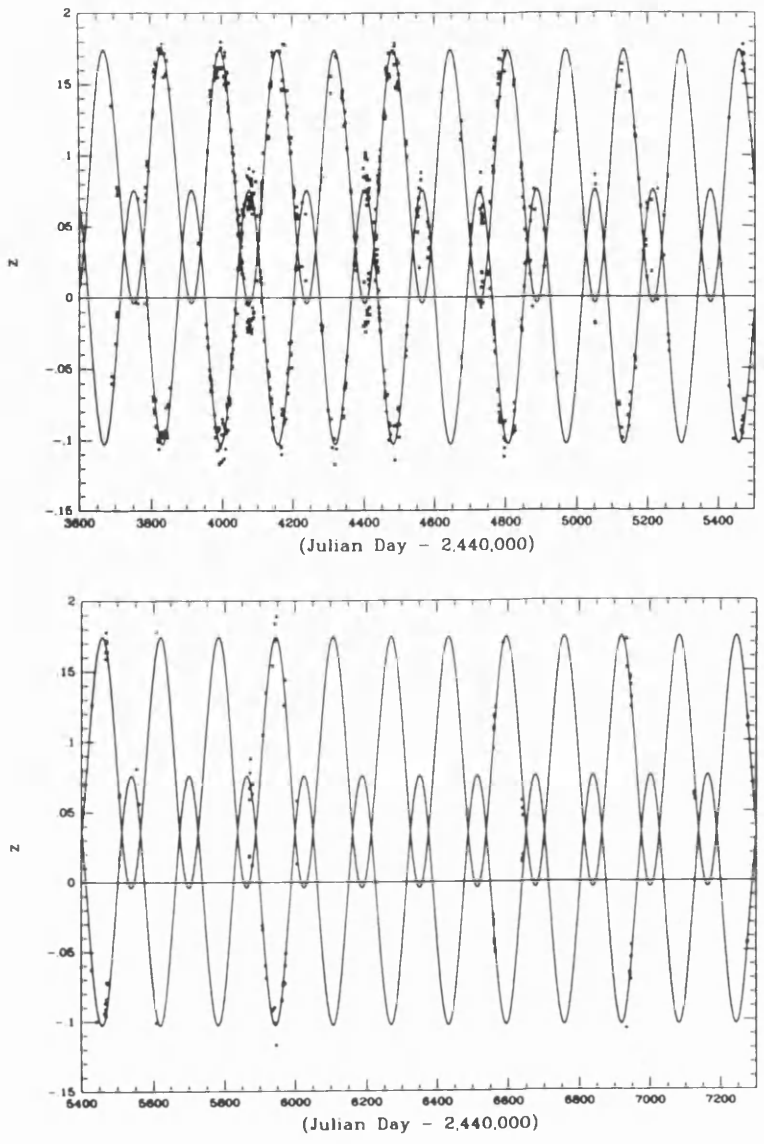

Fig. 1.4. Doppler shift observations of SS433 over a 10 yr period. The solid line indicates the best fit to the simple kinematic model (from Margon and Anderson, 1989).

emission features. The more dominant of the short-term periods is 6.28 days with an amplitude $\sim$ 10% of the 164 day precessional motion; the second is 5.83 days (Katz et al. 1982). A simple interpretation of the 6.28 day period, using linear perturbation theory, has been discussed at length by Katz et al. (1982): The companion star exerts a gravitational torque on the accretion disc which, when averaged over one binary period, provides a steady torque to drive the counterprecession of the disc. One component of this torque has a period given by the synodic orbital period derived from the 13.08 day orbital and 164 day mean precession period. This periodic torque induces 'nodding' motions in the orientation of the accretion disc about the mean precessional motion. If the direction of the jets is governed by the orientation of the disc then these nodding motions will be detectable in the moving-line Doppler shifts. This theory however fails to predict the large observed amplitude of the 5.8 day period; a problem which has been resolved by the generalised nodding model of Collins and Newsom (1986).

As mentioned above, the 6.28 day and 5.83 day periods are simply synodic combinations of the 164 day precession and 13.08 day orbital periods. As their periods are conveniently small, these short-term periods provide an excellent means of accurately determining the binary orbital period. The period of the binary orbit is expected to change with time as a result of mass loss through the relativistic jets (van den Heuvel et al., 1981; Anderson, Margon and Grandi, 1983a). Consequently, the detection of any change in the orbital period through the analysis of the Doppler shifts of the moving lines attributable to the nodding motion provides a means of determining the mass loss rate and thus the jet kinetic energy independently of the observed intensity of the radiation from the jets. This technique is not dependent on knowledge of the true form of the precession instability since $1/164 \ll 1/13.08$. Margon and Anderson (1989), utilising this method, found an upper limit on any change in the orbital period of the binary system to be $|\dot{P}_{13}| < 8 \times 10^{-6}$. These nutations have also been employed as a means of investigating the structure of the accretion disc.

The second class of deviation is evident as extended periods of time during which the predictions of the simple kinematic model are systematically shifted with respect to the data. The reason for this discrepancy is not well understood though its presence indicates that either the model precession period is wrong and/or unstable or that the precession clock is more complicated than anticipated (Margon, 1984). Anderson, Margon and Grandi (1983b) investigated the instability of the 164 day precessional period of the jets through several deterministic models. Their analysis showed that the more complicated 7-parameter and sinusoidal models were better able (though not completely successfully) to reproduce the fluctuations seen in the observations. Further, they deduced that the amplitude of the noise was no greater than that observed in the 35 day X-ray period of Her X-1, in which precession is also likely as the driving clock, and that it consequently contains information on how the fluid accretion disc and companion star precess. Hjellming and Johnston (1986) discussed a model where these systematic deviations from the simple kinematic model arise from the presence of two underlying clocks of periods of order 152 days and 175 days. The beat period of $\sim 2\,000$ days of these sinusoidal variations is superposed on the 164 day precessional period. Margon and Anderson (1989) point out that the two period model of Hjellming and Johnston (1986) is essentially the same as the sinusoidal model of Anderson, Margon and Grandi (1983). In their more recent analysis of the deterministic models, Margon and Anderson (1989) concluded that the nature of the instability of the precessional clock is obscure and probably not increasing, that both the 6 and 7-parameter models are almost certainly not correct and that the inferred period of the sinusoidal model has decreased to $1\,299 \pm 24$ days. However, they could not determine whether the sinusoidal model had any physical significance or whether it simply fitted the data on account of the large number of free parameters (9) in the model.

Even after subtraction of empirical fits to the 164 day period instability and the precession and nodding motions from the best-fit model there still exist apparently random deviations of several thousand kilometers per second that are variable predominantly on a time-scale of days.

These constitute the third type of deviation. This 'jittering' motion shows no obvious 164 day phase dependence so eliminating scenarios where stochastic variations of some of the model parameters, such as the jet velocity, are responsible for the deviations. Katz and Piran (1982) have noted that the deviations are compatible with a stochastic jitter in the beam pointing direction of magnitude comparable to or smaller than the jet opening angle. During these stochastic excursions, the jets show evidence of moving as a solid body (Margon and Anderson, 1989): when the red beam has insufficient red-shift, the blue beam has excess blue-shift and vice versa. The anticorrelation is not quite exact and appears to be transmitted on time scales of several days or less. This observation has led Margon and Anderson (1989) to suggest that most of the collimation and pointing of the jets occurs very close to the jet source rather than in the outer regions of a thick accretion disc as is believed to be the case in active galactic nuclei.

The 'kinematic' model provides a beautiful, simplistic explanation of the moving line features and is accepted by most (see Kundt (1985, 1987) for dissent; §1.6.6) as the canonical scenario for SS433. However, it completely fails to address many of the perplexing physical problems posed by the system: the characteristics of the constituent star(s), the mechanisms that power, collimate and precess the jets and the evolutionary path that culminated in the formation of SS433.

§1.4 Basic Information

§1.4.1 General Data

The source of the optical emission in SS433, known also as V1343 Aquilae, is located at $\alpha(1950) = 19^h\,09^m\,21.282^s \pm 0.003^s$, $\delta(1950) = 04°\,53'\,54.04'' \pm 0.05''$ in the epoch of 1980 (de Veght and Gehlich, 1979; Kaplan et al., 1980) and has corresponding galactic coordinates $l = 39.7°$, $b = -2.2°$ (Margon, 1984). The compact radio and X-ray sources are coincident with the optical source within the bounds of measurement uncertainty.

The distance to SS433 can be uniquely determined from the radio maps by comparing the radio brightness distribution with the helical pattern expected from the twin precessing jets though in most cases it is assumed that the radio knots are moving at the same velocity as the optical emission line regions. This assumption is supported by the absence of a notable change in the proper motion of the radio components (Spencer, 1984). On the basis of the more reliable distance estimates deduced from the radio observations (VLA: Hjellming and Johnston, 1981b; VLBI: Niell et all., 1981; MERLIN: Spencer, 1984; VLBI: Fejes, 1986; VLBI Vermeulen et al., 1993a), the presently accepted distance to SS433 is ~ 5 kpc. The distance to the SNR remnant W50, based on the surface-brightness diameter relation resulting from the decreasing brightness of SNR with increasing distance from the galactic plane, has been estimated as 3.3 kpc (Caswell and Lerche, 1979) in rough agreement with the estimates of the distance to SS433.

The apparent magnitude of SS433 is $V = 14.22 \pm 0.04$ (Margon et al., 1979a). The

absolute magnitude is $M_V \sim -7$ and the optical continuum spectrum is similar to that of an O5-type star suffering severe interstellar absorption $A_V \sim 8$ mag (Murdin et al. 1980). The bolometric luminosity of the system is $\sim 4.4 \times 10^{39}$ erg/s and the dominant source of optical luminosity resembles a blackbody with a mean colour temperature $\sim 32\,500$ K (Wagner, 1986). The $2 - 10$ keV X-ray luminosity is $\sim 10^{36}$ erg/s (Warwick et al. 1981) and typical radio flux densities (summed over the central and extended sources) are 1 Jy at 3.7 and 6 cm and 0.2 Jy at 2 cm (Hjellming and Johnston, 1981b).

§1.4.2 The System Configuration

SS433 is believed to be a binary system in which both components follow (nearly) circular orbits (Collins and Newsom, 1986) with a period of $\sim$ 13 days. The primary is probably an OB star undergoing Roche-lobe overflow whilst the secondary is a compact object, perhaps a black hole though recent evidence (D'Odorico et al., 1991; see §1.6.1) favours a neutron star. Material from the primary is accreted at a supercritical rate (Zealy et al., 1980) onto the compact component forming a geometrically thick accretion disc. Two highly collimated and oppositely aligned jets moving at approximately a quarter the speed of light emerge from the accretion disc funnels along the disc-normal which precesses in a manner consistent with the kinematic model.

§1.5 Observations

§1.5.1 Gamma-Ray Observations

From an analysis of the data collected by the high-resolution gamma-ray spectrometer on board the HEAO 3 satellite, Lamb et al. (1983) reported the presence of two gamma-ray lines located at energies of about 1.5 and 1.2 MeV. Both lines exhibited fractional linewidths $\Delta E/E$ of $\sim 1\%$ and varied in intensity by a factor of ~ 3 on a time scale of days. Assuming that the lines represent isotropic emission from SS433 then the combined gamma-ray luminosity of both lines is $\sim 2 \times 10^{37}$ erg/s which is of the order of 250 times greater than the 2-10 keV luminosity (Marshall et al., 1979) and is a significant fraction of the jet kinetic energy. The gamma-ray lines were interpreted as blue and red shifted components of the 1.369 MeV line which arises from a nuclear transition of ^{24}Mg from its first excited state to its ground state. Lamb et al. (1983) proposed that the transition was triggered by inelastic collisions of the ^{24}Mg nuclei moving at $\sim 0.26c$ (or equivalently with 33 MeV per nucleon) with ambient protons. If this identification is correct then on the basis of solar abundances of ^{12}C and ^{16}O to ^{24}Mg, intense lines from ^{12}C and ^{16}O should be present. These lines are not observed indicating that either the ^{24}Mg identification is wrong or that the magnesium abundance in SS433 is anomolously high relative to carbon and oxygen. In a cautionary note, Norman and Bodansky (1984) stressed that if the gamma-ray features were due to inelastic scattering of ^{24}Mg nuclei on protons then lines of similar intensity should be observed at ~ 1.4 and ~ 1.8 MeV. Such features have not been

observed indicating that the explanation proposed by Lamb et al. (1983) is possibly wrong. Alternative interpretations for the gamma-ray lines have been formulated by several authors (Kundt, 1985; Boyd et al., 1984; Ramaty et al., 1984; Helfer and Savedoff, 1984). Negative results have been reported by MacCallum et al. (1985) and Geldzahler et al. (1989) casting some doubt on the existence of the gamma-ray lines reported by Lamb et al. (1983).

§1.5.2 X-Ray Observations

In early Ariel (Seward et al., 1976; Ricketts et al., 1981), Uhuru (Forman et al., 1978) and HEAO-1 (Marshall et al., 1979) X-ray observations SS433 appeared as an unremarkable source with a 2-10 keV luminosity of $\sim 10^{36}$ erg/s. At the assumed distance of 5 kpc (Warwick et al., 1981) this corresponds to approximately 0.01% of the total system luminosity (accounting both for the kinetic energy of the jets and the radiation from the jets). The spectrum appears moderately hard ($kT \sim 14$ keV) with evidence for iron line emission at 6.7 keV from Fe XXVII (Marshall et al., 1979) and has the shape of a power law type or relatively hard bremsstrahlung spectrum (Marshall et al., 1979; Rickets et al., 1981). Imaging observations in the range $0.5 - 3$ keV performed by the Einstein X-ray Observatory (Seward et al., 1980) revealed the presence of diffuse X-ray emission associated with the jets extending to at least 30 arc min from SS433 and aligned with the deformation in the W50 shell. The X-ray lumimosity of the central source accounts for about 90% of the total, the remaining 10% being attributable to the X-ray lobes which are morphologically similar to the radio lobes of extragalactic objects (Fig. 1.5). The work of Seward et al. (1980) was extended by Watson et al. (1983) who found the X-ray lobes to be confined within a region subtending $\sim 30°$ at the central object and exhibiting spectral softening with increasing distance from SS433. The spectrum obtained

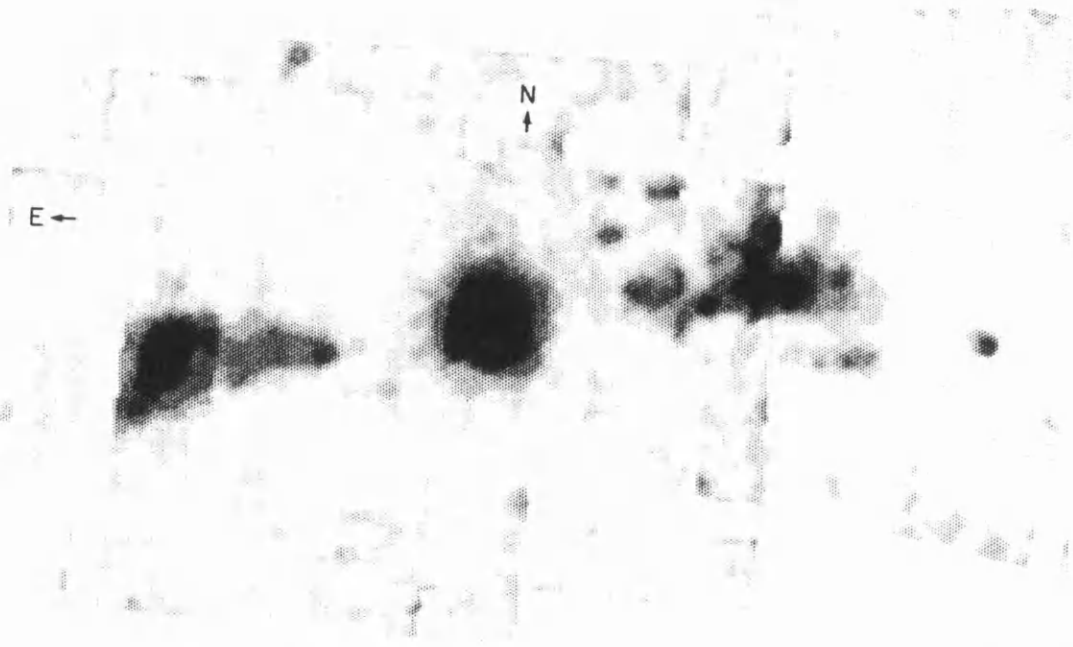

Fig. 1.5. A smoothed IPC X-ray image of SS433 and the surrounding region in ~0.7–4 keV band with 64" pixels. The image is a composite of three separate observations, each corrected for telescope vignetting (from Watson et al., 1983).

with the Einstein X-ray Observatory showed none of the emission lines such as Si XIII and Si XIV expected from a thermal plasma at a temperature of a few keV (Grindlay et al., 1984) so favouring non-thermal models for the central X-ray source (Seaquist et al., 1982; Grindlay et al., 1984).

Better resolution spectral observations from the Exosat observatory (Watson et al., 1986) and corroborative Tenma results (Matsuoka et al., 1986) revealed the presence of the Fe XXV emission line of estimated luminosity $L_{\text{line}} \geq 10^{34}$ erg/s oscillating periodically across the spectrum over a 164 day period in a manner consistent with the kinematic model. The existence of this line seems to suggest a thermal model for the central source. Only the blue shifted component is observed. The red shifted counterpart is presumably obscured by the accretion disc providing constraints on the system geometry and placing an upper limit on the length of the jets over which the X-ray line emission arises as 10^{12} cm (Watson et al., 1986). This X-ray jet length is supported by the results of Stewart et al. (1987) and requires that the jets be accelerated to 0.26c within 10^{12} cm (i.e. in about 100 seconds) and consequently constrains the possible acceleration mechanisms (§1.6.4).

Most of the X-ray emission comes from a small region at the base of the relativistic jets (Watson et al., 1986). When this region is eclipsed by the normal star during primary eclipse, the duration of the eclipse is related to the relative size of the normal star and as a result to the mass ratio q (§1.6.1).

Band (1989) has pointed out that during the period of Einstein observations SS433 was a flaring X-ray source whilst during the Exosat observations it was relatively quiescent. This flaring behaviour would account for the disagreement in the likely model for the emissions during the Einstein and Exosat observations.

Recent Ginga X-ray observations (Brinkmann et al., 1989; Brinkmann et al., 1991) centered on the phases of optical primary minimum indicate that the source spectrum is extremely hard and best fitted with a thermal bremsstrahlung law and that the jets are precessing retrograde with respect to the orbital binary motion.

§1.5.3 Optical and Infrared Observations

The mean colour temperature (§1.4.1) indicates that the spectrum of SS433 probably peaks in the UV part of the spectrum. However, because SS433 is located very close to the galactic plane the UV emissions are severely attenuated making observations in this band very problematic. In the remainder of this section I will discuss in succession the stationary spectral lines, the moving spectral lines and, finally, the photometric observations.

The stationary spectral lines originate in the atmospheres of the normal star and the accretion disc and in the stream of accreting matter between the two. The dominant features in the stationary spectrum are the Balmer and He I emission lines; the equivalent width of the Hα has exceeded 500Å and was responsible for the inclusion of the object in the SS catalogue. On occasion, both the He I and Balmer emission lines display P-Cygni absorption wings. The

He II λ4686 and λ10124 emissions, typical of cataclysmic variables and galactic X-ray binaries, are also present as well as the particularly strong C III–N III λ4640-4650 emission blend (Margon, 1984) and the O I λ8446 (Mammano et al., 1980; Margon et al., 1979b) emission feature. The emission line profiles are complex and vary on time scales of less than a day. The spectrum is particularly deficient in absorption lines with only the strong O I λ7773 and some Fe II lines being intrinsic to the source, the remainder being due to interstellar absorption.

The lines referred to as 'stationary' do not occur at their rest wavelengths and in fact vary with a period of approximately 13 days (Crampton, Cowley and Hutchings, 1980). The periodic variations of the H and He I emission lines and the Fe II lines first indicated the binary nature of SS433. From the amplitude of these variations the projected velocity was determined to be 73 km/s. This velocity was incorrectly interpreted as representing the orbital motion of the compact object (Crampton, Cowley and Hutchings, 1980). Observations of the He II λ4686, believed to be formed close to the compact object, showed a similar 13 day modulation (Crampton and Hutchings, 1981). If this identification is correct then the modulation of the He II λ4686 line represents the binary motion of the compact object. The amplitude of this modulation is $K = 195\,\mathrm{km/s}$, with a lower limit of $K = 150\,\mathrm{km/s}$, which corresponds to a mass function

$$\begin{aligned} f_m &= \frac{(M_\star \sin i)^3}{(M_\star + M_\mathrm{X})^2} \\ &= 1.035 \times 10^{-7} \left(K/\mathrm{km\,s^{-1}}\right)^3 (P_{13}/\mathrm{day}) \, (\sin i)^{-3} \, M_\odot \\ &= 10.6\,(4.6)\, M_\odot \end{aligned} \tag{1.3}$$

where $M_\star$ and M_X are the masses of the normal star and the compact object respectively, i is the system inclination and the bracketed mass function represents the lower limit. This would seem to indicate the presence of a massive companion. However, the He II λ4686 line in the spectra obtained by Crampton and Hutchings (1981) displayed a complex and unresolved profile making it difficult to distinguish the true orbital motion from strength variations of the line components. In a more recent investigation, D'Odorico et al. (1991) measured the orbital modulation of the resolved He II λ4686 line and determined the amplitude of the Doppler modulation to be $K = 112 \pm 5\,\mathrm{km/s}$ corresponding to a mass function $f_m = 2.0 \pm 0.3 M_\odot$ which is significantly lower than that derived by Crampton and Hutchings (1981). The different velocity amplitudes observed for the He II lines and the other stationary lines can be explained if the other stationary lines are formed in the stream of material which, because of Roche lobe overflow, leaves the normal star and flows onto the compact object. The velocity of the accretion flow is smaller than the orbital velocity and since the He II lines are formed near the compact object their velocity amplitude will be greater than that of the other emission lines. This explanation also accounts for the phase difference observed between the He II line and the other emission lines.

During the photometric eclipse of the accretion disc, the intensity of the He λ4686 line decreases slightly but never undergoes total eclipse. From this observation it can be deduced that the line is formed in an extended region such as the accretion disc corona and not in some localised hot-spot.

Spectral observations in the optical (λ4674-5549) and near infra-red (λ8355-8987) (Filippenko et al., 1988) seem to show that the stationary Paschen lines (λ8755, 8670 and 8603) are double peaked with splittings of $\sim 290\,\mathrm{km/s}$. The observations were made at the point in the precessional phase just before the first crossing of the moving lines and at a point in the orbital phase close to the secondary eclipse. If these lines occur in the outer regions of the accretion disc then they constitute the first direct evidence of emission from the accretion disc. The splittings may result from rotation of the accretion disc.

Analysis of the moving emission lines provided the first indication of the jets in SS433. Extensive observations of the lines have been made by numerous authors (e.g. Margon et al., 1980, 1981, 1982; Ciatti et al., 1981,1983; Mammano et al., 1980). These observations show that the most dominant line is Hα with a luminosity of $\sim 10^{35}\,\mathrm{erg/s}$. Also present in the moving spectrum are the remaining Balmer series, He I lines and in the infrared, the Paschen and Brackett series. The moving emission lines are unpolarized (Liebert et al., 1979) and have typical line widths of several thousand kilometers per second from which an upper limit on the opening angle of the jet of $\theta \approx 0.1$ radians can be inferred (Begelman et al., 1980). The range of line profiles extends from the very complex (Margon et al., 1979a, 1980; Murdin et al., 1980) to the Gaussian (Margon et al., 1984). Considerable changes are observed both in the profile and intensity of the lines on a time scale of less than a day. These intensity variations include occasions where the blue and red shifted emission lines disappear/reappear in synchronisation with one another with a time delay between the jets of less than one day. This indicates that the radiating regions in each jet are less than 100 AU apart. Apart from these intensity variations, indvidual lines have been observed to brighten then fade at one particular frequency (Murdin et al., 1980) to be replaced by a similar configuration at a slightly different frequency. This has been termed 'bullet' behaviour. Each bullet takes on average $\sim$ 10 hrs to reach maximum brightness then dims with a typical radiative lifetime of $\sim$ 2 days (Vermeulen et al., 1993c). As discussed in §1.3.2, the Doppler shifted emission lines do not strictly follow the predictions of the kinematic model, exhibiting both nodding motions and jitter. The most rapid photometric and spectroscopic variations so far observed occurred on a timescale of $15-20$ minutes (Kopylov et al., 1986) and appeared to be correlated with the intensity of the stationary Hα emission (Asadullaev and Cherpashchuk, 1986) suggesting that both sets of lines are produced by the same excitation mechanism. There is no evidence of He II lines and particularly the λ4686 line which is prominent in the stationary line system. The absence of the He II lines constrains the temperature of the emitting material to be between about 5 000 and 40 000 K with the most likely range, on the basis of the behaviour of the cooling function, being $\sim 10\,000 - 20\,000\,\mathrm{K}$.

The complexity of the moving line profiles, attributable to them being comprised of several

components, indicates that the density of the jets is not homogeneous and instead rather clumpy. Theoretical considerations indicate that the filling factor, f_f, of the optical line emitting material in the jets is such that $f_f \ll 1$ (Bodo et al., 1985; Begelman et al., 1980). This is generally much smaller than the limit $f_f \leq 0.01$ deduced from line profile fitting (Borisov and Fabrika, 1987).

A lower limit for the length of the optically emitting region of the jets, $l_{\rm opt}$, can be deduced from a Black body limit argument (Begelman et al., 1980):

$$l_{\rm opt} > 1.6 \times 10^{12}\, \theta^{-\frac{1}{2}}\, T_4{}^{-1}\, (L_{\rm H\alpha})_{35}{}^{\frac{1}{2}}\ {\rm cm} \tag{1.4}$$

where θ is the jet opening angle, T is the thermal temperature of the region and $L_{\rm H\alpha}$ is the luminosity of the Hα line. The spectroscopic variations on a time scale of minutes mentioned above indicate that the emitting region is relatively compact with $l_{\rm opt} \leq 10^{13}$ cm which is in agreement with the variability observations of Kopylov et al. (1986) and Asadullaev and Cherepashchuk (1986). In contrast, the spectroscopic data of Borisov and Fabrika (1987) indicates that $l_{\rm opt} \approx 10^{15}$ cm.

Brown, Cassinelli and Collins (1991) have discussed possible mechanisms for heating the Hα bullets out to distances of 5×10^{14} cm and turning the emission off at 10^{15} cm. They impose the requirements that there be sufficient heating in the observed emission region, that the bullets be dense enough to suppress forbidden lines and to emit enough Hα by recombination and that the lines are neither too broad nor display deceleration. Solutions for spherical bullets heated radiatively by emissions from SS433 exist only for very massive (10^{26} g) bullets which have an angular radius of $\sim$ 0.03 radians at the central source and have a number density $n_e \sim 10^{10}\,{\rm cm}^{-3}$. Such a solution is very improbable since the inferred kinetic luminosity is $\sim 10^{41}$ erg/s. For heating by collisions from the wind of the companion star, solutions exist for bullet masses $\sim 10^{24}$ g, number densities $n_e \sim 10^{11.5}\,{\rm cm}^{-3}$ and an angular radius of $\sim 10^{-3}$ radians. The required wind-loss rates are in the range $\sim 10^{-6} - 10^{-3}\, M_\odot/{\rm yr}$, the lower end of which is appropriate for SS433. It seems therefore that collisional interaction with the stellar wind is responsible for heating the optical bullets.

SS433 is a relatively bright (V$\sim$14) star which is photometrically accessible to small telescopes. Consequently, numerous observations of the optical continuum have been made by means of narrowband (Anderson et al., 1983b) and broadband (Henson et al., 1983; Kemp et al., 1986; Mazeh et al., 1987; Zwitter, Calvani and D'Odorico, 1991 and references therein). The optical continuum spectrum resembles a blackbody of mean colour temperature $\sim$ 32 500K and appears hotter when the brighter precessing object is seen pole-on and cooler when seen nearest equator-on (Wagner et al., 1986). This variation corresponds to an amplitude in the B-V colour index of $0.08^{\rm m}$ and may result from gravity darkening in the normal star or the thick accretion disc, or perhaps from high temperature funnels in the accretion disc. Anderson et al. (1983b) had previously proposed that the accretion disc is thick with a diameter-to-thickness ratio

of $\sim 3/2$.

Observations in the U, B and V colour bands show the temporal behaviour of the source to be erratic with a typical scatter from the smooth light curve of about 0.3^m in V and 0.25^m in B. The source is variable on a wide range of time scales, from hours to years though there exists no evidence for marked variations on time scales much less than an hour (Lebedev et al., 1981).

Both the 13 and 162 day periods are clearly observed in the photometric data. The 13 day orbital period is responsible for the two broad minima observed in the B and V bands. The primary minimum occurs at the same phase as the maximum positive radial velocity of the stationary Balmer emission lines and occurs half of an orbital period before the secondary minimum. The primary and secondary minima are interpreted as eclipses of the accretion disc by the normal star and vice versa respectively. In addition, the orbital phase difference between this primary minimum and the zero phase of the 6.3 day nodding motions is the same as that between the Balmer and H II emission line velocities (Crampton and Hutchings, 1981). Since the nodding motions can only realistically originate near the compact object, the presence of the common phase offset conclusively proves that the He II line represents the true orbital motion of the compact object. In the U band, the primary minimum is fairly deep whilst the secondary minimum appears not to be present.

Observations in the B and V bands (Cherespaschuk, 1981) indicate that SS433 is an eclipsing binary system in which the average brightness-temperature of the disc is about twice that of the normal star. At the average brightness maximum, the accretion disc contributes at least 60% of the total optical luminosity of the system.

Long-term V band observations (Kemp et al., 1986), indicate the presence of the 162 day precessional period. The detection of a positive 'hump' in the 162 day light curve at around the secondary optical minimum, but not at the primary minimum, was interpreted as indicating the presence of a thick accretion disc. A Fourier analysis of the same data (Mazeh et al., 1987) reveals the presence of the 13 day binary period and a periodicity of 6.54 days which corresponds to the first harmonic of the orbital period.

Recent observations (Zwitter et al., 1991) indicate that the photometric variability of SS433 consists of three separate classes distinguished by their characteristic time scale Δt: a) $\Delta t \geq 6$ hours represents orbital and precessional motion of the system components. A disc-like outflow such as might occur in the supercritical accretion regime may also contribute; b) 30mins $\leq \Delta t \leq$ 6hrs, possibly the result of an extended corona surrounding the jets and c) $\Delta t \leq$ 30mins, may be linked to the activity of the central engine which could account for the variable brightness of the exposed funnels in the thick accretion disc.

§1.5.4 Radio Observations

This section consists of two complimentary parts: The first relates particularly to radio observations of the extended regions of emission formed by the jets of SS433 whilst the second details

the environment of SS433, namely the supernova remnant W50.

The radio emissions from SS433 have been observed extensively by various means. These include the VLA and MERLIN maps which have an angular resolution in excess of 0.1 arcsec corresponding to $\sim 10^{16}$ cm at 5 kpc and the VLBI maps which have a resolution of ~ 0.01 arcsec. The emissions exhibit quiescent and flaring modes (Fielder et al., 1987; Bonsignori-Facondi et al., 1986; Vermeulen et al., 1993b) with a typical quiescent flux density of ~ 0.7 Jy at 2695 MHz, often doubling during outbursts. The total radio luminosity of the source is $\sim 10^{32}$ erg/s. On the basis of this rate of energy loss, Spencer (1984) has estimated that the power source must have an energy output in excess of $\sim 10^{38}$ erg/s.

The VLA maps show that the morphology of the extended structure evolves over a time scale of days producing a 'corkscrew' type pattern on the plane of the sky (Hjellming and Johnston, 1981a; Gilmore et al., 1981). These changes can be attributed to the ballistic motion of material ejected from the jets. This is a natural extension of the optical kinematic model to the radio regime. A superposition of the jet trajectories as predicted by the kinematic model onto the radio maps makes possible a derivation of the model's free parameters, an estimate of the distance to the source and the removal of the degeneracy between the inclination of the precession and rotation axes to the line of sight (§1.2). In addition this analysis shows the sense of the jet rotation to be clock-wise. The precessing beams are observed to extend to a distance $\sim 2 \times 10^{17}$ cm from the central source (Hjellming and Johnston, 1986) though no emission is detected at greater distances as the jets impinge on the shell of W50. The emission has a spectral index $\alpha = -0.6$ ($S \propto \nu^{\alpha}$) characteristic of optically thin synchrotron emission.

The MERLIN observations show the radio emission to lie predominately on the locus predicted by the kinematic model. The beams do not have a uniform flux density and are composed of discrete knots (Spencer, 1984). These knots are observed to form in pairs, their formation coinciding with radio outbursts, and as they move away from the central source with constant velocity, their brightness decays according to a power law with a time constant of 35 days.

The VLBI maps indicate the presence of diffuse emission (Romney et al., 1987) in addition to the presence of many discrete features. These discrete emission features may be connected with the flaring seen in the radio flux density (Bonsignori-Facondi et al., 1986). The radio emissions, as in the MERLIN observations, generally lie on the locus predicted by the kinematic model though deviations have been reported (Romney et al., 1987). The radio flux density varies on time scales of weeks or months (Fielder et al., 1987; Johnston et al., 1981, 1984) and flares on time scales ranging from a few hours to a few minutes (Seaquist et al., 1979; Seaquist, 1981b). The angular size of the central source is greater than about 5 mas (Geldzahler, Downes and Shaffer, 1981) corresponding to ~ 20 AU at 5 kpc. Vermeulen et al. (1993a), using a complex VLBI system based on one north American and five European sited radio-telescopes, have obtained high resolution observations of SS433 on 6 separate occasions at intervals of 2 days. Their radio maps (Fig. 1.6a) show a strong and variable unresolved core (< 10 marcs)

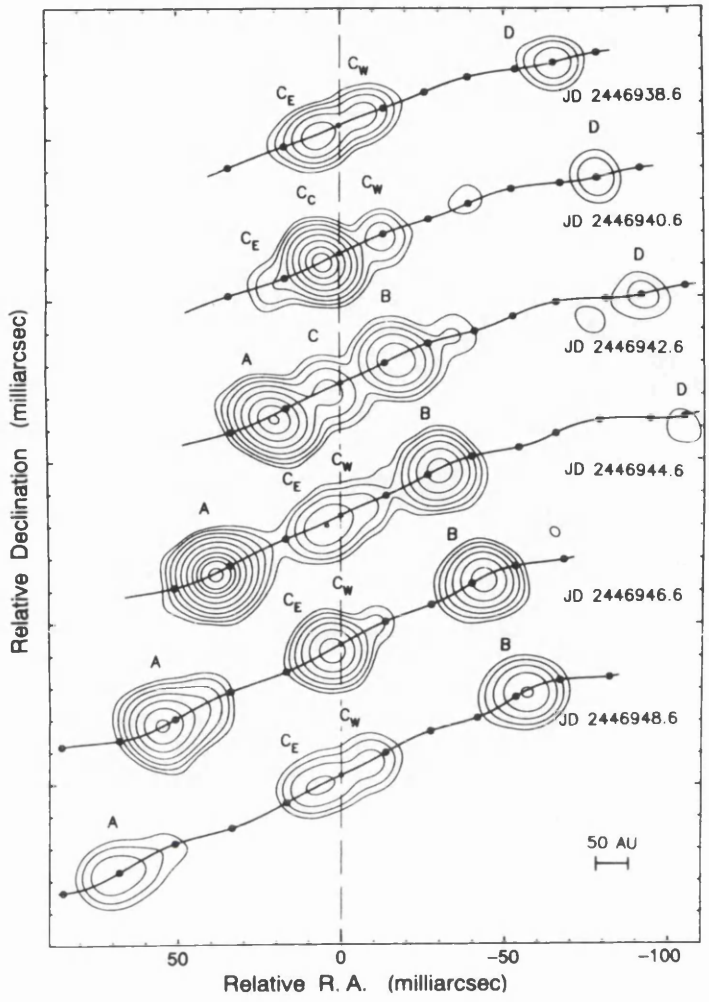

Fig. 1.6a. European VLBI Network images of SS433 observed at two-day intervals. The same absolute contour levels are displayed for all six images which are positioned with equal vertical offsets between their respective centres. The authors' preferred choice for the location of the binary system is shown by the vertical dashed line. The locus of emission predicted by the kinematic model, including nodding motion, is drawn through each image. The markers indicate ejection age intervals of 2 days along the locus whilst the labels refer to the individual features displayed in Fig. 1.6b (from Vermeulen et al., 1993a).

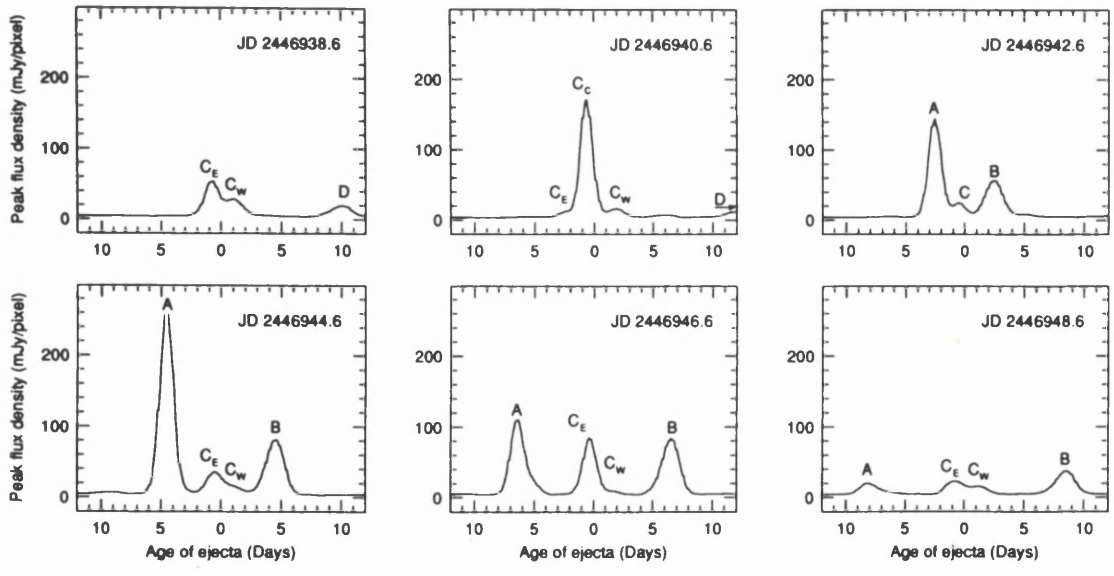

Fig. 1.6b. Crosscuts through the images in Fig. 1.6a along the locus of emission predicted by the kinematical model. All crosscuts have been drawn to the same (arbitrary) intensity scale (from Vermeulen et al., 1993a).

and a series of discrete emission regions located on the predicted precession locus. Crosscuts through these maps along the kinematic model curve (Fig. 1.6b) show a high contrast between the knots and the intervening regions. There appears to be a 'brightening-zone' located at $\sim$ 250 AU from the central source (Vermeulen et al., 1993a) which may occur when one blob overtakes the bow-shock of its immediate predecessor. Even though the blobs move at the same speed, this overtaking is possible since the ejection direction precesses and the bow-shock is directed backwards at the Mach angle from the foremost face of the leading blob. Beyond the brightening zone the blobs fade as they expand adiabatically. Assuming each blob to be a sphere 15 marcs in diameter, a distance to SS433 of 5 kpc and a spectral index of -0.65, Vermeulen et al. (1987) have estimated the luminosity of each blob to be $\sim 5 \times 10^{30}$ erg/s and the energy of each blob to be $\sim 7 \times 10^{41}$ erg.

SS433 is located very near the centre of W50, believed by most workers to have originated from a supernova explosion. This evolutionary path has been challenged by Königl (1983) who has postulated that the shell of W50 may be an expanding interstellar bubble which is driven by a strong stellar wind emanating from the normal star in the SS433 system. The angular dimensions of the ellipsoidal shell of the nebula are 2° along the longer axis by 1°. The scale of W50 is vast: material travelling in the jets at 0.26c takes between 1 000 and 1 500 years to traverse the interior of the shell (Vermeulen, 1989).

The source of radio emission from SS433 is synchrotron radiation, suggesting the presence of a magnetic field which must be ordered because of the high levels of polarization, up to 40% at 2.7 GHz, in some parts of the structure (Downes et al., 1981). Protruding beyond the eastern and western boundaries of W50 are regions of radio emission centered about a position angle of 100°. The central location of SS433 within W50 and the close correspondence between the position angles of the ansae and the precession cone axis (§1.3.1) clearly indicates that the jets of SS433 are interacting with W50; puncturing the shell to form the radio ansae. The angle subtended by the ansae at the core (Geldzahler, Pauls and Salter, 1980) is considerably less than the angle subtended by the precession cone at the core (Niell, Lockhart and Preston, 1981) indicating that the jets are possibly being focused by the ambient medium within W50.

§1.6 Theories

§1.6.1 The Binary System

The standard approach in modelling the binary system is to is to adopt the following geometrical assumptions:

- SS433 is a binary system in which the component orbits are (almost) circular.
- The normal star is phase-locked with the orbital motion and the rotation axis of the star is approximately perpendicular to the orbital plane.
- The normal star fills its Roche lobe.

• The angle i in the kinematic model represents the inclination of the orbital plane to the line of sight.

All that then needs be specified is the geometry of the accretion disc; a feature which obviously makes any predictions model dependent.

On the basis of the above assumptions the mass function (Eq. 1.3) can be expressed as

$$f_m \approx \frac{M_X}{q(1+q)^2} = \frac{M_\star}{(1+q)^2} \qquad \text{where} \qquad q = \frac{M_X}{M_\star} \,. \tag{1.5a,b}$$

Once the mass ratio q is known, the mass function determines the nature of the compact object. Theoretical estimates for the mass ratio have been made by many groups. I will consider several of these below.

Leibowitz (1984) assumed the accretion disc to be cylindrical and the normal star to be a sphere of uniform brightness. By fitting this 10 parameter model to the observed light curve, Leibowitz (1984) found the precession to be retrograde and $q \geq 0.8$ at the 95% confidence level. Adopting the mass function of Crampton and Hutchings (1981), this value for the mass ratio, by Eq. (1.5a), implies that $M_X > 27(12) M_\odot$ where the term in parentheses (as in the rest of this section) corresponds to the lower mass function evaluation. These results indicate that the compact object is a black hole. They do not however represent evidence for a black hole on account of the many additional approximations made.

Antokhina and Cherepashchuk (1987) interpreted the optical light curves in a 6 parameter model in which the accretion disc was approximated by an oblate spheroid. Their model indicates that the normal star fills its Roche lobe with its equatorial region contacting the Roche lobe of the compact object. They found $q > 0.25$ at the 99% confidence corresponding to $M_X > 4.1\,(1.8)\,M_\odot$ by the mass function of Crampton and Hutchings (1981). Model predictions for mass ratios marginally greater than this lower limit do not agree with observations. Taking into account all the observational data Antokhina and Cherespaschuk (1987) preferred the mass ratio $q = 1.2$ and the resulting solution $M_\star = 52\,M_\odot$ and $M_X = 62\,M_\odot$. The accretion disc was found to be thick with an oblateness in the range $0.2 - 0.5$ and a bolometric luminosity in the range $1.4 \times 10^{39} - 1.7 \times 10^{31}$ erg/s, close to or in excess of the critical Eddington limit.

An alternative approach to fitting the entire light curve to the model predictions, as in the two cases discussed above, is to model particular aspects of the light curve such as the width or depth of an eclipse. Such an approach requires fewer model parameters and is simpler but does not represent the system as accurately as the first method. This alternative approach was adopted by Leibowitz et al. (1984) in their analysis of V band light curves. The width of the primary eclipse was estimated to be $(0.30 \pm 0.02) P_{13}$. No flat bottom was detected in the light curve indicating that the accretion disc was not completely eclipsed. The accretion disc was assumed to be geometrically thin and its surface normal aligned along the instantaneous jet axis. Within their model the no-totality condition and the eclipse width constrained $q > 0.43$ corresponding to the solution $M_X > 9.5(4.3) M_\odot$.

Stewart et al. (1987) analysed X-ray eclipse data obtained from the EXOSAT satellite. The X-ray eclipse was coincident with the optical primary minimum providing strong model-independent evidence for the primary minimum being the eclipse of the compact object by the normal star. Their model assumed the accretion disc to be a torus with a triangular cross section and the X-ray emission from the red shifted jet to be obscured by the accretion disc (Watson et al., 1986). The depth and duration of the X-ray eclipse were then used in conjunction with the model assumptions to provide constraints on the relative dimensions of the system components. The X-ray emitting region of the jets was found to be $\sim 10^{12}$ cm long and the accretion disc was deduced to be thick and, assuming a constant disc density, to have a mass in excess of $\sim 10^{-8} M_{\odot}$. Combined optical and X-ray light curve data restricted the mass ratio to the range $1.5 > q > 0.8$. Adopting the mass function of Crampton and Hutchings (1981), the masses of the components for $q = 0.8$ are $M_{\star} \sim 34.3\,(14.9)\,M_{\odot}$ and $M_{\rm X} \sim 27.6\,(11.9)\,M_{\odot}$ and for $q = 1.5$ the masses are $M_{\star} \sim 66\,(29)\,M_{\odot}$ and $M_{\rm X} \sim 100\,(43)\,M_{\odot}$. The inferred stellar radius of $\sim 3 \times 10^{12}$ cm is consistent with a massive normal component. Stewart et al., (1987) noted that a mass ratio of $q \approx 0.1$, required for the compact component to have a mass of $1.4 M_{\odot}$, was marginally allowed by the X-ray constraints but excluded by the optical data. They concluded that all the observations were consistent with both the optical and compact components having masses greater than $10 M_{\odot}$.

Brinkmann et al. (1989) employed the conventional approach to analyse Ginga X-ray observations taken during primary eclipse. With the standard assumption that the primary fills its Roche lobe they determined the mass ratio to be $q = 0.1496$ with corresponding masses for the two components of the system $M_{\star} = 14 M_{\odot}$ and $M_{\rm X} = 2.1 M_{\odot}$. They noted that a slightly longer duration of the eclipse, or possible obscuration of the central parts of the jets by a thick disc, would lower the mass of the compact component making it impossible to distinguish whether the compact object is a neutron star or a black hole. Brinkmamm et al. (1989) concluded that two of the standard assumptions, specifically that the primary fills its Roche lobe and that it rotates synchronously with the binary orbit, required revision.

There have been numerous other recent models not discussed here (e.g. Zwitter and Calvani, 1989, 1990; Kawai et al., 1989) all of which, like those detailed above, favour a black hole as the compact candidate but do not completely eliminate a neutron star as the alternative.

It is evident from Eq. (1.3) that the mass function is proportional to K^3. The amplitude modulation must therefore be precisely known if reliable values are to be obtained for the masses of the components. In a recent investigation of the He II $\lambda 4686$ line, D'Odorico et al. (1991) found the amplitude of the Doppler modulation to be $K = 112 \pm 5$ km/s corresponding to the mass function $f = 2.0 \pm 0.3\,M_{\odot}$. Adopting the mass ratio $q \approx 0.245$ (Zwitter and Calvani, 1989) and the revised mass function, the corresponding masses of the compact object and the normal star are $M_{\rm X} \approx 0.8 \pm 0.1\,M_{\odot}$ and $M_{\star} \approx 3.2 \pm 0.4\,M_{\odot}$ respectively. These results imply that the compact component is a neutron star rather than a black hole. Given the high quality of the spectra obtained by D'Odorico et al. (1991) a significant error in their derived value of

K seems unlikely. A higher mass ratio could be inferred if the primary is moderately flattened or a wind-type mass flow in the system obscures the X-rays for a small fraction of the eclipse (Brinkmann et al., 1989).

It is evident that there is no consensus on the nature of the binary components though, if the recent Doppler modulation of D'Odorico et al. (1991) is accepted, then at present the neutron star scenario is the marginal favourite.

§1.6.2 The Accretion Disc

The observational evidence for a geometrically thick (e.g. Anderson et al., 1983a; Kemp et al. 1986; Wagner et al. 1986), luminous (eg. Cherespaschuck, 1981) accretion disc is very strong. The presence of a geometrically thick accretion disc is also inferred by the results of modelling the 162 day light curve (§1.6.1) (Leibowitz, 1984; Antokhina an Cherespaschuk, 1987). Super-critical accretion onto the compact object was realised to be the power source for the jets (e.g. Zealy, Dopita and Malin, 1980; Martin and Rees, 1978; Begelman et al., 1980; Sarazin, Begelman and Hatchett, 1980) largely on the basis of the large kinetic energy of the jets and the intensity of the moving emission lines.

Wagner (1986) found the diameter to thickness ratio $d/h \leq 1.3$ indicating that the accretion disc more closely resembles a sphere than a greatly flattened sphere or disc whilst Stewart et al. (1987) found $d/h \sim 0.4$. The latter group additionaly concluded that for the accretion disc to provide the observed degree of obscuration of the red shifted X-ray jet it must have a minimum number density $n_e \sim 10^{13}\,\mathrm{cm}^{-3}$ at a height of 5×10^{11} cm above the orbital plane.

For fully ionized matter in which Thomson scattering provides the main source of opacity, the Eddington luminosity for an object of mass M is

$$L_{\mathrm{Edd}} = \frac{4\pi \mathrm{G} c m_p M}{\sigma_{\mathrm{T}}} = 1.257 \times 10^{38} \frac{M}{M_\odot}\,\mathrm{erg/s} \tag{1.6}$$

where m_p is the proton mass and σ_{T} is the Thomson cross section. This is the maximal luminosity of any non-rotating, stationary, electromagnetically neutral object. Rotating objects can however have $L > L_{\mathrm{Edd}}$. In particular objects with large shear, small vorticity and small density can have $L/L_{\mathrm{Edd}} \gg 1$. These conditions exist in thick accretion discs (Abramowicz, Calvani and Nobili, 1980). The bolometric luminosity of the accretion disc is $\sim 10^{39}\,\mathrm{erg/s}$ (Cherespaschuck, 1981). For a compact object of mass $M \sim M_\odot$ such a luminosity exceeds the Eddington limit by about one order of magnitude. If Thomson scattering is the main source of opacity then, by equating the Eddington luminosity to the accretion luminosity it can be deduced that the critical accretion rate, $\dot{M}_{\mathrm{crit}}$, for accretion onto a central object of radius $R_\star$ is

$$\dot{M}_{\mathrm{crit}} \equiv \frac{4\pi m_p c R_\star}{\sigma_{\mathrm{T}}} = 1.555 \times 10^{-8} \left(\frac{R_\star}{10\mathrm{km}}\right) M_\odot/\mathrm{yr}\,. \tag{1.7}$$

Super-Eddington luminosities are possible only if $\dot{M} > \dot{M}_{\mathrm{crit}}$.

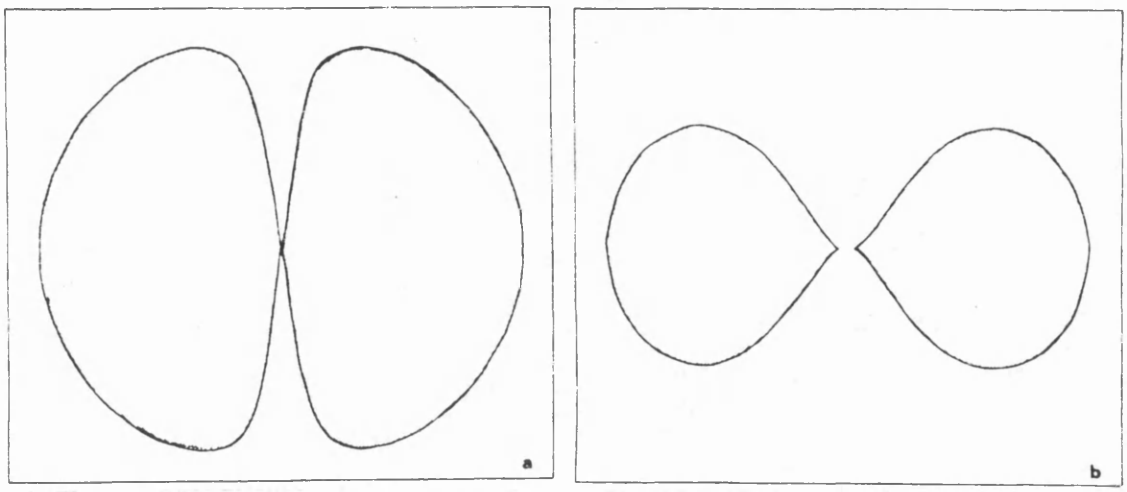

Fig. 1.7. The schematic shape of thick accretion disks: (a) very supercritical accretion as in SS433; (b) mildly supercritical accretion as in AGNs (from Abramowicz et al., 1987).

The shapes of theoretical thick disc models are toroidal and in the limiting case resemble a sphere with two deep, narrow funnels along the rotation axis (Fig. 1.7). A compact object embedded in a thick accretion disc is attractive since accretion in such a deep potential well provides an efficient mechanism for energy generation. This is particularly true for a thick accretion disc in which the accretion rate must be high and possibly super-critical. Consequently the luminosity will be extremely high and may exceed the Eddington limit. In addition the narrow funnels provide a means of collimating and directing the jets. This is of great significance to SS433 where the jets are highly collimated, expanding with a cone half-angle less than 0.1 radians (Begelman et al., 1980), and are oppositely aligned to a very high degree (see §1.6.4).

Abramowicz, Calvani and Nobili (1980) found the main properties of a thick accretion disc orbiting a black and radiating at or beyond the maximal limit to be dependent on the mass of the central object and the ratio $r_{\rm out}/r_{\rm in}$ where $r_{\rm in}$ is the distance from the centre of the compact object to the cusp on the disc located at the formation point of the accretion stream (the inner accretion disc radius) and $r_{\rm out}$ is the limiting distance from the centre of the compact object beyond which the disc can be considered thin. Calvani and Nobili (1980, 1981) have described a model for SS433 based on a thick accretion disc orbiting around a black hole and found the values $r_{\rm in} = 10^6\,{\rm cm}$ and $r_{\rm out} = 10^5\,r_{\rm in}$ to be in agreement with observations. Assuming that $r_{\rm in} \approx R_\star$ then, by Eq. (1.7), the critical accretion rate for a compact object with an inner accretion disc radius $r_{\rm in} = 10^6\,{\rm cm}$ is $\dot{M}_{\rm crit} \approx 1.6 \times 10^{-8}\,M_\odot/{\rm yr}$. In the SS433 system the normal star transfers mass to the accretion disc at a rate of $\sim 10^{-4}\,M_\odot/{\rm yr}$ (van den Heuvel, 1981). Such an accretion rate onto a solar mass compact object evidently constitutes super-critical accretion by about 4 orders of magnitude and amply satisfies the necessary condition for the system to have a super-Eddington luminosity.

§1.6.3 The Precession Mechanism

Following the conception of the kinematic model (Abell and Margon, 1979) and the discovery of the binary nature of SS433 (Crampton, Cowley and Hutchings, 1980), the large periodic Doppler shifts of the moving lines have been ascribed to the precessional motion of the jets about the

orbit-normal of the binary system. This precession is conventionaly interpreted as the response of the spin angular momentum vector to the gravitational interaction of the spinning object with the other member of the binary system. Four models were initially suggested but two of these, namely Lens Thirring and geodetic precession, were eliminated because their predicted precession periods were too slow. The two surviving models for the precessional motion are the 'slaved-disc' model and the dynamical model both of which I will discuss below.

The slaved-disc model was initially developed by Roberts (1974) to explain the 35 day periodicity in the Her-X system and was proposed as a natural explanation of the 164 day precession period in SS433 by Katz (1980). The model has been discussed in the context of SS433 by van den Heuvel, Ostriker and Petterson (1980) and Whitmire and Matese (1980). The basic scenario for the slaved-disc model is as follows: The spin axis of the normal star is misaligned with the orbit-normal of the binary system (as may be the case following a supernova explosion). The gravitational torque applied by the compact object will then force the spin axis of the secondary to precess at a rate dependent on the mass of each component and the dynamical ellipticity parameter ϵ (Roberts, 1974). For small centrifugal distortions, the dynamical ellipticity $\epsilon = {\omega_\star}^2 {R_\star}^3/GM_\star$ where $\omega_\star$, $R_\star$ and $M_\star$ are the angular velocity, radius and mass of the secondary respectively. If the residence time of the accreted material in the disc is short compared to the precession and nodding periods then the accretion disc normal will follow the precessing spin axis of the normal star. In the slaved-disc model the precession is retrograde if the stellar rotation is prograde (Katz, 1981). Such retrograde rotation of the precessing jets has been observed (e.g. Brinkmann, Kawai and Matsuoka, 1989). Whitmire and Matese (1980) showed that a precession period of 164 days for the normal star was possible for reasonable estimates of the dynamical ellipticity parameter.

The dynamical model (Collins, 1985; Collins and Newsom, 1986) describes the motion of the jets in terms of the classical mechanics description of a distorted body undergoing driven precession as a result of the presence of a close companion. This is the same Newtonian driven precession as occurs in the earth-moon-sun system. It is generally accepted that the jets are formed close to one component of the SS433 system. In the dynamical model it is assumed that the companion exerts torques on the source component forcing it to precess. If the jets are constrained to follow the principal axis of this component then they too will precess. The tidal deformation that accompanies any gravitational interaction of sufficient magnitude to produce tidal-forced precession does not affect the dynamical motion of the system except through small changes in the moments of inertia. In the formulation of the dynamical model the components are treated as rigid objects which they certainly are not. Such an approach however is vindicated by the work of Papaloizou and Pringle (1982) and Mestel and Takhar (1972) who have shown that stars will precess as if they are rigid bodies for extended periods of time. For a precession period of 163 days, the dynamical model requires that the spin rate of the precessing object be of the order of the orbital frequency (Collins, Newsom and Boyd, 1981). An interesting feature of pure gravitational precession, be it either Newtonian or general relativistic geodetic

spin-orbit coupling, is that the precession rate does not decay (DeCampli, 1980). In the case of a precessing neutron star this means that the precession rate is not a good indicator of the interior dynamics of the star since it is more sensitive to 'starquakes' and variations in accretion or wind torques.

The choice of model remains controversial. The slaved-disc model requires that the companion star has a misaligned and precessing spin. One problem with this model is that the orbits in SS433 are nearly circular (the orbital eccentricity $\epsilon \sim 0.05$ (Collins and Newsom, 1986)) and binary systems that display such tidal circularisation are unlikely to show evidence for precessional motion (Papaloizou and Pringle, 1982). A difficulty encountered with the driven precession model is that it requires the disc to have a low viscosity (Katz, 1986). This seems unfeasible on account of the observed precession and 6 day periods of the inner regions of the disc (Katz et al., 1982). A possible solution to this problem is a heterogeneous model in which the viscosity is small near the disc midplane and large near its surface layers so that the mass averaged viscosity is low thereby permitting driven precession and the slaving of the inner disc to the outer disc's precession by rapid mass transfer (Katz et al., 1982). The model, however, fails to predict the observed amplitude of one of the 6 day nodding motions (see §1.3.2).

Regardless of the adopted model it is assumed that the jets follow the motion of the disc and remain aligned along its instantaneous axis. The best argument supporting this assumption is that the random deviations in the jet direction are strongly anti-correlated (Katz and Piran, 1982). These minor deviations in the jet orientation are easily detectable through spectroscopy: e.g. a 1° tilt of the jets towards the observer results in a Doppler shift of $\sim 1000\,\mathrm{km/s}$. If the motions of the accretion disc can be determined from these deviations then SS433 presents an invaluable opportunity for the study of accretion disc dynamics.

§1.6.4 Jet Energetics, Collimation and Acceleration

The kinetic luminosity of the jets in SS433 is vast. As discussed in §1.5.3 above, the major axis of W50 is aligned with the jets of SS433 which indicates some interaction of the jets with the ambient medium. Estimates of the work required to expand the supernova shell against the interstellar medium (e.g. Begelman et al., 1980; Zealy et al., 1980; Kirshner and Chevalier, 1980) typically indicate that the kinetic luminosity of the jets must be in excess of $\sim 10^{39}\,\mathrm{erg/s}$. From an upper limit estimate of the change in the orbital period Margon and Anderson (1989) have concluded that mass-loss rates exceeding $10^{-3}\,M_\odot/\mathrm{yr}$, corresponding to jet kinetic energies exceeding $\sim 10^{42}\,\mathrm{erg/s}$, can be excluded. Analysis of cross spectrum data indicates that the kinetic luminosity of the jets lies in the range $10^{39} - 10^{40}\,\mathrm{erg/s}$ (Zwitter et al., 1989) which corresponds to the Eddington luminosity (Eq. 1.6) for a $10 - 100\,M_\odot$ star. It is therefore obvious that if the power source is accretion onto a compact object of mass less than $\sim 10\,M_\odot$, then the Eddington luminosity limit must be exceeded to power the jets.

The narrowness of the moving spectral lines, typically with a width no greater than 10% of their displacement, implies that the opening angle of the jets is less than ~ 0.1 radians

(Begelman et al., 1980). The work of Shakura and Sunyaev (1973) showed that jet collimation by the confining pressure provided by the funnels within a thick accretion disc is possible. This mechanism has been applied to SS433 by several authors (e.g. Davidson and McCray, 1980; Sikora and Wilson, 1981; Calvani and Nobili, 1981; Bodo et al., 1985). Sikora and Wilson (1981) showed that the angle of the beam produced within a thick accretion disc funnel depends on the region in which the beam material originates and, as a rough guide, material originating at a distance less than $\sim GM/c^2$ from the compact object of mass M is collimated with a beam angle comparable to the opening angle of the funnel. Begelman and Rees (1984) have proposed that the jets are collimated by passing through narrow de Lavel nozzles which are situated just beyond the magnetopause of a magnetised neutron star. Eichler (1983) has argued that a jet with a finite opening angle can be focused on entering a homogeneous medium. The focal length is nearly independent of the jet opening angle if all other jet parameters remain the same. The presence of such a process is supported by observational evidence. It has been shown (Krautter et al., 1983; Begelman et al., 1984) that collimation of a relativistic gas propagating in pressure equilibrium into an ambient medium will occur if the ambient pressure decreases more slowly than r^{-4}. Kochanek (1991) has investigated the effect of toroidal magnetic fields embedded in a precessing jet and found that such tori could overcome the transverse expansion and focus the jet. This mechanism is important in SS433 if $L_{39}B_3{}^{-1} \leq 0.05$ where $L = L_{39}10^{39}$ erg/s is the kinetic luminosity and $B = 10^{-3}B_3$ G is the initial toroidal magnetic field. Another possibility, which was tentatively suggested by Davidson and McCray (1980), is that the differential action of radiation pressure on the electrons and ions within the jet may generate an EMF which may be sufficient to drive a current in the jet and consequently induce 'pinching' of the beam in the manner discussed by Benford (1978). The apparent absence of decollimating effects may be indicative of the physical environment in the jet formation region. One such mechanism is gravity decollimation which can be induced in a jet by the strongly curved spacetime surrounding a black hole. If the jet consists of non-interacting particles, the decollimation can easily be obtained by comparing the opening angle of a particular geodesic at infinity with the initial opening angle at the origin of the jet. Lu and Pineault (1988) have investigated the effect of this decollimating mechanism in a Schwarzschild metric and found it to be dominated by collimating effects unless the sonic point of the jets is located very close to the black hole.

The jets are probably accelerated by radiation pressure. This is evident from consideration of the alternative where the pressure is due to ions and electrons: in order for this pressure to deliver a terminal speed of 0.26c, the initial gas sound speed would have to be comparable to this terminal speed which would require a temperature of $\sim 10^{11}$ K (Davidson and McCray, 1980). At such a temperature and for gas densities applicable in SS433, blackbody radiation pressure would exceed the gas pressure by many orders of magnitude. For the gas pressure to be dominant the radiation energy density would have to be well below the appropriate blackbody density which could only occur if the optical depth was to be implausibly low. Consequently,

radiative acceleration is the most frequently discussed mechanism for accelerating the jets in SS433.

The observed constancy of the jet speed over extended periods of time is a problem that needs to be addressed by any prospective acceleration mechanism. One of the earliest attempts was the 'line locking' mechanism proposed by Milgrom (1979b). A similar mechanism had previously been discussed in connection with redshifts in quasars (e.g. Strittmatter and Williams, 1976). For the mechanism to function only the following conditions need be satisfied: i) The intensity of the underlying continuum radiation is sufficient to drive gas away from the compact object; ii) Momentum transfer takes place predominately through Lyman-line absorption by some hydrogenic ion; iii) The continuum flux falls sharply for frequencies (as determined in the source frame) above the Lyman edge of the absorbing ion. The gas that comprises the jet will then be accelerated up to a terminal speed β_t, in units of the speed of light, such that the Lyman edge wavelength in the comoving frame is equal to the Lyman-α wavelength in that same frame. This occurs when $\gamma_t\,(1-\beta_t) = \lambda_c/\lambda_\alpha = 3/4$ (where λ_c is the unshifted Lyman-edge wavelength and λ_α is the comoving Lyman-α wavelength) or equivalently when $\beta_t = 7/25$. This is very close to the observed terminal speed of 0.26c; in reality the agreement is even better because the cut-off in the underlying continuum flux occurs at a slightly greater wavelength than λ_c due to the accumulation of Lyman lines in the environment of the radiation source (Shapiro, Milgrom and Rees, 1986).

The term 'line locking' refers to the fact that once the terminal speed β_t is reached the jet material can neither accelerate nor decelerate: If the jet velocity were to fall below β_t absorption of radiation emitted from below the Lyman edge in the source rest frame would recommence so forcing the jet speed back up to β_t. On the other hand, if the jet velocity were to exceed β_t the momentum transferred to the jet material would drop sharply because the only photons capable of exciting the Lyman lines are those that originate from beyond the Lyman cut-off where the continuum flux is very low. The jet velocity would then drop back down to the terminal speed β_t.

In a detailed analysis of the line locking mechanism, Shapiro, Milgrom and Rees (1986) found the acceleration region to roughly lie in the range $10^{12} L_{38}{}^{\frac{1}{2}} Z^{-4}$ cm to 10^{15} cm (where Z is the nuclear charge of the hydrogenic ion and L_{38} is the total luminosity in units of 10^{38} erg/s) indicating that the heavier the hydrogenic ion, the closer to the compact object the acceleration can begin. If the line locking element is hydrogen then the gas must be highly clumped with a clumping factor ($\langle n^2\rangle/\langle n\rangle^2$) of the order of the square of the Mach flow number whilst if the line-locking element is iron then no clumping at all is necessary. Line locking by both hydrogen and helium can be rejected since they require a minimum initial distance of 2×10^{13} cm and 10^{12} cm respectively whilst observations indicate attainment of a terminal speed within $\sim 10^{12}$ cm from the central source. (A closer starting point results in full ionization and a complete break-down of the line locking mechanism.) Acceleration by the line locking of hydrogenic Fe is marginally possible within the required distance but necessitates that the abundance of Fe in the flow

relative to hydrogen be at least $\sim$ 200 times the solar value. The results of Watson et al. (1986) indicate that the Fe emission in the jets has an equivalent width typical for material with cosmic abundances so ruling out Fe as the line locking element. It is evident that the line locking mechanism has severe problems in its application to SS433 and is probably not the initial acceleration mechanism though it is possible that it plays some rôle as a 'speed governor' once the jet material has been accelerated to near the terminal speed.

Radiative acceleration within a thick accretion disc has been investigated as a possibility for SS433 by several authors (e.g. Davidson and McCray, 1980; Calvani and Nobili, 1981; Bodo et al., 1985; Nobili, Calvani and Turolla, 1985; Icke 1989; Eggum, Coroniti and Katz, 1985). The maximum radiation pressure within the disc funnel must be comparable to the emergent kinetic energy density of the jet corresponding to blackbody temperatures between $10^{5.6}$ and $10^{7.4}$ K and certainly not much higher than 10^8 K (Davidson and McCray, 1980). Calvani and Nobili (1981) found that plasma beams can be accelerated to relativistic velocities and collimated within the accretion funnel. Bodo et al. (1985) investigated a two-phase jet model which is an adaptation of the stellar wind theory model of Ferrari et al. (1984, 1985) that had been proposed initially as a means of modelling jet acceleration in active galactic nuclei. The gas within the accretion disc funnels is assumed to be optically thin. The jets are accelerated to relativistic terminal speeds which are dependent on the funnel geometry and the radiation field within the funnel at distances less than 10^9 cm from the central source. The emergent beams have a temperature $\geq 10^7$ K. The jets then cool and fragment, as a result of thermal instabilities, forming condensations with a temperature $\leq 10^4$ K which then act as the sources of the moving emission lines. These small clouds then evaporate at distances of $\sim 10^{15}$ cm , in agreement with the observed length of the optical jets, due to conduction from the hotter inter-cloud medium. The density contrast in such jets is $\sim 10^3$ and the corresponding clumping factor is no greater than $\sim 10^{\frac{3}{4}}$. However, imposing the condition that the flow within the funnel be optically thin has the disadvantage of constraining the mass efflux rate, and efficiency, to rather low levels (Sikora and Wilson, 1981) in contradiction to the observations. The model adopted by Icke (1989) differs from the rest since it assumes that the jets are not continuous but instead consist of discrete clouds or 'bullets'. This is the approach that I have followed and will leave a detailed analysis of this mechanism till later. One possible objection to such models is their low efficiency: to retain the form of an accretion disc with a funnel opening angle of $\sim$ 0.1 radians, requires about 99% of the infalling energy leaving only 1% to contribute towards the radiation and kinetic energy of the jets (Abramowicz, Calvani and Nobili, 1980).

A greater efflux rate can be achieved if the jet is dense and so capable of trapping radiation. Begelman and Rees (1984) have suggested that this radiation may be introduced into the gas by mechanical mixing near the surface of a neutron star which could be achieved either by highly inhomogeneous accretion or by the magnetosphere of the neutron star driving shocks into the gas. Adiabatic expansion of the jet subject to inertial confinement by the funnel walls utililses the energy of the trapped photons as well as their momenta to drive the jet so increasing

the efficiency of the process. The final jet velocity is dependent primarily on the magnetic moment and period of the neutron star and is quite insensitive to the mass inflow rate whilst the predicted jet kinetic energy flux is in the range $\sim 10^{39-40}$ erg/s. The drawback however is that the lateral force exerted on the funnel walls increases the funnel aperture and decreases their potential for collimation.

Eggum, Corranti and Katz (1985) performed a numerical simulation of the coupled dynamics of the accretion disc and the jet and found the mass efflux rate to be below that occurring in SS433. Katz (1987) has proposed that this discrepancy may be explained by an instability in the balance between photoionization and radiative recombination inherent in flows subject to radiation pressure. If these instabilities grow then clumping factors up to 10^8 may form. These density enhancements would then be sufficient to reconcile the low mass efflux rates predicted by supercritical accretion disc models with the strong intensity of the moving line emissions.

§1.6.5 Alternative Theories

As an alternative to the kinematic model Kundt (1985, 1987) has proposed that the moving emission lines are emitted near the inner edge of an accretion disc at a distance of 10^7 cm from the centre of a 1.4 $M_\odot$ neutron star. The spin of the neutron star is inclined at 53° to the orbital plane and forces the inner edge of the accretion disc into its rotational plane via its corotating magnetosphere. The moving emission lines are then emitted in the approximate region of the two intersections of the inner accretion disc with the outer one. The torque between the neutron star and the accretion disc forces the neutron star to precess. Within this model the kinematic model parameters are: $i = 67°$, $\theta = 53°$ and $\beta > 0.9999$. The distance to SS433 becomes 3 ± 0.5 kpc.

Fabian et al. (1986) have proposed a phenomenological triple star scenario for SS433 as an alternative to the conventional binary model. They suggested that SS433 consists of a short period binary ($\sim$ 1.5 days) orbiting a massive OB star. The close binary then precesses in a manner similar to the Earth-Moon system. Mass transfer takes place either within or on this close binary leading to the formation of jets. Eclipses within the close binary system should produce a 1.5 day photometric modulation which to date has not been observed.

Manka and Bednárek (1992) have suggested a string theory interpretation of SS433 in which a captured, precessing ellipsoidal loop of a superconducting cosmic string both modulates the speed of the jets and collimates them.

A novel alternative to radiative acceleration has been proposed by Harrison (1990). The jets originate in some way at the surface of a neutron star where the protons have a kinetic energy equal to the pion mass (139.57 MeV/c^2). Harrison (1990) assumes the typical escape energy for a proton from a neutron star to be equal to the muon mass (105.66 MeV/c^2). Consequently, far from the neutron star the protons have an energy equal to the pion-muon mass difference which fortuitously corresponds to a proton moving with speed 0.262c. The pion rich condensates necessary for this process may be formed deep in the interior of the neutron star

as a result of rapid oscillations induced by some thermodynamic instability perhaps at a particularly evolutionary stage. These condensates then rise to the surface of the neutron star, expanding rapidly as they do so, following the path of least resistance along the rotation axis of the neutron star and emerge from the surface as hypersonic jets. This scenario is similar to terrestrial volcano theory where hot magma replaces the pion rich condensates.

§1.7 The Evolutionary Track

In common with the massive X-ray binaries, the SS433 system is composed of an early-type star plus a compact object. The main discriminating factor appears to be the accretion rate: in SS433 this is $\sim 10^{-4} - 10^{-3} M_{\odot}$/yr whilst in X-ray binaries the rate is typically less than $\sim 10^{-8} M_{\odot}$/yr and corresponds to the Eddington limit. The possible progenitor for SS433 may have been a massive X-ray binary (van den Heuvel, 1981) with a period between that of Vela X-1 (8.96 days) and 4U1223-62 (34.5 days). The possible sequence of evolutionary phases has been discussed by van den Heuvel (1981) and is illustrated in Fig. 1.8. Beginning from an unevolved system consisting of a $20M_{\odot}$ star and an $8M_{\odot}$ star (phase a) the anticipated evolution is as follows:

The more massive component evolves faster and begins to fill its Roche lobe and transfer matter onto the less massive component (phase b). After completion of the first phase of mass transfer the system is a Wolf-Rayet binary and consists of a WR star and a massive OB star (phase c). After a further period of about 5×10^6 yr, the WR star explodes as a supernova to become a compact object. Due to the asymmetry of the supernova explosion the compact star receives a randomly oriented 'kick' velocity. The impact of the SN shell on the OB star causes a disruption but does not destroy the entire system which becomes a run-away star. The run-away velocities of the remaining components are of similar magnitude and are less than the initial orbital velocity of the OB star and independent of the kick velocity (De Cuyper, 1981). If the compact object formed in the SN explosion is a pulsar, an active period of $\sim 10^4$ yr may begin (phase d) as is observed in the Crab pulsar. Once this activity has ceased the system will probably lie dormant for about $\sim 10^6$ yr until the OB star has evolved into a supergiant and begins to oveflow its Roche-lobe or emit a strong stellar wind. The compact companion now becomes an X-ray source (phase f) which is eventually quenched when the accretion occurs on the thermal timescale of the supergiant over a period of about $3 - 10 \times 10^4$ yr . These stages constitute the standard evolutionary scenario for an X-ray binary. The accretion rate is now $10^{-4} - 10^{-3} M_{\odot}$ /yr and far in excess of the critical accretion rate of $\sim 10^{-8} M_{\odot}$/yr. This accreted matter is expelled from the system by the super-Eddington luminosity from the compact star in directions perpendicular to the accretion disc which may grow to fill its Roche lobe (phase g). The matter ejected in the beams will carry angular momentum from the system causing the orbital period to decrease which, after $\sim 10^4$ yrs, will lead to the formation of a very close binary system comprised of the evolved core of the massive star and the compact

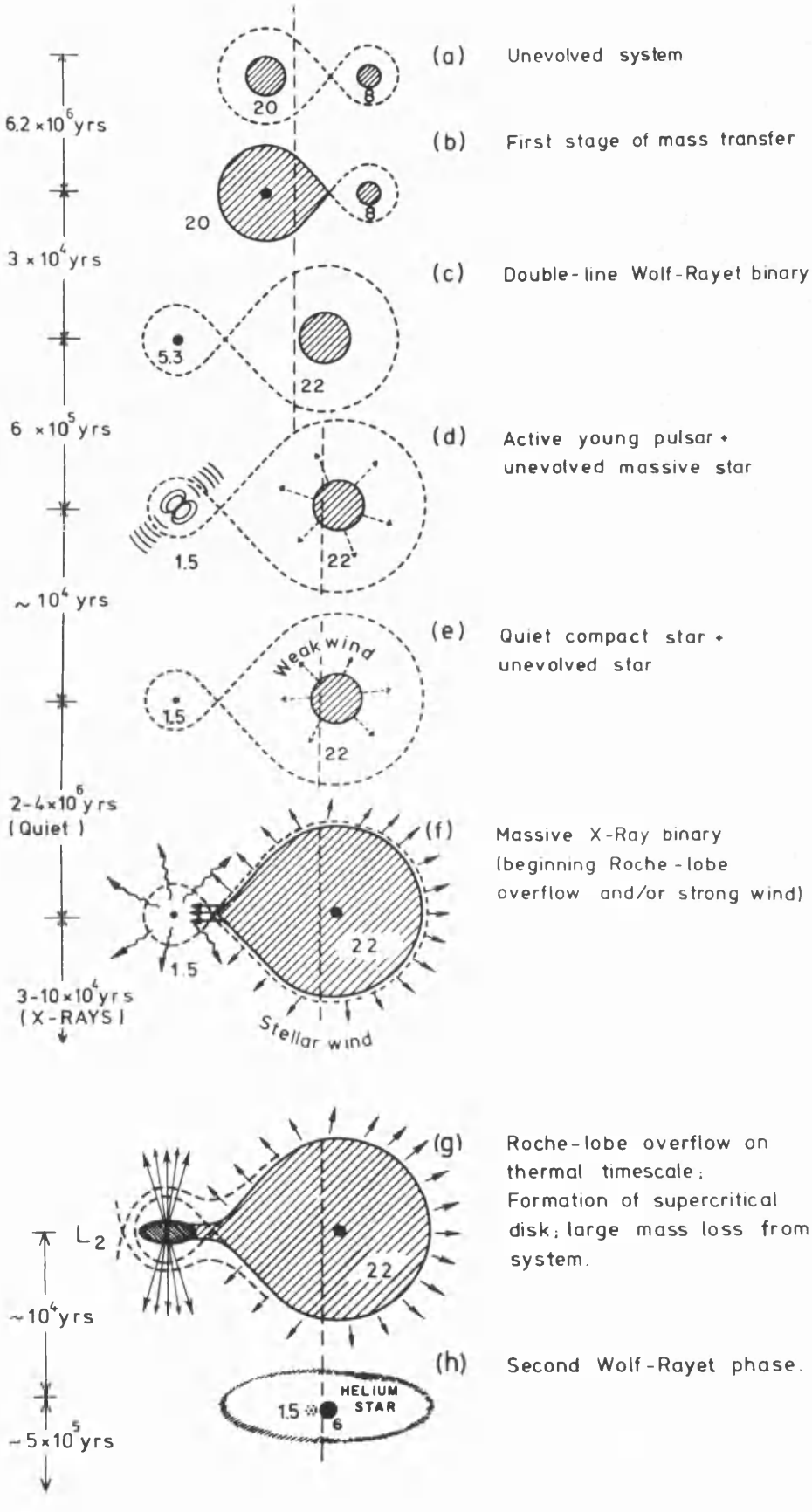

Fig. 1.8. The standard evolutionary sequence for a massive close binary system up to the X-ray stage, frames (a) to (f) inclusive, plus the expected further evolution of a massive X-ray binary, frames (g) and (h) (from van den Heuvel, 1981).

object. If the core mass is $\sim 6 - 8\, M_{\odot}$ it will probably resemble a WR star (phase h).

If this is indeed the evolutionary path then any supernova remnant formed in the process should have disappeared long ago. This requires that W50 has been formed solely by the jets of SS433 (van den Heuvel, 1981). An alternative scenario which does permit the existence of a young SN remnant is 'tandem' evolution. In this model the system begins with two stars with near equal mass. The evolutionary phases are illustrated in Fig. 1.9.

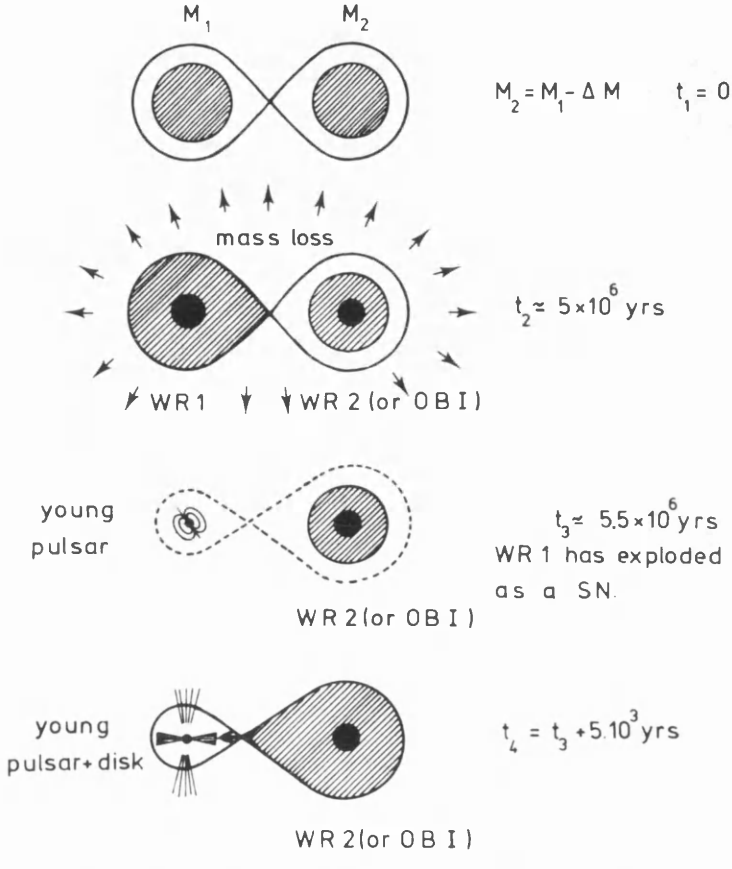

Fig. 1.9. The possible evolution of a massive close binary with an initial mass ratio close to unity. When the more massive companion explodes, its companion already is a post main-sequence star which soon afterwards begins to overflow its Roche lobe. This leads to the formation of a supercritical accretion disk around a young compact star. The system may, at that time, still be surrounded by a SN remnant (from van den Heuvel, 1981).

§1.8 Analogous Objects

Obvious similarities exist between SS433 and active galactic nuclei, including radio galaxies and quasi-stellar objects: both exhibit well collimated relativistic outflows. Indeed this similarity was the motivation behind the twin-jet model of Fabian and Rees (1979). The jets in an AGN, as in SS433, are believed to be formed by the accretion of matter onto a compact object which then dissipate their energy in double radio lobes. In both cases this dissipation occurs over a length scale many orders of magnitude greater than the scale on which the jets are formed. The radio maps of the extended structure of SS433 have a corkscrew appearance and are morphologically similar to radio maps of AGN indicating that precession too plays a rôle in AGN though with a period in excess of $\sim$ 10 000 years. There are obvious differences: the principal emissions

from SS433 are recombination lines produced by a thermal plasma moving at 0.26c whilst the emission from extragalactic jets is largely nonthermal synchrotron radiation from relativistic electrons. An additional dissimilarity, noted briefly in §1.3.2, is the region in which the jets are collimated and directed: in SS433 this seems to occur close to the jet source whilst in AGN the same function is believed to be performed by the outer regions of a geometrically thick accretion disc. The best evidence for any analogy between SS433 and extragalactic jets would be the observation of jet velocities of 0.26c; jet velocities in AGN are highly relativistic and to date, none have been found with velocities comparable to those in SS433. It seems that SS433 may not simply represent a scaled down version of an AGN though the case is by no means closed.

It is reasonable to conclude that, since SS433 is so distant, the galactic density of such objects is very low and that only a few may exist in our Galaxy. It is not inconceivable that all but one of these is obscured leaving SS433 as the only observable representative of its class in the entire Galaxy.

To date, none of the galactic objects proposed as belonging to the same class as SS433 such as the binary system Circ X-1 (Bradt and McClintock, 1983) and the bipolar nebula surrounding HD 44179 (Webster, 1979) have displayed the spectra necessary to warrant membership. If the high absolute magnitude estimated for SS433 (see §1.4.1) is a generic feature then it should be possible to observe analogous objects in the Magellanic Clouds. If present in M31, such an object would be within the spectroscopic range of large telescopes. In either case the outstanding problem is knowing exactly where to look.

Chapter 2

Theoretical Prelude

§2.1 Introduction

The theoretical framework for the physical mechanism of radiative acceleration is formed, principally, by the disciplines of special relativity and radiative transfer. In Part I of this two part chapter I will clarify some common terms and definitions encountered in special relativity and radiative transfer. This is followed by the introduction of a couple of useful Lorentz invariants (i.e. quantities which are the same in all Lorentz frames) and some transformations that are of importance in Part II as well as a discussion of the physical phenomena of Doppler shift and aberration. As will become evident in later chapters, these phenomena play a crucial rôle in governing the speed of the jet. Part II begins with comment on the advantages that fragmented jets have over their continuous counterparts and with speculation on the means of formation of such fragmented jets. Building from the theoretical foundations laid in Part I, I conclude Part II with a derivation of the general vector equation of motion for a spherical jet fragment moving in the time independent radiation field of a blackbody emitter.

For a more complete analysis of the topics discussed in Part I the reader should consult: for special relativity e.g. Rindler (1982) and for radiative transfer and special relativity e.g. Mihalas and Mihalas (1984) and Rybicki and Lightman (1979) and for radiative transfer e.g. Swihart (1981) and Shu (1991).

Part I

§2.2 Special Relativity

The theory of special relativity is based on two fundamental principles, both postulated by Einstein. The first is the relativity principle which states that all inertial frames are totally equivalent for performing all physical experiments with the implication that all the laws of physics must have an invariant form. The second principle, commonly referred to as the universality of the speed of light, states that the speed of light is the same in any inertial frame regardless of the motion of the source. The latter postulate is incompatible with the Galilean transformation in which space and time are separate entities. Compatability is retained by the coupling of space and time into one entity known as spacetime and by the introduction of the Lorentz transformation.

§2.2.1 The Lorentz Transformation

Consider two inertial frames $\angle S$ and $\angle S'$ each containing a cartesian coordinate lattice. Suppose that $\angle S'$ is moving with uniform velocity v in the z-direction of $\angle S$ with both frames having coincided at $t = t' = 0$; the standard frame configuration. Invoking both postulates and imposing the constraint that any transformations be linear yields the standard Lorentz transformation equations

$$x' = x \quad , \quad y' = y \quad , \quad z' = \gamma(z - vt) \quad , \quad t' = \gamma\left(t - \frac{vz}{c^2}\right) \qquad (2.1a,b,c,d)$$

where the Lorentz factor γ is given by

$$\gamma(v) = \frac{1}{\sqrt{1 - \frac{v^2}{c^2}}} \, . \qquad (2.2)$$

Suppose now that $\angle S'$ moves with a velocity $\underline{v}$ in an arbitrary direction relative to $\angle S$ with both sets of cartesian axes aligned and having coincided at $t = 0 = t'$. A similar but more complex argument to that outlined above gives the general Lorentz transformation

$$t' = \gamma\left(t - \frac{\underline{v} \cdot \underline{x}}{c^2}\right) \quad , \quad \underline{x}' = \underline{x} + \left\{[\gamma - 1]\frac{\underline{v} \cdot \underline{x}}{v^2} - \gamma t\right\}\underline{v} \qquad (2.3a,b)$$

which can be expressed in matrix block form as

$$\begin{pmatrix} ct' \\ \underline{x}' \end{pmatrix} = \begin{pmatrix} \gamma & -\gamma\underline{\beta} \\ -\gamma\underline{\beta} & \mathrm{I} + [\gamma - 1]\frac{\underline{\beta}\,\underline{\beta}}{\beta^2} \end{pmatrix} \begin{pmatrix} ct \\ \underline{x} \end{pmatrix} = \Lambda \begin{pmatrix} ct \\ \underline{x} \end{pmatrix} \qquad (2.4)$$

where $\underline{\beta} = \underline{v}/c$, $\underline{\beta}\,\underline{\beta}$ is a 3×3 dyadic, I is the 3×3 identity matrix and the Lorentz factor now has the form

$$\gamma(\underline{v}) = \frac{1}{\sqrt{1 - \frac{\underline{v} \cdot \underline{v}}{c^2}}} \, . \qquad (2.5)$$

The 4×4 matrix Λ in Eq. (2.4) above is referred to as the general boost matrix.

§2.2.2 Four-Vectors and Relativistic Kinematics

The laws of physics when expressed as tensor equations containing four-vectors and four-tensors are covariant under Lorentz transformation. Therefore, expressed in this form, they satisfy the principle of relativity. Consequently, relativistic generalisations of standard non-relativistic expressions can be derived by re-expressing them in four-tensor form.

Let X^μ be the contravariant four-vector generalisation of the position vector $\underline{x}$ represented by

$$X^\mu = (X^0, \underline{x}) \qquad (2.6)$$

where the time-component X^0 is equal to ct and the conventional three-vector $\underline{x}$ consists of the three components (X^1, X^2, X^3). The norm of the differential of this four-vector defines the invariant interval ds^2

$$ds^2 \equiv dX^\mu dX_\mu = c^2 dt^2 - d\underline{x} \cdot d\underline{x} \tag{2.7}$$

which is null for all photon paths.

The proper time interval $d\tau$, for a moving particle, is identical to the time interval dt measured by a clock attached to the particle for which, obviously, $d\underline{x} = 0$ and $ds^2 = c^2 d\tau^2$. Equating this invariant interval with that of Eq. (2.7), dividing through by $c^2 dt^2$ and taking the positive square root gives the useful relation

$$\frac{d\tau}{dt} = \frac{1}{\gamma(\underline{v})} \,. \tag{2.8}$$

Since the proper time is a world scalar and X^μ is a contravariant four-vector, the quantity $dX^\mu/d\tau$ is also a contravariant four-vector and, as stated earlier, must satisfy the principle of relativity. The appropriate expression for four-velocity is then

$$V^\mu \equiv \frac{dX^\mu}{d\tau} = \frac{d}{d\tau}(ct, \underline{x}) = \gamma(\underline{v}) \frac{d}{dt}(ct, \underline{x}) = \gamma(\underline{v}) (c, \underline{v}) \tag{2.9}$$

where use has been made of the relation given by Eq. (2.8). It is trivial to show from Eq. (2.9) that the four-velocity has a constant magnitude given by

$$V^\mu V_\mu = c^2 \,. \tag{2.10}$$

Continuing in a logical manner it is apparent that the appropriate definition for four-acceleration is

$$A^\mu \equiv \frac{dV^\mu}{d\tau} = \gamma(\underline{v}) \frac{d}{dt} \{\gamma(\underline{v}) (c, \underline{v})\} \tag{2.11}$$

whilst that for four-momentum is

$$P^\mu \equiv m_o V^\mu = \gamma(\underline{v}) m_o (c, \underline{v}) = m (c, \underline{v}) = (mc, \underline{p}) \tag{2.12}$$

where m_o is the particle rest mass and $m = \gamma m_o$ is the relativistic mass. The appropriate form for the four-force is

$$F^\mu \equiv \frac{dP^\mu}{d\tau} = \frac{d}{d\tau}(m_o V^\mu) \,. \tag{2.13}$$

For a particle of constant rest mass m_o, Eq. (2.13) can be written as

$$F^\mu = m_o \frac{dV^\mu}{d\tau} = m_o A^\mu \, . \tag{2.14}$$

Differentiation of Eq. (2.10) with respect to proper time gives

$$\frac{d(V_\mu V^\mu)}{d\tau} = 2V_\mu \frac{dV^\mu}{d\tau} = 0 \tag{2.15}$$

which with Eq. (2.14) gives the useful relation

$$V_\mu F^\mu = 0 \, . \tag{2.16}$$

Equation (2.16) shows that the four-force for a particle of constant rest mass is orthogonal to the four-velocity in space-time. If the four-force vector is given by

$$F^\mu = (F^0, \underline{F}) \tag{2.17}$$

then Eqs. (2.9) and (2.16) imply that for a particle of constant rest mass

$$F^0 = \frac{\underline{F} \cdot \underline{v}}{c} \, . \tag{2.18}$$

If the three-vector part of the four-force is now expressed as

$$\underline{F} = \gamma(\underline{v})\, \underline{f} \tag{2.19}$$

where $\underline{f}$ is the conventional three-force, then it follows from Eqs. (2.17) and (2.18) that the four-force has the form

$$F^\mu = \gamma(\underline{v}) \left(\frac{\underline{f} \cdot \underline{v}}{c}, \underline{f} \right) \, . \tag{2.20}$$

Last is the null photon-propagation four-vector K^μ which is defined as

$$K^\mu = (k, \underline{k}) \tag{2.21}$$

where the magnitude of the three-wave vector $|\underline{k}| = 2\pi\nu/c$. I shall define the raypath vector $\hat{\underline{k}}$ as being a unit three-vector in the direction of photon propagation such that

$$\hat{\underline{k}} = \frac{\underline{k}}{k} \, . \tag{2.22}$$

§2.3 Elementary Radiative Transfer

§2.3.1 Specific Intensity

In general, a radiation field is a function of both position and time and at some given position has a distribution in both angle and frequency. The specific intensity $I_\nu(\underline{x}, \hat{\underline{k}}, t)$ of radiation at position $\underline{x}$ and at time t travelling in direction $\hat{\underline{k}}$ with frequency ν is a quantity which describes the radiation field and is defined such that the amount of energy transported by the radiation in the frequency range ν to $\nu + \mathrm{d}\nu$ across an area element $\mathrm{d}A$ with unit normal $\hat{\underline{n}}$ in the time interval $\mathrm{d}t$ into the solid angle $\mathrm{d}\Omega$ around $\hat{\underline{k}}$ is

$$\mathrm{d}E_\nu = I_\nu(\underline{x}, \hat{\underline{k}}, t)\, \hat{\underline{k}} \cdot \hat{\underline{n}}\, \mathrm{d}A\, \mathrm{d}\Omega\, \mathrm{d}\nu\, \mathrm{d}t \ . \tag{2.23}$$

In vacuo, the monochromatic specific intensity I_ν is a conserved along any raypath and has the SI units $[I_\nu] = \mathrm{Jm^{-2}s^{-1}Hz^{-1}steradian^{-1}}$.

§2.3.2 Angular Moments of the Specific Intensity

(a) *Energy Density*

Consider a cylinder of length $\mathrm{c}dt$ and end area $\mathrm{d}A$ within a radiation field of energy density per unit solid angle per unit frequency $U_\nu(\Omega)$. The energy within this cylinder will be

$$\mathrm{d}E_\nu = U_\nu(\Omega)\, \mathrm{c}dt\, \mathrm{d}A\, \mathrm{d}\nu\, \mathrm{d}\Omega \ . \tag{2.24}$$

All of the energy within this cylinder will exit in a time $\mathrm{d}t$. Therefore

$$\mathrm{d}E_\nu = I_\nu\, \mathrm{d}t\, \mathrm{d}A\, \mathrm{d}\nu\, \mathrm{d}\Omega \ . \tag{2.25}$$

Equating Eqs. (2.24) and (2.25) gives

$$U_\nu(\Omega) = \frac{I_\nu}{\mathrm{c}} \tag{2.26}$$

which, when integrated over all solid angles, gives the monochromatic energy density

$$u_\nu = \int U_\nu(\Omega)\mathrm{d}\Omega = \frac{1}{\mathrm{c}} \int I_\nu \mathrm{d}\Omega \ . \tag{2.27}$$

The mean monochromatic specific intensity is given by

$$J_\nu = \frac{1}{4\pi} \int I_\nu\, \mathrm{d}\Omega \tag{2.28}$$

Therefore,

$$u_\nu = \frac{4\pi J_\nu}{\mathrm{c}} \ . \tag{2.29}$$

(b) *Energy Flux*

The monochromatic energy flux in the direction $\hat{\underline{k}}$ is

$$\underline{\mathcal{F}}_\nu = \int I_\nu \, \hat{\underline{k}} \, \mathrm{d}\Omega \tag{2.30}$$

and the energy flux in the direction $\hat{\underline{k}}$ is

$$\underline{\mathcal{F}} = \int_0^\infty \underline{\mathcal{F}}_\nu \, \mathrm{d}\nu \, . \tag{2.31}$$

The monochromatic energy flux normal to a surface element $\mathrm{d}A$ with unit normal $\hat{\underline{n}}$ is

$$\mathcal{F}_\nu = \hat{\underline{n}} \cdot \underline{\mathcal{F}}_\nu = \int I_\nu \, \hat{\underline{k}} \cdot \hat{\underline{n}} \, \mathrm{d}\Omega = \int I_\nu \, \cos\theta \, \mathrm{d}\Omega \, , \tag{2.32}$$

where θ is the angle between $\hat{\underline{k}}$ and $\hat{\underline{n}}$, and the energy flux normal to the surface is

$$\mathcal{F} = \int_0^\infty \mathcal{F}_\nu \, \mathrm{d}\nu \, . \tag{2.33}$$

(c) *Momentum Flux*

Since the momentum of a photon of energy E is E/c, the momentum flux across a surface with unit normal $\hat{\underline{n}}$ in the direction $\hat{\underline{k}}$ and in the frequency range ν to $\nu + \mathrm{d}\nu$ is

$$\underline{p}_\nu = \frac{\mathcal{F}_\nu}{\mathrm{c}} \, \hat{\underline{k}} \, . \tag{2.34}$$

The monochromatic momentum flux normal to the surface is

$$p_\nu = \underline{p}_\nu \cdot \hat{\underline{n}} = \frac{1}{\mathrm{c}} \int I_\nu \, \cos^2\theta \, \mathrm{d}\Omega \tag{2.35}$$

and the momentum flux normal to the surface is

$$p = \int_0^\infty p_\nu \, \mathrm{d}\nu \, . \tag{2.36}$$

In general, different components of a stress tensor denote the rate of momentum transfer across surfaces with specific orientations. In dyadic notation the above result can be expressed as

$$\mathbf{p} = \frac{1}{\mathrm{c}} \int \int I_\nu \, \hat{\underline{k}} \, \hat{\underline{k}} \, \mathrm{d}\Omega \, \mathrm{d}\nu \tag{2.37}$$

where $\mathbf{p}$ is the radiation stress tensor.

§2.3.3 The Equation of Radiative Transfer

The transport of radiation through matter is described by the equation of radiative transfer which can be expressed in the form

$$\frac{1}{c}\frac{\partial I_\nu}{\partial t} + \underline{k}\cdot\underline{\nabla} I_\nu = \frac{1}{4\pi}\rho j_\nu - \rho\kappa_\nu^{abs} I_\nu - \rho\kappa_\nu^{sca} I_\nu + \rho\kappa_\nu^{sca}\int \varphi_\nu(\underline{\hat{k}},\underline{\hat{k}}')\, I_\nu(\underline{\hat{k}}')\,\mathrm{d}\Omega' \qquad (2.38)$$

where ρ is the mass density, j_ν is the emissivity per unit mass, κ_ν^{abs} is the total absorption opacity, κ_ν^{sca} is the total scattering opacity and $\varphi_\nu(\underline{\hat{k}},\underline{\hat{k}}')$ is the probability of a photon within the solid angle $\mathrm{d}\Omega'$ about $\underline{\hat{k}}'$ being scattered into the solid angle $\mathrm{d}\Omega$ about $\underline{\hat{k}}$. The sum of each of the positive terms on the right hand side of Eq. (2.38) denotes the increase in the specific intensity per unit length along the raypath whilst the sum of each of the negative terms denotes the decrease in the specific intensity per unit length along the raypath. The scattering probability satisfies normalisation and reversability constraints such that

$$\int \varphi_\nu(\underline{\hat{k}},\underline{\hat{k}}')\,\mathrm{d}\Omega' = \int \varphi_\nu(\underline{\hat{k}},\underline{\hat{k}}')\,\mathrm{d}\Omega = 1\ . \qquad (2.39)$$

The emissivity j_ν consists of two distinct components; one resulting from spontaneous emission and the other from induced emission. In the rest frame of the gas, the spontaneous emission component is usually isotropic whilst the induced emission component exhibits the same directional dependence as the specific intensity. For this reason the contribution from the induced emission component is conventionally absorbed into the $-\rho\kappa_\nu^{abs} I_\nu$ term. The resulting κ_ν^{abs} is termed the 'true absorption corrected for stimulated emission'. The quantity

$$\kappa_\nu = \kappa_\nu^{abs} + \kappa_\nu^{sca} \qquad (2.40)$$

is called the total opacity (corrected for stimulated emission) or just the opacity. If the light travel time across an object is much less than any of its evolutionary timescales, the time dependence in the equation of radiative transfer (Eq. 2.38) can be dropped leaving

$$\underline{\hat{k}}\cdot\underline{\nabla} I_\nu + \rho\,\kappa_\nu I_\nu = \rho\left(\frac{1}{4\pi} j_\nu + \kappa_\nu^{sca}\Phi_\nu\right) \qquad (2.41)$$

where Φ_ν is the specific intensity weighted by the angular phase function for scattering and is given by

$$\Phi_\nu(\underline{\hat{k}},\underline{x}) = \int \varphi(\underline{\hat{k}},\underline{\hat{k}}')\, I_\nu(\underline{\hat{k}}',\underline{x})\,\mathrm{d}\Omega'\ . \qquad (2.42)$$

For isotropic scattering $\varphi = 1/4\pi$ and Φ_ν, by Eq. (2.28), then equals the mean intensity J_ν. Defining the source function by

$$S_\nu(\underline{\hat{k}},\underline{x}) \equiv \frac{1}{\kappa_\nu}\left(\frac{j_\nu}{4\pi} + \kappa_\nu^{sca}\Phi_\nu\right)\ , \qquad (2.43)$$

and denoting some path-length along the raypath by s such that $\hat{\underline{k}} \cdot \underline{\nabla} = \mathrm{d}/\mathrm{d}s$, permits Eqn. (2.41) to be expressed as

$$\frac{\mathrm{d}I_\nu}{\mathrm{d}s} + \rho\,\kappa_\nu I_\nu = \rho\,\kappa_\nu S_\nu \ . \tag{2.44}$$

Further simplification of Eq. (2.44) is possible by the introduction of a variable called the optical depth defined by

$$\tau_\nu \equiv \int_{s_0}^{s} \rho\kappa_\nu \,\mathrm{d}s \tag{2.45}$$

where s_0 is arbitrary and simply corresponds to the point at which the optical depth is zero. A medium is termed optically thick when $\tau_\nu > 1$ and optically thin when $\tau_\nu < 1$.

§2.3.4 Thermal Radiation

Any radiation field that is in thermodynamic equilibrium and that can be characterised by a unique distribution function that depends solely on the absolute temperature is a thermal radiation field. A good approximation to such a state occurs in the deep interior of stars or dense accretion discs where $|\nabla T|/\rho\kappa T \ll 1$ and the radiation is in equilibrium with the matter at a very uniform temperature. Thermal radiation is described by the Planck function which can be derived by invoking Bose-Einstein quantum statistics. It takes the form

$$B_\nu(T) = \frac{2h\nu^3/\mathrm{c}^2}{\exp(h\nu/kT) - 1} \tag{2.46}$$

and is the isotropic specific intensity of a system in thermal equilibrium. Such radiation is usually referred to as blackbody radiation and is emitted by a blackbody or perfect radiator. The integrated Planck function is defined by

$$B(T) = \int B_\nu(T)\,\mathrm{d}\nu = \frac{2\pi^4 k^4}{15\mathrm{c}^2h^3}T^4 = \frac{\mathrm{ac}}{4\pi}T^4 \tag{2.47}$$

where a is the radiation constant and is given by

$$\mathrm{a} = \frac{8\pi^5 k^4}{15\mathrm{c}^3h^3} \ . \tag{2.48}$$

This is related to the Stefan-Boltzmann constant σ through

$$\sigma = \frac{\mathrm{ac}}{4} \tag{2.49}$$

and thus, since the surface energy flux, $\mathcal{F}$, of a sphere of uniform brightness B is simply πB,

$$\mathcal{F} = \sigma T^4 \tag{2.50}$$

which is the Stefan-Boltzmann law.

A two-component gas is in strict thermodynamic equilibrium when both components of the gas are in statistical equilibrium. This occurs when the distribution of photons is given by the Planck function whilst the distribution in the energy of the matter particles is given by Maxwell-Boltzmann statistics. If the photon distribution function differs from that given by the Planck function but the material particle distribution is still given by Maxwell-Boltzmann statistics then the (matter component of the) gas is in local thermodynamic equilibrium. In this case the emissivity has a thermal value which is given by Kirchhoff's law

$$j_\nu = 4\pi\kappa_\nu^{abs} B_\nu(T) \,. \tag{2.51}$$

§2.3.5 The Eddington Approximation and Limb Darkening

Integral to the above approximation are the assumptions that the radiator geometry is planar, that radiation traversing the radiator is scattered isotropically and that the opacity of the radiator's atmosphere is gray, or independent of frequency. In the deep layers of the atmosphere far from the boundary at which $\tau = 0$, the specific intensity becomes very nearly isotropic. The Eddington approximation consists of the further assumption that this holds for all depths leading to the following identification for the radiation pressure

$$p \approx \frac{1}{3}u = \frac{4\pi J}{3c} \tag{2.52}$$

where J is the mean frequency integrated specific intensity; the mean monochromatic specific intensity is given by Eqs. (2.28) and (2.29). By solving the equation of radiative transfer for a static, gray atmosphere in radiative equilibrium it can readily be shown that the emergent, frequency integrated specific intensity is

$$I(\mu, \tau = 0) = \frac{3}{4\pi}\mathcal{F}(\mu + \tau_0) \tag{2.53}$$

Identification of the integration constant can be made by noting that the emergent, surface energy flux is given by

$$\mathcal{F} = 2\pi \int_0^1 \mu I(\mu, 0)\, \mathrm{d}\mu \tag{2.54}$$

which with Eq. (2.53) leads to the deduction that $\tau_0 = 2/3$. Hence the emergent specific intensity is

$$I(\mu, 0) = \frac{3}{5} I(1, 0)\left(\mu + \frac{2}{3}\right) \,. \tag{2.55}$$

The above equation gives the limb darkening in the Eddington approximation; the emergent specific intensity at the limb ($\mu = 0$) is 2/5 the value of the emergent specific intensity at the centre ($\mu = 1$). The gas temperature varies with optical depth according to

$$T^4 = \frac{3}{4} T_{eff}^4 \left(\tau + \frac{2}{3} \right) . \tag{2.56}$$

Thus, the gas temperature and the effective temperature are identical at a continuum optical depth of 2/3 whilst at the surface $T(0) = 0.8409\, T_{eff}$.

§2.4 Transformations, Invariants and Phenomena

§2.4.1 The Phase Space Density Function

Consider an arbitrary radiation field and some infinitesimal volume element $\mathrm{d}^3\underline{x} = \mathrm{d}x\,\mathrm{d}y\,\mathrm{d}z$ at position $\underline{x}$ within the field. The average number of photons $\mathrm{d}N$ with wave vector $\underline{k}$ that are within the volume element $\mathrm{d}^3\underline{x}$ at time t is

$$\mathrm{d}N = f(\underline{x}, \underline{k}, t)\, \mathrm{d}^3\underline{x}\, \mathrm{d}^3\underline{k} \tag{2.57}$$

where $f(\underline{x}, \underline{k}, t)$ is the phase space density function or the distribution function. It can be proven that the phase space volume $\mathrm{d}^3\underline{x}\, \mathrm{d}^3\underline{k}$ is a Lorentz invariant. Since $\mathrm{d}N$ is a countable quantity and, therefore, also a Lorentz invariant it can be deduced that

$$f(\underline{x}, \underline{k}, t) = \text{Lorentz invariant} . \tag{2.58}$$

The energy in the volume element attributable to the photons in the solid angle $\mathrm{d}\Omega$ around $\underline{k}$ with a wave vector of magnitude between k and $k + \mathrm{d}k$ where $k = 2\pi\nu/\mathrm{c}$ is

$$\mathrm{d}E_\nu = \mathrm{h}\nu\, f(\underline{x}, \underline{k}, t)\, k^2\, \mathrm{d}\Omega\, \mathrm{d}k\, \mathrm{d}^3\underline{x} = \mathrm{h}\nu\, f(\underline{x}, \frac{2\pi\nu}{\mathrm{c}}\hat{\underline{k}}, t) \left(\frac{2\pi\nu}{\mathrm{c}} \right)^2 \mathrm{d}\Omega\, \frac{2\pi}{\mathrm{c}}\, \mathrm{d}\nu\, \mathrm{d}^3\underline{x} . \tag{2.59}$$

§2.4.2 The Lorentz Invariant I_ν/ν^3

Comparing Eqs. (2.24) and (2.59) for identical volume elements ($\mathrm{d}^3\underline{x} = \mathrm{c}\mathrm{d}t\,\mathrm{d}A$) it can be seen that the phase space density function $f(\underline{x}, \underline{k}, t)$ is proportional to U_ν/ν^3. Utilising Eq. (2.26), which relates the monochromatic energy density per unit solid angle to the specific intensity, and the Lorentz invariance of the phase space density function (Eq. 2.58) then gives the required result that

$$\frac{I_\nu}{\nu^3} = \text{Lorentz invariant} . \tag{2.60}$$

§2.4.3 Transformation of a Raypath Vector

Let the photon-propagation four-vector in $\angle S'$, by analogy with Eq. (2.21), be given by $K'^{\mu} = (k', \underline{k}')$. Then using the general boost matrix Λ given in Eq. (2.4) it is simple to show that

$$k' = \gamma(k - \underline{\beta} \cdot \underline{k}) \qquad \underline{k}' = -\gamma\underline{\beta} + \underline{k} + [\gamma - 1]\frac{\underline{\beta} \cdot \underline{k}}{\beta^2}\underline{\beta} \,. \tag{2.61a,b}$$

From the definition of the raypath vector given by Eq. (2.22) it is then obvious that the raypath vector transforms according to

$$\hat{\underline{k}}' = \frac{\hat{\underline{k}} + \left[(\gamma - 1)\frac{\underline{\beta} \cdot \hat{\underline{k}}}{\beta^2} - \gamma\right]\underline{\beta}}{\gamma(1 - \underline{\beta} \cdot \hat{\underline{k}})} \,. \tag{2.62}$$

§2.4.4 Doppler Shift

Recalling that $k = 2\pi\nu/c$ and using Eq. (2.22), Eq. (2.61a) can be re-expressed as

$$\nu' = \gamma(1 - \underline{\beta} \cdot \hat{\underline{k}})\nu \tag{2.63}$$

which describes the physical phenomenon known as Doppler shift: If in the standard frame configuration, a source at rest in $\angle S$ at an inclination θ to the z-axis emits radiation at a frequency ν then the same source observed in $\angle S'$ will have a lower frequency ν' given by $\nu' = \gamma(1 - \beta\cos\theta)\nu$. If this source is located on the z-axis such that $\theta = 0$ and the primed observer moves towards/recedes from the source with speed $c\beta$ then the observed frequency will be higher/lower by a factor $\sqrt{\frac{1+\beta}{1-\beta}} / \sqrt{\frac{1-\beta}{1+\beta}}$. The transverse Doppler effect occurs when the source location is perpendicular to the direction of motion. In this case $\theta = \pi/2$ and the frequency of the radiation observed in the primed frame is, by Eq. (2.63), higher by a factor γ than that observed in $\angle S$.

§2.4.5 Aberration

Let the source be located at the origin of a standard spherical coordinate system. In the standard frame configuration one can, without loss of generality set $\phi = 0$, such that the raypath vector $\hat{\underline{k}} = (\sin\theta, 0, \cos\theta)$. Substituting this expression into Eq. (2.62), setting $\hat{\underline{k}}' = (\sin\theta', 0, \cos\theta')$ and equating each component gives

$$\sin\theta' = \frac{\sin\theta}{\gamma(1 - \beta\cos\theta)} \qquad \cos\theta' = \frac{\cos\theta - \beta}{1 - \beta\cos\theta} \tag{2.64a,b}$$

which upon further manipulation yield the aberration formula

$$\tan\theta' = \frac{\sin\theta}{\gamma(\cos\theta - \beta)} \,. \tag{2.65}$$

Equation (2.65) is worthy of some discussion. In the limit $\beta \rightarrow 1$

$$\tan\theta' \rightarrow -\frac{1}{\gamma}\cot\left(\frac{\theta}{2}\right) \tag{2.66}$$

indicating that in the (standard configuration) primed frame the photons are incident in a narrow cone in the direction of the negative z'-axis. Consider radiation emitted in the plane $\theta = \pi/2$. Clearly, in the highly relativistic limit the perceived angle that this radiation makes with the z'-axis when observed from the primed frame, by Eq. (2.66), approximates to the very small angle $\pi - 1/\gamma$; the radiation appears to come from in front of the observer. If a source emits isotropically in $\angle S$ then half of all the photons will be emitted into the hemisphere with $\theta < \pi/2$ and the rest into the hemisphere with $\theta > \pi/2$. Consequently half of all the photons incident in $\angle S'$ will have $\theta' > \pi - 1/\gamma$ whilst very few will be incident with $\theta' \ll \pi - 1/\gamma$. This effect is known as relativistic beaming and along with the phenomenon of Doppler shift has important consequences, as will become clear later, for the relativistic motion of particles within a radiation field.

§2.4.6 Transformation of an Element of Solid Angle

In the co-moving frame $\angle S'$ an element of solid angle has the form

$$\mathrm{d}\Omega' = \sin\theta'\,\mathrm{d}\theta'\,\mathrm{d}\phi' = -\mathrm{d}\mu'\,\mathrm{d}\phi' \tag{2.67}$$

where θ' and ϕ' are the standard spherical polar coordinates and $\mu' = \cos\theta'$. In the standard frame configuration, $\cos\theta'$ transforms according to Eq. (2.64*b*) which upon differentiation gives

$$\mathrm{d}\mu' = \frac{\mathrm{d}\mu}{\gamma^2(1-\beta\mu)} = \left(\frac{\nu}{\nu'}\right)^2 \mathrm{d}\mu \tag{2.68}$$

where the last equality has been deduced using the Doppler shift formula, Eq. (2.63). It is clear from Eqs. (2.1*a*, *b*) that in the standard frame configuration the azimuthal angle ϕ' is invariant under Lorentz transformation and that therefore $\mathrm{d}\phi' = \mathrm{d}\phi$. It is then evident from Eq. (2.68) that in the standard frame configuration

$$\nu^2\,\mathrm{d}\mu\,\mathrm{d}\phi = \text{Lorentz invariant}\,. \tag{2.69}$$

Equation (2.69) must also be true for a general Lorentz boost. Therefore, by Eqs. (2.63), (2.67) and (2.69), an element of solid angle transforms according to

$$\mathrm{d}\Omega' = \frac{\mathrm{d}\Omega}{\gamma^2(1-\underline{\beta}\cdot\hat{\underline{\mathrm{k}}})^2}\,. \tag{2.70}$$

§2.4.7 Transformation of a Three-Force

Assume for the interim, by analogy with Eq. (2.17), that the four-force vector F'^{μ} in $\angle S'$ has the form $F'^{\mu} = (F'^{0}, \underline{F}')$. Then from the inverse of the matrix Λ given in Eq. (2.4) and by Eq. (2.20) it can easily be shown that the three-vector component of the four-force acting on a body of constant rest mass transforms according to

$$\gamma \underline{f} = \gamma F'^{0} \underline{\beta} + \underline{F}' + (\gamma - 1) \frac{\underline{F}' \cdot \underline{\beta}}{\beta^2} \underline{\beta} \,. \tag{2.71}$$

A comparison of the expression for F'^{μ} and Eq. (2.20) indicates that the four-force vector in $\angle S'$ must, since $\underline{v} = 0$ in this frame, have the form $F'^{\mu} = (0, \underline{f}')$ and that therefore Eq. (2.71) can be rewritten as

$$\underline{f} = \frac{1}{\gamma} \left[\underline{f}' - \frac{\underline{f}' \cdot \underline{\beta}}{\beta^2} \underline{\beta} \right] + \frac{\underline{f}' \cdot \underline{\beta}}{\beta^2} \underline{\beta} \tag{2.72}$$

which is the required transformation equation for a three-force.

Part II

§2.5 Fragmented Jets: Their Advantages and Formation

The temporal and spatial density structure of the jets in SS433 varies over several orders of magnitude. Observational evidence for this conclusion, from both optical and radio observations, is unambiguous: The narrowness of the moving emission lines, which have a typical width of $\sim 1\,300$ km/s (Vermeulen, 1989), indicates that the optical jets are fairly smooth on a length scale of $\sim 10^{13}$ cm, but are variable on length scales of $10^{14} - 10^{15}$ cm, whilst VLBI radio observations (Vermeulen et al., 1987) clearly show that the jets are formed from a series of evolving 'blobs'.

At present there exist no concrete theoretical reasons or conclusive observational evidence to exclude the possibility that the jets are formed by the successive ejection of discrete gaseous blobs from the vicinity of the compact object. Indeed, if the jet structure close to the jet source is inferred from the observed jet structure of the optical and radio jets then it would seem more probable that the jets are composed of gaseous blobs rather than from a continuous stream of material. If such a fragmented jet were to be accelerated principally by hydrodynamic processes, the inherent nature of which is to maintain a constant jet momentum density, the expected jet velocity would certainly not be constant. Such an outcome would be incompatible with observations which clearly show that the jet velocity in SS433 is constant to a very high degree as if governed by external factors. Therefore, it would appear appropriate to investigate the acceleration in a near constant external radiation field of such gaseous blobs or 'bullets' as their optical facsimiles have been termed. **Such an investigation is the purpose of**

this thesis. However, before deriving the general equation of motion of such bullets, I will discuss some of the inherent advantages that a discretely composed jet has over its continuous counterparts and the possible sequence of events that may lead to the formation of discrete parcels of material near the compact object. This latter topic is, by its very nature, largely conjecture.

Continuous jets encounter severe difficulties when they impinge on density enhancements within the medium through which they are propagating. Such interactions force the jet to bend, though it is possible for the jets to bend through a limited angle only before a disruptive shock forms across the jet (Icke, 1989). These shocks have a lower probability of forming in a gaseous bullet and thus a jet formed from such entities is more likely to survive encountering a density enhancement. For matter in a continuous jet to access the driving radiation field, the optical depth along the jet axis to the region of interest must be less than of order unity. Such optical depth problems do not arise in jets composed of gaseous bullets where the driving surface of the bullet, the rear surface, is easily identifiable. Of course such bullets also have a front surface which presumably could lead to a rapid deceleration of the bullet on impact with the ambient medium that may exist within the funnel. This problem can be resolved if the bullets are embedded in a comoving stream of diffuse gas as would appear to be the case in SS433.

As regards the production of the bullets, consider first the case where the accreting object is a spinning neutron star. If the pulsar is not totally buried and the magnetosphere reaches as far out as the speed-of-light cylinder then the spin rate will decrease in the same manner as an exposed pulsar (Davidson and McCray, 1980). Material from the outer regions of the disc will spiral inwards as the angular momentum is conveyed outwards through viscous dissipation. For such a cocoon-enclosed pulsar the accreted material aquires a constant angular momentum per unit mass dependent on the neutron star spin rate (Davidson, Pacini and Salpeter, 1971) leading to the formation of an effective centrifugal-gravitational potential Φ per unit mass. As more matter is accreted and heats up the potential well fills up to $\Phi \approx 0$ producing an hour-glass shaped central funnel. Accreted matter that has an abnormally low angular momentum or high temperature may 'evaporate' from the inner walls of the funnel and enter the acceleration region. The rate of in-fall will increase as the density of the material in the toroidal potential well increases resulting eventually in the presence of a considerable amount of material within the funnel. This matter will be confined by the pressure of the dense torus and will be driven towards the symmetry axis of the configuration by the lateral component of the radiation force. It will then be subject to the greatest outward driving force since the hottest part of the funnel will be directly behind the bullet. As the gaseous bullet accelerates rapidly its leading surface will experience a ram pressure as it impacts on the ambient medium within the funnel which, in conjunction with the aberrated radiation pressure and the pressure provided by the funnel walls, will confine the material as it accelerates to a locus centred on the moving bullet. If the compact object is a black hole, then a similar centrifugal barrier to that discussed above for

a spinning neutron star will evolve but of course no angular momentum will be provided for the accreting material by the black hole, nor will there be any congregation of matter in the vicinity of the black hole. As with the neutron star, material will spiral inwards as angular momentum diffuses outwards but only up to a radius $r \approx 6GM/c^2$ where M is the mass of the black hole (Davidson and McCray, 1980). At smaller radii general relativistic effects dictate that material will spiral inwards without further loss of angular momentum. There is no reason for the angular momentum per unit mass in the upper reaches of the accretion disc to fall below the lower limit in the disc equatorial plane. Consequently, if the thickness of the accretion disc is considerably greater than $\sim 6GM/c^2$, a centrifugal barrier will be present permitting the formation of a funnel. (In SS433 the disc thickness is probably $> 10^{11}$ cm (see §1.6.2) which is roughly 4 orders of magnitude greater than $6GM/c^2$ for a $10\,M_\odot$ black hole.) Material that enters this funnel will be subject to equivalent confining pressures found in the neutron star funnel and will be driven away from the central black hole as a gaseous bullet.

§2.6 Derivation of the Equation of Motion

Consider two coordinate systems: an unprimed system ($\angle$K) in the rest frame of the radiator and a primed system ($\angle$K′) in which the radiatively driven bullet, assumed to be spherical, is instantaneously at rest. In the unprimed frame the sphere moves with velocity $\underline{v} = c\underline{\beta}$. The radiation force experienced by the sphere will be evaluated in the primed frame and the equation of motion derived from the transformation of this expression back to the unprimed frame.

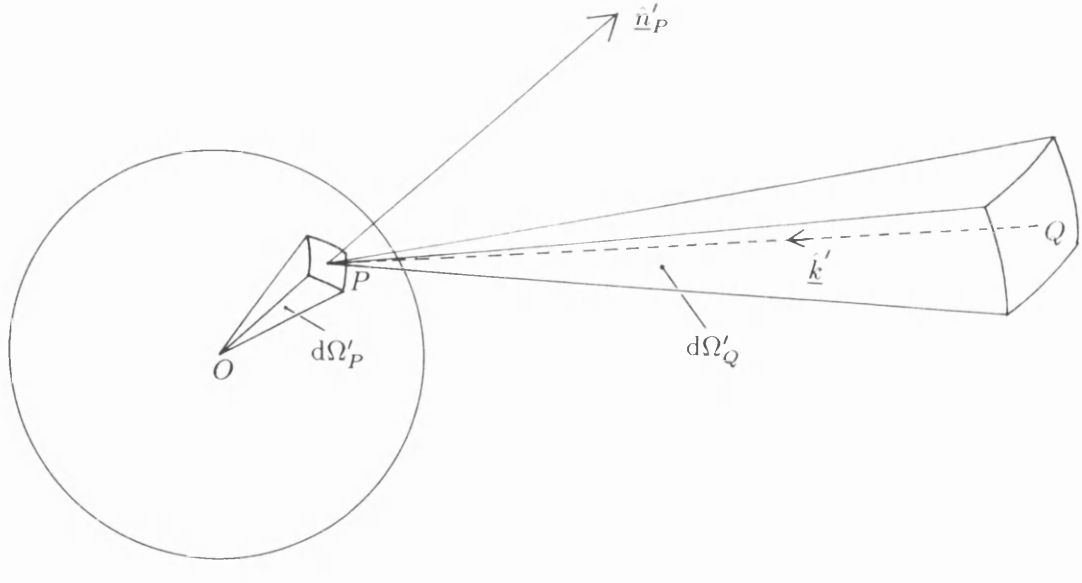

Fig. 2.1. The configuration geometry as observed in the instantaneous rest frame of the bullet: radiation originating from a surface element of the radiator at Q impinges on a surface element of the bullet, with unit normal $\hat{\underline{n}}'_P$, at P within a solid angle $d\Omega'_Q$ about a direction $\underline{k}'$. The solid angle subtended by the area element on the surface of the bullet, located at P, at the centre of the bullet, O, is $d\Omega'_P$.

Now consider an area element on the surface of the sphere at P and an area element on the surface of the blackbody radiator at Q which subtends a solid angle $d\Omega'_Q$ at P (Fig. 2.1).

The differential momentum flux at P due to photons incident within a solid angle $\mathrm{d}\Omega'_Q$ about $\hat{\underline{k}}'$ and in the frequency range ν' to $\nu' + \mathrm{d}\nu'$ is

$$\mathrm{d}\underline{p}'_{\nu'} = \frac{B_{\nu'}(T')}{\mathrm{c}} \mathrm{d}\Omega'_Q \, \hat{\underline{k}}' \tag{2.73}$$

where $B_{\nu'}(T')$ is the specific intensity of the blackbody radiator as observed in the rest frame of the bullet. Let the surface area element on the sphere at P be denoted

$$\mathrm{d}\underline{A}' = r'^2 \mathrm{d}\Omega'_P \, \hat{\underline{n}}'_P \tag{2.74}$$

where r' is the radius of the sphere, $\mathrm{d}\Omega'_P$ is the solid angle subtended by the area element P at the centre of the sphere and $\hat{\underline{n}}'_P$ is the outward normal at P. The differential force at P due to photons incident within a solid angle $\mathrm{d}\Omega'_Q$ about $\hat{\underline{k}}'$ and in the frequency range ν' to $\nu' + \mathrm{d}\nu'$ is

$$\mathrm{d}^2\underline{f}'_{\nu'} \equiv -(\mathrm{d}\underline{A}' \cdot \mathrm{d}\underline{p}'_{\nu'}) \hat{\underline{k}}' = r'^2 \frac{B_{\nu'}(T')}{\mathrm{c}} \mathrm{d}\Omega'_P \, \mathrm{d}\Omega'_Q \, (\hat{\underline{k}}' \cdot \hat{\underline{n}}'_P) \hat{\underline{k}}' \, . \tag{2.75}$$

Using the Lorentz invariant B_ν/ν^3 (Eq. 2.60) and the Lorentz transformation $\nu = \gamma(1 + \hat{\underline{k}}' \cdot \underline{\beta})\nu'$ (Eq. 2.63) where the Lorentz factor $\gamma = 1/\sqrt{1-\beta^2}$ (Eq. 2.5) this can be expressed as

$$\begin{aligned} \mathrm{d}^2\underline{f}'_{\nu'} &= -r'^2 \left(\frac{\nu'}{\nu}\right)^3 \frac{B_\nu(T)}{\mathrm{c}} \mathrm{d}\Omega'_P \, \mathrm{d}\Omega'_Q \, (\hat{\underline{k}}' \cdot \hat{\underline{n}}'_P) \hat{\underline{k}}' \\ &= -r'^2 \frac{B_\nu(T)}{\mathrm{c}} \mathrm{d}\Omega'_P \, \mathrm{d}\Omega'_Q \frac{\hat{\underline{k}}' \cdot \hat{\underline{n}}'_P}{\gamma^3(1 + \hat{\underline{k}}' \cdot \underline{\beta})^3} \hat{\underline{k}}' \, . \end{aligned} \tag{2.76}$$

Using the expression for the Doppler shift (Eq. 2.63) and that for the transformation of the raypath vector (Eq. 2.62) it is possible to show that

$$\mathrm{d}\nu' = \frac{\mathrm{d}\nu}{\gamma(1 + \hat{\underline{k}}' \cdot \underline{\beta})} \, . \tag{2.77}$$

Integrating Eq. (2.76) over all frequencies ν', by Eqs. (2.47), (2.49) and (2.77), yields

$$\begin{aligned} \mathrm{d}^2\underline{f}' = \int_0^\infty \mathrm{d}^2\underline{f}_{\nu'} \, \mathrm{d}\nu' &= -\frac{r'^2}{\mathrm{c}} \mathrm{d}\Omega'_P \, \mathrm{d}\Omega'_Q \frac{\hat{\underline{k}}' \cdot \hat{\underline{n}}'_P}{\gamma^4(1 + \hat{\underline{k}}' \cdot \underline{\beta})^4} \left[\int_0^\infty B_\nu(T) \, \mathrm{d}\nu\right] \hat{\underline{k}}' \\ &= -\frac{r'^2}{\mathrm{c}} \frac{\sigma}{\pi} T^4(-\hat{\underline{k}}(\hat{\underline{k}}', \underline{\beta})) \, \mathrm{d}\Omega'_P \, \mathrm{d}\Omega'_Q \frac{\hat{\underline{k}}' \cdot \hat{\underline{n}}'_P}{\gamma^4(1 + \hat{\underline{k}}' \cdot \underline{\beta})^4} \hat{\underline{k}}' \end{aligned} \tag{2.78}$$

where $T(-\hat{\underline{k}})$ is the temperature observed in the direction $-\hat{\underline{k}}$ with the relationship between $\hat{\underline{k}}$ and $\hat{\underline{k}}'$ being given by Eq. (2.62). The three-force acting on the sphere, as measured in the

instantaneously comoving frame ($\angle$K′), is found by integrating Eq. (2.78) over all solid angles and therefore has the form

$$\underline{f}' = -\frac{r'^2\sigma}{\pi c}\frac{1}{\gamma^4}\int_{\Omega'_P}\int_{\Omega'_Q}\frac{T^4(-\underline{\hat{k}}(\underline{\hat{k}}',\underline{\beta}))(\underline{\hat{k}}'\cdot\underline{\hat{n}}'_P)\underline{\hat{k}}'}{(1+\underline{\hat{k}}'\cdot\underline{\beta})^4}\,d\Omega'_P\,d\Omega'_Q\,. \tag{2.79}$$

Since the integrand is suitably continuous for all physical values of $\underline{\beta}$ the order of integration may be reversed giving

$$\underline{f}' = -\frac{r'^2\sigma}{\pi c}\frac{1}{\gamma^4}\int_{\Omega'_Q}\frac{T^4(-\underline{\hat{k}}(\underline{\hat{k}}',\underline{\beta}))\,\underline{\hat{k}}'}{(1+\underline{\hat{k}}'\cdot\underline{\beta})^4}\left[\int_{\Omega'_P}\underline{\hat{k}}'\cdot\underline{\hat{n}}'_P\,d\Omega'_P\right]d\Omega'_Q\,. \tag{2.80}$$

To facilitate the integration over Ω'_P in Eq. (2.80) I will assume that all parallel raypath vectors incident on the surface of the sphere denote the paths of photons with the same frequency ν'. This will certainly be true for an infinite, isothermal radiator. However, for a radiator with a non-uniform temperature profile it is an approximation equivalent to assuming that the sphere is small in comparison to the length-scale of any temperature variation.

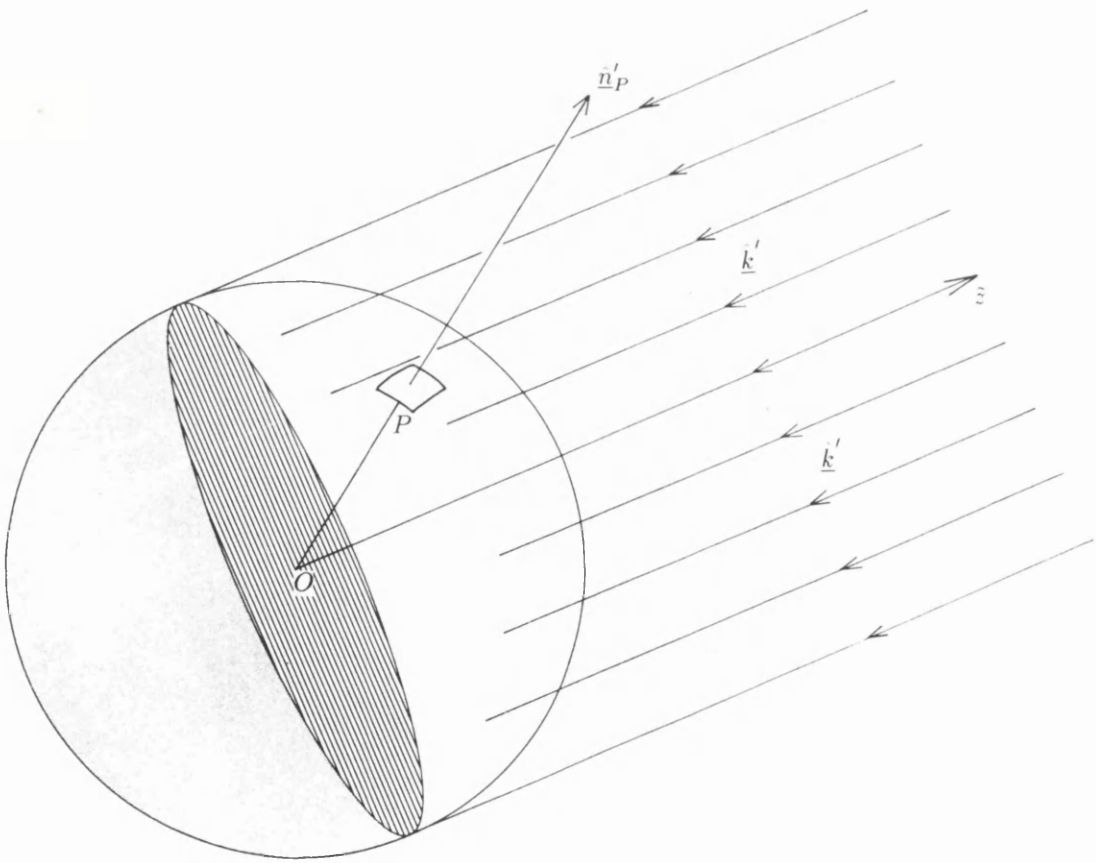

Fig. 2.2. In the transformed basis, located in the instantaneous rest frame of the bullet, the $\tilde{z}$-axis is aligned opposite to some direction of the incident radiation, $\underline{\hat{k}}'$. The photons incident upon the surface of the bullet in this arbitrary direction are assumed to have the same frequency, ν', and collectively illuminate precisely one half of the total bullet surface area.

The integration over Ω'_P is then most easily performed in the transformed basis (denoted by a tilde) obtained by rotating the primed basis centred on the bullet such that the new z-axis, $\tilde{z}$, is aligned opposite to some direction of the incident radiation (Fig. 2.2). In this basis

$$\underline{\hat{k}}' = -(0,0,1) \qquad \text{and} \qquad \underline{\hat{n}}'_P = (\sin\tilde{\theta}\cos\tilde{\phi}, \sin\tilde{\theta}\sin\tilde{\phi}, \cos\tilde{\theta}) \tag{2.81a,b}$$

and the integral over Ω'_P reduces to

$$\int_{\Omega'_P} \underline{\hat{k}}' \cdot \underline{\hat{n}}'_P \, \mathrm{d}\Omega'_P = -\int_0^{2\pi} \mathrm{d}\tilde{\phi} \int_0^{\frac{\pi}{2}} \cos\tilde{\theta}\sin\tilde{\theta}\,\mathrm{d}\tilde{\theta} = -\pi \, . \tag{2.82}$$

Hence on substituting Eq. (2.82) into Eq. (2.80) the three-force experienced by the sphere can be expressed as

$$\underline{f}' = \frac{\sigma D}{\pi c}\frac{1}{\gamma^4}\int_{\Omega'_Q} \frac{T^4(-\underline{\hat{k}}\,(\underline{\hat{k}}', \underline{\beta}))\underline{\hat{k}}'}{(1+\underline{\hat{k}}'\cdot\underline{\beta})^4}\,\mathrm{d}\Omega'_Q \tag{2.83}$$

where $D = \pi r'^2$ is the cross-sectional area of the sphere. It now only remains to transform Eq. (2.83) to the unprimed basis.

As detailed in Part I, (Eq. 2.62) a raypath vector $\underline{\hat{k}}'$ transforms according to

$$\underline{\hat{k}}' = \frac{\underline{\hat{k}} + \left[(\gamma-1)\frac{\underline{\beta}\cdot\underline{\hat{k}}}{\beta^2} - \gamma\right]\underline{\beta}}{\gamma(1-\underline{\beta}\cdot\underline{\hat{k}})}$$

and the element of solid angle $\mathrm{d}\Omega'_Q$ (Eq. 2.70) transforms according to

$$\mathrm{d}\Omega'_Q = \frac{\mathrm{d}\Omega_Q}{\gamma^2(1-\underline{\beta}\cdot\underline{\hat{k}})^2} \, .$$

It is trivial to show from Eq. (2.62) that

$$1 + \underline{\hat{k}}'\cdot\underline{\beta} = \frac{1}{\gamma^2(1-\underline{\beta}\cdot\underline{\hat{k}})} \tag{2.84}$$

which, along with Eqs. (2.62) and (2.70), when substituted into Eq. (2.83) yields

$$\underline{f}' = \frac{\sigma D}{\pi c}\gamma \int_{\Omega_Q} T^4(-\underline{\hat{k}})\left\{\underline{\hat{k}} + \left[(\gamma-1)\frac{\underline{\beta}\cdot\underline{\hat{k}}}{\beta^2} - \gamma\right]\underline{\beta}\right\}(1-\underline{\beta}\cdot\underline{\hat{k}})\,\mathrm{d}\Omega_Q \, . \tag{2.85}$$

The three-force, recalling Eq. (2.72), transforms according to

$$\underline{f} = \frac{1}{\gamma}\left[\underline{f}' - (\underline{f}'\cdot\underline{\beta})\frac{\underline{\beta}}{\beta^2}\right] + (\underline{f}'\cdot\underline{\beta})\frac{\underline{\beta}}{\beta^2}$$

Hence, Eq. (2.89) can alternatively be written as

$$\underline{\beta} \times \left(\underline{\beta} \times \frac{\mathrm{d}\underline{\beta}}{\mathrm{d}t} \right) + \frac{\mathrm{d}\underline{\beta}}{\mathrm{d}t} = \frac{\sigma D}{\pi \mathrm{m_o c^2}} \frac{1}{\gamma^3} \int_{\Omega_Q} T^4(-\hat{\underline{k}}) \left\{ \hat{\underline{k}} - \gamma^2 (1 - \underline{\beta} \cdot \hat{\underline{k}}) \underline{\beta} \right\} (1 - \underline{\beta} \cdot \hat{\underline{k}}) \, \mathrm{d}\Omega_Q \qquad (2.92)$$

where, in a cartesian coordinate basis the general velocity vector $\underline{\beta}$ (in units of the speed of light) has the form

$$\underline{\beta} = \begin{pmatrix} \beta_x \\ \beta_y \\ \beta_z \end{pmatrix} \qquad (2.93)$$

and the raypath vector $\hat{\underline{k}}$ is given by

$$\hat{\underline{k}} = \begin{pmatrix} \sin\theta \cos\phi \\ \sin\theta \sin\phi \\ \cos\theta \end{pmatrix} . \qquad (2.94)$$

In the following chapters I will investigate solutions to this equation for various funnel geometries and temperature profiles with particular emphasis on those with model parameters applicable to SS433.

Chapter 3

Motion Above an Infinite, Isothermal Radiator

§3.1 Introduction

To begin the analysis of solutions to the general vector equation of motion derived in chapter 2 I will consider the simplest possible case: a bullet of constant radius moving above an infinite isothermal planar or conical radiator in which gravitational effects are ignored. I shall investigate axial motion above such a radiator and progress to general off-axis motion. The correspondence of the radiator geometries is obvious: the infinite plane represents an idealised thin accretion disc whilst the infinite cone represents an idealised thick accretion disc funnel.

§3.2 Axial Motion

§3.2.1 The Axial Equation of Motion

Let the radiator be orientated such that for the plane, the surface normal is aligned along the z-axis of a cartesian coordinate basis, whilst for the cone, such that the axis of generation is aligned along the z-axis. An axial velocity vector will then have the form

$$\underline{\beta} = \begin{pmatrix} 0 \\ 0 \\ \beta_z \end{pmatrix} \tag{3.1}$$

and the vector equation of motion (Eq. 2.89) will be given by

$$\begin{pmatrix} \dot{\beta}_x \\ \dot{\beta}_y \\ \gamma^2 \dot{\beta}_z \end{pmatrix} = \frac{\sigma D}{\pi m_o c^2} \frac{1}{\gamma} \int_0^{2\pi} \int_0^{\theta_o} T^4\left(-\hat{\underline{k}}(\theta,\phi)\right) \underline{\Upsilon}(\underline{\beta};\theta,\phi)\,(1-\beta_z\cos\theta)\sin\theta\,\mathrm{d}\theta\,\mathrm{d}\phi \tag{3.2}$$

where

$$\dot{\beta}_i = \frac{\mathrm{d}\beta_i}{\mathrm{d}t}, \qquad \underline{\Upsilon}(\underline{\beta};\theta,\phi) = \hat{\underline{k}} - \gamma^2\,(1-\underline{\beta}\cdot\hat{\underline{k}})\,\underline{\beta} = \begin{pmatrix} \sin\theta\cos\phi \\ \sin\theta\sin\phi \\ \gamma^2(\cos\theta-\beta_z) \end{pmatrix} \tag{3.3a,b}$$

and θ_o corresponds to the angle of incidence which a photon emitted at infinity makes with the positive z-axis. If the temperature profile of the radiator is azimuthally symmetric such that

$T(-\underline{\hat{k}}(\theta,\phi)) = T(\theta)$ then the integral over ϕ in Eq. (3.2) is trivial and yields

$$\begin{pmatrix} \dot{\beta}_x \\ \dot{\beta}_y \\ \gamma^2\dot{\beta}_z \end{pmatrix} = \frac{\sigma D}{\pi \mathrm{m_o c^2}} \frac{1}{\gamma} \int_0^{\theta_o} T^4(\theta)\, \underline{\Psi}(\underline{\beta};\theta)\,(1-\beta_z\cos\theta)\sin\theta\,\mathrm{d}\theta \tag{3.4}$$

where

$$\underline{\Psi}(\underline{\beta};\theta) = \int_0^{2\pi} \underline{\Upsilon}(\underline{\beta};\theta,\phi)\,\mathrm{d}\phi = \begin{pmatrix} 0 \\ 0 \\ 2\pi\gamma^2(\cos\theta-\beta_z) \end{pmatrix} . \tag{3.5}$$

Equations (3.4) and (3.5) clearly demonstrate that if the motion of the bullet is initially axial then it remains so for all later times, as would be expected from consideration of the symmetry of the problem alone. If the radiator is assumed to be isothermal such that $T(\theta) = T$ then Eq. (3.4) further simplifies and, by Eq. (3.5), the axial equation of motion has the form

$$\dot{\beta}_z = \frac{2\sigma D T^4}{\mathrm{m_o c^2}} \frac{1}{\gamma} \int_0^{\theta_o} (\cos\theta - \beta_z)\,(1-\beta_z\cos\theta)\,\sin\theta\,\mathrm{d}\theta \tag{3.6}$$

which, by means of the substitution $\mu = \cos\theta$, can be re-expressed as

$$\begin{aligned} \dot{\beta}_z &= \frac{2\sigma D T^4}{\mathrm{m_o c^2}} \frac{1}{\gamma} \int_{\mu_o}^{1} (\mu-\beta_z)\,(1-\beta_z\mu)\,\mathrm{d}\mu \\ &= \frac{\sigma D T^4}{\mathrm{m_o c^2}} \frac{1}{3\gamma} \left[-2\beta_z\mu^3 + 3(1+\beta_z{}^2)\mu^2 - 6\beta_z\mu\right]_{\mu_o}^{1} \end{aligned} \tag{3.7}$$

where $\mu_o = \cos\theta_o$ and the Lorentz factor $\gamma = 1/\sqrt{1-\beta_z^2}$. The acceleration is thus dependent on the bullet parameters, namely mass and radius, through the ratio $D/\mathrm{m_o}$, dependent on the radiator geometry through the integral limit μ_o and, on account of the proportionality to T^4, is sensitive to the blackbody temperature of the driving radiation field. Equation (3.7) can readily be made dimensionless† yielding

$$\dot{\beta}_{z_d} = \frac{\mathrm{d}\beta_z}{\mathrm{d}t_d} = \frac{1}{3}\sqrt{1-\beta_z^2}\left[-2\beta_z\mu^3 + 3(1+\beta_z{}^2)\mu^2 - 6\beta_z\mu\right]_{\mu_o}^{1} \tag{3.8}$$

where

$$t_d = Wt \qquad \text{and} \qquad W = \sigma D T^4/\mathrm{m_o c^2} . \tag{3.9a,b}$$

The parameter W obviously represents the ratio of the power intercepted by the bullet to its rest mass energy and, on account of its proportionality to $\dot{\beta}_{z_d}$, must be large to ensure rapid

† A variable that has been made dimensionless is denoted by the subscript 'd'.

acceleration. Since the parameter D represents the cross-sectional area of the bullet, Eq. (3.9*b*) can alternatively be expressed as

$$W = \frac{\sigma\pi}{c^2}\frac{r'^2T^4}{m_o} \approx 2\times 10^{-24}\frac{r'^2T^4}{m_o}\ . \tag{3.10}$$

It should be recalled from §2.6 that for an isothermal radiator, the derived equations of motion are exact even if the size of the bullet is comparable to that of the cone. The only constraint imposed on the bullet radius is therefore obvious: r' must be such that the bullet fits within the funnel. As remarked in §3.1, the bullet radius has been assumed constant and therefore, if the bullet is initially at rest or approximately so such that $r \approx r'$, its radius must satisfy

$$r \leq z_o \sin\alpha \tag{3.11}$$

where z_o is the starting height of the bullet centre above the apex and α is the half-opening angle of the conical radiator. Hence, by Eqs. (3.10) and (3.11),

$$W \leq 2\times 10^{-24}\frac{T^4}{m_o}z_o^2\sin^2\alpha\ . \tag{3.12}$$

This is a general upper bound on the parameter W, the absolute upper bound occurring when the bullet is optically thin. If the bullet is composed of fully ionized hydrogen and is optically thin, the total cross-section that it presents to incident radiation is $D = N_e\sigma_T$ where N_e is the total number of electrons within the bullet and σ_T is the Thomson cross-section. The maximum value of the parameter W is then given by

$$W_{max} = \frac{\sigma\sigma_T}{(m_e+m_p)c^2}T^4 = \frac{m_e}{m_e+m_p}W_e \approx 2.5\times 10^{-26}T^4 \tag{3.13}$$

where W_e represents the parameter W for a single electron. A rough lower bound can be placed on W by assuming that at formation the bullet number density is comparable to stellar central densities; typically $n_e \sim 10^{32}\,m^{-3}$. For such a number density, the bullet radius is

$$r = \left[\frac{3}{4\pi}\left(\frac{m_o}{m_e+m_p}\right)\frac{1}{n_e}\right]^{\frac{1}{3}} \approx 1.1\times 10^{-2}m_o^{\frac{1}{3}} \tag{3.14}$$

and consequently the approximate range for the parameter W is

$$2.4\times 10^{-28}\frac{T^4}{m_o^{\frac{1}{3}}} \leq W \leq 2\times 10^{-24}\frac{T^4}{m_o}z_o^2\sin^2\alpha \leq 2.5\times 10^{-26}T^4\ . \tag{3.15}$$

For SS433 in particular, physical constraints imposed on the bullets if they are to be collisionally heated (Brown, Cassinelli and Collins, 1991) indicate that they subtend an angular radius of ~ 0.01 radians at the central source and have a mass in the range $5\times 10^{20} \leq m_o \leq 10^{21}$ kg. VLBI observations (Vermeulen, 1989) have revealed that the blobs are produced,

on average, every 2-5 days. Since the kinetic luminosity $L_{\mathrm{K.E.}} = \dot{m}v^2/2$ of the jets is $10^{39} - 10^{40}$ erg/s, the bullets must have masses in the approximate range $6 \times 10^{21} \leq \mathrm{m_o} \leq 10^{23}$ kg. The line widths of the moving optical lines suggest that the jet opening angle is less than 0.1 radians (Begelman et al., 1980) whilst the temperature at the base of the jets probably lies between 5×10^8 K and 8×10^8 K (Brinkmann et al., 1991).

The neglect of gravitational effects is a justified approximation. Regardless of how the jet acceleration works, the X-ray observations (§1.5.2) indicate that the emergent bullets are already moving at the terminal speed of 0.26c within a distance of $\sim 10^{10}$ m from the central engine which necessitates that the driving radiation force must greatly exceed the force of gravity. This does not, however, mean that gravity is negligible over the entire length of the accretion funnel from the immediate vicinity of the compact object outwards. This can readily be appreciated by comparing the resultant radiation force $\underline{f}_{rad}$ experienced by the bullet within the funnel with the force of gravity $\underline{f}_{grav}$. By Eq. (3.8), with $\beta_z = 0$ and $\mu_o = -\cos\alpha$, the radiation force is approximately given by

$$\underline{f}_{rad} = 5.9 \times 10^{16} T_8^4 \left(\frac{z}{10\mathrm{km}}\right)^2 \alpha_{-2}^4 \, \underline{\hat{e}}_z \tag{3.16}$$

where α_{-2} is the constant angular radius of the bullet in units of 10^{-2} radians. If one ignores any general relativistic effects and neglects the mass attributable to the accretion disc and considers only that of the central compact object M_x, the gravitational force is given by

$$\underline{f}_{grav} = -1.3 \times 10^{33} \frac{(M_X/M_\odot)\,\mathrm{m}_{o_{21}}}{(z/10\mathrm{km})^2} \, \underline{\hat{e}}_z \tag{3.17}$$

where $T_8 = T/10^8$ K and similarly $\mathrm{m}_{o_{21}} = \mathrm{m_o}/10^{21}$ kg. For outward acceleration to be possible, in the absence of any other forces, $f_{rad} > f_{grav}$ or equivalently, by Eqs. (3.16) and (3.17),

$$z/10\mathrm{km} > 1.2 \times 10^4 \frac{[(M_X/M_\odot)\,\mathrm{m}_{o_{21}}]^{\frac{1}{4}}}{T_8\,\alpha_{-2}} \, . \tag{3.18}$$

Thus, outward acceleration of the bullet is not possible for distances less than $\sim 10^8$ m from the central engine which, although large, is small compared to the probable upper limit of $\sim 10^{10}$ m over which the acceleration takes place. Indeed, the derived bound of $\sim 10^8$ m will likely be smaller in reality on account of the decrease in temperature of the funnel walls with increasing distance from the compact object. In addition, for the system (disc) to be in equilibrium outside the jets, the disc material must be supported against gravity by a combination of rotation and a temperature near the surface of the compact object in excess of 10^8 K which will further lower the limit on z in Eq. (3.18). This temperature constraint can be deduced by equating the radiation pressure at the surface of the compact object to the pressure attributable to gravitational attraction. If one neglects any contribution to the support of the disc by the centripetal force and assumes that the accretion disc is spherical, has a radius much greater

than that of the compact object, is of uniform density and is in hydrostatic equilibrium then, by solving the hydrostatic equation of equilibrium it can be shown that the pressure at the surface of the compact object $P(R_X)$ is given by

$$P(R_X) \approx \frac{3G}{8\pi}\frac{M_{ad}^2}{R_{ad}^4}\left[1+2\left(\frac{M_X}{M_{ad}}\right)\left(\frac{R_{ad}}{R_X}\right)\right] \tag{3.19}$$

where the subscripts 'ad' and 'X' refer to the accretion disc and the compact object respectively. If this gravitational pressure is countered solely by radiation pressure then, in the limit where $R_{ad} \gg R_X$, the temperature at the surface of the compact object necessary to support the thick disc is

$$T_8 \sim 1.3\left[\frac{(M_{ad}/10M_\odot)(M_X/M_\odot)}{R_{ad_{10}}^3(R_X/10\text{km})}\right]^{\frac{1}{4}} \text{K} . \tag{3.20}$$

Hence, on the basis of the comments above and by Eq. (3.15), the range of the parameter W appropriate for SS433 is

$$2.4\times10^{-3}\frac{T_8^4}{\mathrm{m}_{o_{21}}^{1/3}} \leq W \leq 0.2\frac{T_8^4 z_{o_8}^2 \alpha_{-2}^2}{\mathrm{m}_{o_{21}}} \leq 2.5\times10^6 T_8^4 \tag{3.21}$$

where, for the inner regions of the jet, T_8 probably lies in the range $5 \leq T_8 \leq 8$. This is of course a great over-simplification. In a more realistic representation of the acceleration funnel the cone should be finite in size and have a surface temperature that decreases with increasing distance from the apex. Such a model will be considered later in chapter 4.

The resultant radiation force $\underline{f}_{rad}$ experienced by a stationary bullet located above an infinite isothermal plane is directed along the normal to the plane and has magnitude

$$f_{rad} = \frac{\sigma T^4}{\mathrm{c}} D . \tag{3.22}$$

If all relativistic effects are ignored then the radiation force experienced by the bullet for all later times will be given by Eq. (3.22) and, for a bullet of constant rest mass, the time taken to accelerate to a speed v will be simply

$$t_v = \frac{\mathrm{m_o} c v}{\sigma T^4}\frac{1}{D} . \tag{3.23}$$

Consequently, the parameter W can be regarded as denoting the time taken for the bullet to accelerate from rest to the speed of light and as such represents a measure of the characteristic timescale of the problem $t_c = 1/W$. For an electron, by Eq. (3.13), $t_c \sim (3.8/T_5)^4$ s whilst for a bullet of mass $\mathrm{m_o} = 10^{21}$ kg and number density $n_e = 10^{32}\,\mathrm{m}^{-3}$, by Eqs. (3.10) and (3.14), the characteristic timescale is $t_c \sim (4.5/T_8)^4$ s. Note, however, that the assumptions adopted

above are at best inaccurate and that the outlined arguments provide a crude description of the parameter W.

§3.2.2 The Plane

The plane represents a specific case of the general conical radiator in which the semi-angle $\alpha = \pi/2$. A photon emitted infinitely far from the bullet will, in the rest frame of the radiator, make an angle $\theta_0 = \pi/2$ with the positive z-axis. Thus $\mu_0 = 0$ and the dimensionless, axial equation of motion, by Eq. (3.8), is

$$\dot{\beta}_{z_d} = \frac{1}{3}\sqrt{1-\beta_z^2}\,(3{\beta_z}^2 - 8\beta_z + 3) \ . \tag{3.24}$$

From inspection of Eq. (3.24) it is clear that a physical solution to $\dot{\beta}_{z_d} = 0$ exists. This occurs at $\beta_z = \beta_\infty$ where

$$\beta_\infty = \frac{4-\sqrt{7}}{3} \approx 0.4514 \tag{3.25}$$

is the terminal speed of the bullet above the plane. The terminal speed is clearly independent of the parameter W, unlike the acceleration which is directly proportional to W.

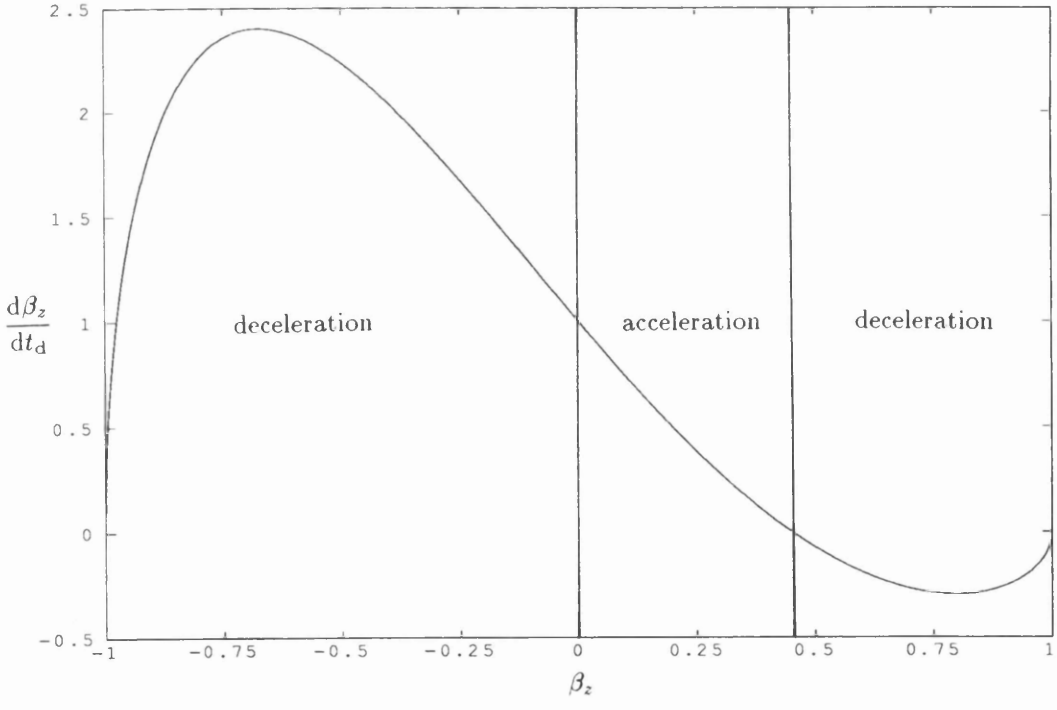

Fig. 3.1. The dimensionless acceleration experienced by a spherical bullet moving axially above an infinite, isothermal, planar radiator plotted as a function of the bullet speed (in units of c).

A plot of $\mathrm{d}\beta_z/\mathrm{d}t_\mathrm{d}$ as a function of β_z (Fig. 3.1) contains two distinct deceleration regions with the first, for motion towards the radiator ($-1 < \beta_z < 0$), having a maximum at $\beta_z \approx -0.674$ and the second, for motion away from the radiator but at a speed in excess of the terminal speed ($\beta_\infty < \beta_z < 1$), having a minimum at $\beta_z \approx 0.797$. Between these two deceleration bands lies the acceleration region ($0 \leq \beta_z < \beta_\infty$).

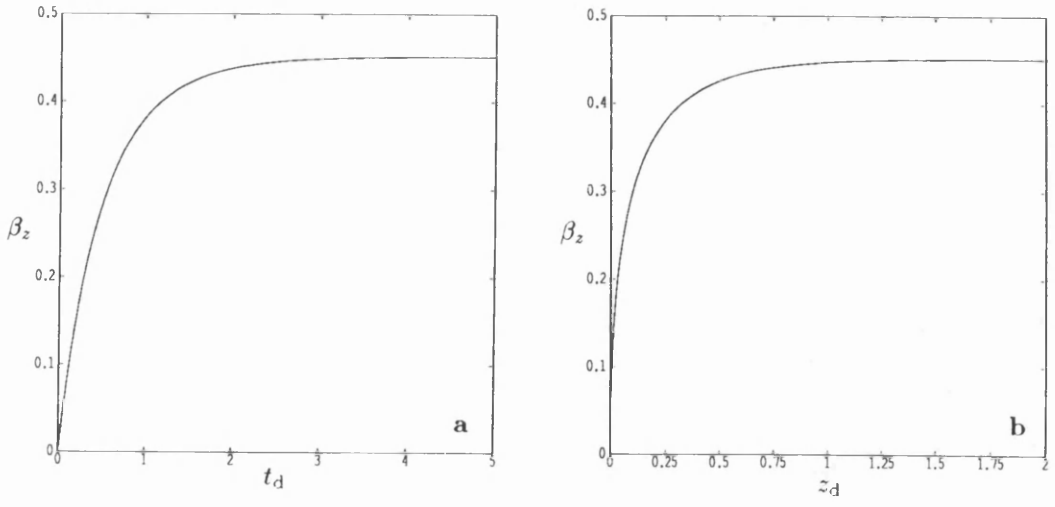

Figs. 3.2a,b. The results of integrating the equation of motion for a bullet moving above an infinite, isothermal, planar radiator with the initial condition β=0: (a) speed (in units of c) versus dimensionless time; (b) speed (in units of c) versus dimensionless distance.

β_{z_o}	1%	0.1%
0	2.685	4.145
−0.9	3.180	4.640
+0.9	3.471	4.937

Table 3.1. The degree of terminal speed attainment. The columns headed 1% and 0.1% show the dimensionless time, t_d, taken for a bullet with the selected initial speeds, β_{z_o}, to be within 1% and 0.1% of the terminal speed respectively.

The terminal speed is, in reality, an asymptotic limit that the bullet approaches as its journey time and its distance from the plane tend to infinity. The results of a numerical integration of Eq. (3.24) for a bullet with an initial speed $\beta_z = 0$ are shown in Figs. 3.2a,b whilst the dimensionless attainment times for both this bullet and those with initial speeds of ± 0.9c are tabulated in Table 3.1. The latter initial velocities have no particular physical significance but they do illustrate what appears at first sight to be a peculiarity: Inspection of Table 3.1 shows that a bullet with initial velocity -0.9c has a more rapid degree of terminal speed attainment than an identical bullet with initial velocity $+0.9$c. This is indeed bizarre if one recalls, from Eq. (3.25), that $\beta_\infty \approx 0.4514$. An understanding of the reasons for this behaviour can be appreciated from Fig. 3.3 which depicts the comoving angle of incidence θ' (with respect to the z'-axis) of a photon emitted infinitely far from the bullet as a function of β_z and from Fig. 3.4 which shows the ratio of frequencies ν'/ν as a function of β_z for photons emitted infinitely far from the bullet ($\theta = \pi/2$) and for photons emitted from the region of the plane directly below the bullet ($\theta = 0$). These graphs are of course representations of the phenomena of Doppler shift and aberration which I have already discussed in §2.4.4 and §2.4.5 respectively. It is evident from Fig. 3.3 that for any $\beta_z \neq 0$, photons emitted infinitely far from the bullet will, in the comoving frame, appear to be incident from ahead. These photons thus serve always to decelerate the bullet. As the magnitude of the bullet's velocity increases it can be seen from Fig. 3.4 that the energy of these photons and of course their momenta, as perceived in the bullet frame, also increases; particularly so for $|\beta_z| >\sim 0.5$. This, in tandem with their increasingly

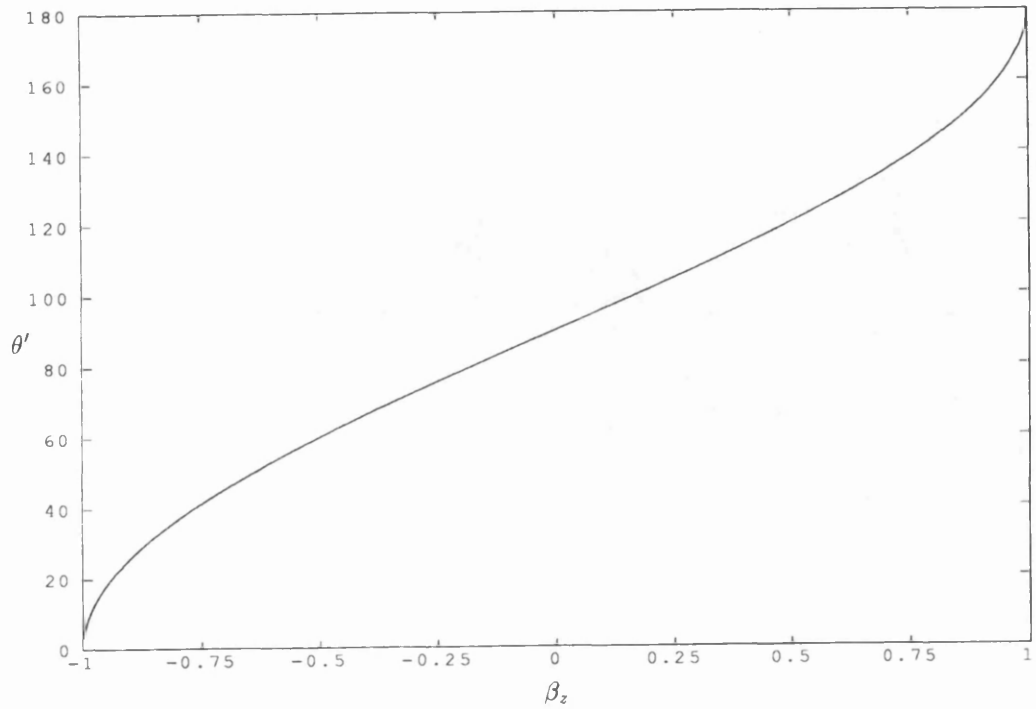

Fig. 3.3. The angle of incidence (with respect to the positive z'-axis), as observed in the rest frame of the bullet, of a photon emitted infinitely far from the bullet versus the axial bullet speed.

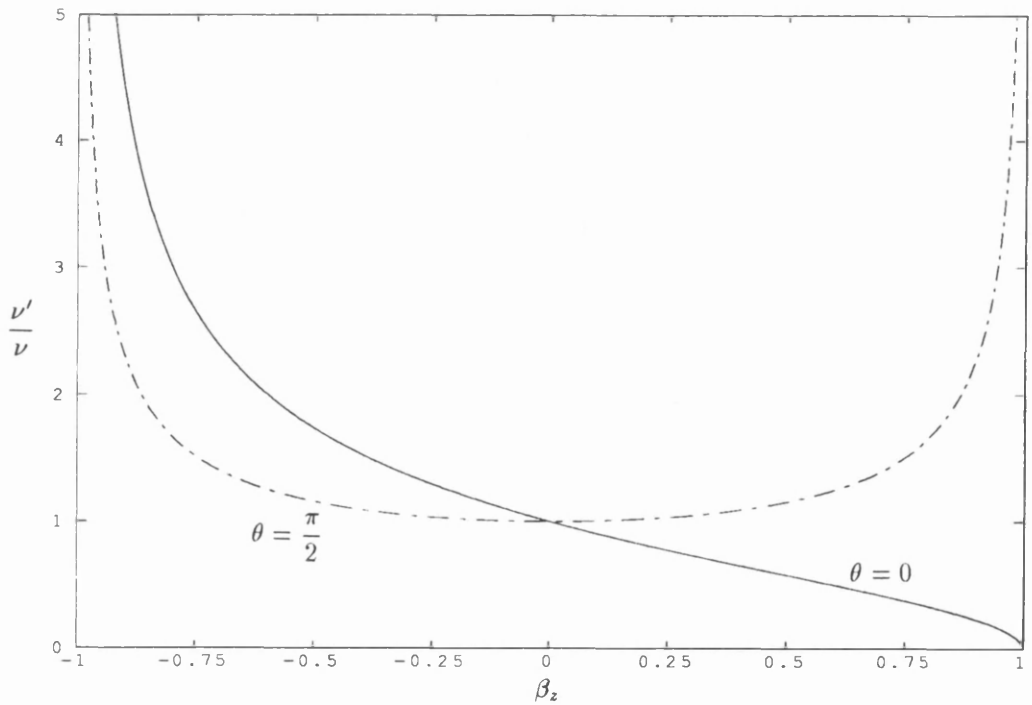

Fig. 3.4. The ratio ν'/ν versus β_z for photons emitted infinitely far from the bullet, $\theta=\pi/2$, (dashed-dotted line) and for photons emitted from the region immediately below the bullet, $\theta=0$, (full line).

more forward direction of incidence, means that photons emitted from the extremities of the radiator act dynamically to reduce the magnitude of the bullet's velocity. Photons emitted from the region directly below the bullet suffer negligible aberration and are therefore always incident within some small solid angle about the z-axis. These photons will always drive a bullet away from the planar surface and can therefore act to decelerate or accelerate the bullet depending on the direction of its motion. From Fig. 3.4 it can be appreciated that, on account of the Doppler shift of these photons, a bullet moving highly relativistically towards the plane will be rapidly decelerated by photons emitted from directly below it whilst a bullet moving highly relativistically away from the plane will be accelerated at a considerably reduced rate by the same photons. It can be realised, therefore, that all photons emitted by the radiating plane act to decelerate a bullet moving towards it whilst only those emitted from its extremities decelerate a bullet moving at a super-terminal speed. This enhanced deceleration experienced by bullets moving towards the plane and the tendency of photons emitted from the region of the plane directly below the bullet always to drive the bullet from the plane regardless of whether it has a super-terminal speed or not make it possible for a highly relativistic bullet directed towards the plane to have a more rapid degree of terminal speed attainment than an identical bullet moving with the same speed away from the plane. This tendency is manifest in Fig 3.1 by the generally greater magnitude of the 'negative' deceleration region compared to the 'positive' deceleration region.

The zero end-points which occur at $|\beta_z| = 1$ in Fig. 3.1 are worthy of explanation. A material particle can never attain $|\beta_z| = 1$ but in the limit $|\beta_z| \to 1$, $|\mathrm{d}\beta_z/\mathrm{d}t_\mathrm{d}| \to 0$ indicating that a super-relativistic bullet suffers minimal deceleration. This does not mean that the magnitude of the radiation force on the bullet also tends to zero; on the contrary, the magnitude of the radiation force tends to infinity. The axial three-force experienced by a body of constant rest mass $\mathrm{m_o}$ moving at speed β_z, by Eqs. (2.11), (2.14), (2.19) and (2.87), is

$$f_z = \mathrm{m_o}\gamma^3 \mathrm{c}\,\frac{\mathrm{d}\beta_z}{\mathrm{d}t}\ . \tag{3.26}$$

Thus, by Eq. (3.24), the axial radiation force experienced by the bullet is

$$f_z = \mathrm{m_o\,c}\,W\frac{3\beta_z^2 - 8\beta_z + 3}{3(1-\beta_z^2)} \tag{3.27}$$

which, by the introduction of the dimensionless radiation force $f_{z_\mathrm{d}} = f_z/\mathrm{m_o c}W$, can be re-expressed as

$$f_{z_\mathrm{d}} = \frac{3\beta_z^2 - 8\beta_z + 3}{3(1-\beta_z^2)}\ . \tag{3.28}$$

Clearly, therefore, $f_{z_\mathrm{d}} \to \pm\infty$ as $\beta_z \to \mp 1$. The dimensionless radiaton force is, of course, zero only at $\beta_z = \beta_\infty$.

As already mentioned, the principal driving force originates from photons emitted from the region on the radiating plane directly below the bullet whilst the principal inhibiting force originates from photons emitted infinitely far from the bullet. The differentiation between driving and decelerative photons can be made more precise: In the comoving frame, all photons incident with $\theta' > \pi/2$ decelerate the bullet whilst those incident with $\theta' < \pi/2$ drive the bullet. By the aberration formula (Eq. 2.65) a photon incident at an angle $\theta' = \pi/2$ in the comoving frame is observed in the rest frame of the radiator to be incident at an angle θ_* where

$$\theta_* = \arccos \beta_z \ . \tag{3.29}$$

Therefore, in the radiation source rest frame, all photons incident at an inclination θ to the positive z-axis in the range $0 \leq \theta \leq \theta_*$ ($\beta_z \leq \mu \leq 1$) accelerate the bullet whilst all photons incident in the range $\theta_* \leq \theta \leq \pi/2$ ($0 \leq \mu \leq \beta_z$) decelerate the bullet. The individual contribution made by both photon fluxes to the motion of the bullet can now be deduced. Let the total acceleration of the bullet be given by

$$\dot{\beta}_{z_d} = \dot{\beta}_{z_d}^{accn} - \dot{\beta}_{z_d}^{decn} \tag{3.30}$$

where $\dot{\beta}_{z_d}^{accn}$ and $\dot{\beta}_{z_d}^{decn}$ are the contributions to the total dimensionless axial acceleration by the accelerative and decelerative photon fluxes respectively. Then, by Eq. (3.8),

$$\dot{\beta}_{z_d}^{accn} = \frac{1}{3}\sqrt{1-\beta_z^2}\,(3+\beta_z)\,(1-\beta_z)^3 \tag{3.31a}$$

and

$$\dot{\beta}_{z_d}^{decn} = \frac{1}{3}\sqrt{1-\beta_z^2}\,(3-{\beta_z}^2)\,{\beta_z}^2 \ . \tag{3.31b}$$

The behaviour of $\dot{\beta}_{z_d}^{accn}$ and $\dot{\beta}_{z_d}^{decn}$ as a function of β_z are shown in Fig. 3.5. The solid angles subtended by the two photon fluxes at the bullet in the radiation source rest frame are

$$\Omega_{accn} = 2\pi \int_0^{\arccos\beta_z} \sin\theta \, d\theta = 2\pi\,(1-\beta_z) \tag{3.32a}$$

$$\Omega_{decn} = 2\pi \int_{\arccos\beta_z}^{\frac{\pi}{2}} \sin\theta \, d\theta = 2\pi\,\beta_z \tag{3.32b}$$

Evidently, as the bullet accelerates from rest, Ω_{accn} decreases linearly with β_z whilst Ω_{decn} increases from zero linearly with β_z up to $2\pi\beta_\infty$.

From the discussion above it is intuitively obvious that the terminal speed above an infinite planar radiator with a temperature profile that decays from the centre outwards will be greater

than that above an infinite isothermal plane. This problem will be addressed quantitatively in chapter 4.

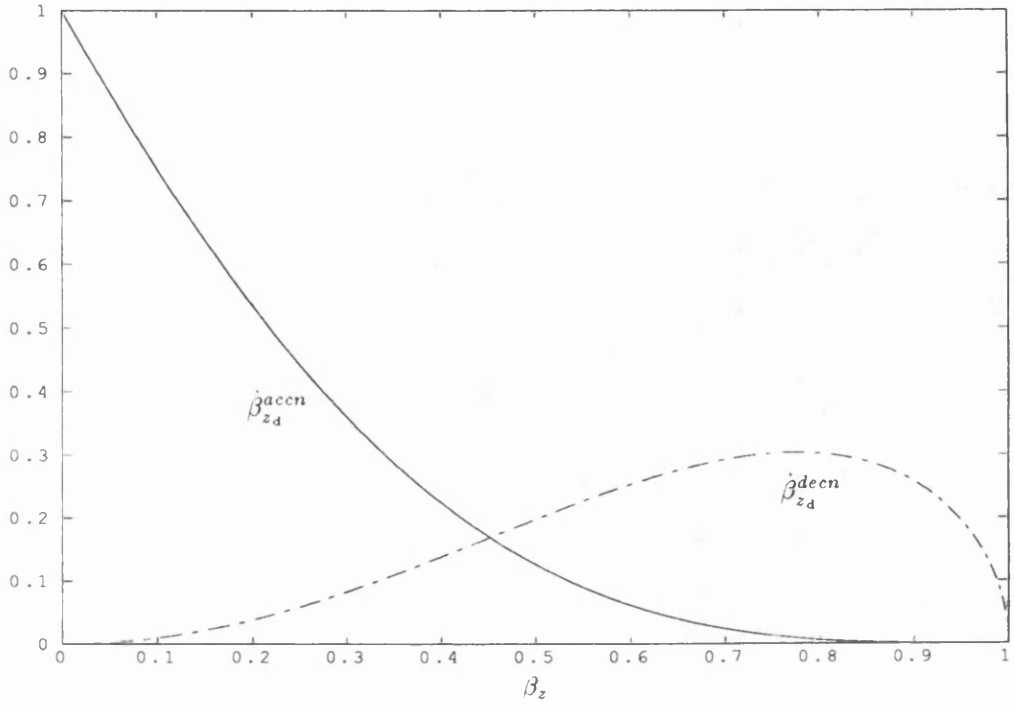

Fig. 3.5. The accelerative and decelerative components of the total dimensionless, axial acceleration versus the axial speed of the bullet. The crossover point marks the terminal speed.

The behaviour of a bullet subject to a small perturbation ϵ from the terminal speed can readily be deduced by linearising Eq. (3.24): Let the bullet be perturbed by a small amount ϵ form the terminal speed β_∞ such that

$$\beta_z = \beta_\infty + \epsilon \tag{3.33}$$

where $|\epsilon| \ll 1$. Substitution of Eq. (3.33) into Eq. (3.24) yields

$$\frac{\mathrm{d}\epsilon}{\mathrm{d}t_\mathrm{d}} = \frac{2}{3}\sqrt{1-\beta_\infty^2}\,(3\beta_\infty - 4)\,\epsilon + o(\epsilon^2) \tag{3.34}$$

which, ignoring terms of $o(\epsilon^2)$ and higher, can be integrated to give

$$\begin{aligned}\epsilon(t_\mathrm{d}) &= \epsilon \exp\left\{\left[\frac{2}{3}\sqrt{1-\beta_\infty^2}\,(3\beta_\infty - 4)\right] t_\mathrm{d}\right\} \\ &\approx \epsilon \exp\left\{-1.574\, t_\mathrm{d}\right\} \ .\end{aligned} \tag{3.35}$$

Thus, the dimensionless e-folding time for reversion back to the terminal speed is ~ 0.635 which is, from inspection of Fig. 3.2a, comparable for the time taken by the same bullet to accelerate from rest to approximately one third of the speed of light.

§3.2.3 The Cone

A photon emitted from the surface of an infinite conical radiator of semi-angle α, infinitely far from the bullet will make an angle $\theta_0 = \pi - \alpha$ with the positive z-axis. Hence $\mu_0 = -\cos\alpha$ and by Eq. (3.8) the dimensionless axial equation of motion is

$$\dot{\beta}_{z_d} = \frac{1}{3}\sqrt{1-\beta_z^2}\left\{3\beta_z^2\sin^2\alpha - 2\beta_z(4+\cos^3\alpha+3\cos\alpha)+3\sin^2\alpha\right\} . \qquad (3.36)$$

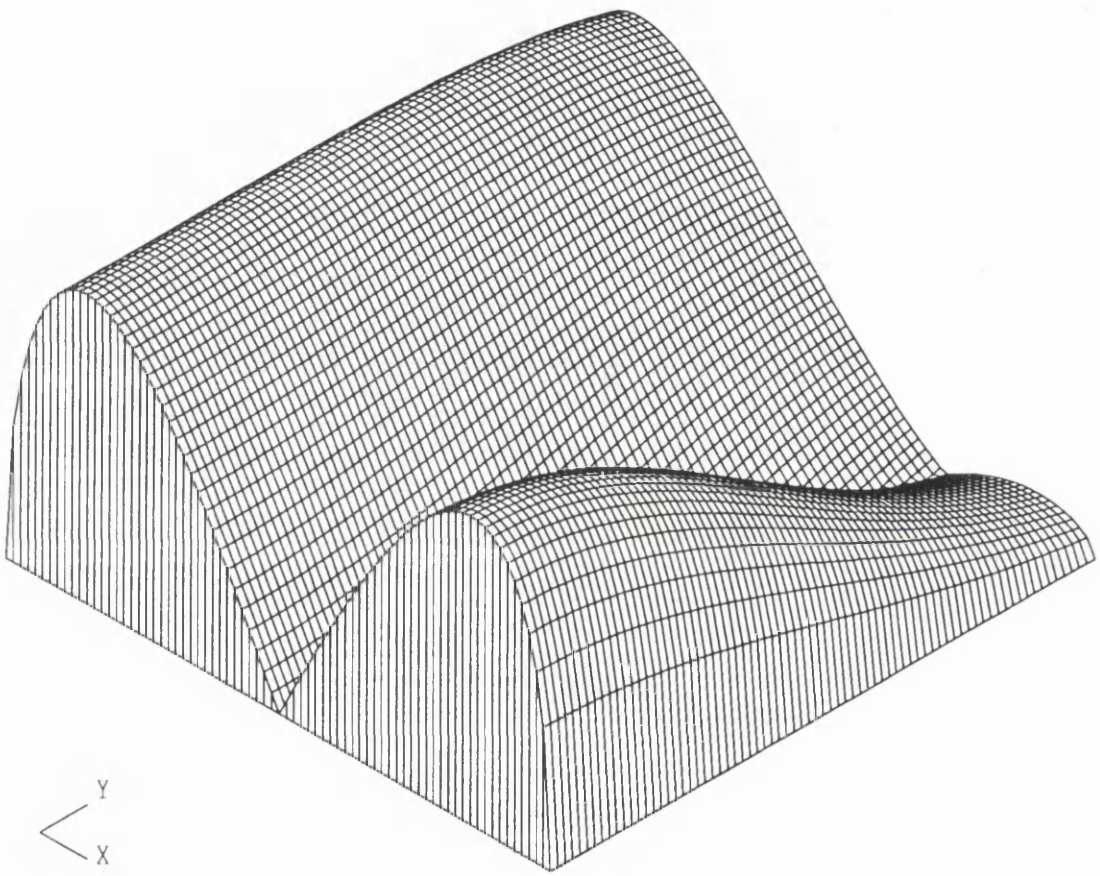

Fig. 3.6. An isometric projection of the magnitude of the dimensionless bullet acceleration plotted as a function of the bullet speed, β_z, and the funnel semi-angle. The bullet speed increases from -1 to 1 along the base axis labeled X whilst the funnel semi-angle, α, increases from 0° to 90° along the base axis labeled Y. The bottom of the trough marks the domain in β_z and α for which the bullet moves at a constant speed.

An isometric projection of the magnitude of the dimensionless bullet acceleration as a function of the semi-opening angle of the cone and the bullet speed is shown in Fig. 3.6. The clearly defined trough delineates the region where the dimensionless acceleration is zero and therefore corresponds to the terminal speed of the bullet for a given cone opening angle. By setting the dimensionless acceleration equal to zero, it can easily be shown that the functional dependence of the bullet terminal speed β_∞ on the cone semi-opening angle α is given by

$$\beta_\infty(\alpha) = p(\alpha) - \sqrt{p^2(\alpha)-1} \qquad \text{where} \qquad p(\alpha) = \frac{4+\cos^3\alpha+3\cos\alpha}{3\sin^2\alpha} . \qquad (3.37a,b)$$

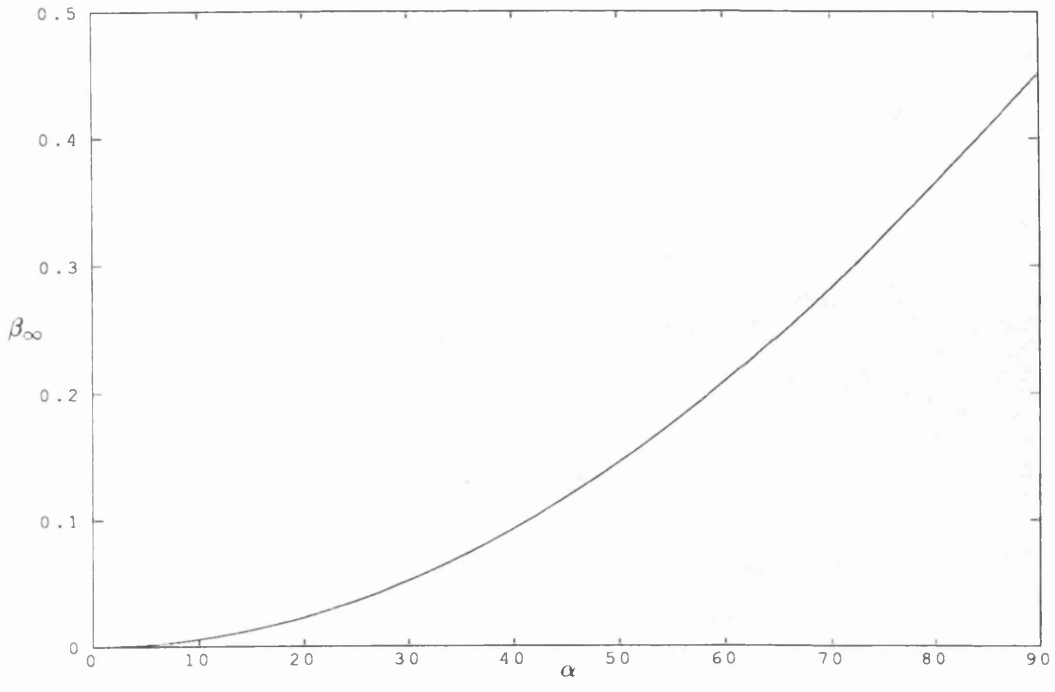

Fig. 3.7. The terminal speed, β_∞, versus the funnel semi-angle, α, in degrees.

A plot of the terminal speed as a function of the semi-opening angle α is shown in Fig. 3.7. Although Eqs. (3.37a, b) are valid for $\alpha > 90°$ these values have not been displayed since such inverted conical radiators have no physical significance. For the bullet to have a terminal speed of 0.26c, the same as that observed in SS433, the required semi-opening angle of the cone is $\sim 67.1°$. This is far greater then the funnel opening angles predicted to occur in the accretion discs of compact objects undergoing highly supercritical accretion such as SS433. The required half-opening angle of $\sim 67.1°$ is also incompatible with the observations which indicate that a representative half-opening angle is $\sim 1°$ unless the bullet is much smaller than the funnel. This latter condition may be satisfied if the radiation field within the funnel contributes significantly to the collimation process (see §3.3.2 and §3.3.3).

For cones with small half-opening angles, using the standard trigonometric power series expansions (Gradshteyn and Ryzhik, 1980),

$$\cos\alpha = 1 - \frac{1}{2}\alpha^2 + \frac{1}{24}\alpha^4 - \cdots \tag{3.38a}$$

$$\cos^3\alpha = 1 - \frac{27}{28}\alpha^2 + \frac{81}{96}\alpha^4 + \cdots \tag{3.38b}$$

$$\csc^2\alpha = \frac{1}{\alpha^2} + \frac{1}{3} + \frac{1}{15}\alpha^2 + \frac{2}{189}\alpha^4 + \cdots \tag{3.38c}$$

it is possible to show that

$$p(\alpha) = \frac{8}{3\alpha^2}\left\{1 - \frac{53}{192}\alpha^2 - \frac{59}{3840}\alpha^4 + \cdots\right\} \tag{3.39}$$

and

$$\sqrt{p(\alpha)^2 - 1} = \frac{8}{3\alpha^2}\left\{1 - \frac{53}{192}\alpha^2 - \frac{329}{3840}\alpha^4 + \cdots\right\} \tag{3.40}$$

and that thus, the terminal speed is dependent on α according to

$$\beta_\infty(\alpha) = \frac{3}{16}\alpha^2 + \cdots . \tag{3.41}$$

Hence, the terminal speed for a bullet within a funnel with an half-opening angle of $\sim 1°$ is $\sim 5 \times 10^{-5}$c which is approximately three orders of magnitude less than the observed velocity of the optical bullets. It is obvious that narrow, isothermal funnels are totally unsuitable for the attainment of high terminal speeds. The reason for the decrease in the terminal speed with decreasing opening angle evident in Fig. 3.7 is simple: as α decreases a greater proportion of the radiation that impinges on the surface of the bullet originates from regions more directly ahead of the bullet. These photons impede the acceleration and restrict the terminal speed to lower values. The degree to which these inhibiting photons limit the terminal speed will be less in reality since the surface temperature of the funnel walls will decrease with increasing distance from the central compact component making the attainment of higher terminal speeds possible. In chapter 4 I will consider the temperature gradients required for this effect to be important in SS433.

For completeness, consider the limiting case in which $\alpha = 0$. In this limit Eq. (3.36) reduces to

$$\dot{\beta}_\mathrm{d} = -\frac{16}{3}\sqrt{1-\beta^2}\,\beta \tag{3.42}$$

which represents motion within an isotropic radiation field. Consequently there can be no preferred direction; the bullet's velocity vector, in the absence of all other forces, will be rectilinear and will therefore have a single component which has been denoted by β. Integration of Eq. (3.42) yields

$$\gamma(t_\mathrm{d}, \gamma_\circ) = \frac{1 - h(t_\mathrm{d}, \gamma_\circ)}{1 + h(t_\mathrm{d}, \gamma_\circ)} \qquad \text{where} \qquad h(t_\mathrm{d}, \gamma_\circ) = \frac{\gamma_\circ - 1}{\gamma_\circ + 1}\exp(-\frac{32}{3}t_\mathrm{d}) \tag{3.43a,b}$$

and $\gamma_\circ$ is the Lorentz factor of the bullet at $t_\mathrm{d} = 0$. These equations can readily be solved for β to give

$$\frac{\beta(t_\mathrm{d}, \gamma_\circ)}{\beta_\circ} = \frac{(1 + \Gamma_\circ)\exp(-\frac{16}{3}t_\mathrm{d})}{1 + \Gamma_\circ \exp(-\frac{32}{3}t_\mathrm{d})} \qquad \text{where} \qquad \Gamma_\circ = \frac{\gamma_\circ - 1}{\gamma_\circ + 1}\,. \tag{3.44a,b}$$

The kinetic energy of a bullet with (constant) rest mass m_0 and Lorentz factor γ, in units of the rest mass energy, is $E_{\mathrm{KE_d}} = \gamma - 1$. Hence, by Eqs. (3.43$a,b$), the rate of kinetic energy loss for a bullet moving within an isotropic radiation field is given by

$$\dot{E}_{\mathrm{KE_d}} = \frac{\mathrm{d}(\gamma - 1)}{\mathrm{d}t_\mathrm{d}} = -\frac{64}{3}\frac{h(t_\mathrm{d}, \gamma_0)}{[1 - h(t_\mathrm{d}, \gamma_0)]^2} \,. \tag{3.45}$$

An obvious application of Eqs (3.43a,b), (3.44a,b) and (3.45) is to the motion of a bullet through the microwave background, the spectrum of which can be fitted remarkably well by a blackbody with a temperature of $T = 2.735 \pm 0.06$ K (Mather et al., 1990). In this context the term 'bullet', rather than referring to a conglomeration of matter as it has previously, is most applicable to a free particle such as an electron for which, by Eq. (3.13), $t_\mathrm{d} \approx 2.6 \times 10^{-21}\, t$.

Consider now the contribution made to the total dimensionless acceleration by the accelerative and decelerative photon fluxes. As in the planar case, all photons incident in the range $0 \leq \theta \leq \theta_*$ ($\beta_z < \mu \leq 1$) accelerate the bullet and therefore $\dot{\beta}_z^{accn}$ for an infinite, isothermal cone is identical to that for an infinite, isothermal plane which is given by Eq. (3.31a). The range of incidence angles for the decelerative photon flux in the conical case is $\theta_* < \theta \leq \pi - \alpha$ ($-\cos\alpha \leq \mu < \beta_z$) and thus, by Eq. (3.8),

$$\dot{\beta}_{z_\mathrm{d}}^{decn} = -\frac{1}{3}\sqrt{1 - \beta_z^2}\,(\beta_z + \cos\alpha)^2\,(\beta_z^2 - 2\beta_z\cos\alpha - 3) \,. \tag{3.46}$$

The important point to note is that the contribution made by the driving photons is independent of the cone semi-angle whilst the decelerative contribution increases as α decreases for a given β_z. The solid angle subtended by the driving photon flux at the bullet, as observed in the radiation source rest frame, is also independent of α and is given by Eq. (3.32a) whilst the solid angle subtended by the decelerative photon flux is

$$\Omega_{decn} = 2\pi \int_{\arccos\beta_z}^{\pi-\alpha} \sin\theta \,\mathrm{d}\theta = 2\pi(\beta_z + \cos\alpha) \,. \tag{3.47}$$

The behaviour of $\Omega_{accn}/\Omega_{rad}$ and $\Omega_{decn}/\Omega_{rad}$, where $\Omega_{rad} = \Omega_{accn} + \Omega_{decn}$ is the solid angle subtended by the entire radiation field, as a function of α for a terminal speed bullet is shown in Fig. 3.8. As the cone angle increases the proportion of the radiation field which contributes to the acceleration increases whilst the proportion that contributes to the deceleration decreases. This coincides with an increase in the terminal speed of the bullet.

Equation (3.36) can be linearised to reveal the behaviour of the bullet under small perturbations from the terminal speed. By Eqs. (3.33) and (3.37a,b), such an analysis indicates that

$$\frac{\mathrm{d}\epsilon}{\mathrm{d}t_\mathrm{d}} = -\frac{1}{\beta_\infty}(1 - \beta_\infty^2)^{\frac{3}{2}} \sin^2\alpha\,\epsilon \tag{3.48}$$

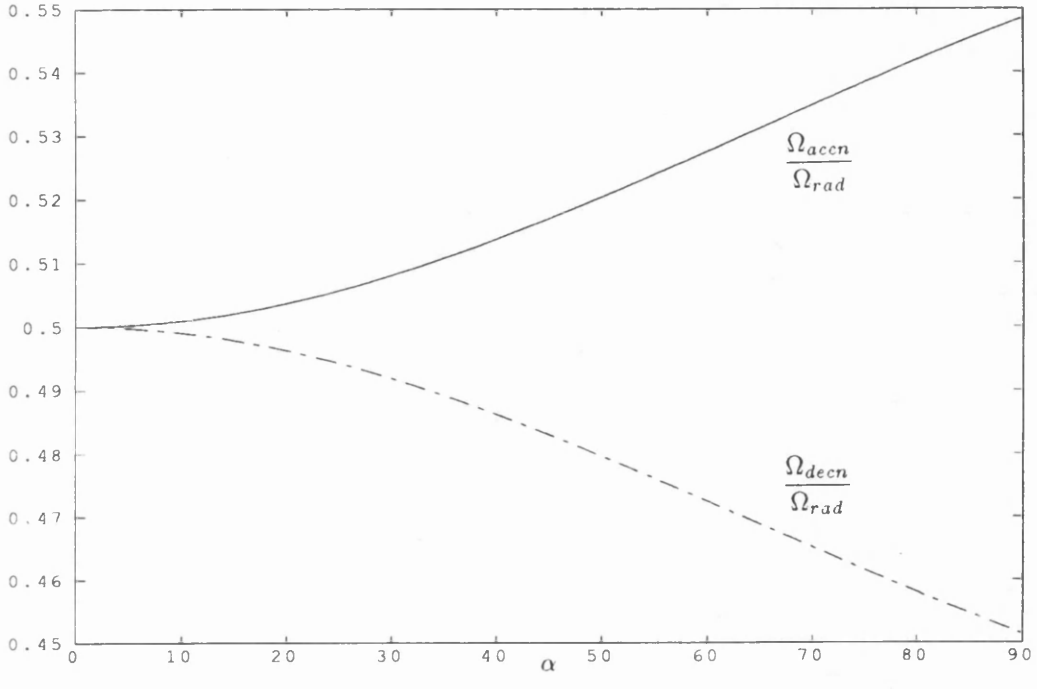

Fig. 3.8. The respective ratios $\Omega_{accn}/\Omega_{rad}$ and $\Omega_{decn}/\Omega_{rad}$ versus the funnel semi-angle, α, for a bullet moving at the terminal speed given by Eqs. (3.37*a*,*b*).

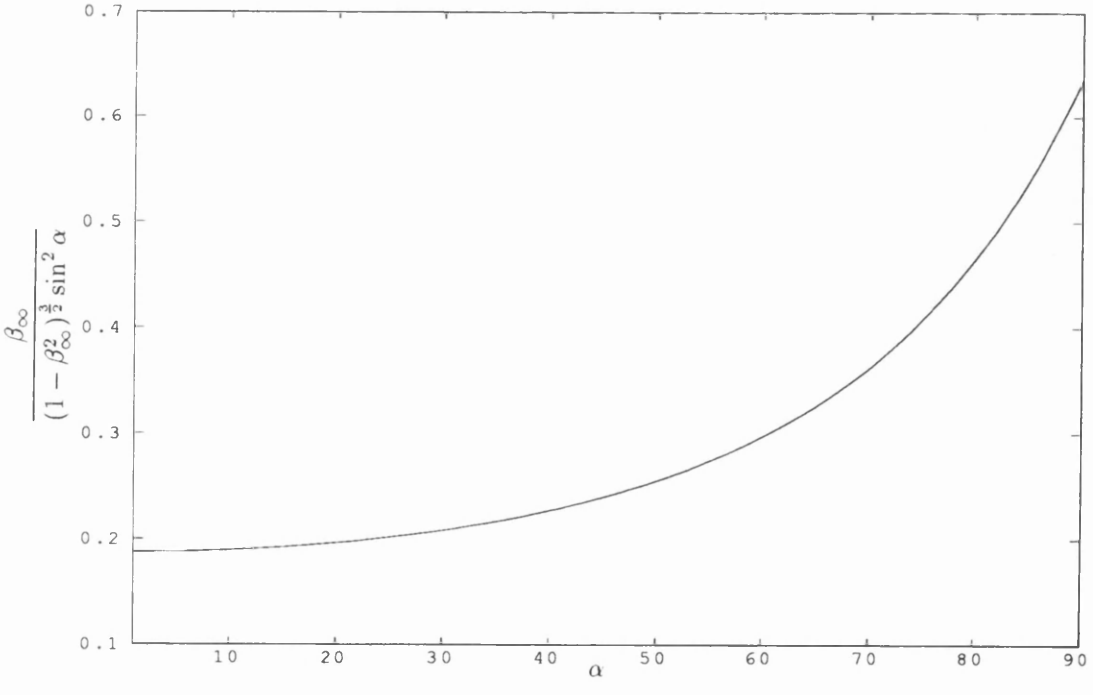

Fig. 3.9. The e-folding time for reversion back to the terminal speed versus the funnel semi-angle, α, for a bullet moving axially within an infinite, isothermal funnel.

which can be integrated to give

$$\epsilon(t_{\rm d}) = \epsilon \exp\left\{-\left[\frac{1}{\beta_\infty}(1-\beta_\infty^2)^{\frac{3}{2}}\sin^2\alpha\right] t_{\rm d}\right\} . \tag{3.49}$$

A plot of the dimensionless e-folding time for reversion back to the terminal speed as a function of α in the range $1^\circ \leq \alpha \leq 90^\circ$ is shown in Fig. 3.9. For small opening angles, by Eqs. (3.41) and (3.49),

$$\epsilon(t_{\rm d}) = \epsilon \exp\left\{-\frac{16}{3} t_{\rm d}\right\} . \tag{3.50}$$

Thus, for narrow funnels, the dimensionless e-folding time is independent of the semi-opening angle of the cone and is equal to 3/16.

§3.3 Non-Axial Motion

§3.3.1 The Off-Axis Equation of Motion

Let the radiator be oriented as in §3.2.1 and let the bullet move with a general velocity above the radiator. The general velocity vector is given by Eq. (2.93) and, by Eqs. (2.92) and (2.94), the general equation of motion of the bullet will have the form

$$\underline{\beta} \times \left(\underline{\beta} \times \frac{{\rm d}\underline{\beta}}{{\rm d}t}\right) + \frac{{\rm d}\underline{\beta}}{{\rm d}t} = \frac{\sigma D}{\pi {\rm m_o c^2}} \frac{1}{\gamma^3} \int_0^{2\pi} \int_0^{\theta_\circ} T^4\big(-\hat{\underline{k}}(\theta,\phi)\big)\, \underline{\Upsilon}(\underline{\beta};\theta,\phi)\, \zeta(\underline{\beta};\theta,\phi)\, \sin\theta \, {\rm d}\theta \, {\rm d}\phi \tag{3.51}$$

where

$$\zeta(\underline{\beta};\theta,\phi) = 1 - \underline{\beta}\cdot\hat{\underline{k}} = 1 - \beta_x \sin\theta\cos\phi - \beta_y \sin\theta\sin\phi - \beta_z\cos\theta \tag{3.52}$$

and

$$\underline{\Upsilon}(\underline{\beta};\theta,\phi) = \hat{\underline{k}} - \gamma^2\zeta(\underline{\beta};\theta,\phi)\underline{\beta} = \begin{pmatrix} \sin\theta\cos\phi - \gamma^2\zeta(\underline{\beta};\theta,\phi)\beta_x \\ \sin\theta\sin\phi - \gamma^2\zeta(\underline{\beta};\theta,\phi)\beta_y \\ \cos\theta - \gamma^2\zeta(\underline{\beta};\theta,\phi)\beta_z \end{pmatrix} . \tag{3.53}$$

If the temperature profile of the radiator is azimuthally symmetric such that $T(\theta,\phi) = T(\theta)$, the integration over ϕ can be readily performed. Making use of the results

$$\int_0^{2\pi} \zeta^2(\underline{\beta};\theta,\phi)\, {\rm d}\phi = \pi\left\{2 - 4\beta_z\cos\theta + (\beta_x^2+\beta_y^2)\sin^2\theta + 2\beta_z^2\cos^2\theta\right\} = \pi\,\xi(\underline{\beta};\theta) \tag{3.54a}$$

$$\int_0^{2\pi} \zeta(\underline{\beta};\theta,\phi)\, {\rm d}\phi = 2\pi(1-\beta_z\cos\theta) \tag{3.54b}$$

$$\int_0^{2\pi} \begin{Bmatrix}\cos\phi \\ \sin\phi\end{Bmatrix} \zeta(\underline{\beta};\theta,\phi)\, {\rm d}\phi = -\pi \begin{Bmatrix}\beta_x \\ \beta_y\end{Bmatrix} \sin\theta , \tag{3.54c}$$

integration of Eq. (3.51) over ϕ yields

$$\underline{\beta} \times \left(\underline{\beta} \times \frac{\mathrm{d}\underline{\beta}}{\mathrm{d}t} \right) + \frac{\mathrm{d}\underline{\beta}}{\mathrm{d}t} = -\frac{\sigma D}{\mathrm{m_o c^2}} \frac{1}{\gamma^3} \int_0^{\theta_\circ} T^4(\theta) \begin{pmatrix} \beta_x \sin^2\theta + \gamma^2 \xi(\underline{\beta};\theta)\, \beta_x \\ \beta_y \sin^2\theta + \gamma^2 \xi(\underline{\beta};\theta)\, \beta_y \\ -2(1-\beta_z \cos\theta)\cos\theta + \gamma^2 \xi(\underline{\beta};\theta)\, \beta_z \end{pmatrix} \sin\theta \, \mathrm{d}\theta \tag{3.55}$$

where $\xi(\underline{\beta};\theta)$ is defined by Eq. (3.54a). By invoking the vector identity given by Eq. (2.91), multiplying the x and y components by β_x and β_y respectively and adding the resulting equations it is trivial to show that

$$\begin{aligned} &(\underline{\beta} \cdot \dot{\underline{\beta}})(\beta_x^2 + \beta_y^2) + \frac{1}{\gamma^2}(\beta_x \dot{\beta}_x + \beta_y \dot{\beta}_y) = \\ &-\frac{\sigma D}{\mathrm{m_o c^2}} \frac{1}{\gamma^3} \int_0^{\theta_\circ} T^4(\theta) \left\{ (\beta_x^2 + \beta_y^2) \sin^2\theta + \gamma^2 \xi(\underline{\beta};\theta)(\beta_x^2 + \beta_y^2) \right\} \sin\theta \, \mathrm{d}\theta \, . \end{aligned} \tag{3.56}$$

If the component β_r is now defined by

$$\beta_r = \sqrt{\beta_x^2 + \beta_y^2} \qquad \text{then} \qquad \dot{\beta}_r = \frac{\beta_x \dot{\beta}_x + \beta_y \dot{\beta}_y}{\sqrt{\beta_x^2 + \beta_y^2}} \tag{3.57a,b}$$

and, if $\beta_x^2 + \beta_y^2 \neq 0$ as indeed they must for off-axis motion, Eq. (3.55) can be rewritten as

$$(\underline{\beta} \cdot \dot{\underline{\beta}})\underline{\beta} + \frac{1}{\gamma^2}\dot{\underline{\beta}} = -\frac{\sigma D}{\mathrm{m_o c^2}} \frac{1}{\gamma^3} \int_0^{\theta_\circ} T^4(\theta) \begin{pmatrix} \beta_r \sin^2\theta + \gamma^2 \xi(\underline{\beta};\theta)\, \beta_r \\ -2(1-\beta_z \cos\theta)\cos\theta + \gamma^2 \xi(\underline{\beta};\theta)\, \beta_z \end{pmatrix} \sin\theta \, \mathrm{d}\theta \tag{3.58}$$

where the general velocity vector $\underline{\beta}$ has the form

$$\underline{\beta} = \begin{pmatrix} \beta_r \\ \beta_z \end{pmatrix} . \tag{3.59}$$

The β_r term now denotes the velocity component perpendicular to the z-axis whilst the β_z term retains its original meaning. This simplification of Eq. (3.55) reflects not only the azimuthal symmetry of the temperature profile of the radiator but also its infinite extent. For motion above such a radiator there are only two orthogonal velocity components and any motion must therefore be confined to a plane. The plane of the motion is determined by both the initial velocity of the bullet and by its initial position. If the radiator is isothermal such that $T(\theta) = T$ then, by means of the substitution $\mu = \cos\theta$, Eq. (3.58) further simplifies to

$$(\underline{\beta} \cdot \dot{\underline{\beta}}_{\mathrm{d}})\,\underline{\beta} + \frac{1}{\gamma^2}\dot{\underline{\beta}}_{\mathrm{d}} = -\frac{1}{\gamma^3} \int_{\mu_\circ}^{1} \begin{pmatrix} \beta_r(1-\mu^2) + \gamma^2 \xi(\underline{\beta};\mu)\beta_r \\ -2(1-\beta_z \mu)\,\mu + \gamma^2 \xi(\underline{\beta};\mu)\beta_z \end{pmatrix} \mathrm{d}\mu \tag{3.60}$$

where

$$\xi(\underline{\beta},\mu) = (2\beta_z^2 - \beta_r^2)\,\mu^2 - 4\beta_z \mu + \beta_r^2 + 2 \tag{3.61}$$

and the parameter W (Eq. 3.9b) has been absorbed in the usual manner to make the equation dimensionless. Solving Eq. (3.60) for $\dot{\beta}_{r_d}$ and $\dot{\beta}_{z_d}$ yields the coupled system of differential equations given by

$$\dot{\beta}_{r_d} = -\frac{1}{\gamma}\beta_r \int_{\mu_o}^{1} \left\{ (\beta_r^2 - 2\beta_z^2 - 1)\,\mu^2 - 2\beta_z \mu + (1 - \beta_r^2) + \xi(\underline{\beta}; \mu) \right\} \, \mathrm{d}\mu \tag{3.62a}$$

$$\dot{\beta}_{z_d} = \frac{1}{\gamma} \int_{\mu_o}^{1} \left\{ (2\beta_z^2 - \beta_r^2 - 2)\,\beta_z \mu^2 + 2(1 - \beta_z^2)\,\mu + \beta_r^2 \beta_z - \xi(\underline{\beta}; \mu)\,\beta_z \right\} \, \mathrm{d}\mu \tag{3.62b}$$

which upon substitution of Eq. (3.61) and integration over μ yield

$$\dot{\beta}_{r_d} = \frac{1}{3}\sqrt{1 - \beta_r^2 - \beta_z^2}\left\{3(1 - \mu_o^2)\,\beta_z + (-\mu_o^3 + 9\mu_o - 8)\right\}\,\beta_r \tag{3.63a}$$

$$\dot{\beta}_{z_d} = \frac{1}{3}\sqrt{1 - \beta_r^2 - \beta_z^2}\left\{3(1 - \mu_o^2)\,\beta_z^2 - 2(-\mu_o^3 - 3\mu_o + 4)\,\beta_z + 3(1 - \mu_o^2)\right\} \, . \tag{3.63b}$$

§3.3.2 The Plane

In this case $\mu_o = 0$ and Eqs. (3.63a, b) reduce to

$$\dot{\beta}_{r_d} = \frac{1}{3}\sqrt{1 - \beta_r^2 - \beta_z^2}\,\{3\beta_z - 8\}\,\beta_r \tag{3.64a}$$

$$\dot{\beta}_{z_d} = \frac{1}{3}\sqrt{1 - \beta_r^2 - \beta_z^2}\,\{3\beta_z^2 - 8\beta_z + 3\} \, . \tag{3.64b}$$

It can be seen immediately that if $\beta_r = 0$ then Eq. (3.64b) simplifies to Eq. (3.24) which describes purely axial motion and, in addition, that $\dot{\beta}_{r_d} = 0$ indicating that the motion remains axial for all later times. Since $3\beta_z - 8 < 0$ for all β_z and $0 < 1/\gamma \leq 1$ for all β_z and β_r, it can be deduced that motion parallel to the plane is damped. An illustrative numerical solution to Eqs. (3.64a, b) with an initial velocity $\underline{\beta} = (0.5, 0)$ is shown in Figs. 3.10a,b. The velocity component parallel

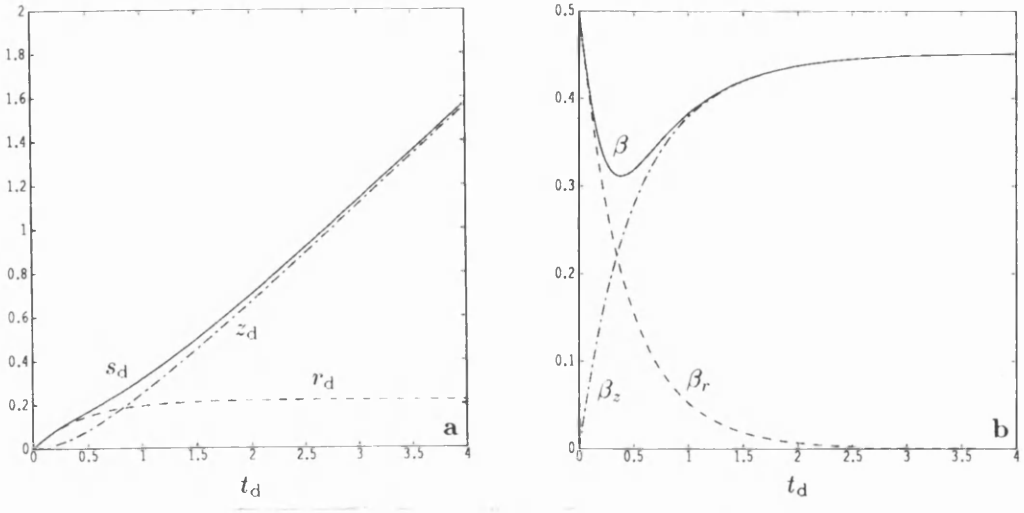

Figs. 3.10a,b. A numerical solution of Eqs. (3.64a,b) with the initial condition $\underline{\beta}$=(0.5,0): (a) dimensionless distance versus dimensionless time; (b) dimensionless speed versus dimensionless time. The distance traversed by the bullet from its release point is $s_d = \sqrt{z_d^2 + r_d^2}$ whilst the bullet's speed $\beta = \sqrt{\beta_r^2 + \beta_z^2}$.

to the radiating surface is strongly damped on a characteristic time scale comparable to that for terminal speed attainment. The form of the solution for $\beta_z(t_d)$ in Fig. 3.10b is very similar to that for axial motion illustrated in Fig. 3.2a. This is to be expected given the likeness of Eqs. (3.24) and (3.64b). The solutions are, however, not identical: for a given β_z and any mutually realisable non-zero β_r, the axial acceleration component for a bullet moving off-axis is reduced by a factor

$$g = \sqrt{\frac{1-\beta_r^2-\beta_z^2}{1-\beta_z^2}} \tag{3.65}$$

compared to an identical bullet moving axially with the same β_z above the same radiating plane. Obviously, as β_r increases the factor g decreases and the axial acceleration component decreases proportionately and, consequently, the terminal speed attainment time increases.

In the Newtonian limit ($\beta \ll 1$), Eqs. (3.64a,b) decouple to yield

$$\dot{\beta}_{r_d} \simeq -\frac{8}{3}\beta_r \Leftrightarrow v_r \simeq v_{r_o} \exp\left(-\frac{8}{3}t_d\right) \tag{3.66a}$$

$$\dot{\beta}_{z_d} \simeq 1 \Leftrightarrow v_z \simeq ct_d + v_{z_o} \ . \tag{3.66b}$$

Evidently, in this limit, there is no terminal speed though the velocity component parallel to the surface of the plane is exponentially damped with an dimensionless e-folding time of 3/8. It must however be reiterated that Eqs. (3.66a,b) are only valid for $\beta \ll 1$ and, since the terminal speed β_∞ is the same for all bullet and plane configurations, the equations apply only to the initial stages of the motion of a bullet released with a small initial velocity.

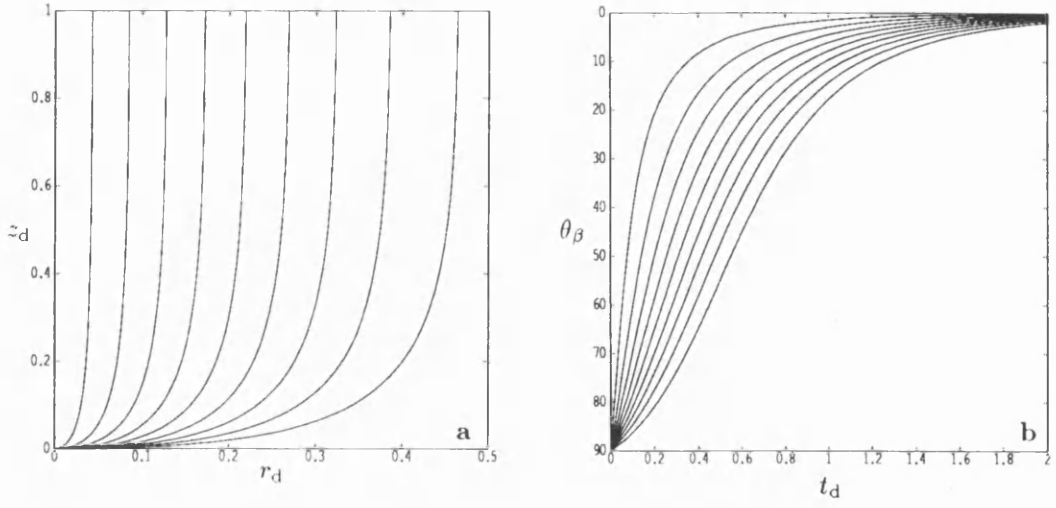

Figs. 3.11a,b. Collimation above an infinite, isothermal planar radiator: (a) the dimensionless distance normal to the plane, z_d, versus the dimensionless distance parallel to the plane, r_d; (b) the angle, θ_β, which the bullet's velocity vector makes with the positive z-axis versus the dimensionless time. In both illustrations the bullet's initial, axial velocity component is zero whilst the initial velocity component parallel to the surface of the radiator increases from 0.1c to 0.9c, in increments of 0.1c, from left to right.

Equations (3.64a, b) provide a means of deducing the degree to which the infinite, planar, isothermal blackbody surface can collimate radiatively driven material. Illustrations of this are provided by Figs. 3.11a,b and Fig. 3.12. Even in the extreme case where $\beta_{r_\circ} = 0.9$, it can be seen from Fig. 3.11a that a bullet will be closely aligned with the normal to the plane within a dimensionless distance (parallel to the surface) of 0.5 units. This corresponds to a physical distance of $c/2W$ metres and since, by Eq. (3.21), the minimum value of the parameter W is $\sim 2.4 \times 10^{-3} T_8^4 / \mathrm{m}_{\circ 21}^{\frac{1}{3}}$, represents an upper bound on the distance $r \sim 6.3 \times 10^{10} \mathrm{m}_{\circ 21}^{\frac{1}{3}} / T_8^4$ metres. The angle which the bullet's velocity vector makes with the $z-$axis is given by

$$\theta_\beta = \arctan\left(\frac{\beta_r}{\beta_z}\right) \tag{3.67}$$

and is plotted as a function of the dimensionless time in Fig. 3.11b. As one would expect, those bullets which have the lowest values of $\beta_{r_\circ}$ are collimated the most rapidly. The dimensionless time taken for a bullet to achieve the marked degree of collimation as a function of $\beta_{r_\circ}$ is shown in Fig. 3.12. For all but the most extreme values of $\beta_{r_\circ}$, the radiatively driven bullet is collimated to within 2°, 1° and 0.5° of the normal to the plane in $\sim$ 2, 2.5 and 3 dimensionless time units respectively. Since the initial condition $\beta_{z_\circ} = 0$ has been assumed these values represent upper bounds on the time taken to achieve the designated degree of collimation for all $\beta_{z_\circ}$ in the range $0 \leq \beta_{z_\circ} < \beta_\infty$. Hence, it can be concluded that, for example, all radiatively driven bullets moving above an isothermal, planar blackbody radiator with an initial velocity $(\beta_{r_\circ}, \beta_{z_\circ})$, where $0 \leq \beta_{z_\circ} < \beta_\infty$, will be collimated to within 1° of the normal to the plane within 2.5 dimensionless time units of being exposed to the radiation field. This represents an upper limit, by Eq. (3.21), of $\sim 10^{-2} \mathrm{m}_{\circ 21}^{\frac{1}{3}} / T_8^4$ days.

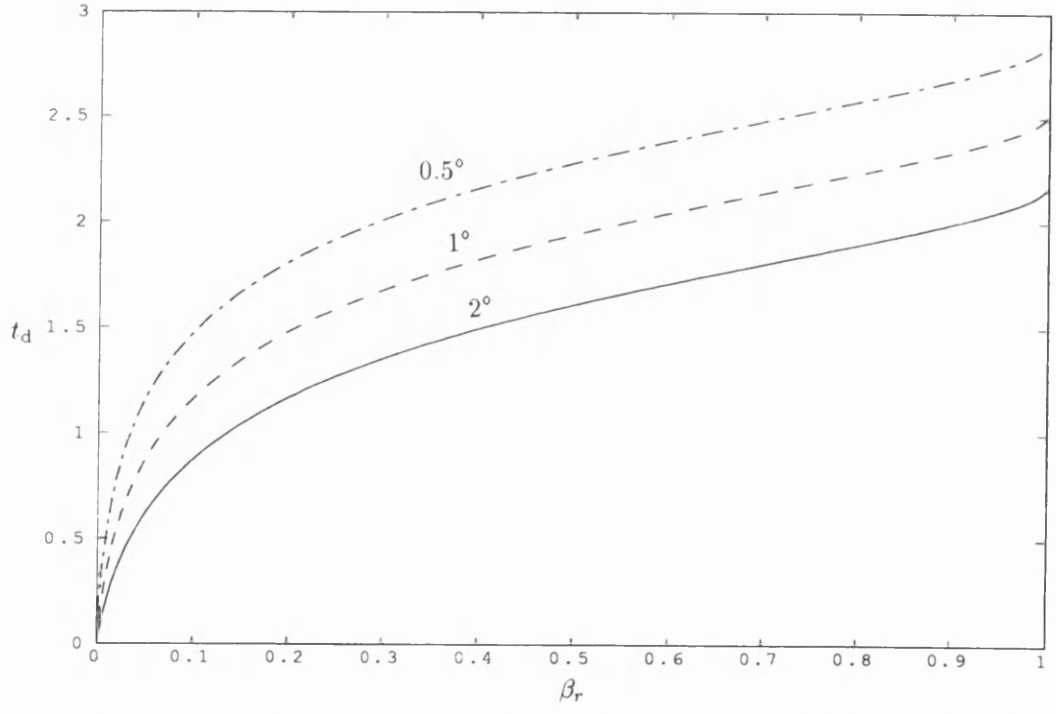

Fig. 3.12. The dimensionless time, t_d, taken for the bullet's velocity vector to make the labeled angle, θ_β, with respect to the plane normal, plotted as a function of the initial velocity component, $\beta_{r_\circ}$, parallel to the surface of the radiating plane. The initial velocity component along the surface normal, $\beta_{z_\circ}$ is zero in all cases.

Since both β_r and β_z are functions of t_d and $\dot{\beta}_{z_d} \neq 0$ for all β_r and for all β_z in the range $0 \leq \beta_z < \beta_\infty$, the chain rule may be invoked to re-express Eqs. (3.64a, b) in the separable form

$$\frac{\mathrm{d}\beta_r}{\beta_r} = \frac{3\beta_z - 8}{3\beta_z^2 - 8\beta_z + 3}\mathrm{d}\beta_z \ . \tag{3.68}$$

By the integral result (Gradshteyn and Ryzhik, 1980; result no. 2.103:5)

$$\int \frac{(Mx + N)\,\mathrm{d}x}{A + 2Bx + Cx^2} = \frac{M}{2C}\ln\left|A + 2Bx + Cx^2\right| + \frac{NC - MB}{2C\sqrt{B^2 - AC}}\ln\left|\frac{Cx + B - \sqrt{B^2 - AC}}{Cx + B + \sqrt{B^2 - AC}}\right|, \tag{3.69}$$

which is valid for $AC < B^2$, Eqn. (3.68) can then be integrated to give

$$\beta_r(\beta_z) = \beta_{r_\circ}\sqrt{\frac{|3\beta_z^2 - 8\beta_z + 3|}{|3\beta_{z_\circ}^2 - 8\beta_{z_\circ} + 3|}}\left[\left|\frac{3\beta_z - 4 + \sqrt{7}}{3\beta_z - 4 - \sqrt{7}}\right|\left|\frac{3\beta_{z_\circ} - 4 - \sqrt{7}}{3\beta_{z_\circ} - 4 + \sqrt{7}}\right|\right]^{\frac{2}{\sqrt{7}}} . \tag{3.70}$$

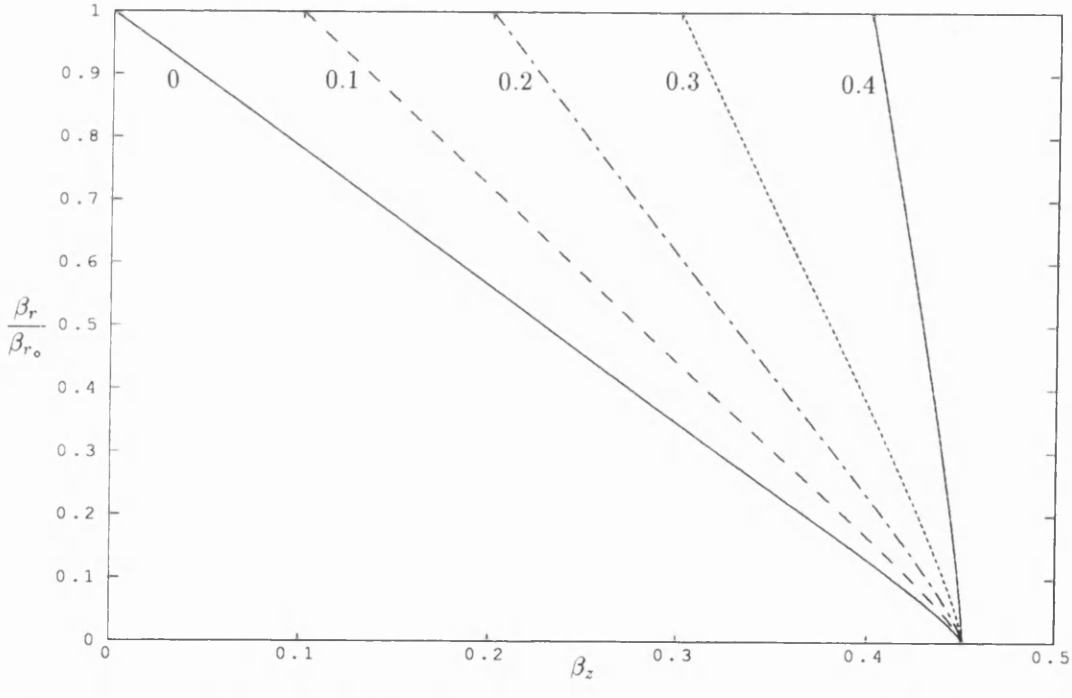

Fig. 3.13. The ratio $\beta_r/\beta_{r_\circ}$ versus the velocity component β_z along the surface normal for the labeled values of the initial velocity component $\beta_{z_\circ}$.

The nature of $\beta_r(\beta_z)/\beta_{r_\circ}$ for several $\beta_{z_\circ}$ in the range $0 \leq \beta_{r_\circ} < \beta_\infty$ is shown in Fig. 3.13. The solutions are very nearly linear except in the immediate locality of $\beta_z = \beta_\infty$. If the solutions are assumed linear over their entire range then it is simple to show that an approximation for $\beta_r(\beta_z)$ is given by

$$\beta_r(\beta_z) \approx \beta_{r_\circ}\left\{\frac{\beta_\infty - \beta_z}{\beta_\infty - \beta_{z_\circ}}\right\} \tag{3.71}$$

where $\beta_{z_\circ} \leq \beta_z \leq \beta_\infty$.

§3.3.3 The Cone

As in §3.2.3, $\mu_o = -\cos\alpha$ and Eqs. (3.63a, b) therefore simplify to

$$\dot{\beta}_{r_d} = \frac{1}{3}\sqrt{1-\beta_r^2-\beta_z^2}\left\{3\sin^2\alpha\beta_z + (\cos^3\alpha - 9\cos\alpha - 8)\right\}\beta_r \qquad (3.72a)$$

$$\dot{\beta}_{z_d} = \frac{1}{3}\sqrt{1-\beta_r^2-\beta_z^2}\left\{3\sin^2\alpha\beta_z^2 - 2(\cos^3\alpha + 3\cos\alpha + 4)\beta_z + 3\sin^2\alpha\right\} . \qquad (3.72b)$$

As indicated earlier, the motion of the bullet is confined to the plane which is determined by both its initial velocity and its starting position. Without resorting to a numerical integration of the equations of motion it is possible to deduce that any bullet which is released with a non-axial velocity component will eventually have an axial trajectory which need not necessarily coincide with the symmetry axis of the radiator but will be coplanar with it. This follows from the fact that $\dot{\beta}_{r_d} = 0$ only for $\beta_r = 0$ and $\dot{\beta}_{r_d} < 0$ for all β_z. Thus, for example, the radial velocity component of a bullet released with a non-zero radial velocity component on the symmetry axis of the cone will decrease in magnitude and tend towards zero. The bullet will then have a near axial trajectory which will not coincide with the symmetry axis of the cone. This behaviour is particular to the infinite geometry of the radiator and can best be appreciated by considering the radiation void as viewed by an observer at rest with respect to the radiation source and located instantaneously at the centre of the bullet (assuming for the interim that the bullet is transparent to the incident radiation). This observer, regardless of position within the radiation field, will perceive the radiation void (since it is infinitely distant) to be circular and to subtend a solid angle constant in time at their location. These observations will be identical to those made on the true axis of symmetry of the radiator. Consequently, once the radial component has been damped to near zero, the bullet trajectory will lie along one of the infinite number of these axial vectors only one of which passes through the apex of the cone and truly describes the symmetry axis of the cone.

In the above it is implicitly assumed that the initial conditions are such that the bullet does not collide with the funnel walls. This need not be the case and obviously if such a collision does take place then the ejection of the bullet will be impeded and perhaps prevented. Equations (3.72a, b) plus the simplistic constraints outlined below provide a means of determining the initial conditions for which ejection is possible: Let the bullet be released at time $t_d = 0$ on the true axis of symmetry of the cone at a height z_{d_o} above the apex with a velocity $\underline{\beta}_o$ at an inclination θ_{β_o} to the z-axis. Suppose that after some time interval t_d the bullet centre is located at a height z_{t_d} above the apex and at a radial distance r_{t_d} from the true symmetry axis and is moving with a velocity $\underline{\beta}$ at an inclination θ_β to the z-axis. Assume that if any contact between the bullet centre and the funnel wall is fuller than a grazing contact then the bullet is captured. For a cone of semi-angle α it then follows that

(a) ejection is guaranteed if $\theta_{\beta_o} \leq \alpha$

(b) ejection is guaranteed if $\theta_\beta \leq \alpha$ and $r_{t_d} \leq z_{t_d} \tan\alpha$

(c) ejection is possible if $\theta_\beta \geq \alpha$ and $r_{t_d} \leq z_{t_d} \tan\alpha$

(d) ejection is impossible if $\theta_\beta > \alpha$ and $r_{t_d} > z_{t_d} \tan\alpha$

and the problem reduces to finding a $\underline{\beta}_o$ such that at some later instant $\theta_\beta = \alpha$ at $r_{t_d} = z_{t_d} \tan\alpha$. The results of such calculations, for selected initial, dimensionless release heights $z_{d_o} = (W/c)\, z_o$ and cone half-angles of 1° and 0.5°, are depicted in the logarithmic polar diagrams of Figs. 3.14a-d. As one would expect, the permissible release speeds are less for the cone with the smaller opening angle and increase with the release height. These graphs highlight the role that the radiation pressure can play in collimating the bullets so permitting ejection in cases where one would naively expect the bullet to be captured: If one assumed that following release the bullet travelled ballistically within the funnel then only those bullets that had initial release inclinations θ_{β_o} in the range $0 \leq \theta_{\beta_o} \leq \alpha$ would be ejected. This is evidently not the case as Figs 3.14a-d illustrate and it can consequently be appreciated that the radiation pressure can contribute significantly to the collimation of the jet.

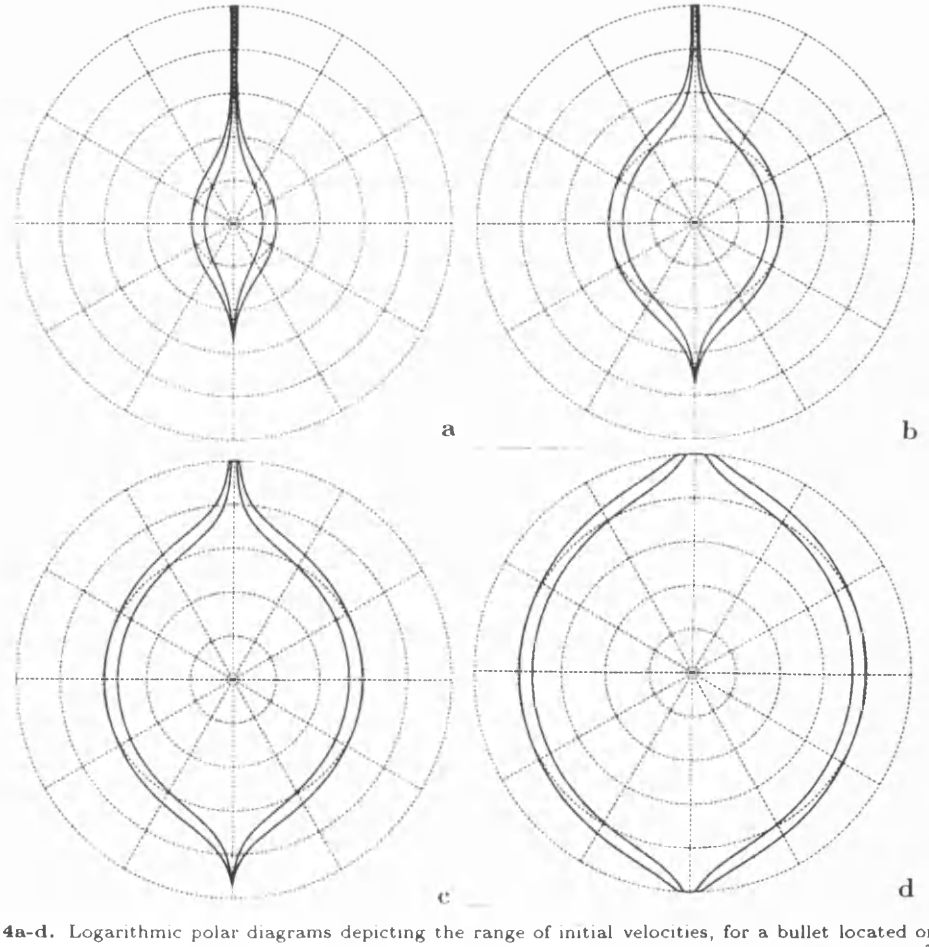

Figs. 3.14a-d. Logarithmic polar diagrams depicting the range of initial velocities, for a bullet located on-axis, for which escape is possible. The initial, dimensionless heights of the bullet above the funnel apex are: **a** 10^{-3}; **b** 10^{-2}; **c** 10^{-1} and **d** 10^{0}. The initial speed is plotted logarithmically along the radius of each diagram, each step inwards corresponding to a decrease in the speed by a factor of 10. The outer circle corresponds to a speed of 1 (in units of c) whilst the inner circle corresponds to a speed of 10^{-4}, the centre of each diagram corresponds to a release speed of zero. The angle of release with respect to the positive z-axis increases in increments of 30° in a clock-wise direction around the periphery of each digram with the funnel axis being directly upwards in all cases. The inner closed curve represents a funnel of semi-angle 0.5° whilst the outer closed curve represents a funnel of semi-angle 1°. A bullet which has an initial velocity vector which lies within either closed curve will escape from that particular configuration.

§3.4 Conclusions

The analysis of this chapter has revealed that the motion of a bullet above or within an infinite planar or conical blackbody radiator with an azimuthally symmetric temperature profile is confined to a plane which is determined by both the initial velocity of the bullet and its initial location. If, at the outset, the motion is axial then it remains so for all later times. Remember that in the context of the infinite plane, the term axial refers to any trajectory that is perpendicular to the planar surface whilst in the context of an infinite cone it refers to any trajectory that is parallel to the geometrical axis of symmetry of the cone but which need not necessarily coincide with it. The rate of acceleration of the bullet is proportional to the parameter W which is defined as the power intercepted by the bullet divided by its rest mass energy. The parameter W is, on account of its proportionality to the fourth power of the temperature of the radiator, sensitive to temperature as too, consequently, is the rate of acceleration.

There exist terminal speeds for motion above both infinite planar and conical radiator geometries which are, in all cases, independent of the parameter W and which represent an asympotic limit that the bullet approaches as both its journey time and distance above the release point tend to infinity. The terminal speed above an infinite isothermal planar radiator is approximately 0.4514c and occurs when the decelerative momentum flux of the blue-shifted and considerably aberrated photons emitted from the extremities of the plane is exactly balanced by the driving momentum flux of the red-shifted and minimally aberrated photons emitted from the region of the plane directly below the bullet. The terminal speed within an infinite isothermal conical radiator is a function of the cone opening angle and decreases from the limiting planar value to zero for motion within an isotropic radiation field. For narrow funnels the terminal speed is proportional to the square of the opening angle and in particular, for an half-opening angle of 1° appropriate for SS433, the terminal speed is $\sim 5 \times 10^{-5}$c which is markedly less than the value of 0.26c observed in the jets of SS433. Indeed, the half-opening angle necessary for a terminal speed of 0.26c is 67.1°. Narrow, infinite, isothermal conical funnels are wholly unsuitable for the radiative acceleration of gaseous bullets to mildly relativistic speeds. The radiation pressure can, however, contribute significantly to the collimation of the ejected bullets.

Chapter 4

Motion Above Non-Isothermal and Finite Radiators

§4.1 Introduction

Continuing from the analysis completed in chapter 3, I begin this chapter with an investigation of the motion of a bullet moving above an infinite, planar radiator for which the frequency integrated specific intensity is given by the Eddington limb darkening approximation and in addition by a generalisation to this approximation. Following this, the motion of a bullet moving within an infinite, conical radiator with an exponentially decaying temperature profile is considered. Applicability of the model to SS433 is achieved by ensuring that the e-folding distance of the temperature profile is consistent with the observations. Attention is then turned to the study of motion above a finite, isothermal planar radiator and then briefly to motion above a spherical, isotropic radiator in which the applicability of Newtonian dynamics to high speed stellar winds is considered. The concluding section consists firstly of an analysis of the behaviour of a bullet subjected to the radiation field of a finite, isothermal funnel and latterly to the motion of a bullet within a finite funnel for which the run of temperature with distance from the funnel apex is given by that of a polytropic gas of index $n_p = 3$ which is of relevence to radiation dominated regimes.

§4.2 Motion Above an Infinite, Planar Limb Darkened Radiator

The gas temperature at all points on the surface ($\tau = 0$) of a planar, limb darkened radiator is the same and although the temperature increases with optical depth according to Eq. (2.56) such that the radiator is, by definition, non-isothermal the surface of the radiator is an isothermal plane. The emergent frequency integrated specific intensity is, however, attenuated towards the limb according to Eq. (2.55) and therefore the contribution made to the emergent energy flux by the outer regions of the plane is diminished. Indeed, it can be shown that half of the surface energy flux is attributable to emergent photons with raypath vectors inclined at less than 41° to the plane normal. It is in this restricted sense that I intend the description 'non-isothermal' to apply.

In the derivation of Eq. (2.92) it was assumed that the radiation field was Planckian and that therefore, the frequency integrated specific intensity was given by Eq. (2.47). Suppose instead that the radiator is subject to the constraints discussed in §2.3.5; the emergent, frequency

integrated specific intensity will exhibit limb darkening and, in the Eddington approximation, will be given by Eq. (2.55). Consequently, in this regime Eq. (2.92) will take the form

$$\underline{\beta} \times (\underline{\beta} \times \dot{\underline{\beta}}) + \dot{\underline{\beta}} = \frac{D}{m_o c^2} \frac{1}{\gamma^3} \int_{\Omega_Q} I(-\hat{\underline{k}}, 0) \left\{ \hat{\underline{k}} - \gamma^2 (1 - \underline{\beta} \cdot \hat{\underline{k}}) \underline{\beta} \right\} (1 - \underline{\beta} \cdot \hat{\underline{k}}) \, d\Omega_Q \, . \tag{4.1}$$

§4.2.1 The Axial Equation of Motion

In accordance with the notation adopted in §3.2 and by Eq. (2.54), the equation of motion (Eq. 4.1) can be expressed as

$$\begin{pmatrix} \dot{\beta}_x \\ \dot{\beta}_y \\ \gamma^2 \dot{\beta}_z \end{pmatrix} = \frac{D}{m_o c^2} \frac{1}{\gamma} \int_0^{2\pi} \int_0^{\pi/2} \frac{3}{5} I(1,0) \left(\cos\theta + \frac{2}{3} \right) \underline{\Upsilon}(\theta, \phi) (1 - \beta \cos\theta) \sin\theta \, d\theta \, d\phi \tag{4.2}$$

where $\underline{\Upsilon}(\theta, \phi)$ is given by Eq. (3.3b). As in the case of the isothermal blackbody radiator, the only azimuthal dependence occurs in the $\underline{\Upsilon}(\theta, \phi)$ term which again constrains any bullet released with zero velocity component parallel to the plane surface to have a trajectory along the normal for all later times. Introducing the substitution $\mu = \cos\phi$ and performing the integrating over ϕ yields the axial equation of motion

$$\begin{aligned} \dot{\beta}_z &= \frac{2\pi}{5} I(1,0) \frac{D}{m_o c^2} \frac{1}{\gamma} \int_0^1 (3\mu + 2)(\mu - \beta_z)(1 - \beta_z \mu) \, d\mu \\ &= \frac{\pi}{30} I(1,0) \frac{D}{m_o c^2} \frac{1}{\gamma} (24\beta_z^2 - 59\beta_z + 24) \end{aligned} \tag{4.3}$$

for which the terminal speed is

$$\beta_\infty = \frac{59 - \sqrt{1177}}{48} \approx 0.5144 \, . \tag{4.4}$$

Consider now a generalisation of the Eddington limb darkening approximation given by

$$I(\mu, 0) = \frac{1}{1 + A_o} I(1,0)(A_o \mu + 1) \, . \tag{4.5}$$

where A_o is the limb darkening parameter. This expression represents limb brightening for $-1 < A_o < 0$ and limb darkening for $A_o > 0$ with the value $A_o = 3/2$ corresponding to limb darkening in the Eddington approximation. If the emergent, surface energy flux is independent of A_o then, by Eq. (2.54), the frequency integrated specific intensity emergent normal to the surface must be such that

$$I(1,0) = \frac{3}{\pi} \frac{A_o + 1}{2A_o + 3} \mathcal{F} \, . \tag{4.6}$$

The equation of motion then has the form

$$\dot{\beta}_z(\beta_z, A_o) = \frac{1}{3}\frac{D\mathcal{F}}{m_o c^2}\frac{1}{\gamma}\left\{3\beta_z^2 - \frac{3}{2}\left(\frac{9A_o + 16}{2A_o + 3}\right)\beta_z + 3\right\} \tag{4.7}$$

which reduces to that for motion above an isothermal blackbody radiator in the limit where $A_o \to 0$ and $\mathcal{F} = \sigma T^4$ or equivalently when the effective temperature T_{eff} of the limb darkened radiator is the same as the temperature T of the blackbody.

The terminal speed is a function of the parameter A_o and is given by

$$\beta_\infty(A_o) = \frac{(9A_o + 16) - \sqrt{17A_o^2 + 96A_o + 112}}{4(2A_o + 3)} . \tag{4.8}$$

The lower bound on the terminal speed occurs in the extreme limb brightening limit ($A_o \to -1$) when $\beta_\infty \to (7 - \sqrt{33})/4 \approx 0.3139$ whilst the upper bound occurs in the extreme limb darkening limit ($A_o \to \infty$) when $\beta_\infty \to (9 - \sqrt{17})/8 \approx 0.6096$. Between these limiting values, the function $\beta_\infty(A_o)$ is monotonic (Fig. 4.1). The rôle that the photons emitted from the limb of the radiator have in governing the terminal speed of the bullet is evidenced by the decrease in the terminal speed as the frequency integrated specific intensity emergent from the radiator limb increases relative to that emergent from the point on the radiator immediately below the bullet.

Linearising Eq. (4.7) reveals that the dimensionless e-folding time, τ_d, for reversion back to the terminal speed following a small perturbation is

$$\tau_d(A_o) = \frac{2(2A_o + 3)}{\sqrt{[1 - \beta_\infty^2(A_o)]\,(17A_o^2 + 96A_o + 112)}} , \tag{4.9}$$

a plot of which is shown in Fig. 4.2. It is evident that this e-folding time increases monotonically from a lower limit of ~ 0.367 to an upper limit of ~ 1.224 as A_o increases from -1. This behaviour results in the dimensionless attainment time taken by the bullet to reach a substantial fraction of its terminal speed increasing with A_o.

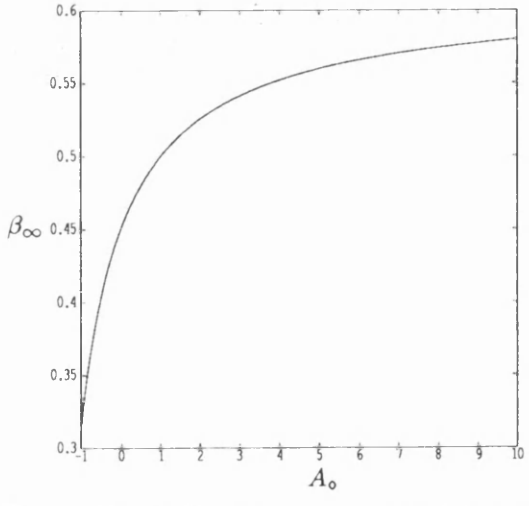

Fig. 4.1. The terminal speed, β_∞, versus the limb darkening parameter, A_o, for motion above an infinite, planar radiator for which the emergent, frequency integrated specific intensity is given by a generalisation to the Eddington limb darkening approximation (Eq. 4.5).

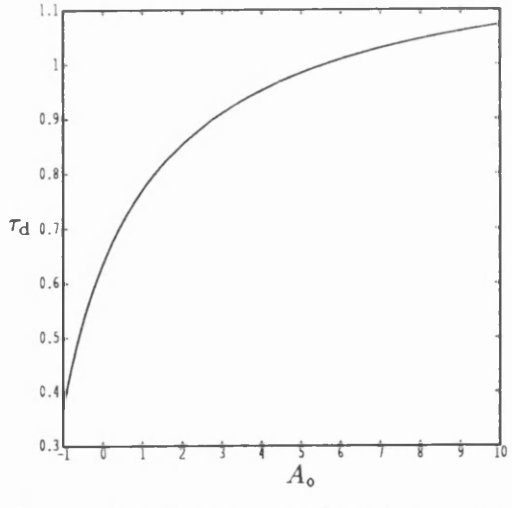

Fig. 4.2. The dimensionless e-folding time, τ_d, for reversion back to the terminal speed versus the limb darkening parameter, A_o, for motion above the radiatior described in the caption to Fig. 4.1.

§4.2.2 The Off-Axis Equation of Motion

If the emergent, frequency integrated specific intensity is given by the generalisation to the Eddington limb darkening expression (Eq. 4.5) then it can be shown, in the manner outlined in §3.3.1, that the component equations of motion are given by

$$\dot{\beta}_{r_d} = \frac{1}{3}\sqrt{1-\beta_r^2-\beta_z^2}\left\{3\beta_z - \frac{3}{4}\left(\frac{15A_0+32}{2A_0+3}\right)\right\}\beta_r \qquad (4.10a)$$

$$\dot{\beta}_{z_d} = \frac{1}{3}\sqrt{1-\beta_r^2-\beta_z^2}\left\{3\beta_z^2 - \frac{3}{2}\left(\frac{9A_0+16}{2A_0+3}\right)\beta_z + 3\right\} . \qquad (4.10b)$$

Since the braced term in Eq. (4.10a) is negative for all physical values of β_z and A_0, the velocity component parallel to the planar surface is always damped. In addition, since the terminal speed is attained when $\dot{\beta}_{r_d} = \dot{\beta}_{z_d} = 0$, Eq. (4.10$a$) implies that the terminal speed is achieved when $\beta_r = 0$ and therefore all motion above an infinite, planar radiator for which the emergent, frequency integrated specific intensity is either limb darkened or brightened is ultimately parallel to the radiating surface normal.

The effect that the limb darkening coefficient has on dampening the velocity component parallel to the planar surface, and thus in aiding collimation, can be appreciated from the ratio given by

$$\frac{\dot{\beta}_{r_d}(A_0;\beta_r,\beta_z)}{\dot{\beta}_{r_d}(0;\beta_r,\beta_z)} = 1 - f(A_0;\beta_z) \quad \text{where} \quad f(A_0;\beta_z) = \frac{19}{4(8-3\beta_z)}\frac{A_0}{2A_0+3} . \qquad (4.11a,b)$$

As one would expect, $f(A_0;\beta_z)$ is positive for those values of the parameter A_0 which correspond to a limb darkened radiating plane and vice versa for a limb brightened plane. This indicates that motion parallel to the plane surface is more strongly attenuated when the radiator is limb brightened than when it is limb darkened. This behaviour is due to the increased energy flux incident at the bullet from the limb of the radiator when the radiating plane is limb brightened as opposed to limb darkened. Also, it is obvious from Eq. (4.10a) that, for a given value of the limb darkening parameter, A_0, and the magnitude of the velocity component parallel to the z-axis, $|\beta_z|$, the velocity component β_r is most strongly damped when the direction of motion is downwards towards the plane.

§4.3 Motion Above an Infinite, Conical Radiator with an Exponential Temperature Profile

As a first step towards the investigation of an astrophysically more realistic temperature profile I will now introduce the ad hoc assumption that the temperature profile decays exponentially with increasing radial distance r from the base of the accretion funnel. The blackbody temperature

profile of the inner surface of the accretion disc will then have the form

$$T(r) = T_0 \exp\left(-\frac{r}{H}\right) \tag{4.12}$$

where T_0 is the temperature at the funnel base and H is some scale height. If z is the height of the bullet centre (assumed to be located axially) above the cone apex and θ is the inclination of an incident photon trajectory with respect to the positive z-axis (observed in the rest frame of the radiator) then from Fig. 4.3 it can be deduced that

$$r(\theta, z; \alpha) = \left[\frac{\sin\theta}{\sin(\theta + \alpha)}\right] z \tag{4.13}$$

and consequently the temperature profile can be re-expressed as

$$T(\theta, z; \alpha, H) = T_0 \exp\left\{-\left[\frac{\sin\theta}{\sin(\theta + \alpha)}\right] \frac{z}{H}\right\} . \tag{4.14}$$

By Eqs. (3.4) and (3.5) the axial equation of motion is then given by

$$\dot{\beta}_z = 2\frac{\sigma D T_0^4}{m_0 c^2} \frac{1}{\gamma} \int_0^{\pi-\alpha} \exp\left\{-4\left[\frac{\sin\theta}{\sin(\theta + \alpha)}\right] \frac{z}{H}\right\} (\cos\theta - \beta_z)(1 - \beta_z \cos\theta) \sin\theta \, d\theta . \tag{4.15}$$

The important feature of Eq. (4.15) is the explicit dependence of the integrand on z. This means that, unlike all the examples considered so far, the problem is no longer scale invariant. Integration of the equation of motion is now more complex and is most readily achieved numerically.

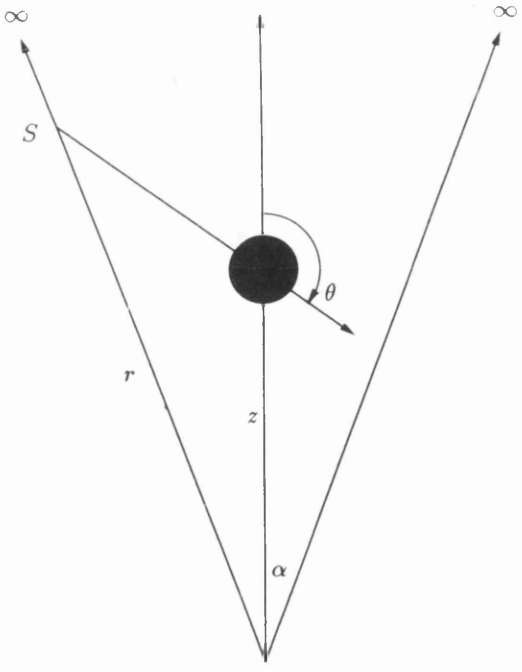

Fig. 4.3. If the bullet's radius is smaller than the characteristic length-scale of the temperature variation on the funnel wall then, all photons originating from the point S, which is a slant height r above the funnel base, will approximately make an angle θ with respect to the positive z-axis when they impinge on the bullet's surface, the centre of which is located at a height z above the apex. Note that for simplicity I have sketched the bullet as a sphere although it will, in all likelihood on account of Lorentz contraction, be observed as an oblate spheroid in the rest frame of the funnel.

As was mentioned in chapter 2, the derived equation of motion will be a valid approximation only if the bullet is small in comparison to the typical length-scale of any temperature variation on the interior surface of the accretion funnel. In the context of this particular problem the imposed constraint is that the scale height H be much greater than the bullet radius r_b. Before proceeding further it is therefore necessary to determine the value of the scale height appropriate for SS433 and to ensure that the aforementioned condition is satisfied.

The bolometric luminosity of the accretion disc is $\sim 10^{32}$ J/s (10^{39} erg/s) (Cherespaschuck; 1981). If the disc is assumed to be spherical and to have a radius R_{ad} then its bolometric luminosity will simply be

$$L_{bol} = 4\pi R_{ad}^2 \sigma T_{eff}^4 \tag{4.16}$$

and therefore

$$T_{eff_4} \approx \frac{3.4}{\sqrt{R_{ad_{10}}}} \text{ K} \tag{4.17}$$

where the effective temperature and accretion disc radius have been expressed in units of 10^4 K and 10^{10} metres respectively. This expression is in good agreement with the observations of Wagner (1986) which indicate that the dominant source of optical luminosity in SS433 resembles a hot blackbody with a radius of $\sim 30 R_\odot$ ($R_{ad_{10}} \sim 2$) and mean colour temperature $\sim 32\,500$ K. The assumption that the disc is spherical is well justified; indeed if the disc is the principal source of optical luminosity then its diameter to thickness ratio is less than about 1.3 (Wagner; 1986) and it is, consequently, better represented by a sphere than a greatly flattened sphere or disc. The surface temperature of the most luminous optical source in SS433, however, is certainly not uniform. Temporal variations of the colour temperature are consistent with von Zeipel gravity darkening of the optical star or thick accretion disc and also with the presence of high temperature accretion funnels. Since the inclination of the orbital plane to the line of sight is $\sim 79°$ (see §1.3.1 and §1.6.1) and since the semi-angle of the cone formed by the precession of the jets about the normal to the orbital plane is $\sim 20°$, the inclination of the accretion funnels to the line of sight is never less than $\sim 59°$. Thus, because the accretion funnels are very narrow, radiation that originates deep within them can never be observed directly by a terrestrial observer; only radiation scattered from the funnel mouth can be observed. For this scattered radiation to account for the observed variation in the colour temperature, the temperature at the funnel base needs to be extremely hot (Wagner, 1986). The presence of a blue shifted iron line (Watson et al., 1986) indicates that the temperature at the base of the jets exceeds $\sim 5 \times 10^7$ K whilst hydrodynamical modelling of the jets provides acceptable fits to the data for temperatures at the funnel base between $\sim 5 \times 10^8$ K and 8×10^8 K (Brinkmann et al., 1991). A base temperature of $\sim 8 \times 10^8$ K is, therefore, a reasonable estimate.

Now at the disc surface $T(R_{ad}) = T_{eff}$, and by Eq. (4.12),

$$H_{10} = \frac{R_{ad_{10}}}{9.2 + \log(T_{0_8}/T_{eff_4})} \tag{4.18}$$

which, by Eq. (4.17), can be expressed as

$$H_{10} \approx \frac{R_{ad_{10}}}{8 + \log(T_{0_8}\sqrt{R_{ad_{10}}})} \,. \tag{4.19}$$

In the present context the term 'disc surface' refers to the surface of the sphere of radius R_{ad} from which most of the luminosity originates. This, therefore, represents the surface at which the transition of the disc material from the optically thick to the optically thin regime occurs; the disc atmosphere, though, may extend out to radii in excess of R_{ad}. For a feasible central temperature of 8×10^8 K the scale height for a disc of radius 10^9 m is, by Eq. (4.19), 1.3×10^8 m whilst for a disc of radius 10^{10} m the scale height is 10^9 m. Thus, a typical scale height is $H_{10} \sim 0.1 R_{ad_{10}}$ which is suitably large to warrant the unquestioned earlier assumption that the funnel walls do indeed radiate as a blackbody.

Since the maximum possible bullet radius at a height z above the apex of a narrow cone of semi-angle α is approximately $z\alpha$, the maximum radius of a bullet at a distance of one scale height above the apex will simply be $H\alpha \approx 10^{-2}H$ for semi-angles appropriate for SS433. Thus, if a maximum radius bullet is released at a height less than $\sim H$ above the apex the necessary condition detailed above is satisfied and Eq. (4.15) is therefore a justified approximation. I will return to this topic later.

Introduction of the dimensionless variables

$$\tilde{z}_{\rm d} = \frac{z}{H} \quad , \quad \tilde{t}_{\rm d} = \frac{\rm c}{H} t \quad \text{and} \quad \tilde{X} = \frac{H}{\rm c} W, \tag{4.20a,b,c}$$

where the parameter W is defined by Eq. (3.9b) with the isothermal temperature T being replaced by the temperature T_0 at the base of the accretion funnel, allows the identifications

$$\beta_z = \frac{{\rm d}\tilde{z}_d}{{\rm d}\tilde{t}_d} \equiv \dot{\tilde{z}}_{\rm d} \quad \text{and} \quad \dot{\beta}_z = \frac{\rm c}{H}\frac{{\rm d}^2\tilde{z}_{\rm d}}{{\rm d}\tilde{t}_{\rm d}^2} \equiv \frac{\rm c}{H}\ddot{\tilde{z}}_{\rm d} \tag{4.21a,b}$$

and permits Eq. (4.15) to be expressed as

$$\ddot{\tilde{z}}_{\rm d} = 2\tilde{X}(1 - \dot{\tilde{z}}_{\rm d}^2)^{\frac{1}{2}} \int_0^{\pi-\alpha} \exp\left\{-4\left[\frac{\sin\theta}{\sin(\theta+\alpha)}\right]\tilde{z}_{\rm d}\right\}(\cos\theta - \dot{\tilde{z}}_{\rm d})(1 - \dot{\tilde{z}}_{\rm d}\cos\theta)\sin\theta\,{\rm d}\theta \,. \tag{4.22}$$

The dimensionless variables defined by Eq. (4.20a,b,c) have been ascribed tildes to differentiate them from very similar dimensionless variables that will appear in later sections.

The results of numerical integrations of Eq. (4.22) for selected values of the cone semi-angle, each evaluated at $\tilde{z}_d = 0$, are illustrated in Figs. 4.4a,b. From Fig. 4.4a it can be seen that as α decreases from the maximum value of 90° the dimensionless ratio $\dot{\beta}_z/W \equiv \ddot{\tilde{z}}_d/\tilde{X}$ develops a turning point which decreases in magnitude and peaks at increasing values of $\tilde{z}_d$. This is a direct result of the integrand in Eq. (4.22) being explicitly dependent on $\tilde{z}_d$ and represents what was meant by the earlier reference to 'scale invariance': The radiative acceleration experienced by the bullet is a function of its speed *and* its height above the cone apex.

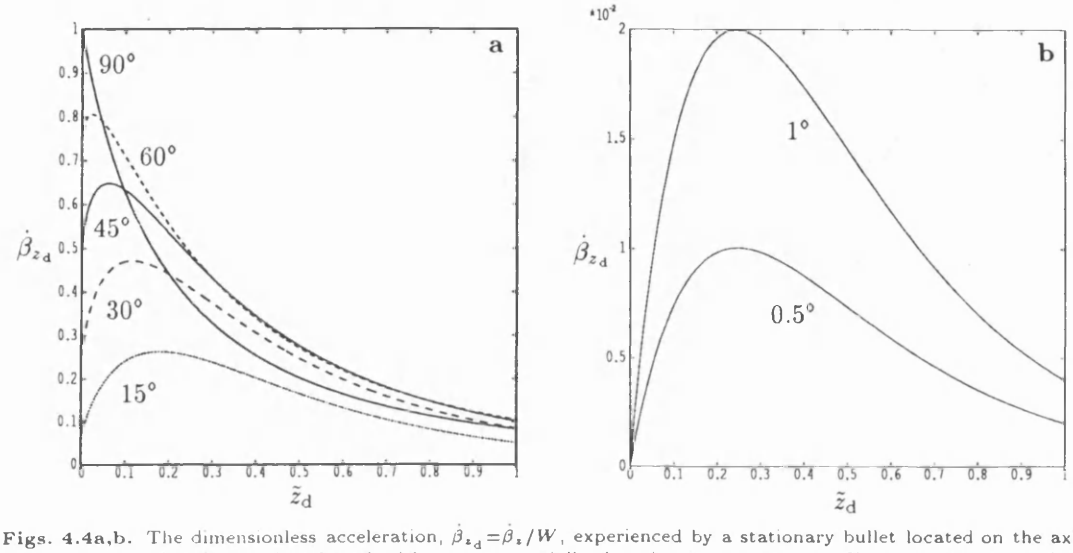

Figs. 4.4a,b. The dimensionless acceleration, $\dot{\beta}_{z_d}=\dot{\beta}_z/W$, experienced by a stationary bullet located on the axis of symmetry of an infinite, conical funnel with an exponentially decaying temperature profile versus the dimensionless height, $\tilde{z}_d$, of the bullet centre above the funnel base for selected values of the funnel semi-angle.

The problem, however, does become scale-invariant in the limit where $H \rightarrow \infty$ or equivalently as $\tilde{z}_d \rightarrow 0$ when the radiator is effectively isothermal. From Eq. (3.36), in the limit where $\beta_z = 0$, it is evident that $\dot{\beta}_z/W = \sin^2\alpha$. Thus, for a stationary bullet confined within a narrow, isothermal cone, the initial radiative acceleration is proprtional to α^2. As was shown in chapter 3, the terminal speed is also proportional to α^2 and the terminal speeds that can be achieved are, consequently, well below the value of 0.26c observed in SS433. In Fig. 4.4b the ratio $\dot{\beta}_z/W$ is depicted as a function of $\tilde{z}_d$ for semi-opening angles of 0.5° and 1° degrees. The maximum value of $\dot{\beta}_z/W$ occurs at $\tilde{z}_d \approx 0.25$ which, if one recalls that realistic scale heights are $\sim 0.1 R_{ad_{10}}$, is well within the funnel. It has a magnitude of $\sim 2 \times 10^{-2}$ for a funnel semi-angle of 1° and $\sim 10^{-2}$ for a funnel semi-angle of 0.5°. These values are respectively ~ 65 and ~ 130 times greater than those for motion within isothermal cones with identical opening angles. This fact per se does not ensure that any terminal speed, should it exist, will be high but it does however mean that the rate of terminal speed attainment will be greater for bullets which begin their motion in the general locality of the maxima.

Before entering into a more detailed analysis of Eq. (4.22) it is prudent to first determine suitable values for the dimensionless release height of the bullet, $\tilde{z}_{0_d}$, and for the parameter $\tilde{X}$. I will first consider $\tilde{z}_{0_d}$: By Eq. (3.14) the minimum bullet radius is $\sim 10^5 \mathrm{m}_{o_{21}}^{\frac{1}{3}}$ metres which, for motion within a narrow funnel, necessitates that the bullet be released at a height

$$z_{0_7} \geq \mathrm{m}_{o_{21}}^{\frac{1}{3}} \alpha_{-2}^{-1} . \tag{4.23}$$

Now for radiative acceleration to be viable the outward radiative force experienced by the bullet must exceed the inward attraction of gravity. Noting from Fig. 4.4b that $\dot{\beta}_z/W \sim 10^{-2}$ for semi-angles $\sim 1°$, it can be shown that the rough inequality that needs be satisfied is

$$z_{0_5} \geq 1.8\, \mathrm{m}_{0_{21}}^{\frac{1}{2}} \alpha_{-2}^{-\frac{1}{2}} T_{0_8}^{-1} \,. \tag{4.24}$$

Both inequalities are therefore satisfied if the minimum release height is $\sim 10^7$ metres. Since typical scale heights are of the order $10^8 - 10^9$ m, suitable initial dimensionless release heights $\tilde{z}_{0_d}$ need be greater than $\sim 10^{-2}$.

In deriving typical values for the dimensionless parameter $\tilde{X}$ it should first be recalled from Eq. (4.20*c*) that the parameter $\tilde{X}$ is given by the product of the parameter W, discussed in detail in the previous chapter, and the light crossing time across one scale height. Evidently, from what has been said immediately above and by Eq. (4.20*b*), H/c lies in the approximate range $1/3 \leq H/\mathrm{c} \leq 10/3$ and therefore, by Eq. (3.21),

$$8.0 \times 10^{-4} T_{0_8}^4 \mathrm{m}_{0_{21}}^{-\frac{1}{3}} R_{ad_{10}} \leq \tilde{X} \leq 6.7 \times 10^{-1}\, T_{0_8}^4 z_{0_8}^2 \alpha_{-2}^2 \mathrm{m}_{0_{21}}^{-1} R_{ad_{10}} \,. \tag{4.25}$$

In the initial stages of its motion, with which I am concerned here, the bullet will be extremely optically thick; the absolute upper bound present in Eq. (3.21) applies when the bullet is optically thin and as a result can be ignored for the interim. Adopting 8×10^8 K as the likely upper limit on the central temperature, Eq. (4.25) implies that the upper bound on the dimensionless parameter $\tilde{X}$ is

$$\tilde{X}_{max} \sim 2.7 \times 10^3 z_{0_8}^2 \alpha_{-2}^2 \mathrm{m}_{0_{21}}^{-1} R_{ad_{10}} \,. \tag{4.26}$$

Familiarised now with the basic model parameters it is worthwhile reconsidering in more detail the condition under which the invocation of Eqs. (3.4) and (3.5) was made and ascertaining the degree of its validity. As I stated at the beginning of this section, the bullet must be much smaller than the scale height of the temperature profile if the approximation is to be a good one. Obviously, therefore, the equation of motion (Eq. 4.22) is most accurate when the bullet is small and least accurate when the bullet is large. In addition, from consideration of the geometry of the problem (with the bullet assumed to be at rest with respect to the accretion funnel for simplicity) it can readily be appreciated that for a selected incident raypath vector, agreement on the temperature in the reverse of that direction between observers located respectively at the points on the illuminated hemisphere furthest from and closest to the funnel apex is best when the raypath vector is aligned parallel to the normal to the funnel surface. Agreement is poorest when the raypath vector is perpendicular to the surface normal. This configuration arises for the regions of the funnel furthest from the apex where the temperature can be considered as being zero and the effect of any inaccuracies nullified as a result. The same

however does not apply to regions near the funnel apex. In the 'worst case' scenario the bullet is released at a height of $\sim H$ (the reasons for which will become clear later) above the apex where it completely fills the funnel. If the raypath vector is, for the purposes of illustration, selected to be parallel to the positive $z-$axis and the funnel semi-angle is 0.01 radians then the temperature seen in the reverse direction by an observer located directly above the apex will be T_0 whilst for an observer located on the periphery of the illuminated hemisphere it will, by Eq. (4.12), be $T_0 e^{-1} \approx 0.34 T_0$. In this case the approximation is fair. On the other hand, for the best case scenario the bullet radius is $\sim 10^5$ m and the peripheral observer will see, for an accretion disc of radius 10^9 m, a temperature of $T_0 e^{-0.1} \approx 0.90 T_0$ K and for an accretion disc of radius 10^{10} m a temperature of $T_0 \exp^{-0.01} \approx 0.99 T_0$ K. In both these estimates use has been made of the fact that $H_{10} \sim 0.1 R_{ad_{10}}$. Therefore, when the bullet radius is close to or at the minimum value, the approximation that the temperature of the funnel observed in a certain direction from different locations on the surface of the appropriate hemisphere is the same, is valid.

Numerical integration of Eq. (4.22) reveals that terminal speeds do exist for motion within a conical accretion funnel with an exponentially decaying surface temperature. This statement needs qualification: for a given set of initial conditions, integration of the equation of motion beyond $\tilde{t}_d \approx 10^{15}$ yields, to a precision of at least 10 significant decimal places, exactly the same speed. Further, the release point of the bullet (assumed to commence its motion from rest) must be close to the base of the accretion funnel. Precise quantification of the term 'close' is difficult since it is dependent on the value of the parameter $\tilde{X}$. As a rough guide the initial release height can be regarded as being close if it is less than $\sim H$. The reasons for this will become clear later. If this is not so, or if the parameter $\tilde{X}$ is not adequately large, the bullet will not be accelerated to sufficiently high speeds at which the relativistic effects responsible for governing the bullet's speed can become effective.

From the form of the integral in Eq. (4.22) it is obvious that $\ddot{\tilde{z}}_d \rightarrow 0$ as $\tilde{z}_d \rightarrow \infty$ and, therefore, the bullet asymptotically approaches its true terminal speed, β_∞, in the limit $\tilde{t}_d \rightarrow \infty$. The speed of the bullet after 10^{15} time units is then a truncation of the true terminal speed. However, since the attainment time for the bullet to reach a significant fraction of its true terminal speed is $\sim 10^3$ units, integration over an interval of 10^{15} units (representing a physical time of at least $\sim 10^7$ years) is suitably large to provide a very accurate approximation to the true terminal speed. In this section and those that follow I will adopt the convention that the terminal speed of the bullet, β_{15}†, is the speed of the bullet after a period of presence within the driving radiation field of 10^{15} time units.

From an extended data base formed by ten years worth of data, Margon and Anderson (1989) found the best fit to the Doppler shifts of the moving lines, within the framework of the kinematic model, to be made by a jet with speed (0.2602 ± 0.0013)c. The deviation in the speed of the jet permissible within the confines of this model, and its other more complex variants, is

† The notation should be self-explanatory.

extremely small, typically representing only 1 part in every 200. Since the true terminal speed β_∞ represents an upper bound on the bullet's speed, any further deviance in its speed once it has attained 99.5% of this value will be less than 1 part in 200. This is the criterion that I have imposed on the data illustrated in Figs. 4.5a,b,c which represent motion within a cone of semi-angle 1°.

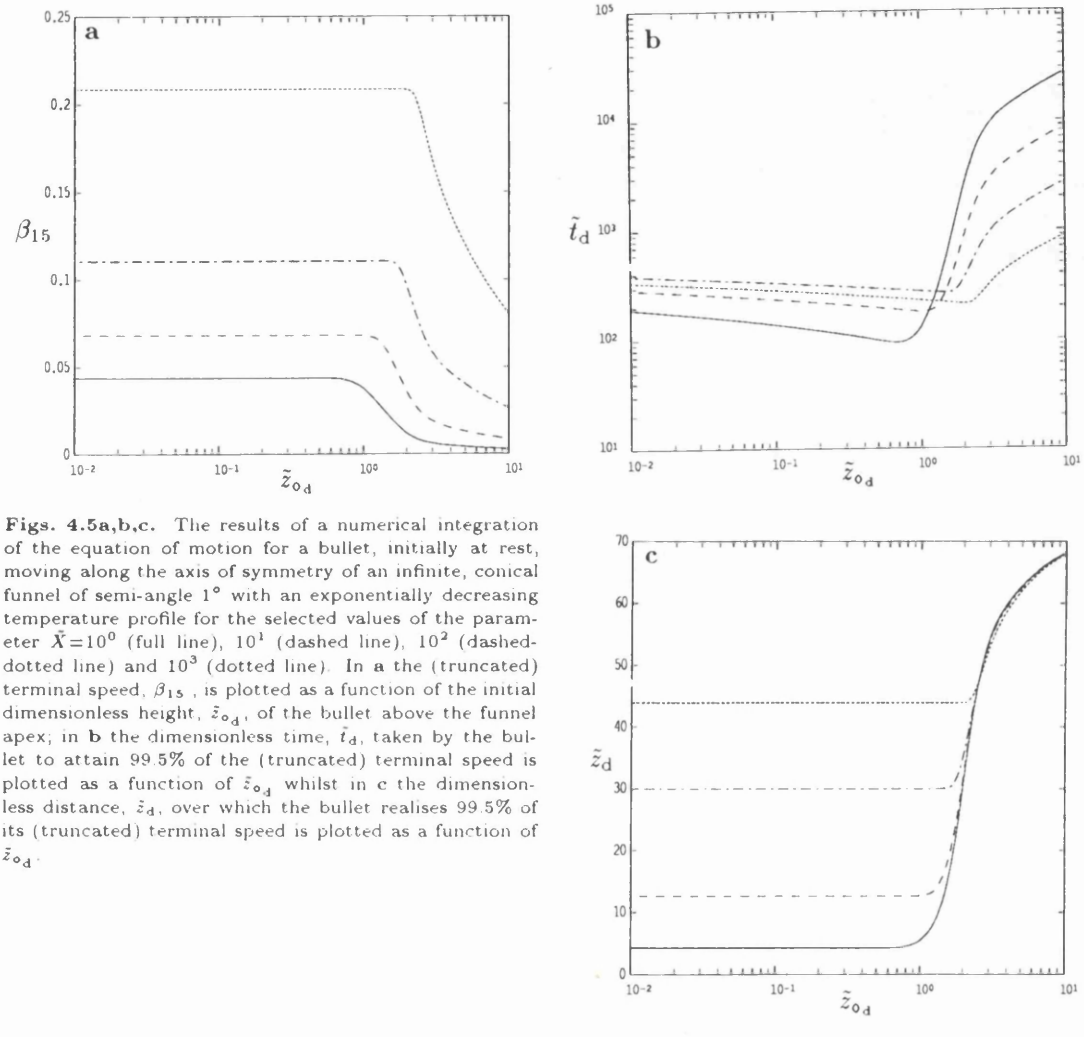

Figs. 4.5a,b,c. The results of a numerical integration of the equation of motion for a bullet, initially at rest, moving along the axis of symmetry of an infinite, conical funnel of semi-angle 1° with an exponentially decreasing temperature profile for the selected values of the parameter $\tilde{X}=10^0$ (full line), 10^1 (dashed line), 10^2 (dashed-dotted line) and 10^3 (dotted line). In **a** the (truncated) terminal speed, β_{15} , is plotted as a function of the initial dimensionless height, $\tilde{z}_{0_d}$, of the bullet above the funnel apex; in **b** the dimensionless time, $\tilde{t}_d$, taken by the bullet to attain 99.5% of the (truncated) terminal speed is plotted as a function of $\tilde{z}_{0_d}$ whilst in **c** the dimensionless distance, $\tilde{z}_d$, over which the bullet realises 99.5% of its (truncated) terminal speed is plotted as a function of $\tilde{z}_{0_d}$.

In Fig. 4.5a the terminal speed is depicted as a function of the initial dimensionless release height for various values of the dimensionless parameter $\tilde{X}$. It can be seen that the terminal speed is remarkably independent of the release height for values of $\tilde{z}_{0_d}$ up to ~ 1. Beyond this value the terminal speed falls off dramatically and the point at which the fall-off occurs increases marginally with $\tilde{X}$. Thus, to maximise the terminal speed for a specific value of $\tilde{X}$ the bullet needs to be released with an initial dimensionless height less than ~ 1. In addition the terminal speed increases with the parameter $\tilde{X}$ yielding, for example, $\beta_{15} = 0.20846$ for $\tilde{X} = 10^3$. From inspection of Eq. (4.26) it is apparent that values of the parameter $\tilde{X} \sim 10^3$ are permissible. The prospects for the attainment of terminal speeds $\sim 0.26c$ appear promising. I will consider this topic in more detail later.

In Fig. 4.5b the dimensionless time taken for the bullet to attain 99.5% of the terminal speed is plotted as a function of the dimensionless release height. The minimum attainment time

also occurs at $\tilde{z}_{0_d} \sim 1$, increasing slightly with $\tilde{X}$. The increase in the dimensionless attainment time with $\tilde{z}_{0_d}$ for $\tilde{z}_{0_d} \leq 1$ is relatively small e.g. with $\tilde{X} = 10^3$ the minimum attainment time is ~ 213 units occurring at $\tilde{z}_{0_d} = 2$ whilst for $\tilde{z}_{0_d} = 10^{-1}$ and 10^{-2} the attainment times are ~ 286 and ~ 338 units respectively. Since $H/c \sim 1$ (in units of time), by Eq. (4.20*b*), $\tilde{t}_d \sim t$ and it can therefore be appreciated that these time-scales are very similar to the acceleration time-scale in SS433 which, on the basis of an estimated X-ray region of length $\sim 10^{10}$ m, is of the order of 100 seconds (Watson et al., 1986).

Figure 4.5c illustrates the dimensionless distance traversed by the bullet (measured from the cone apex), as a function $\tilde{z}_{0_d}$, in attaining 99.5% of its terminal speed. As before, the initial dimensionless release height $\tilde{z}_{0_d} \sim 1$ marks a critical boundary: for $\tilde{z}_{0_d}$ greater than ~ 1 the attainment distance increases rapidly whilst for $\tilde{z}_{0_d}$ less than ~ 1 the attainment distance shows very little dependence on $\tilde{z}_{0_d}$. In addition, the attainment distance increases with $\tilde{X}$; a fact which is attributable to an increase in the terminal speed with $\tilde{X}$. For $\tilde{X} = 10^3$ the attainment distance is ~ 44 units which is, since $H_{10} \sim 0.1 R_{ad_{10}}$, very roughly $4R_{ad}$ metres. Although such a distance lies outwith what has been defined here as the surface of the accretion disc it is still of the same order of magnitude as the radius of the accretion disc and is comparable to the length-scale within which the jets are accelerated to their terminal speed.

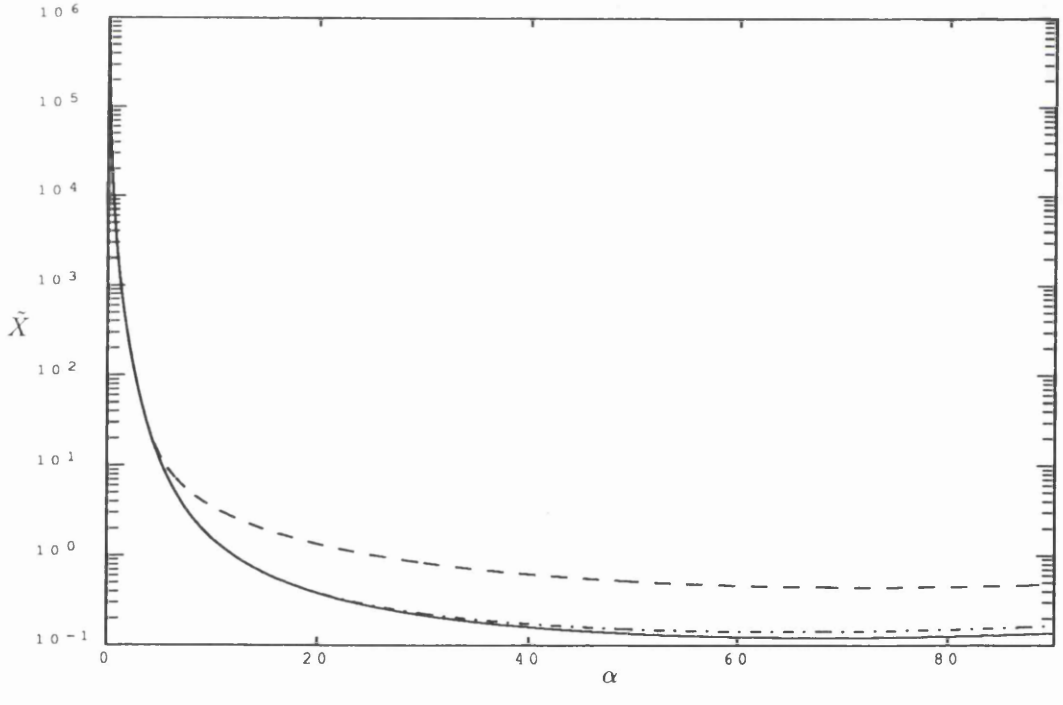

Fig. 4.6. The value of the parameter $\tilde{X}$ which permits the attainment of a truncated terminal speed of 0.2602c versus the funnel semi-angle, α, for selected values of the initial, dimensionless height $\tilde{z}_{0_d}$. The dashed line corresponds to $\tilde{z}_{0_d}$=1.0, the dashed-dotted line corresponds to $\tilde{z}_{0_d}$=0.1 and the full line corresponds to $\tilde{z}_{0_d}$=0.01.

The values of the parameter $\tilde{X}$ necessary for the bullet to attain a terminal speed of $(0.2602 \pm 0.0001)c$ as a function of the funnel semi-angle for several values of the initial dimensionless scale height are shown in Fig 4.6. The parameter $\tilde{X}$ is very insensitive to $\tilde{z}_{0_d}$ for $\tilde{z}_{0_d} \leq 1$ and $\alpha \leq 4°$: for the values of $\tilde{z}_{0_d}$ displayed, the critical value of $\tilde{X}$ for $\alpha = 0.5°$ is 1.2085×10^4

whilst for $\alpha = 1°$ the appropriate value of $\tilde{X}$ is 2.0524×10^3. For funnel semi-angles in excess of $\sim 4°$, particularly with $\tilde{z}_{0_d} \geq 1$, the value of the parameter $\tilde{X}$ necessary for the attainment of $\beta_{15} = 0.2602$ becomes increasingly sensitive to the initial, dimensionless release height.

The insensivity of the parameter $\tilde{X}$ required for the bullets to attain a particular terminal speed to the initial release height for narrow funnels is an extremely significant feature. Of a host of perplexing facets associated with SS433, the most bewildering is probably the remarkably constant speed of its jets. The results displayed here indicate that if the funnel semi-angle is less than $\sim 4°$ and that the material that forms the bullets enters the accretion funnel at a distance less than about one scale height from the funnel apex then the terminal speed of the ejected bullets will, for a specific α, depend solely on the parameter $\tilde{X}$. This fact, in addition to several assumptions, permits conjecture on the degree of variability in the accretion rate: If it is assumed that any variation in the angular size of the accretion funnels occurs on a time-scale much greater than the rate of bullet formation and that bullet formation takes place at a relatively constant height above the funnel apex then the bullet radius should be constant to a good degree. Since the parameter $\tilde{X}$ (Eq. 4.20*c*) is proportional to $r_b^2 T_0^4/\mathrm{m_o}$ the ratio $T_0^4/\mathrm{m_o}$ must then, within the context of this particular model, remain constant if the bullet ejection speed is also to be constant. This either requires that both T_0 and $\mathrm{m_o}$ are individually constant or, and I think more likely, it requires that T_0 and $\mathrm{m_o}$ vary in time but in a manner such that $T_0^4/\mathrm{m_o}$ is always constant. The most probable source of variation in these two parameters is a change in the accretion rate $\dot{M}_{ac}$. The characteristic boundary layer blackbody temperature for thin disc accretion onto a compact object is proportional to $\dot{M}_{ac}^{1/4}$ (Frank, King and Raine, 1985). If this applies to thick discs too, a fact which is certainly not assured, then the bullet's mass must also be proportional to the accretion rate. Assuming that the rate of bullet formation is related directly to their rate of ejection then the bullets are formed on average every 3-5 days (Vermeulen, 1989). For an approximately constant bullet mass this observation then restricts the accretion rate to vary by a factor of about 2 at most.

Making use of the relation $H_{10} \sim 0.1 R_{ad_{10}}$ and of Eq. (4.20*a*), Eq. (4.26) may be alternatively expressed as

$$\tilde{X}_{max} \sim 2.7 \times 10^5 z_{0_d}^2 \alpha_{-2}^2 \mathrm{m}_{o_{21}}^{-1} R_{ad_{10}}^3 \tag{4.27}$$

It is evident from inspection of Fig. 4.5a that in order to maximise the attainable terminal speed (with $\beta_{15} \sim 0.2$) for a selected value of the parameter $\tilde{X}$, a bullet needs to be released at a dimensionless height no greater than about 2 units from the funnel base. This condition, in conjunction with Eq. (4.27), then implies that

$$\tilde{X}_{max} \sim 1.1 \times 10^6 \alpha_{-2}^2 \mathrm{m}_{o_{21}}^{-1} R_{ad_{10}}^3 \, . \tag{4.28}$$

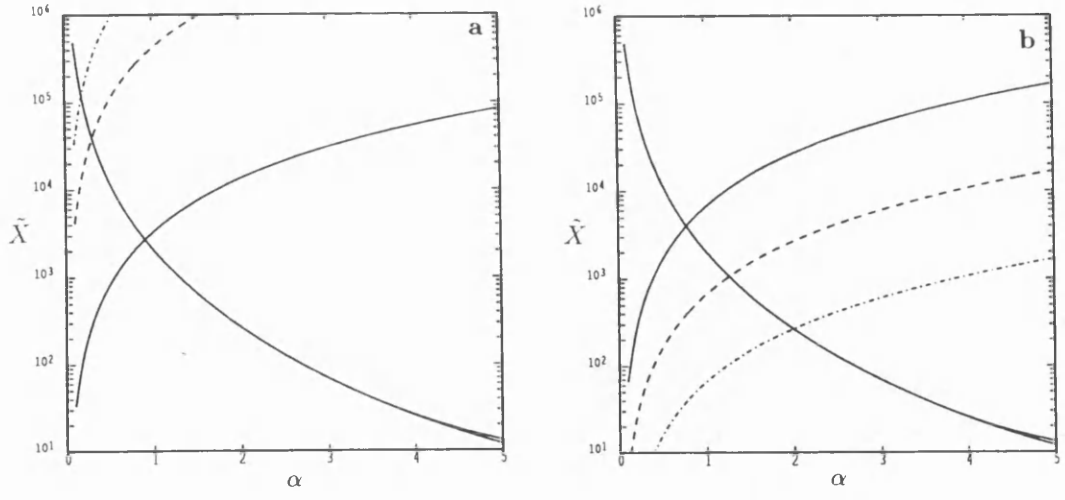

Figs. 4.7a,b. Graphical solutions to the limiting funnel semi-angle problem. In both **a** and **b** the full line running from top left to bottom right, where it eventually bifurcates, represents the data displayed in Fig. 4.6. In **a** the parameter $\tilde{X}$ is plotted as a function of α and the lines running from bottom left to top right represent $\tilde{X}_{max}$ for a bullet of mass 10^{21} kg and an accretion disc of radius $R_{ad_{10}}$=0.1 (full line), 0.5 (dashed line) and 1.0 (dashed-dotted line). All funnel semi-angles less than that which, for a given set of parameters, marks that intersection are precluded if a terminal speed of 0.2602c is to be possible. In **b** the parameter $\tilde{X}$ is again plotted as a function of α whilst the lines running from bottom left to top right represent $\tilde{X}_{max}$ for an accretion disc of radius $R_{ad_{10}}$=0.1 and a bullet of mass $m_{o_{21}}$=0.5 (full line), 5.0 (dashed line) and 50.0 (dashed line). As in **a**, all semi-angles smaller than that which marks a given intersection are precluded, for those model parameters, if a terminal speed of 0.2602c is to be achieved.

By utilising the data displayed in Fig. 4.6 and the constraint on the parameter $\tilde{X}$ imposed by Eq. (4.28) it is possible to deduce the limiting funnel semi-angle below which, for a given set of the parameters $m_{o_{21}}$ and $R_{ad_{10}}$, attainment of a terminal speed of 0.2602c is not possible. Graphical solutions to this problem are depicted in Figs. 4.7a and b. The full line running from top left to bottom right in both Figs. 4.7a and b represents the data displayed in Fig. 4.6. It is therefore formed from the superposition of three distinct lines which can clearly be seen to branch into two for $\alpha \geq 4°$. In Fig. 4.7a the lines running from bottom left to top right denote the value of $\tilde{X}_{max}$ for $m_{o_{21}} = 1$ and selected values of $R_{ad_{10}}$. Each intersection marks the limiting value of α for the given parameters $m_{o_{21}}$ and $R_{ad_{10}}$. Thus, for a bullet of mass 10^{21} kg and an accretion disc of 10^{10} m the funnel semi-angle must be greater than $\sim 0.2°$ if a terminal speed of 0.2602c is to be possible. For $R_{ad} = 5 \times 10^9$ and 10^9 metres the corresponding semi-angles are $\sim 0.3°$ and $\sim 0.9°$ respectively. The bullet mass need not be 10^{21} kg, though, from the form of Eq. (4.28) the upper limit on the parameter $\tilde{X}$ is more sensitive to variations in the radius of the accretion disc than to variations in the mass of the bullet. The effect that changing the bullet mass has on the limiting semi-angle for an accretion disc of radius 10^9 m is displayed in Fig. 4.7b. The striking feature of Figs. 4.7a and b is that the limiting values for α are very similar to the accepted semi-angle of the accretion funnel in SS433, believed to be in the range $0.5° \leq \alpha \leq 1°$. This indicates that, for this particular model, the terminal speed of the jets in SS433 is very close to, if not at the highest, that can possibly be achieved.

As has been discussed, once the bullet has reached a speed equal to $0.995\beta_{15}$ any further deviation in its speed will be proportionately comparable to the observational uncertainties in the speed of the jets in SS433. Therefore, for a speed of 0.2602c the required terminal speed is $\beta_{15} = 0.2615$. For a funnel of half-opening angle $\sim 0.5°$, such a terminal speed necessitates

that $\tilde{X} = 1.2261 \times 10^4$ whilst for a half opening angle of 1° the required value of the parameter $\tilde{X}$ is 2.086×10^3. The results of numerical integrations of Eq. (4.22) with these values of the parameter $\tilde{X}$ and corresponding semi-angle are illustrated in Figs. 4.8a,b and c.

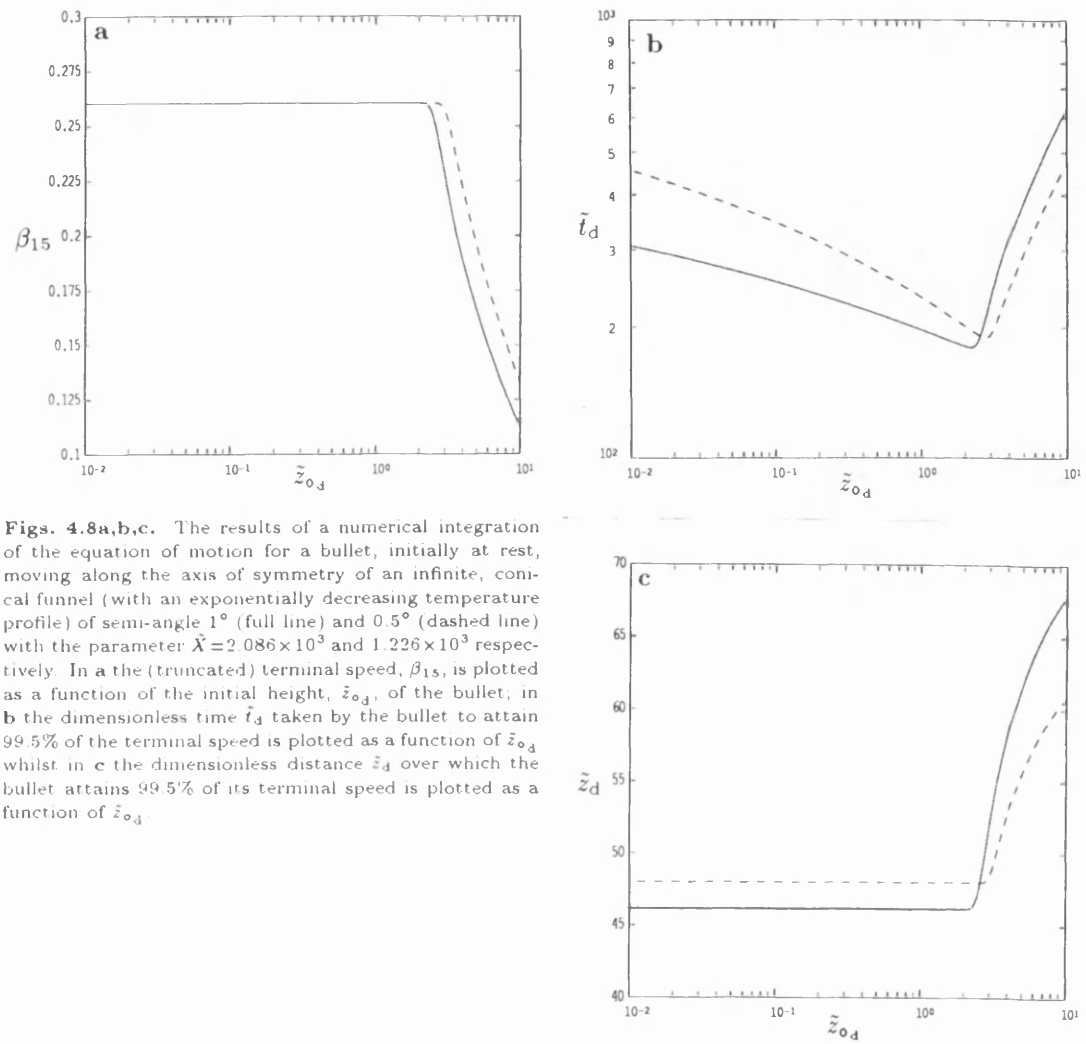

Figs. 4.8a,b,c. The results of a numerical integration of the equation of motion for a bullet, initially at rest, moving along the axis of symmetry of an infinite, conical funnel (with an exponentially decreasing temperature profile) of semi-angle 1° (full line) and 0.5° (dashed line) with the parameter $\tilde{X}=2.086\times10^3$ and 1.226×10^3 respectively. In **a** the (truncated) terminal speed, β_{15}, is plotted as a function of the initial height, $\tilde{z}_{o_d}$, of the bullet; in **b** the dimensionless time $\tilde{t}_d$ taken by the bullet to attain 99.5% of the terminal speed is plotted as a function of $\tilde{z}_{o_d}$ whilst in **c** the dimensionless distance $\tilde{z}_d$ over which the bullet attains 99.5% of its terminal speed is plotted as a function of $\tilde{z}_{o_d}$.

From inspection of Fig. 4.8a it can be seen that the attainment speed, specifically selected to be 0.2602c, is extremely well behaved up to $\tilde{z}_d \approx 2$ for $\alpha = 1°$ and up to $\tilde{z}_d \approx 2.5$ for $\alpha = 0.5°$. The dimensionless time-scales taken by the bullet to attain 99.5% of the terminal speed, or equivalently to reach a speed of 0.2602c, are shown in Fig. 4.8b. For a semi-angle of 1° the minimum attainment time is approximately 179 units whilst for $\alpha = 0.5°$ the corresponding time is roughly 189 units. A representative minimum time-scale is, therefore, about 184 units. For an accretion disc of radius 10^9 m and a core temperature of 8×10^8 K ($H_{10} = 0.13R_{ad_{10}}$) this corresponds to a physical time of about 80 seconds whilst for a disc of radius 10^{10} m ($H_{10} = 0.1R_{ad_{10}}$) this represents a period of approximately 614 seconds. These time-scales are in excellent agreement with the interval of $\sim$ 100 seconds over which the bullets in SS433 must be accelerated to their terminal speed. For rapid terminal speed attainment it is obviously advantageous for the disc radius to be $\sim 10^9$ metres rather than $\sim 10^{10}$ metres. Indeed for $R_{ad} \approx 10^9$ m an attainment time inside approximately 100 seconds is possible within a funnel

of semi-angle 0.5° for $\tilde{z}_{0_d}$ in the rough range $1.1 \times 10^{-1} \leq \tilde{z}_{0_d} \leq 3.7$ and with $\alpha = 1°$ for $\tilde{z}_{0_d}$ in the approximate range $0.27 \times 10^{-2} \leq \tilde{z}_{0_d} \leq 3.0$.

The dimensionless distance from the apex of the accretion funnel at which the speed of 0.2602c is reached is, from Fig. 4.8c, $\sim$ 48 units for $\alpha = 0.5°$ and $\sim$ 46 units for $\alpha = 1°$. A representative distance is, therefore, $\sim$ 47 units which, for a disc of radius 10^9 m, corresponds to a physical distance of $\sim 6R_{ad}$ whilst for a disc of radius 10^{10} m it corresponds to a physical distance of $\sim 5R_{ad}$.

The inclination of the accretion disc normal (which is aligned parallel to the funnel axis) to the line of sight is never less than $\sim 59°$ and the acceleration region is, as a result, always occluded to the terrestrial observer. X-ray observations (§1.5.2) indicate that the length of the acceleration region is no more than $\sim 10^{10}$ m which, on the basis of the information above, suggests that the accretion disc radius needs to be less than $\sim 1.7 \times 10^9$ metres. This poses an obvious problem: If the disc radius is at most $\sim 1.7 \times 10^9$ m then how can the bullets be obscured from the observer up to distances $\sim 10^{10}$ metres from the centre of the accretion disc? One possible solution is that the bullet is 'camouflaged' by the strong stellar wind emanating from the companion OB star and by an intense wind originating from the surface of the accretion disc. With respect to the latter point, it should be recalled that the compact object is likely undergoing supercritical accretion and is therefore predisposed to emanating an intense wind. The terminal speed of the stellar wind is $v_w = 500$ km/s and the mass loss rate is $\dot{M}_w = 3 \times 10^{-5} M_\odot$/yr to within a factor of 2 in both instances (Wagner, 1983). The radial optical depth of the wind from infinity to the surface of the star can readily be shown to be given by $\tau_\infty = \sigma_T \dot{M}_w / 4\pi v_w \bar{m} R_\star$, where $\bar{m}$ is the mean mass per particle of the winds constituents. Thus, assuming the wind to consist predominately of hydrogen and assuming a stellar radius $R_\star \sim 30R_\odot$ (Wagner, 1986), the radial optical depth of the wind is $\tau_\infty \sim 0.6$ which may be sufficient to provide the required degree of obscuration. The optical depth along a non-radial path will exceed the value quoted above and therefore the optical depth along an observer's line of sight will, in all likelihood, exceed 0.6 so enhancing the obscuring effect of the wind thus aiding in the camouflaging of the emerging bullets.

Finally, if the disc radius is $\sim 10^9$ m then, from Fig. 4.7a, for a bullet mass of $\sim 10^{21}$ kg the funnel semi-angle needs be greater than $\sim 0.9°$ if a terminal speed of 0.2602c is to be achieved. A rough lower bound on the bullet mass is 5×10^{20} kg (Brown, Cassinelli and Collins; 1991) which, on the basis of the data depicted in Fig. 4.7b, excludes funnel semi-angles less than approximately 0.8°. Therefore, the preferred geometrical funnel parameters for the acceleration of bullets to 0.26c within 10^{10} metres are $R_{ad} = 10^9$ metres and $\alpha = 1°$.

§4.4 Motion Above a Finite, Isothermal Plane

In deriving Eq. (2.92) it was assumed that all parallel raypath vectors incident on the surface of the bullet denoted the paths of photons with the same frequency. For an infinite, isothermal

plane this assumption is completely justified but for a finite, isothermal plane it is valid only in a certain limit. Consider Fig. 4.9a: If the inclination, θ, with respect to the positive z-axis of some raypath vector incident on the surface of the sphere (which for the purposes of this discussion is at rest with respect to the plane) is less than $\pi/2 - \delta$ then all the co-parallel raypath vectors together illuminate an hemisphere of the bullet. For all such raypath vectors the assumption expressed by Eq. (2.82) and invoked in the derivation of Eq. (2.92) is fully justified. This is not so however if $\theta > \pi/2 - \delta$; in this case the hemisphere is only partially, rather than completely, illuminated and the assumption declared by Eq. (2.82) becomes inaccurate. Rather than embarking on an esoteric quest to quantify the effect of these finite size effects precisely, I will instead determine the regime for which Eq. (2.92) is a valid approximation and explore the motion of a bullet above a finite, isothermal radiator within these limits.

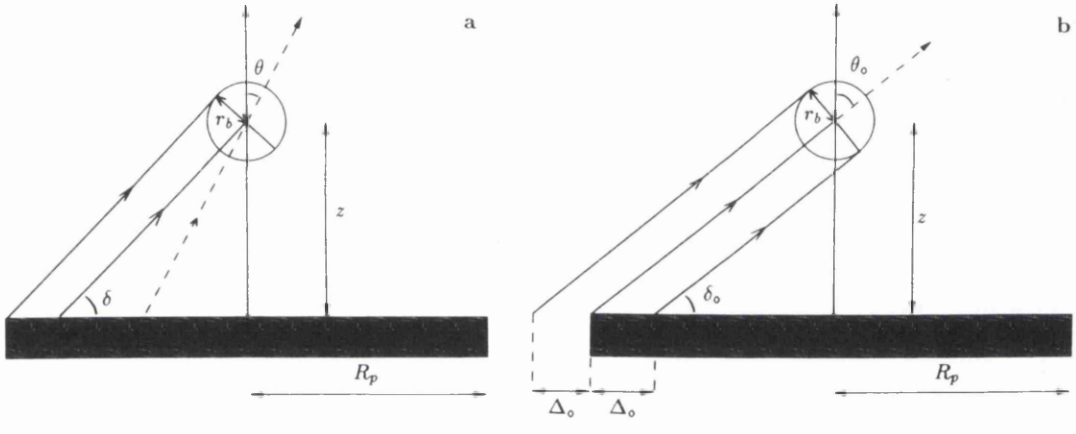

Figs. 4.9a,b. A schematic representation of the model geometry for motion above a finite, isothermal plane. See the text for a discussion.

It is evident from Fig. 4.9b that for the approximation to be good the length Δ_0 must be much less than the radius of the plane. If this is not so then a (comparatively) substantial region beyond the extremity of the radiating plane, where the temperature is strictly zero, will be attributed with a temperature identical to that of the plane itself. From Fig. 4.9b it can readily be deduced that

$$\sin\delta_0 = \frac{r_b}{\Delta_0} = \frac{z}{\sqrt{R_p^2 + z^2}} \tag{4.29}$$

and therefore

$$\Delta_0 = \frac{r_b}{z}\sqrt{R_p^2 + z^2}\ . \tag{4.30}$$

The condition that needs be satisfied is, consequently,

$$\frac{r_{b_d}}{z_d}\sqrt{1 + z_d^2} \ll 1 \tag{4.31}$$

where

$$r_{b_d} = \frac{r_b}{R_p} \qquad \text{and} \qquad z_d = \frac{z}{R_p} \,. \tag{4.32a,b}$$

The inequality denoted by Eq. (4.31) can never be satisfied unless $r_{b_d} \ll 1$. This is an intuitively obvious constraint. If the condition $r_{b_d} \ll 1$ is indeed satisfied then it can be deduced from Eq. (4.31) that the condition $z_d \gg r_{b_d}$ must also be met if the approximation is to be good for $z_d \ll 1$. Thus, for example, when considering an optically thin hydrogen plasma for which the characteristic 'bullet radius' is $\sim \sqrt{\sigma_T}$ the approximation is valid, to all intents and purposes, from the surface of the radiator upwards.

The angle of incidence (with respect to the positive z-axis) of photons originating from the edge of the radiator is, from Fig. 4.9b,

$$\theta_o = \cos^{-1}\left\{\frac{z_d}{\sqrt{1+z_d^2}}\right\} \,. \tag{4.33}$$

Therefore, by comparison with Eq. (3.7), the axial equation of motion is

$$\dot{\beta}_z = 2\frac{\sigma D T^4}{m_o c^2}\frac{1}{\gamma}\int_{\frac{z_d}{\sqrt{1+z_d^2}}}^{1} (\mu - \beta_z)(1 - \beta_z \mu)\, d\mu \tag{4.34}$$

which, again with reference to Eq. (3.7) and with the introduction of the dimensionless variables

$$t_d = \frac{c}{R_p}t \quad , \quad \dot{z}_d = \frac{dz_d}{dt_d} = \beta_z \quad , \quad \ddot{z}_d = \frac{d^2 z_d}{dt_d^2} = \frac{R_p}{c}\dot{\beta}_z \quad \text{and} \quad X = \frac{R_p}{c}W \tag{4.35a,b,c,d}$$

where W is defined by Eq. (3.9b), can readily be integrated to yield

$$\ddot{z}_d = \frac{1}{3}X(1-\dot{z}_d^2)^{\frac{1}{2}}\left[\{3\dot{z}_d^2 - 8\dot{z}_d + 3\} + \frac{z_d}{(1+z_d^2)^{\frac{3}{2}}}\left\{2(4z_d^2+3)\dot{z}_d - 3(1+z_d^2)^{\frac{1}{2}}(1+\dot{z}_d^2)z_d\right\}\right] \,. \tag{4.36}$$

As with the temperature profile discussed in the immediately preceding section, the equation of motion is explicitly dependent on the dimensionless variable z_d and as a result the problem is not, in general, scale invariant. Of course, in the limit where the radius of the plane tends to infinity the variable $z_d \to 0$ and Eq. (4.36) reduces to the scale invariant equation of motion given by Eq. (3.24). It is trivial to show from Eq. (4.36) that for $\dot{z}_d = 0$,

$$\ddot{z}_d = \frac{X}{1+z_d^2} \,. \tag{4.37}$$

From a comparison of this result with Eq. (3.24) it is obvious that the initial radiative acceleration of a stationary bullet located on axis at a dimensionless height z_d above a finite, isothermal plane is a factor $1 + z_d^2$ less than that for motion above an infinite, isothermal plane.

The terminal speed of the bullet, by definition, is approached as $t_{\rm d} \rightarrow \infty$ or equivalently as $z_{\rm d} \rightarrow \infty$. In this limit Eq. (4.36) simply indicates that $\ddot{z}_{\rm d} \rightarrow 0$. This result could easily have been deduced using common sense and it unfortunately reveals nothing new about the terminal speed of the bullet. Information on this subject is best obtained by adopting a numerical approach.

Prior to investigating Eq. (4.36) in more detail I will first discuss the suitable range of the model parameters. For radiative acceleration to be possible along the normal axis of the disc above an accreting object of mass $M_\star$ the elementary inequality

$$\frac{W{\rm c}}{1+z_{\rm d}^2} \geq \frac{{\rm G}M_\star}{R_p^2 z_{\rm d}^2} \, , \tag{4.38}$$

must be satisfied. This can be solved for $z_{\rm d}$ yielding

$$z_{\rm d} \geq \sqrt{\frac{Z_a}{1-Z_a}} \qquad \text{where} \qquad Z_a \equiv \frac{\rm G}{\rm c}\frac{M_\star}{R_p^2 W} \, . \tag{4.39a,b}$$

Hence, for radiative acceleration to be viable the parameter Z_a must be in the range $0 \leq Z_a < 1$; for any $Z_a > 1$ gravity dominates. The maximum value of the parameter W is achieved in the limit where the matter to be accelerated is optically thin. Therefore, for a fully ionised hydrogen plasma, by Eqs. (3.13) and (4.39b), the lower limit for the parameter Z_a is

$$Z_{a_{min}} \approx 18\,(M_\star/M_\cdot) R_{p_{10}}^{-2} T_4^{-4} \, . \tag{4.40}$$

In many physical situations the accretion disc is sufficiently thin that the movement of material within the disc can be modelled as a two dimensional gas flow; this is the thin disc approximation. If the disc is assumed to be optically thick in the z-direction then each area element, at a radial distance r from the disc centre, will radiate as a blackbody with a temperature (Frank, King and Raine; 1985) given by

$$T(r) = T_\star \left[1 - \left(\frac{R_\star}{r}\right)^{\frac{1}{2}}\right]^{\frac{1}{4}} \tag{4.41}$$

where $T_\star$ is a characteristic temperature which can be expressed as

$$T_\star = \left(\frac{3{\rm G}M_\star \dot{M}}{8\pi R_\star^3 \sigma}\right)^{\frac{1}{4}} \tag{4.42a}$$

$$= 4.1 \times 10^4 \dot{M}_{13}^{\frac{1}{4}} (M_\star/M_\cdot)^{\frac{1}{4}} R_{\star_7}^{-\frac{3}{4}} \ {\rm K} \tag{4.42b}$$

$$= 1.3 \times 10^7 \dot{M}_{14}^{\frac{1}{4}} (M_\star/M_\cdot)^{\frac{1}{4}} R_{\star_4}^{-\frac{3}{4}} \ {\rm K} \, . \tag{4.42c}$$

Equation (4.42b) is appropriate if the accreting object is a white dwarf whilst Eq. (4.42c) is applicable if the accreting object is a neutron star. It should be noted in passing that the

luminosity of the whole disc, obtained by integrating $\sigma T^4(r)$ over both surfaces of the disc, is $L_{ad} = \frac{1}{2} L_{acc}$ where the accretion luminosity is given by

$$L_{acc} = \frac{GM\dot{M}}{R_\star} . \tag{4.43}$$

The remaining luminosity originates from a very hot boundary layer close to the surface of the accreting object. I will not consider such complexities here but will merely adopt the temperature $T_\star$ as being characteristic of the surface temperature of the accretion disc. On this basis, by Eq. (4.40), typical minimum values for the parameter Z_a are $\sim 6.4 \times 10^{-2} R_{p_{10}}^{-2}$ and $\sim 6.3 \times 10^{-12} R_{p_{10}}^{-2}$ for an accreting white dwarf and neutron star respectively. Recalling that $Z_a < 1$ for radiative acceleration, these expressions imply that the radius of the accretion disc must be greater than $\sim 2.5 \times 10^9$m for an accreting white dwarf and greater than $\sim 2.5 \times 10^4$m for an accreting neutron star. For an accretion disc of radius 10^{10}m, Eq. (4.39*a*) then implies that $z_d > 0.26$ for motion above a white dwarf whilst $z_d > 2.5 \times 10^{-6}$ for motion above a neutron star. In reality the respective lower bounds on z_d will likely be considerably less on account of the thermal energy of the plasma. Even so it is clear that the conditions for the radiative acceleration of matter from the immediate vicinity of an accreting white dwarf are not favourable.

The upper bound on the parameter X, by Eqs. (3.13) and (4.35*d*), is

$$X_{max} \approx 8.3 \times 10^{-9} R_{p_{10}} T_4^4 \tag{4.44}$$

whilst the lower bound on the parameter X for which radiative acceleration is possible (in the limit where $z_d \to \infty$) is, by Eqs. (4.35*d*) and (4.39*b*),

$$X_{min} \approx 1.5 \times 10^{-7} (M_\star / M_\odot) R_{p_{10}}^{-1} . \tag{4.45}$$

Thus, for a white dwarf located at the centre of a thin, isothermal accretion disc of radius $\sim 10^{10}$ m the parameter X must, if radiative acceleration is to be at all possible, lie in the approximate range $1.5 \times 10^{-7} \leq X \leq 2.3 \times 10^{-6}$ and in the rough range $1.5 \times 10^{-7} \leq X \leq 2.4 \times 10^4$ for motion above an accreting neutron star.

The results of a numerical integration of Eq. (4.36) for selected values of the parameter X appropriate for an accreting neutron star are shown in Figs. 4.10a,b and c. As in the previous section it was found that the speed the bullet is, to very good accuracy, constant after a period several orders of magnitude less than 10^{15} dimensionless time units. Therefore, in the same vein as §4.3, I have adopted the speed of the bullet after 10^{15} dimensionless time units as representing the (truncated) terminal speed.

From Fig. 4.10a it can be seen that the terminal speed increases with X and, for the values of X depicted, is very much independent of the initial release height up to $z_{0_d} \sim 10^{-1}$.

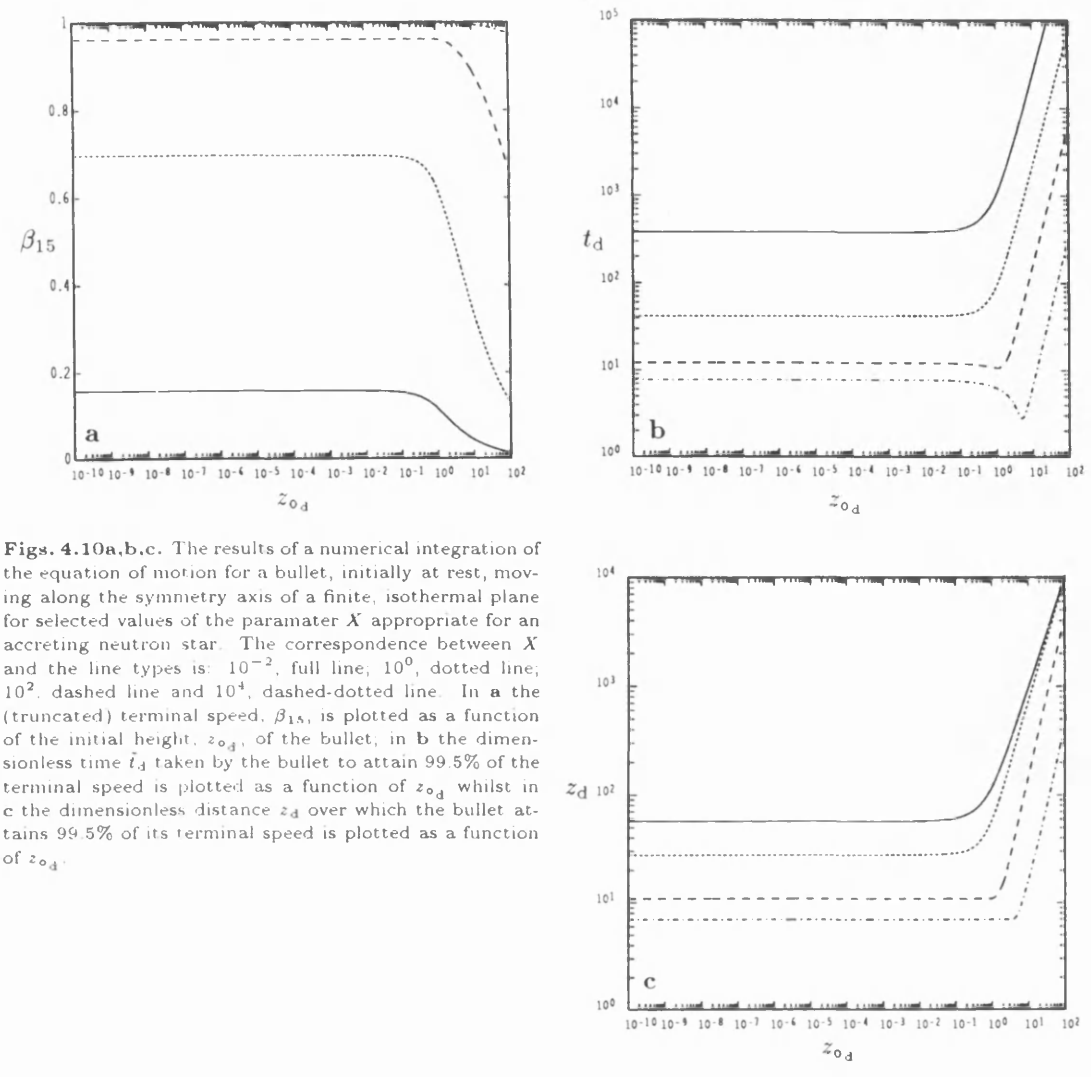

Figs. 4.10a,b,c. The results of a numerical integration of the equation of motion for a bullet, initially at rest, moving along the symmetry axis of a finite, isothermal plane for selected values of the paramater X appropriate for an accreting neutron star. The correspondence between X and the line types is: 10^{-2}, full line; 10^{0}, dotted line; 10^{2}, dashed line and 10^{4}, dashed-dotted line. In **a** the (truncated) terminal speed, β_{15}, is plotted as a function of the initial height, z_{o_d}, of the bullet, in **b** the dimensionless time $\tilde{t}_d$ taken by the bullet to attain 99.5% of the terminal speed is plotted as a function of z_{o_d} whilst in **c** the dimensionless distance z_d over which the bullet attains 99.5% of its terminal speed is plotted as a function of z_{o_d}.

The former fact permits the attainment of high terminal speeds e.g. for $X = 10^4$ the highest achievable terminal speed is $\beta_{15} = 0.9959$. It can readily be appreciated, too, that the terminal speed for axial motion directly above an accreting white dwarf will be low. The same conclusion can also be drawn from simple radiation wind theory in which the terminal wind speed, v_∞, is related to the escape velocity, v_{esc}, from the central compact object and accretion disc luminosity, L_{ad}, by the expression $v_\infty = v_{esc}(L_{ad}/L_{Edd} - 1)^{1/2}$. Since the escape velocity from a white dwarf is ~ 0.01c high terminal speeds are possible only if $L_{ad} \gg L_{Edd}$. This is in contrast to motion above a neutron star for which the escape speed is typically ~ 0.6c thereby permitting relativistic terminal speeds for $L_{ad} \sim L_{Edd}$.

The dimensionless time taken by the bullet to attain 99.5% of its terminal speed as a function of the initial release height is shown in Fig. 4.10b. As a general rule the attainment time is very much independent of the initial, dimensionless starting height for $z_{o_d} \leq 10^{-1}$. For z_{o_d} beyond this rough value the attainment time increases rapidly even though the terminal speed is falling off quickly. A curious feature and exception to this general trend is evidenced by the sudden down-turn in the attainment time which occurs at $z_{o_d} \sim 1$ for $X = 10^4$; the same

behaviour is just discernible in the data set corresponding to $X = 10^3$. For an accretion disc of radius 10^{10}m, by Eq. (4.35*a*), one dimensionless time unit corresponds to a physical time of ~ 33 s and the minimum attainment time for $X = 10^4$ represents a physical time of only ~ 94 seconds. The dimensionless distance above the plane at which the bullet attains 99.5% of its terminal speed is plotted as a function of z_{0_d} in Fig. 4.10c. Clearly there exists a range of initial release heights for each value of the parameter X for which the attainment distance is quite independent of z_{0_d}. This range is coincident with that over which the terminal speed is independent of the initial release height.

§4.5 Motion above a Spherical, Isotropic Radiator

In this section I will consider the rôle that special relativistic effects can play in the radiation driven winds of hot luminous stars. In particular I will investigate these effects for continuum radiation pressure which in stellar winds is due mostly to Thomson scattering opacity. Although stellar wind theory is conventionally conducted in the non-relativistic regime some of the observed terminal wind speeds are marginally relativistic (e.g. the terminal wind speed of the galactic star HD 48099, which is of spectral type O6.5 V, is 3500 km/s (Conti and Underhill; 1988)) and a cursory realtivistic treatment is worthwhile if only to confirm that the Newtonian limit is appropriate.

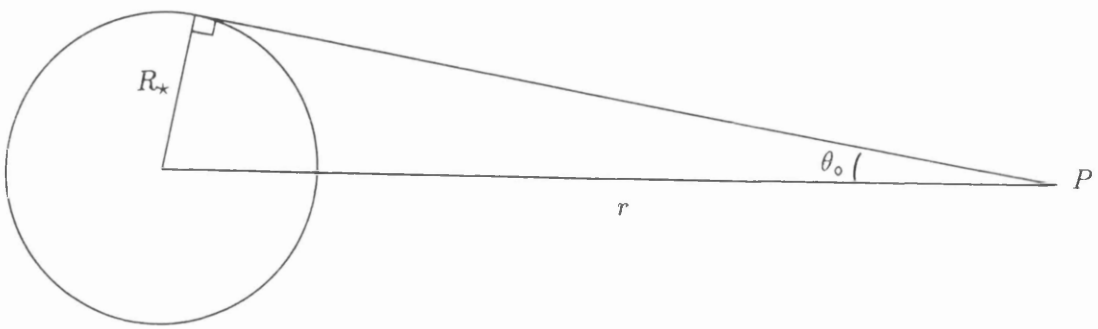

Fig. 4.11. A schematic representation of the model geometry for motion above a star of radius $R_\star$. The star subtends an half-angle θ_0 at the point P, a distance r from the centre of the star.

Consider a star of luminosity $L_\star$ and radius $R_\star$. The energy flux at the point P (Fig. 4.11), a radial distance r from the centre of the star, is

$$\mathcal{F} = \frac{L_\star}{4\pi r^2} \ . \tag{4.46}$$

and the semi-angle subtended by the star at P, observed in the stellar rest frame, is

$$\theta_0 = \sin^{-1}\left(\frac{R_\star}{r}\right) \ . \tag{4.47}$$

The energy flux at this same point is, by Eqs. (2.32) and (2.33), given by

$$\mathcal{F} = \int_0^{2\pi} \mathrm{d}\phi \int_0^{\theta_\circ} I \sin\theta \cos\theta \, \mathrm{d}\theta = \pi I \left(\frac{R_\star}{r}\right)^2 \tag{4.48}$$

and hence, by equating Eqs. (4.46) and (4.48), the frequency integrated specific intensity is

$$I = \frac{L_\star}{4\pi^2 R_\star^2} \, . \tag{4.49}$$

By appealing to Eq. (4.1), the radial equation of motion can be shown to have the form

$$\dot{\beta} = 2\pi \frac{\sigma_{\mathrm{T}}}{\mathrm{m}_p \mathrm{c}^2} \frac{1}{\gamma} \int_0^{\theta_\circ(r)} I \, (\cos\theta - \beta)(1 - \beta\cos\theta) \sin\theta \, \mathrm{d}\theta \tag{4.50}$$

which can be readily integrated to yield

$$\dot{\beta} = \frac{\sigma_{\mathrm{T}}}{\mathrm{m}_p \mathrm{c}^2} \frac{L_\star}{4\pi r^2} (1 - \beta^2)^{\frac{1}{2}} \left\{1 - f(\theta_\circ)\beta + \beta^2\right\} \tag{4.51}$$

where

$$f(\theta_\circ) = \frac{2}{3} \frac{4 - (\cos^2\theta_\circ + 3)\cos\theta_\circ}{\sin^2\theta_\circ} \, . \tag{4.52}$$

The function f is monotonic, decreasing rapidly from a maximum of 8/3 at $r = R_\star$ and asymptoting towards a lower bound of 2 as $r \rightarrow \infty$. By the introducing the parameter

$$\Gamma = \frac{L_\star}{L_{Edd}} \, , \tag{4.53}$$

where L_{Edd} is the Eddington luminosity (Eq. 1.6) and retaining terms of order β and less in Eq. (4.51) it is simple to show that, for $v/\mathrm{c} \ll 1$, the radial acceleration due to continuum radiation pressure alone is given by

$$\frac{\mathrm{d}v}{\mathrm{d}t} = \Gamma \frac{\mathrm{G}M_\star}{r^2} \left\{1 - f(\theta_\circ)\frac{v}{\mathrm{c}}\right\} \, . \tag{4.54}$$

The function f falls off very rapidly with r attaining, for example, a value of $2 + 6.412 \times 10^{-3}$ at $r = 2R_\star$. Thus, for $r > 2R_\star$ Eq. (4.52) is very well approximated by

$$\frac{\mathrm{d}v}{\mathrm{d}t} = \Gamma \frac{\mathrm{G}M_\star}{r^2} \left\{1 - 2\frac{v}{\mathrm{c}}\right\} \tag{4.55}$$

and, consequently, for wind speeds $\sim$ 3000 km/s there will be a typical reduction of $\sim$2% in the continuum radiation pressure due to radiation drag. This will, in all likelihood, have an insignificant effect in the terminal wind speeds predicted by standard theoretical models. The

same cannot, obviously, be said for wind speeds much in excess of $\sim 3000\,\mathrm{km/s}$ and it seems reasonable to conclude that relativistic effects ought to be given consideration in any theoretical modelling where the terminal wind speeds are significantly greater than $\sim 3000\,\mathrm{km/s}$. Whether such objects exist I do not know but AGN's involving black hole accretion are the most likely candidates.

§4.6 Motion Within and Above a Finite Accretion Funnel

§4.6.1 The Isothermal Funnel

Prior to considering a similar geometric configuration with a more realistic temperature profile I will first consider the simplest possible case: the acceleration of an electron-proton pair moving within a finite, isothermal funnel. I shall not attempt to introduce any degree of rigour at this stage but will explore the solutions to the appropriate equation of motion, derived below, which will give an indication of the generic behaviour of the solutions which can be expected in a more representative model. The length-scale of the 'bullet' is negligible in comparison to the dimensions of any physical accretion disc and, therefore, finite size problems need not be considered. I will, for the interim, also ignore any gravitational effects.

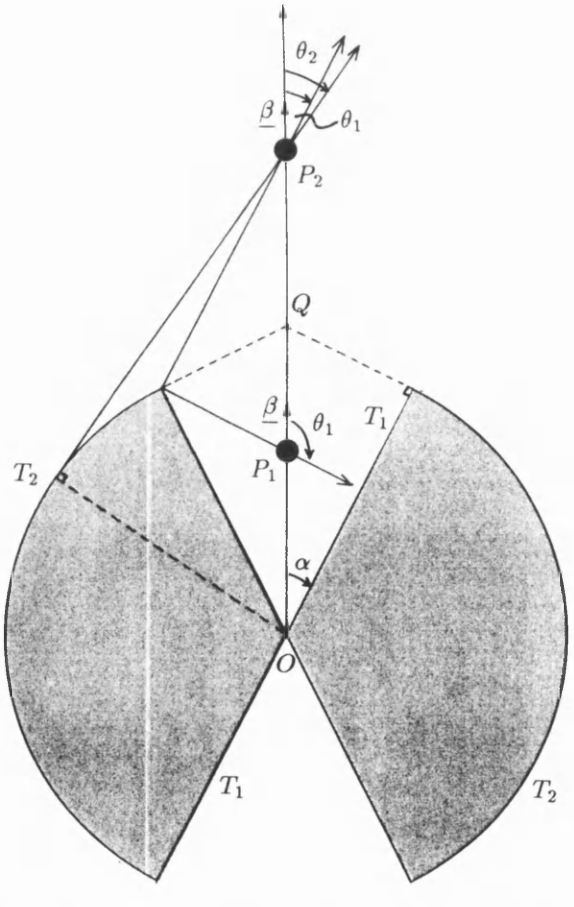

Fig. 4.12. The model geometry for axial motion within and above the funnel of a thick accretion disc as perceived by an observer in the rest frame of the accretion disc. The outer surface of the disc is at a blackbody temperature T_2 and is spherical, with a radius R_{ad}. The accretion funnels are conical, with an opening half-angle α, and isothermal at a blackbody temperature T_1. For any location between O and Q the bullet is illuminated solely by radiation originating from the funnel walls whilst for any location beyond Q the bullet is illuminated by radiation originating from both the funnel walls and the outer surface of the accretion disc.

Consider the depiction of the accretion disc displayed in Fig. 4.12: The interior surface of the disc is at a blackbody temperature T_1 and is conical with a semi-opening angle α. The exterior, spherical surface is at a blackbody temperature T_2 and has a radius R_{ad}. It is evident from consideration of the geometry of the disc (in the disc rest frame) that the 'bullet', or more appropriately in this case test-particle, will experience two distinct radiation regimes. In the first the bullet is driven solely by radiation that originates from within the accretion funnel. This corresponds to any location between the points O and Q in Fig. 4.12. Above the point Q, which is at at a dimensionless distance $z_{\rm d} = \sec\alpha$ above the funnel apex at O, the bullet is driven both by radiation emitted from within the accretion funnel and also by radiation emanating from the exterior surface of the accretion disc. This domain represents the second radiation regime. For some axial bullet location P_1 between O and Q the maximum, limiting angle of incidence of any raypath vector is, from a simple application of the sine rule, given by

$$\theta_1 = \cos^{-1}\left(\frac{z_{\rm d} - \cos\alpha}{\sqrt{1 + z_{\rm d}^2 - 2z_{\rm d}\cos\alpha}}\right) \qquad \text{where} \qquad z_{\rm d} = \frac{z}{R_{ad}} \,. \tag{4.56a,b}$$

For a general, axial location P_2 beyond the point Q the maximum angle of incidence of any photon originating from within the accretion funnel is again given by θ_1 whilst the minimum and maximum angles of incidence of photons emitted by the exterior surface of the disc are θ_1 and

$$\theta_2 = \cos^{-1}\left(\frac{\sqrt{z_{\rm d}^2 - 1}}{z_{\rm d}}\right) \tag{4.57}$$

respectively.

By analogy with Eq. (4.34) and with reference to Eq. (3.7) it can easily be shown that the complete, axial equation of motion can be expressed as

$$\begin{aligned}\ddot{z}_{\rm d} =& \frac{1}{3}X_{ad}\,(1-\dot{z}_{\rm d}^2)^{\frac{1}{2}}\Big[-2\dot{z}_{\rm d}(1-\mu_1^3) + 3(1+\dot{z}_{\rm d}^2)\,(1-\mu_1^2) - 6\dot{z}_{\rm d}(1-\mu_1) + \\ & \mathcal{H}(z_{\rm d} - \sec\alpha)\left(\frac{T_2}{T_1}\right)^4\left\{-2\dot{z}_{\rm d}(\mu_1^3 - \mu_2^3) + 3(1+\dot{z}_{\rm d}^2)\,(\mu_1^2 - \mu_2^2) - 6\dot{z}_{\rm d}(\mu_1 - \mu_2)\right\}\Big]\end{aligned} \tag{4.58}$$

where

$$t_{\rm d} = \frac{\rm c}{R_{ad}}t \;,\; \dot{z}_{\rm d} = \frac{{\rm d}z_{\rm d}}{{\rm d}t_{\rm d}} = \beta_z \;,\; \ddot{z}_{\rm d} = \frac{{\rm d}^2 z_{\rm d}}{{\rm d}t_{\rm d}^2} = \frac{R_{ad}}{\rm c}\dot{\beta}_z \;,\; X_{ad} = \frac{\sigma D T_1^4}{{\rm m_o c^2}}\frac{R_{ad}}{\rm c} \;, \tag{4.59a,b,c,d}$$

$\mathcal{H}(x)$ is the Heaviside function defined such that

$$\mathcal{H}(x) = \begin{cases} 1, & \text{for } x > 0 \\ 0, & \text{for } x < 0 \end{cases} \tag{4.60}$$

and $\mu_{_2^1} = \cos\theta_{_2^1}$.

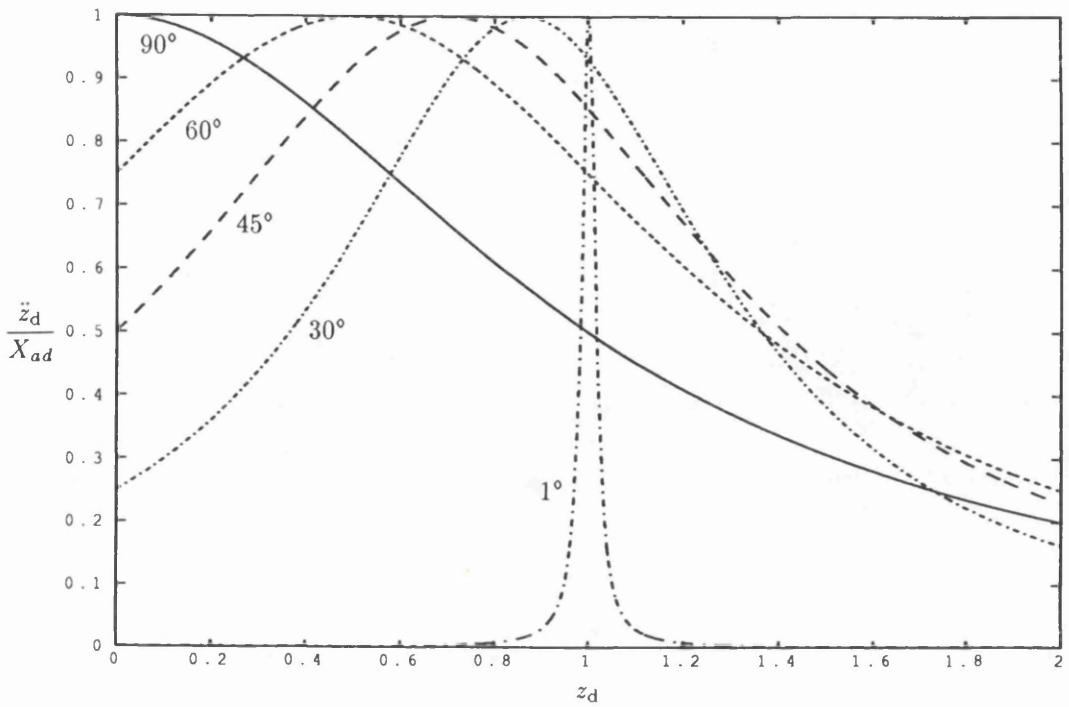

Fig. 4.13. A plot of $\ddot{z}_d/X_{ad} \equiv a_z/(\sigma D T_1^4/m_o c)$ (due to radiation originating from the funnel walls) versus dimensionless height, z_d, for a stationary bullet located on the axis of a finite, isothermal accretion funnel for selected values of the funnel semi-angle.

It can be deduced from Eqs. (4.58) and (4.59c,d) that the contribution made to the radiative acceleration of a stationary bullet by radiation originating from within a finite, isothermal funnel is

$$a_z = \frac{\sigma D}{m_o c} T_1^4 \frac{\sin^2 \alpha}{1 + z_d^2 - 2 z_d \cos \alpha} \; ; \tag{4.61}$$

a graphical illustration of which is shown in Fig. 4.13. This is a factor $1 + z_d^2 - 2z_d \cos\alpha$ less than the equivalent expression for motion within an infinite, isothermal funnel. A feature which is immediately obvious from Fig. 4.13 is the progressive narrowing of the acceleration 'hump' as α decreases. Since the maximum value of a_z occurs at $z_d = \cos\alpha$, or equivalently when the bullet centre is coplanar with the funnel mouth, it is reasonable to expect the bullet to be accelerated as it approaches the top of the accretion funnel; particularly so if the funnel is narrow. Such behaviour would seemingly not augur well for the attainment of a terminal speed in the proximity of the funnel mouth.

It is plausible to conclude that the parameter X_{ad} in Eq. (4.58) will, like its counterparts in §4.3 and §4.4, play a critical rôle in determining the final bullet speed. Though, for the purposes of expediency, I am at present only considering the motion of a test-particle rather than a much larger bullet, it is necessary to ensure that the numerical values of the parameter X_{ad} employed in Eq. (4.58) are appropriate for a massive bullet if the results are to be a good indicator of the behaviour that can be expected in such a model. To this end I will adopt the parameter values $R_{ad} \sim 10^{10}$ m, $m_o \sim 10^{21}$ kg and assume a minimum bullet radius, given by

Eq. (3.14), of $r_b \sim 10^{-2}\mathrm{m}_\odot^{\frac{1}{3}}$ metres. By Eq. (4.59*d*) typical values for the parameter X_{ad} are then

$$X_{ad} \sim 6.6 \times 10^{-2} R_{ad_{10}} \mathrm{m}_{\odot_{21}}^{-\frac{1}{3}} T_8^4 \,. \tag{4.62}$$

Hence for bullet parameters appropriate for SS433 the parameter values $\log_{10} X_{ad} = -2, -1, 0, 1$ and 2 correspond approximately to funnel temperatures $T_1 \sim 0.6, 1.1, 2.0, 3.5$ and 6.2×10^8 K respectively.

The dimensionless time, t_{d}^{ex}, and speed, $\dot{z}_{\mathrm{d}}^{ex}$, of the bullet when it exits the funnel ($z_{\mathrm{d}} = \cos\alpha$) are tabulated in Table 4.1 whilst graphical solutions to the equation of motion (Eq. 4.58) are provided by Figs. 4.14 and 4.15.

	$\log_{10} X_{ad} = -2$		$\log_{10} X_{ad} = 0$		$\log_{10} X_{ad} = 2$	
α	t_{d}^{ex}	$\dot{z}_{\mathrm{d}}^{ex}$	t_{d}^{ex}	$\dot{z}_{\mathrm{d}}^{ex}$	t_{d}^{ex}	$\dot{z}_{\mathrm{d}}^{ex}$
60	11.849	0.0856	2.130	0.3694	1.654	0.4497
45	17.045	0.0916	3.857	0.3597	3.298	0.4494
30	26.560	0.0861	7.929	0.3412	7.251	0.4486
15	58.906	0.0676	27.869	0.3023	27.000	0.4460
5	292.081	0.0425	235.812	0.2332	234.658	0.4368

Table 4.1. The dimensionless time taken by the bullet, with the initial conditions z_{d}=0 and $\dot{z}_{\mathrm{d}}$=0, to exit the accretion funnel and the dimensionless speed at the exit point for selected values of the funnel semi-angle, α, and the parameter X_{ad}.

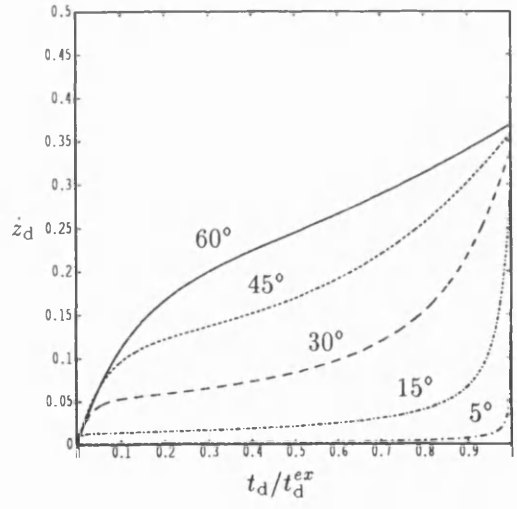

Fig. 4.14. The dimensionless speed of the bullet, $\dot{z}_{\mathrm{d}}$, versus the dimensionless time, t_{d}, scaled by the dimensionless time, t_{d}^{ex}, taken to exit the finite, isothermal funnel for X_{ad}=1 and the indicated values of the funnel semi-angle.

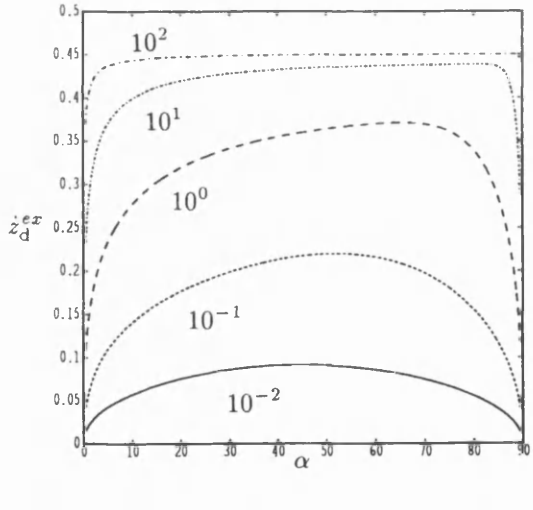

Fig. 4.15. The dimensionless speed, $\dot{z}_{\mathrm{d}}^{ex}$, of the bullet upon exiting the finite, isothermal funnel versus the funnel semi-angle for the indicated values of the parameter X_{ad}.

The rapid acceleration near the funnel mouth alluded to earlier, particularly for the narrower funnels, is clearly visible in the Fig. 4.14. One feature which should be remarked upon and which can readily be seen from inspection of Fig. 4.15 and the tabulated data for $\log_{10} X_{ad} = 2$ is the proximity of the exit speed to the terminal speed above an infinite, isothermal plane given by Eq. (3.25). In fact the speed $\beta_\infty = 0.4514$ represents an absolute upper bound on the *exit* speed from a finite, isothermal funnel.

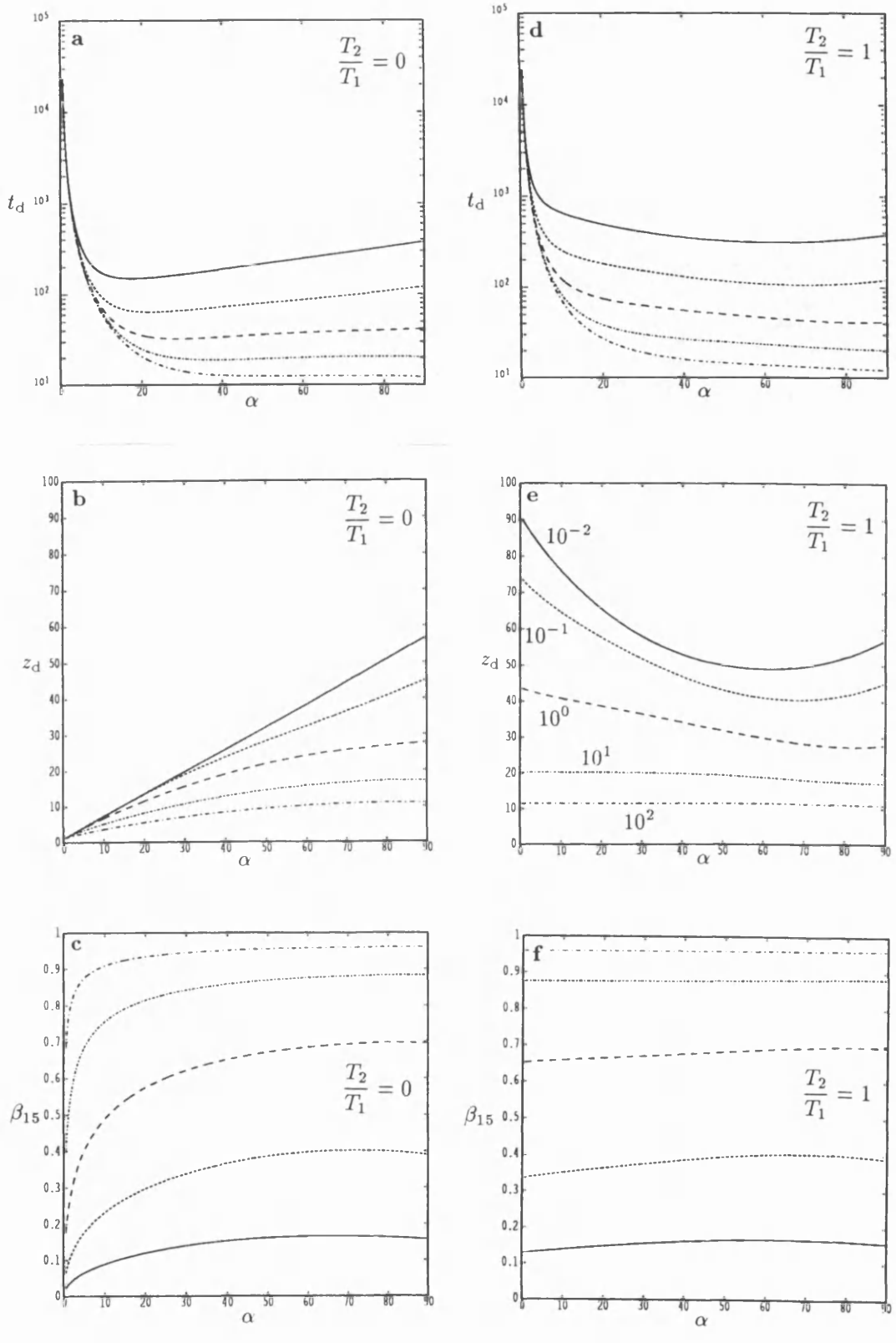

Figs. 4.16a,b,c,d,e,f. Grahpical illustrations of numerical solutions to Eq. (4.58) for axial motion within and above an accretion disc with an outer surface temperature T_2 and inner, funnel temperature T_1 for the indicated values of the parameter X_{ad} and for ratio T_2/T_1=0, plots **a**, **b**, and **c** and for T_2/T_1=1, plots **d**, **e** and **f**. The designation of line attributes to values of the parameter X_{ad} given in **e** applies to all of the graphs. In **a** and **d** the dimensionless time, t_d, taken to attain 99.5% of the (truncated) terminal speed is plotted as a function of the funnel semi-angle; in **b** and **e** the dimensionless distance, z_d, over which 99.5% of the (truncated) terminal speed is achieved is plotted as a function of the funnel semi-angle and in **c** and **f** the (truncated) terminal speed, β_{15}, is plotted as a function of the funnel semi-angle.

The results of integrating the complete equation of motion for selected values of the ratio T_2/T_1 are illustrated in Figs. 4.16a-f. The, by now, familiar convention of assigning the (truncated) terminal speed to be that of the bullet after 10^{15} dimensionless time units has been adopted. The data specific to a funnel of half-opening angle of 0.5° are tabulated in Table 4.2.

	$T_2/T_1 = 0$			$T_2/T_1 = 0.316$			$T_2/T_1 = 1$		
$\log_{10}X_{ad}$	$t_d/10^4$	z_d	β_{15}	$t_d/10^4$	z_d	β_{15}	$t_d/10^4$	z_d	β_{15}
−2	2.347	1.300	0.022	2.453	28.372	0.026	2.417	90.183	0.129
−1	2.336	1.314	0.065	2.373	28.883	0.077	2.358	73.627	0.336
0	2.335	1.325	0.177	2.348	28.201	0.209	2.341	43.600	0.652
1	2.335	1.307	0.403	2.340	23.707	0.465	2.337	20.304	0.876
2	2.335	1.237	0.686	2.337	16.481	0.743	2.336	11.507	0.960

Table 4.2. The dimensionless time and distance taken by the bullet, with the initial conditions z_d=0 and $\dot{z}_d$=0, moving within a finite, isothermal funnel of temperature T_1 and semi-angle 0.5° to attain 99.5% of the (truncated) terminal speed, β_{15}, for selected values of the temperature ratio T_2/T_1 and the parameter X_{ad}. Note that once the bullet has proceeded beyond the funnel limb, $z_d > \cos\theta$, it will be illuminated by a finite, isothermal plane of temperature T_1 and dimensionless radius $R_{p_d} = \sin\alpha$ and when beyond the point Q in Fig. 4.12, $z_d > \sec\alpha$, both by this same finite plane and by an *incomplete* spherical, isothermal radiator of temperature T_2 and dimensionless radius $R_{ad_d} = 1$.

Since the latter part of Eq. (4.58) is proportional to the fourth power of the ratio T_2/T_1, radiation originating from the outer surface of the accretion disc will enhance the terminal speed markedly only if T_2 is roughly comparable to T_1. This is evidenced by Figs. 4.16c,f for which the ratio $(T_2/T_1)^4$ is, respectively, 0 and 1. The increase in the terminal speed over that attainable for $T_2 = 0$ is most significant when the funnel is narrow and negligible for much broader funnels. This trend has an obvious explanation: the solid angle subtended by the exterior surface of the accretion disc at the bullet centre when the funnel opening angle is small is much greater than solid angle subtended by the external surface of the disc at the bullet centre when the funnel semi-angle is large. Enhancement in the terminal speed on account of radiation emanating from the outer surface of the disc is accompanied by an increase in the distance taken by the bullet to attain 99.5% of the terminal speed (Figs. 4.16b,e). This reflects the fact that the bullet continues to accelerate at considerable distances above the funnel mouth and is a feature which is most certainly not observed in SS433.

By Eq. (4.17) the effective temperature of the accretion disc in SS433, assuming a disc radius $R_{ad} = 10^{10}$ m, is $\sim 3.4 \times 10^4$ K. If this temperature is equated to the assumed blackbody temperature T_2 then, for funnel temperatures $T_1 \sim 10^8$ K, the ratio $T_2/T_1 \sim 10^{-4}$ and the contribution made by radiation from the exterior surface of the disc, even for the narrow funnels likely to be present in SS433, in enhancing the terminal speed will be completely negligible. Figures 4.16a,b,c are, therefore, most relevant to SS433.

From the data tabulated in Table 4.2, in particular that data corresponding to $T_2/T_1 = 0$, it can be deduced that a terminal speed of 0.26c can be achieved within an accretion funnel of semi-angle 0.5° if the parameter X_{ad} is in the rough range $10^0 < X_{ad} < 10^1$. For the bullet parameters specified above this corresponds to a perfectly reasonable funnel temperature $T_1 \sim 2 - 3.5 \times 10^8$ K. Recalling from §3.2.3 that the terminal speed within an infinite, isothermal funnel is, for small α, $\beta_\infty \approx 3/16\,\alpha^2$ (Eq. 3.41) *regardless* of the funnel temperature, it is

apparent that an isothermal funnel of finite extent is far superior as a means of radiatively accelerating material to relativistic speeds than its infinite analogue.

For small funnel opening angles the dimensionless time taken by the bullet to attain 99.5% of the terminal speed is insensitive to the parameter X_{ad} and the ratio T_2/T_1 (Figs. 4.16a,d and Table. 4.2). In particular, for a funnel semi-angle of 0.5° and a temperature ratio $T_2/T_1 = 0$ the dimensionless attainment time for a terminal speed $\sim$ 0.26c is approximately 2.3×10^4 units. For an accretion disc radius of 10^{10} m this is, by Eq. (4.59a), equivalent to a period of about one week. This somewhat lengthy timescale is a direct consequence of the bullet being rapidly accelerated only in the latter stages of its motion through the funnel. One would, therefore, expect a bullet released at a considerable fraction of the funnel height above the apex to have a much shorter acceleration time-scale. The attainment distance, again for this specific case, is approximately $1.3R_{ad}$. This is certainly close to the funnel mouth and is of the order of the acceleration region in SS433. However, the physical legitimacy of such an isothermal configuration has to be questioned since the temperature at the surface of a thick accretion disc will undoubtably be much less than at the centre.

In the cursory treatment of the problem described above I circumvented consideration of finite size effects by assuming the bullet to be small and have neglected the effect of gravity. This approach may not be satisfactory for massive bullets depending on their density. I shall address each of these effects below starting first with finite size effects.

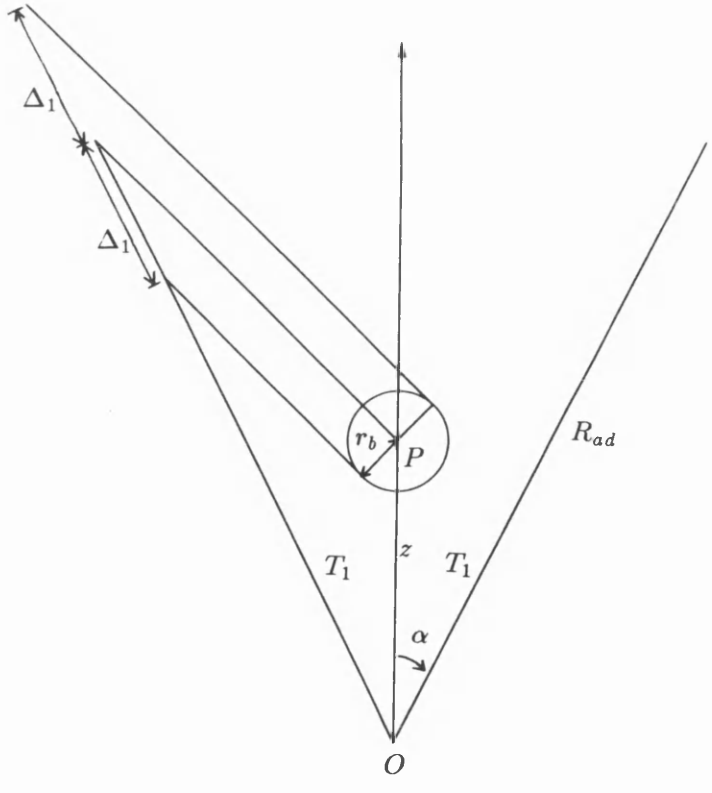

Fig. 4.17. Let the bullet (assumed for simplicity to be at rest) be located on the axis of the finite, isothermal funnel of slant height R_{ad} and semi-angle α with its centre, P, at a height z above the apex. Vectors which graze the surface of the bullet and which are parallel to the raypath vector which intersects both the funnel limb and the bullet centre intersect the (would be) funnel at a distance Δ_1 from the funnel limb.

The geometry to be considered is illustrated in Fig. 4.17. I have, for simplicity, assumed that the bullet is at rest with respect to the accretion disc. For the equation of motion to be a good approximation the length Δ_1 must be substantially less than the accretion disc radius. By application of the sine rule it is a simple matter to show that

$$\Delta_1 = \frac{\sqrt{\left(\frac{1}{z_d} - \cos\alpha\right)^2 + \sin^2\alpha}}{\sin\alpha} r_b \ . \tag{4.63}$$

A graphical representation of this equation for $\alpha = 0.01$ rads is shown in Fig. 4.18. The trough centred on $z_d = 1$ indicates the region where the approximation is most accurate. If the bullet is assumed to have a near minimum radius such that $r_{b_d} \sim 10^{-5} \mathrm{m}_{\circ 21}^{\frac{1}{3}}$ then the dimensionless distance $\Delta_{1_d} \leq 10^{-2}$ for $z_d \geq 0.1$. Finite size effects are, therefore, minimal for dimensionless heights above the funnel apex greater than ~ 0.1 and the equation of motion given by Eq. (4.58) can be regarded as a good approximation in this regime.

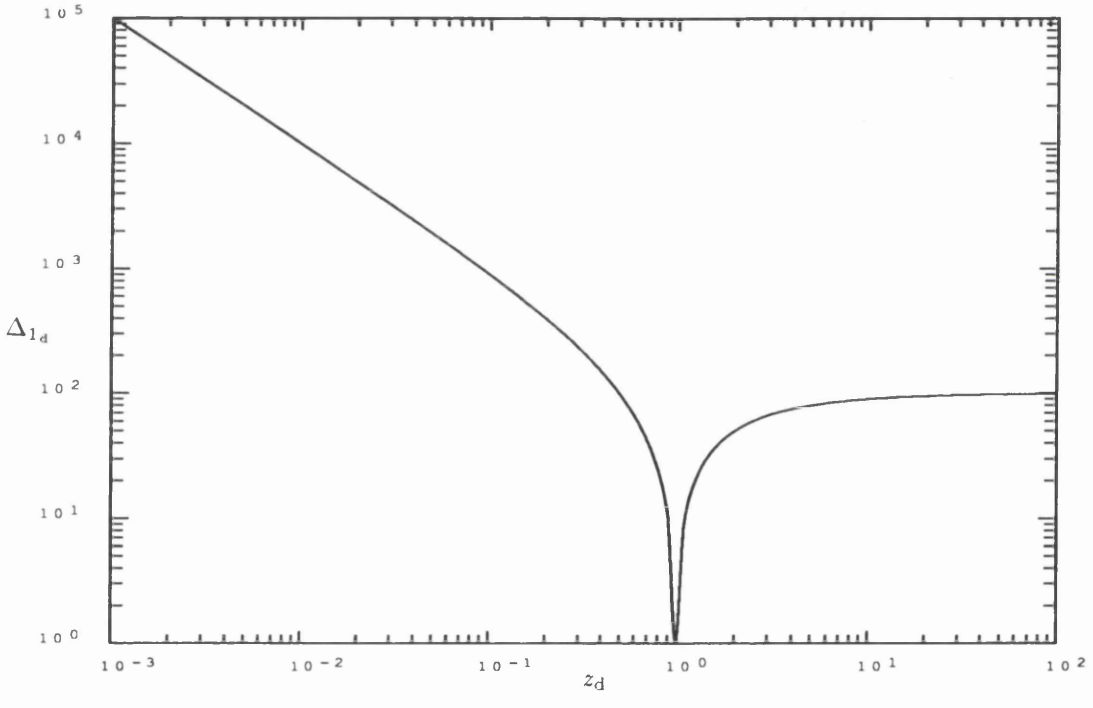

Fig. 4.18. A plot of $\Delta_{1_d} \equiv \Delta_1 / r_b$, given by Eq. (4.63) versus the dimensionless height, z_{o_d}, of the bullet centre above the funnel apex.

For radiation pressure to be capable of driving a massive bullet away from the compact object located at the funnel apex the radiative acceleration experienced by the bullet must exceed the inward acceleration due to gravity. For funnels with small opening angles this may, by Eq. (4.61), be expressed approximately as

$$z_d \geq \frac{\sqrt{Z_b}}{1+\sqrt{Z_b}} \qquad \text{where} \qquad Z_b \approx 2.2 \times 10^{-2} (M_\star / M_\odot)\, \mathrm{m}_\circ^{\frac{1}{3}} R_{ad_{10}}^{-2} T_{1_8}^{-4} \alpha_{-2}^{-2} \tag{4.64a,b}$$

and use has been made of the expression for the minimum bullet radius (Eq. 3.14) in deriving Eq. (4.64*b*). Hence, for a funnel temperature of 10^8 K radiative acceleration is possible for

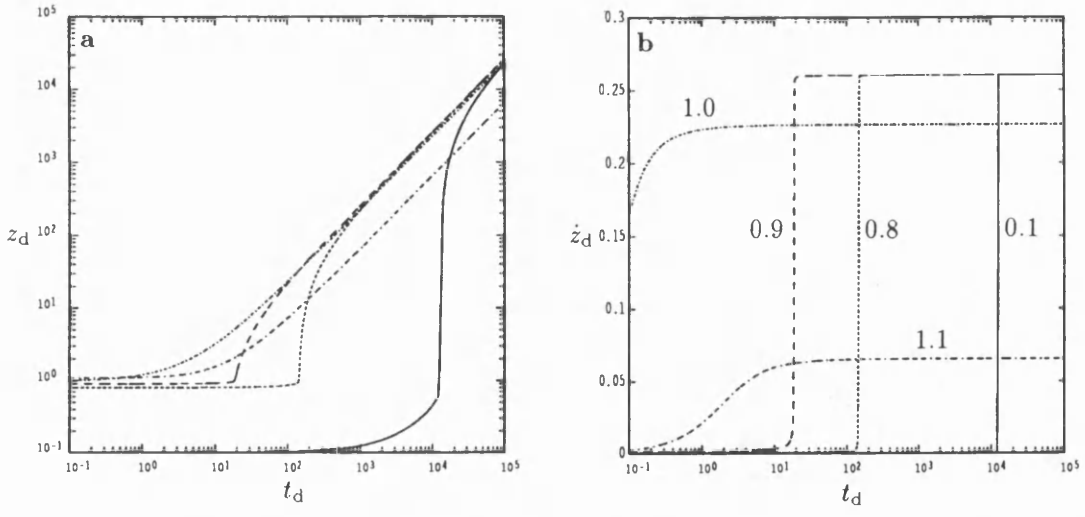

Figs. 4.19a,b. Numerical solutions to Eq. (4.58) for axial motion within and above a finite, isothermal accretion funnel of semi-angle 0.01 radians with the ratio $T_2/T_1=0$ and the parameter $X_{ad}=2.36$ for the values of the initial dimensionless starting height, z_{o_d}, indicated in **b**. In **a** the dimensionless distance z_d is plotted as a function of the dimensionless time t_d whilst in **b** the dimensionless speed of the bullet, $\dot{z}_d$, is plotted as a function of t_d.

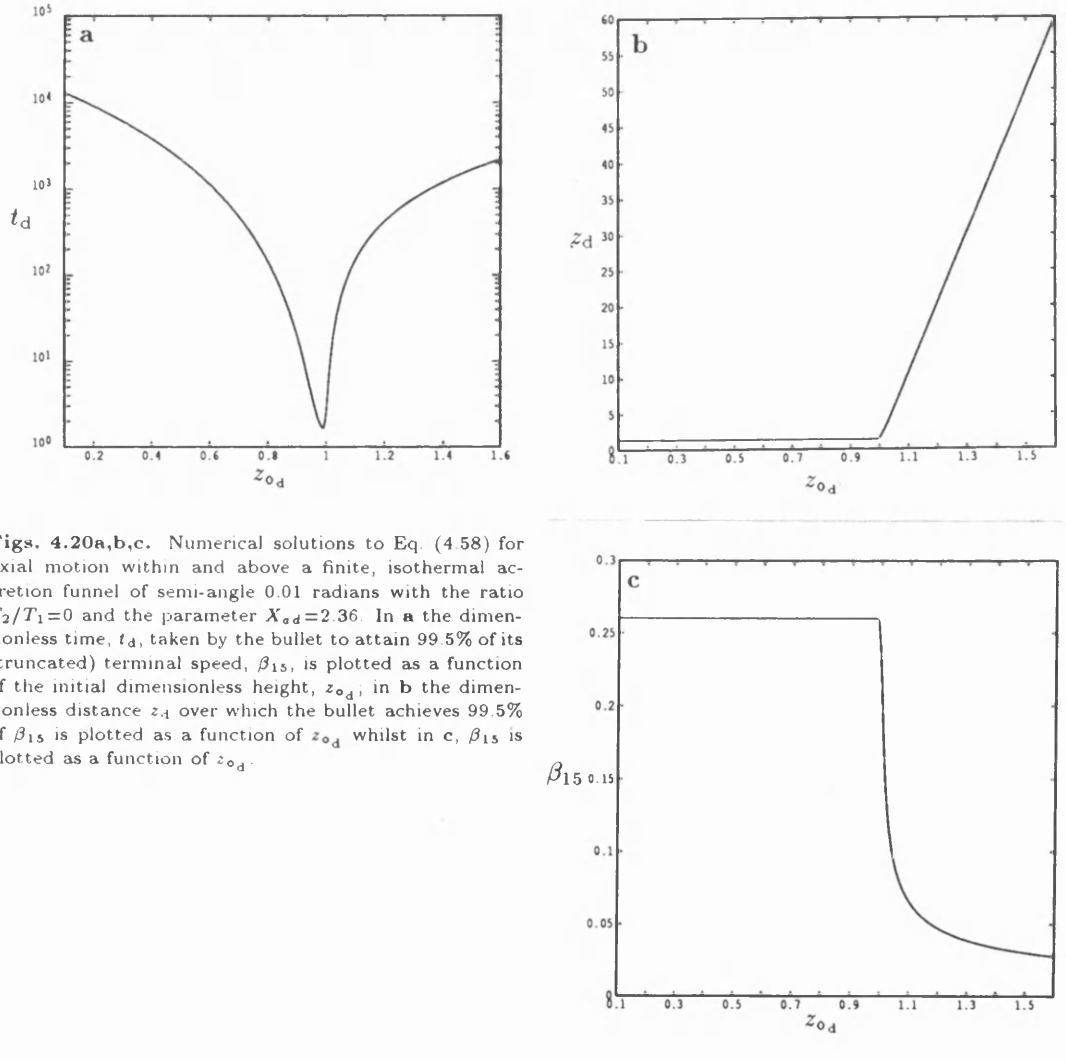

Figs. 4.20a,b,c. Numerical solutions to Eq. (4.58) for axial motion within and above a finite, isothermal accretion funnel of semi-angle 0.01 radians with the ratio $T_2/T_1=0$ and the parameter $X_{ad}=2.36$. In **a** the dimensionless time, t_d, taken by the bullet to attain 99.5% of its (truncated) terminal speed, β_{15}, is plotted as a function of the initial dimensionless height, z_{o_d}; in **b** the dimensionless distance z_d over which the bullet achieves 99.5% of β_{15} is plotted as a function of z_{o_d} whilst in **c**, β_{15} is plotted as a function of z_{o_d}.

dimensionless heights greater than ~ 0.13 whilst for $T_1 = 8 \times 10^8\,\mathrm{K}$, z_d needs be greater than about 2.3×10^{-3} units. These crude criteria, in conjunction with those above deduced from consideration of finite size effects, imply that radiative acceleration is viable and that Eq. (4.58) is a good approximation to the true equation of motion for a massive bullet of radius $r_b \sim 10^{-2}\mathrm{m}_6^{\frac{1}{3}}$ metres and at a dimensionless distance from the funnel apex greater than about 0.1 units.

In the preceding analysis it was found that the contribution made by radiation emanating from the exterior surface of an accretion disc with model parameters suitable for SS433 in enhancing the bullet terminal speed is negligible. This well justified approximation is inherent in what follows. For a funnel of semi-angle 0.01 radians the minimum value of the parameter X_{ad} necessary for the attainment of a terminal speed $\beta_{15} = 0.2602$ is $X_{ad} = 2.36$. For an accretion disc of radius $\sim 10^{10}$ metres and a bullet of minimum cross-section and mass $\sim 10^{21}\,\mathrm{kg}$ this represents a funnel temperature of $\sim 2.4 \times 10^8\,\mathrm{K}$. The dimensionless distance and speed of a bullet radiatively driven along the symmetry axis of a finite, isothermal funnel of semi-angle 0.01 radians with $X_{ad} = 2.36$ are plotted as functions of the dimensionless time for various initial dimensionless heights in Figs. 4.19a,b. These figures indicate, as was suggested earlier, that the time taken by the bullet to attain its terminal speed decreases as the release point approaches the funnel mouth, though for initial release heights immediately below the funnel mouth and beyond the terminal speed falls off dramatically. These points are additionally illustrated by Figs. 4.20a,b and c. The minimum attainment time for a terminal speed of 0.2602c is 1.9 units and occurs for $z_{0_d} = 0.98$ (Fig. 4.20a). For a disc of radius 10^{10} metres this corresponds to a physical attainment time of about 63 seconds. The distance from the funnel apex by which 99.5% of the terminal speed is attained is (Fig. 4.20b) $1.37R_{ad}$. This attainment distance is, like the terminal speed (Fig. 4.20c), very insensitive to the bullet release height for all release heights from *just below* the funnel mouth to much deeper within the funnel. Although these results are pleasingly in keeping with the observations of SS433 it is unreasonable to expect that the accretion funnels in SS433 can be accurately modelled as finite, isothermal radiators. A more realistic temperature profile is considered in §4.6.2 below.

§4.6.2 The Polytropic Funnel

Current accretion disc theory is incomplete and without an archetypal model. However, some of the important properties common to most thick accretion disc models are exemplified by the simple Newtonian equilibrium model in which the gravitational attraction of the central compact object is balanced by a combination of gas pressure, radiation pressure and centripetal force. I will discuss this model briefly below.

The principal simplifications are the invocation of Newtonian dynamics and the assumption that the mass M of the compact object is much greater than the mass of the accretion disc. In the simplest possible case it is further assumed that the specific angular momentum $l = R^2\Omega$ (where R is the radial coordinate in cylindrical polars and Ω is the angular velocity) is constant

throughout the disc. The form of the accretion disc is prescribed by the equipotential surface for the given specific energy of the accreting material. These equipotentials are specified by the expression

$$\sin\theta = \frac{R_K^2}{2rR_K + Er^2} \tag{4.65}$$

(Frank, King and Raine, 1985) where r is the distance from the compact object, the polar angle $\theta = \sin^{-1}(R/r)$, R_K is the radius at which the Keplerian angular velocity Ω_K is such that $R_K^2\Omega_K = l$ and E is the specific energy of the accretion disc material in units of the binding energy, $E_K = GM/2R_K$, of matter in a Keplerian orbit of radius R_K. For the disc to remain bound to the compact object the specific energy E must lie in the range $-1 \leq E < 0$; the most tightly bound configuration occurs for $E = -1$ when the disc becomes a ring of radius R_K whilst the most loosely bound configurations occur as $E \rightarrow 0$. The minimum polar angle, α, can readily be deduced, by differentiating Eq. (4.65) with respect to r, to occur at $r = -R_K/E$. Substituting this expression back into Eq. (4.65) then gives

$$\sin^2\alpha = -E\ . \tag{4.66}$$

Thus, for the formation of a funnel of semi-angle 1° the specific energy of the accreting‡ material needs to be $E \approx -3.05 \times 10^{-4}$. Such a disc is depicted in Fig. 4.21 where the conical nature of accretion funnels is clearly evidenced. It is apparent from Eq. (4.66) that narrow funnels are formed when the accreting material is loosely bound to the central compact object. A direct consequence of this fact is that material near the funnel walls can readily be driven outwards by radiation pressure producing well collimated jets. The temperature of the funnel walls, however, remains completly unspecified by this model.

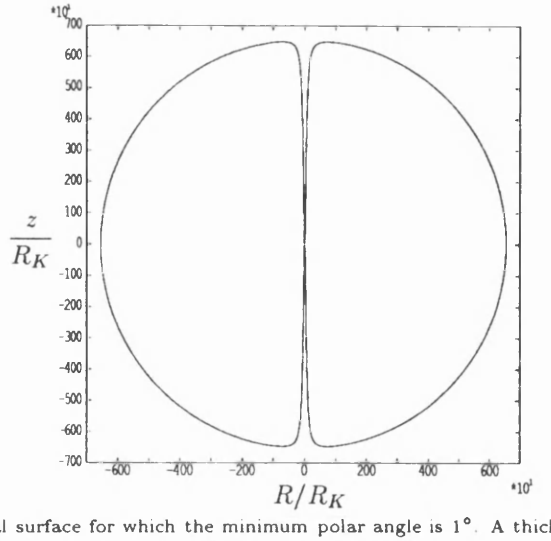

Fig. 4.21. The equipotential surface for which the minimum polar angle is 1°. A thick accretion disc of this general geometrical form is believed to be present in the SS433 system. The ordinate corresponds to the height, z, of the disc in units of the Keplerian radius, R_K, whilst the abscissa denotes the radius, R, of the disc in units of R_K.

‡ Strictly speaking there is no accretion in this nor any other equilibrium model since the disc material is assumed to have a null poloidal velocity component.

To overcome this problem I will assume that the pressure-density relationship within the accretion disc can be expressed by a polytropic equation of state. Such an equation of state is applicable to a gaseous sphere in hydrostatic equilibrium and has physical legitimacy as the generalisation of the observed behaviour of an ideal gas undergoing an adiabatic change. Since the diameter to thickness ratio of the accretion disc in SS433 has been variously estimated to be $\sim$ 1.5 (Anderson, Margon and Grandi, 1983a) and less than 1.3 (Wagner, 1983) and the funnel semi-angle is probably less than 1°, the assumption that the disc is spherical is well justified. The assumption that the disc is in equilibrium is, on the other hand, valid only if the poloidal velocity component of the accreting material is much less than the toroidal velocity component. Adoption of the polytropic equation of state also involves the assumption that the contribution made by the centripetal force to the support of the disc is negligible. Rather than merely quoting the relevant results obtained from the assumption of a polytropic equation of state I will provide an outline of their derivation below.

Define the quantity β_p such that the gas pressure and radiation pressure are given respectively by

$$P_g = \frac{\rho k T}{\mu_m m_h} \equiv \beta_p P_t \qquad \text{and} \qquad P_r = \frac{\mathrm{a}T^4}{3} \equiv (1-\beta_p)\, P_t \tag{4.67a,b}$$

where P_t is the total pressure given by the sum of the radiation and gas pressures. Solving for T by eliminating P_t between Eqs. (4.67a,b) yields

$$T = \left[\frac{3(1-\beta_p)k}{\mu_m m_h \mathrm{a} \beta_p}\right]^{\frac{1}{3}} \rho^{\frac{1}{3}} \tag{4.68}$$

which when substituted back into Eq. (4.67b) gives

$$P_t = \left[\left(\frac{k}{\mu_m m_h}\right)^4 \frac{3}{\mathrm{a}} \frac{1-\beta_p}{\beta_p^4}\right]^{\frac{1}{3}} \rho^{\frac{4}{3}} . \tag{4.69}$$

If the gas pressure is a constant fraction of the total pressure throughout the disc, and by definition therefore β_p a constant, Eq. (4.69) can be more simply expressed as

$$P_t = K\rho^{\frac{4}{3}} \qquad \text{where} \qquad K = \left[\left(\frac{k}{\mu_m m_h}\right)^4 \frac{3}{\mathrm{a}} \frac{1-\beta_p}{\beta_p^4}\right]^{\frac{1}{3}} \tag{4.70a,b}$$

is a constant of proportionality. This equation corresponds to a polytrope of polytropic exponent $\gamma_p = 4/3$ or equivalently of polytropic index $n_p = 3$. In general the pressure-density relationship has the form

$$P_t(r) = K\rho(r)^{\gamma_p} \qquad \text{with} \qquad \gamma_p = \frac{n_p + 1}{n_p} \tag{4.71a,b}$$

Any spherical, gaseous body in hydrostatic equilibrium for which the pressure and density have the radial dependence expressed by Eq. (4.71*a*) is a polytrope. A polytrope of index $n_p = 3/2$ conventionally represents a star in convective equilibrium for which radiation pressure is unimportant whilst a polytrope of index of $n_p = 3$ normally corresponds to a star in radiative equilibrium in which energy is transported by radiation rather than by convection. The latter polytrope is commonly referred to as the standard model and will be discussed further below. For completeness I will just note that a polytrope of index $n_p = 3$ can also represent a relativistic, degenerate electron gas and such a polytropic model therefore presents a means of exploring the internal sructure of exotic entities such as white dwarfs.

By analogy with the deduction of the general polytropic expression for the pressure-density relationship (Eq. 4.70*a*) from Eq. (4.69) it is obvious from Eq. (4.68) that the general polytropic expression for the temperature-density relationship is

$$T(r) = J\rho(r)^{\frac{1}{n_p}} \qquad \text{where} \qquad J = \left[\frac{k}{\mu_m m_h}\frac{3}{\mathrm{a}}\frac{1-\beta_p}{\beta_p}\right]^{\frac{1}{3}} . \tag{4.72a,b}$$

Hence, to determine the run of temperature with radius, the run of density with radius must first be known.

Since the disc is assumed to be spherical and in hydrostatic equilibrium the relationship between the pressure and density at every location within it is specified by the equation

$$\frac{\mathrm{d}P_t}{\mathrm{d}r} = -\frac{GM_{ad}(r)\rho(r)}{r^2} \tag{4.73}$$

where $M_{ad}(r)$ is the mass within a radius r and has the differential form

$$\frac{\mathrm{d}M_{ad}(r)}{\mathrm{d}r} = 4\pi r^2\rho(r) . \tag{4.74}$$

The polytropic equation of state (Eq. 4.71*a*) specifies the relationship between the pressure and density and, therefore, by eliminating P_t between Eqs. (4.71*a*) and (4.73) the run of density with radius can be obtained. The resulting expression has the form

$$\frac{\mathrm{d}}{\mathrm{d}r}\left(\frac{Kr^2(n_p+1)}{n_p\rho^{(n_p-1)/n_p}}\frac{\mathrm{d}\rho}{\mathrm{d}r}\right) = -4\pi \mathrm{G}r^2\rho \tag{4.75}$$

and represents one form of the Lane-Emden equation. The boundary conditions for this non-linear second order differential equation are $\rho(0) = \rho_c$ and $\rho(R_{ad}) = 0$; both the parameter $K(\beta_p)$ and the polytropic index n_p are free parameters. Equation (4.75) is best solved by transforming to the Emden variables, details of which can be found in standard texts such as Clayton (1968), Collins (1989) and, for a more complete treatment, Chandrasekhar (1939). By the introduction of these variables the normalised run of temperature with radius, $\rho(r)/\rho_c$, can be derived from Eq. (4.75) which, when substituted into Eq. (4.72*a*) yields $T(r)/T_c$. The run

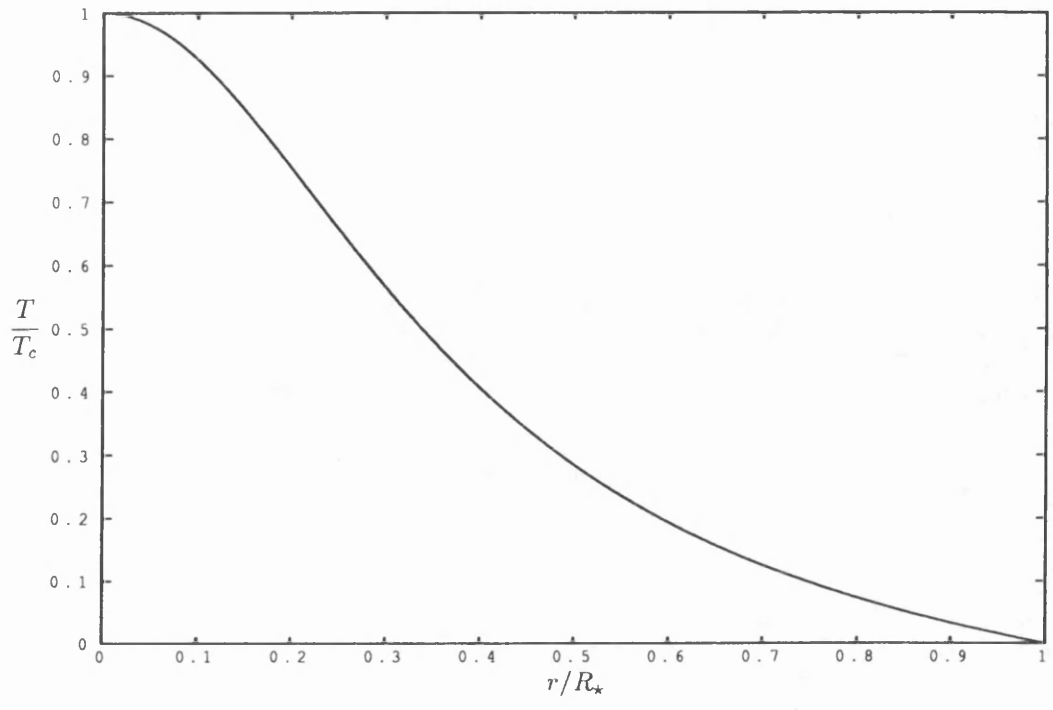

Fig. 4.22. The normalised temperature, T/T_c, versus normalised radius, $r/R_\star$, for the standard model.

of normalised temperature with dimensionless radius for the standard model is illustrated in Fig. 4.22. It should be noted that the predicted surface temperature is 0 K. This follows directly from the imposition of the boundary condition $\rho(R_{ad}) = 0$. Unfortunately analytic solutions to the Lane-Emden equation exist only for $n_p = 0, 1$ and 5; for the remainder, which includes the standard model, the equation has to be solved numerically. For the standard model it can further be shown that the radius, mass and central temperature of the accretion disc are given respectively by

$$R_{ad} = 6.89685 \sqrt{\frac{K}{\pi \mathrm{G}}}\, \rho_c^{-\frac{1}{3}} = 7.73821 \times 10^{10}\, \mu_m^{-\frac{2}{3}} \left(\frac{1-\beta_p}{\beta_p^4}\right)^{\frac{1}{6}} \rho_c^{-\frac{1}{3}}\,, \tag{4.76a}$$

$$M_{ad} = 8.07296\pi \left(\frac{K}{\pi \mathrm{G}}\right)^{\frac{3}{2}} = 18.01011\, \frac{\sqrt{1-\beta_p}}{\mu_m^2 \beta_p^2}\, M_\odot \tag{4.76b}$$

and

$$T_c = J \rho_c^{\frac{1}{3}} = 3.19837 \times 10^6 \left(\frac{1-\beta_p}{\mu_m \beta_p}\, \rho_c\right)^{\frac{1}{3}} \tag{4.76c}$$

By Eqs. (4.76a, b) the central density, ρ_c, may be expressed as

$$\rho_c = 25.72795\, \frac{1}{R_{ad_{10}}^3}\, \frac{M_{ad}}{M_\odot} \tag{4.77}$$

which when substituted into Eq. (4.76c) yields

$$T_{c_6} = 1.37444\, \beta_p\, \mu_m\, \frac{1}{R_{ad_{10}}}\, \frac{M_{ad}}{M_\odot}\,. \tag{4.78}$$

Thus, if the two parameters M_{ad} and the mean molecular weight, μ_m, are specified then the ratio of the gas pressure to total pressure, β_p, is prescribed by Eq. (4.76*b*) and the central temperature, after selection of the disc radius R_{ad}, is subsequently defined by Eq. (4.78). Since $T(r)/T_c$ is also known, the temperature on the funnel surface at any distance from the apex is then specified.

A plot of T_c as a function of the disc mass for a disc of radius 10^{10} m and selected values of the mean molecular weight of the accreting material is illustrated in Fig. 4.23. Clearly central temperatures of $\sim 10^8$ K are not possible unless the disc mass is implausibly large. However, on account of the inverse proportionality of the disc radius to the central temperature (Eq. 4.78), a central temperature in excess of 10^8 K is possible for a disc of radius 10^9 m for all values of the mean molecular weight if the disc mass is greater than approximately $15M_\odot$.

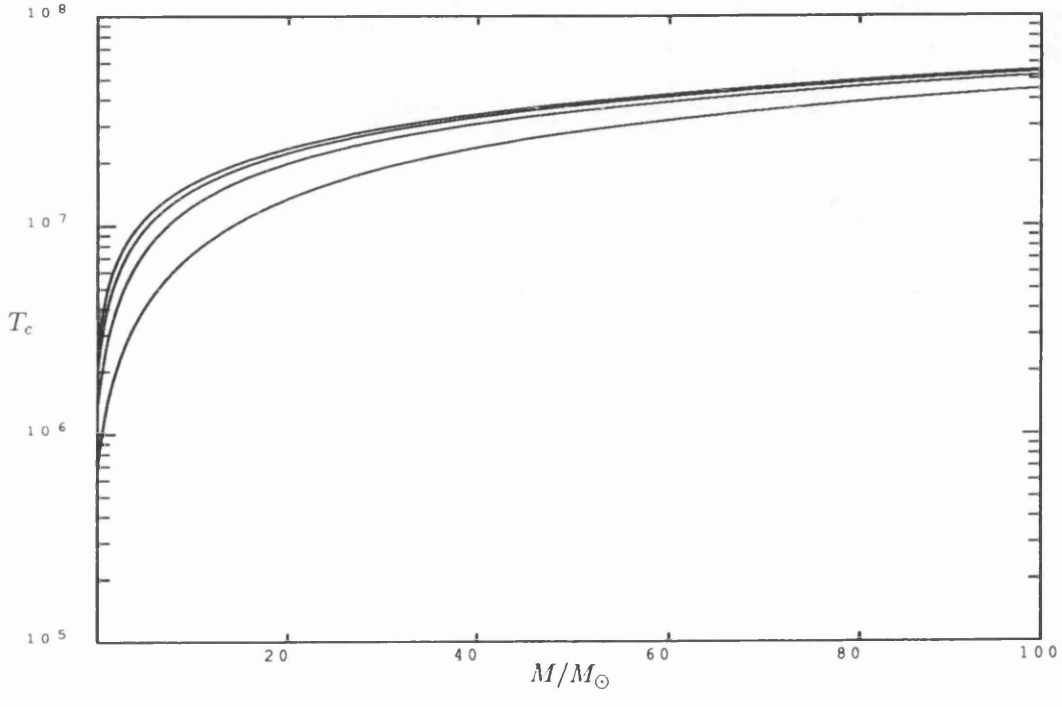

Fig. 4.23. The temperature, T_c (in Kelvin) predicted by the standard model to occur at the disc centre, versus the disc mass, M_{ad}, in solar mass units for selected values of the mean molecular weight, μ_m. The selected values of μ_m are, from top to bottom, 2, 3/2, 1 and 1/2.

Since the surface temperature of the accretion disc is, according to the polytropic model, 0 K the bullets are driven only by radiation originating from within the accretion funnel. It was found in §4.6.1 that the contribution made by radiation emanating from the external surface of the disc in enhancing the terminal speed of the bullets is significant only if the temperature of the disc surface is comparable to that within the funnel. In SS433 this is most certainly not the case and a model disc surface temperature of 0 K constitutes a valid approximation.

I shall now proceed to derive the equation of motion: Assume that the walls of the funnel radiate as a blackbody for which the temperature profile along the funnel surface be given by

$$T(r) = T_c f(r) \tag{4.79}$$

where r is the radial distance from the funnel apex, T_c is given by Eq. (4.78) and $f(r)$ is the numerical solution to the Lane-Emden equation for $n_p = 3$. By Eq. (4.13) the temperature profile can then be expressed as

$$T(\theta, z; \alpha) = T_c g(\theta, z; \alpha) \qquad \text{where} \qquad g(\theta, z; \alpha) = f(r(\theta, z; \alpha)) \; . \tag{4.80a,b}$$

By Eqs. (3.4) and (3.5) the axial equation of motion is then given by

$$\dot{\beta}_z = 2\frac{\sigma D}{\mathrm{m_o c^2}} T_c^4 \frac{1}{\gamma} \int_0^{\theta_1(z;\alpha)} [g(\theta, z; \alpha)]^4 (\cos\theta - \beta_z)(1 - \beta_z \cos\theta) \sin\theta \, \mathrm{d}\theta \tag{4.81}$$

where $\theta_1(z)$ is given by Eqs. (4.56a,b). With reference to Eqs. (4.59a,b,c,d) the equation of motion can further be expressed as

$$\ddot{z}_\mathrm{d} = 2X_{ad}(1 - \dot{z}_\mathrm{d}^2)^{\frac{1}{2}} \int_{\mu_1(z_\mathrm{d};\alpha)}^1 [g(\mu, z_\mathrm{d}; \alpha)]^4 (\mu - \dot{z}_\mathrm{d})(1 - \dot{z}_\mathrm{d}\mu) \, \mathrm{d}\mu \tag{4.82}$$

where, of course, the temperature T_1 in Eq. (4.59d) is now replaced by T_c. The ratio $\ddot{z}_\mathrm{d}/X_{ad}$ for a bullet at rest within a finite, standard model polytropic funnel of semi-angle 0.5° and 1° is shown in Fig. 4.24.

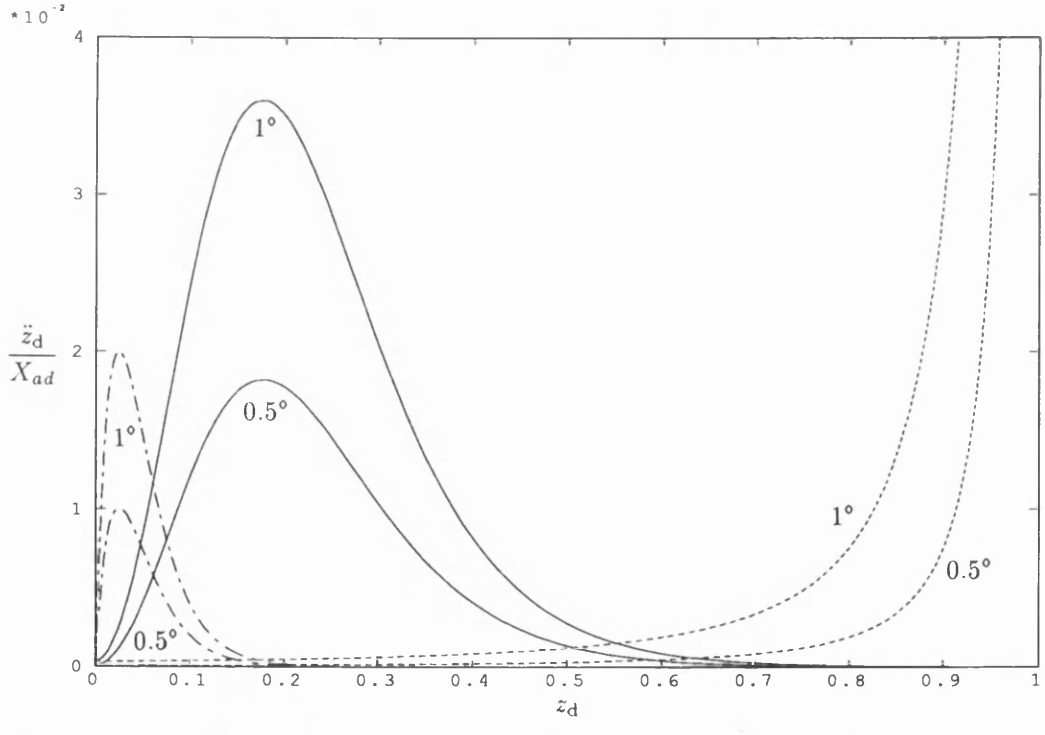

Fig. 4.24. The ratio $\ddot{z}_\mathrm{d}/X_{ad}$ versus z_d for a bullet at rest within a finite, standard model polytropic funnel of semi-angle 0.5° and 1° (full lines). For ease of comparison the ratio $\ddot{z}_\mathrm{d}/X_{ad}$ for a stationary bullet within a finite, isothermal funnel (dashed lines) plus the data depicted in Fig. 4.4b for the exponentially decaying temperature profile (dashed-dotted lines) are, by means of the approximation $\ddot{z}_\mathrm{d} \approx 10 z_\mathrm{d}$, also plotted to the same scale. It should be recalled that the maxima for the plots representing the finite, isothermal funnel have a magnitude of 1 unit.

Before proceeding to integrate the equation of motion (Eq. 4.82) I will first determine the domain in which the bullet release height must lie if acceleration due to radiation pressure is to exceed that due to gravitational attraction.

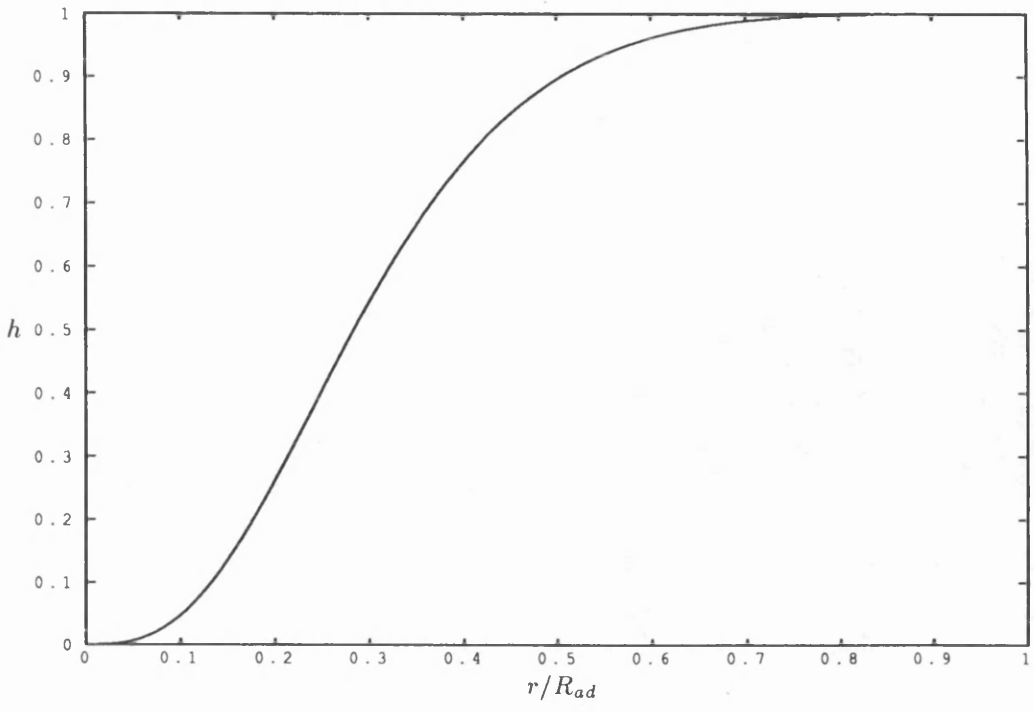

Fig. 4.25. The function h versus the radius, r, in units of the accretion disc radius R_{ad}.

For the standard model only, the mass of accretion disc material within a radius r is independent of the central density and can be simply expressed as

$$M_{ad}(r) = h(r)\, M_{ad} \ . \tag{4.83}$$

The function $h(r)$ is obtained from a numerical solution of the Lane-Emden equation and is displayed in Fig. 4.25. An assumption inherent to Eq. (4.83) is that the mass which can be regarded as 'missing' on account of the presence of the accretion funnels is negligible. This is certainly true for narrow accretion funnels with which I am concerned here: the solid angle occupied by each accretion funnel is approximately $\pi\alpha^2$ and hence the 'missing' mass attributable to each funnel is about $\alpha^2 M_{ad}/4$ which, for a funnel semi-angle of 1° represents $\sim 1.5\times10^{-4} M_{ad}$ for the funnel pair. The acceleration due to Newtonian gravity is, therefore, well expressed as

$$a_g = h(r)\frac{GM_{ad}}{r^2} = 1.32706\, h(z_d)\frac{M_{ad}/M_\odot}{R^2_{ad_{10}} z^2_{\rm d}} \ . \tag{4.84}$$

Consider now the acceleration due to radiation pressure. Let the bullet radius, for a given starting height, be a fraction x of the maximum possible such that the bullet cross-section is

$$D = \pi(xz\sin\alpha)^2 \qquad \text{where} \qquad x < 0 \leq 1 \ . \tag{4.85}$$

Then, by Eqs. (4.78) and (4.82), the radiative acceleration is given by

$$a_r = 1.29173 \times 10^5 x^2 R_{ad_{10}}^{-2} z_d^2 \alpha^2 m_{o_{21}}^{-1} (\beta_p \mu_m)^4 \left(\frac{M_{ad}}{M_\odot}\right)^4 \int_{\mu_1(z_d;\alpha)}^{1} [g(\mu, z_d; \alpha)]^4 \, \mu \, d\mu \qquad (4.86)$$

where α, assumed small, is in degrees. For the bullets to be driven outwards along the funnel axis the obvious condition $a_r > a_g$ must be satisfied. By Eqs. (4.84) and (4.86) this can alternatively be expressed as

$$9.73374 \times 10^4 [h(z_d)]^{-1} x^2 z_d^4 \alpha^2 m_{o_{21}}^{-1} (\beta_p \mu_m)^4 \left(\frac{M_{ad}}{M_\odot}\right)^3 \int_{\mu_1(z_d;\alpha)}^{1} [g(\mu, z_d; \alpha)]^4 \, \mu \, d\mu > 1 \, . \qquad (4.87)$$

In Fig. 4.26 the left-hand side of Eq. (4.87) is shown as a function of z_d from which it is apparent that there exists, for each value of $M_{ad}/M_\odot$, a distinct range over which radiative acceleration is viable; for $M_{ad} \geq 15 M_\odot$ the minimum release height needs to be greater than $\sim 10^{-2} z_d$.

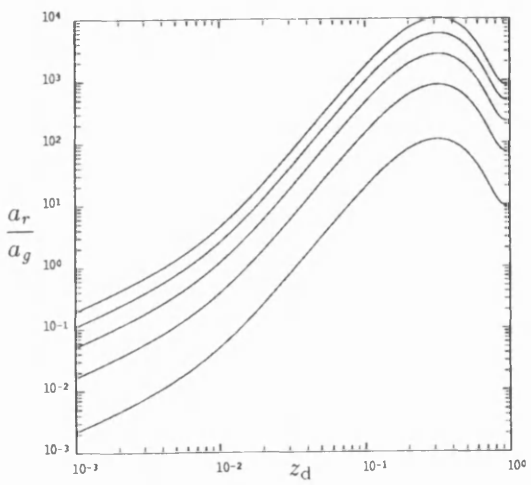

Fig. 4.26. The ratio a_r/a_g given by the left-hand side of Eq. (4.87) versus the dimensionless height, z_d, for the mean molecular weight μ_m=0.5, α=1° and the parameter x=1 for selected values of $M_{ad}/M_\odot$ which, from top to bottom as displayed, are 25, 20, 15, 10 and 5. Since the parameter x has been chosen to equal 1, the bullet cross-section is the greatest permissible and consequently the values of the ratio a_r/a_g shown represent an upper bound.

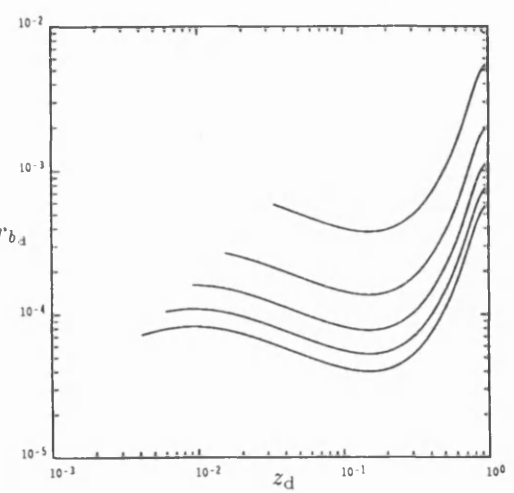

Fig. 4.27. The minimum, dimensionless bullet radius, r_{b_d}, for which radiative acceleration is viable versus the dimensionless release height for selected values of the accretion disc mass. The mean molecular weight μ_m=0.5 whilst the selected values of $M_{ad}/M_\odot$ are, from top to bottom as displayed, 5, 10, 15, 20 and 25.

By determining the value of the parameter x, the remaining parameters remaining fixed, for which the left-hand side of Eq. (4.87) equals 1, it is possible to find the minimum value of the dimensionless bullet radius, for a given initial release height, for which ejection of the bullets is possible. This then permits the suitability of Eq. (4.82) as an approximation to the true, axial equation of motion to be determined. From Fig. 4.27 it can be seen that a dimensionless bullet radius of $\sim 10^{-3}$ units is sufficient to ensure ejection for all accretion disc masses in excess of $\sim 15 M_\odot$. Beyond the funnel mouth it is not important that r_{b_d} be such that $a_r > a_g$. To appreciate this point one need only perform a simple Newtonian energy calculation in which the radiative drive beyond the funnel mouth is assumed to be zero: it is simple to show that if

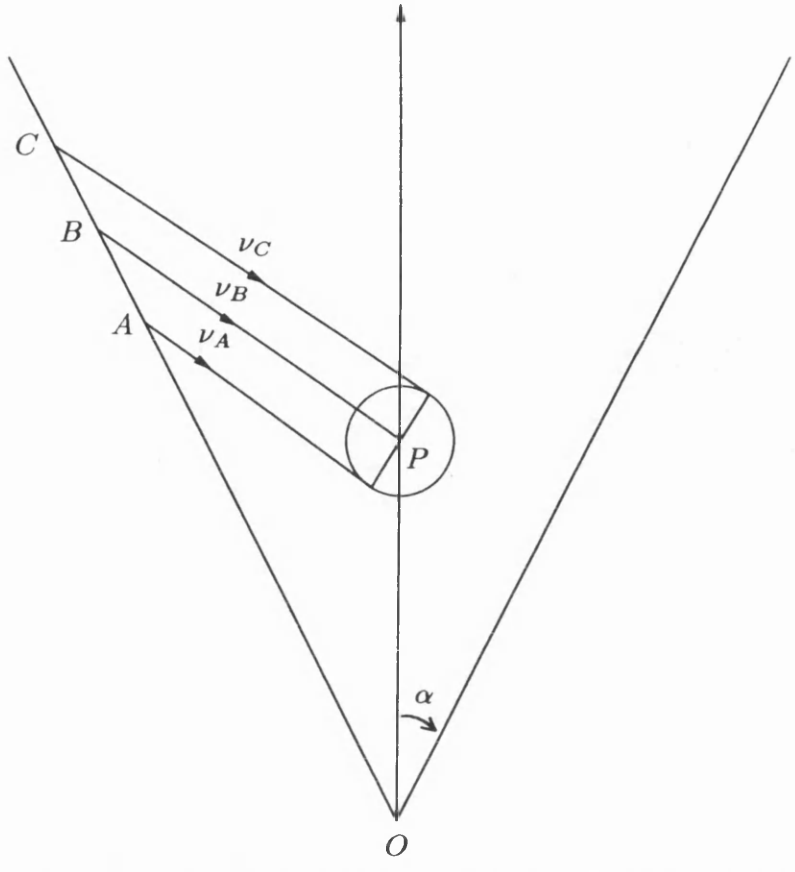

Fig. 4.28. Parallel vectors passing through the centre of the bullet at P and which graze the bullet's surface intersect the funnel wall at the points B and A, C respectively. At A, B and C the funnel wall is at a black body temperature T_A, T_B and T_C respectively.

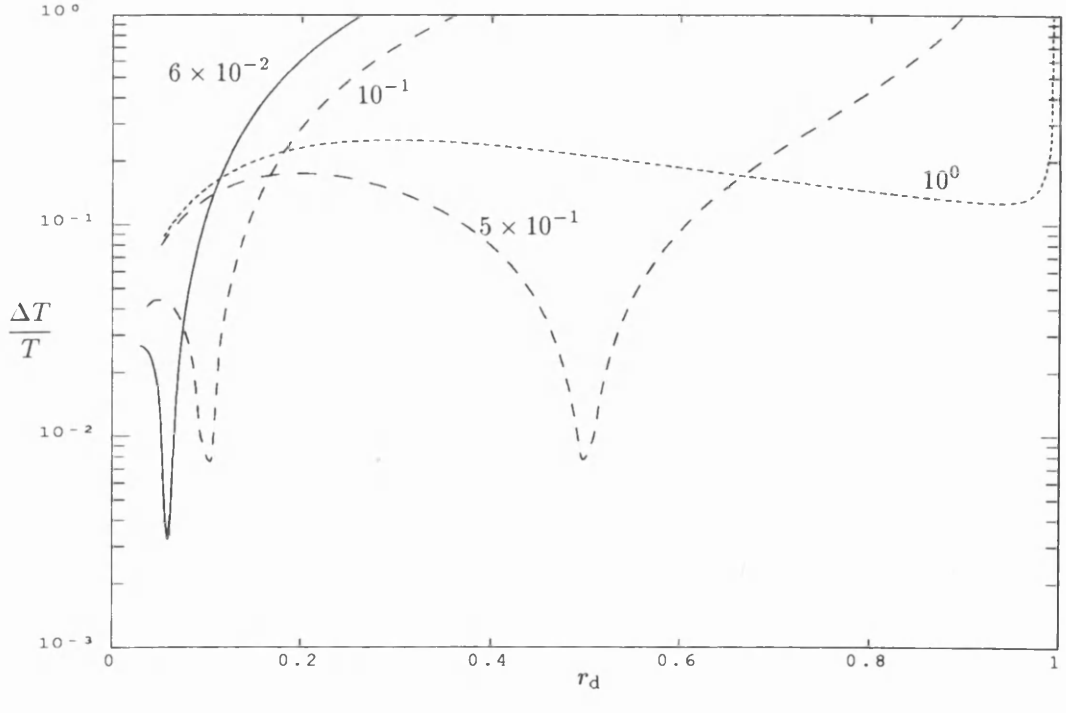

Fig. 4.29. The ratio $\Delta T/T$ versus the dimensionless distance, r_d, of the point of intersection denoted as B in Fig. 4.28 above. The funnel semi-angle is 1° and the bullet has a dimensionless radius $r_{b_d} = 10^{-3}$. The labeled values represent the dimensionless height of the bullet centre above the funnel apex. The bullet is located on the axis of symmetry of the funnel and, for simplicity, is assumed to be at rest with respect to it.

the bullet exit speed is β_{ex} then

$$\Delta\beta \approx 1.48 \times 10^{-7} \frac{M_{ad}/M_{\odot}}{\beta_{ex} R_{ad_{10}}} \qquad \text{where} \qquad \Delta\beta = \beta_{ex} - \beta_{\infty} \; . \tag{4.88}$$

Thus, for example, even for a very massive, compact accretion disc of mass $M_{ad} = 25M_{\odot}$ and radius $R_{ad_{10}} = 0.1$ and an exit speed $\beta_{ex} = 0.2$, the reduction in the speed is only $\Delta\beta = 1.85 \times 10^{-4}$.

Let me now return to the question of the validity of Eq. (4.82) as a representation of the true equation of motion. I will, for expediency, assume that the bullet is at rest with respect to the funnel. Consider the geometry depicted in Fig. 4.28. The approximation adopted in the derivation of Eq. (4.82) is equivalent to assuming that the temperatures T_A, T_B, and T_C at the locations A, B and C on the funnel wall are the same. This will certainly not be so since the temperature predicted by the standard model (Fig. 4.22) is a monotonically decreasing function of r and therefore $T_A > T_B > T_C$. Evidently, for the approximation to be good the ratio $(T_A - T_C)/T_B \equiv \Delta T/T$ must be small. From inspection of Fig. 4.29 it can be seen that the approximation is best for those regions of the funnel closest to the bullet and poorest for regions at or near the funnel mouth. The latter behaviour occurs because at locations near the funnel mouth it is possible for $T_A \gg T_B, T_C$ even though $T_A, T_B, T_C \ll 1$. In the limiting case $T_A > 0$ whilst $T_B = T_C = 0$ and consequently $\Delta T/T \rightarrow \infty$. If the approximation is deemed to become poor when $\Delta T/T \sim 1$, then for initial release heights of $\sim 10^{-1}$, only the funnel surface up to a dimensionless distance of ~ 0.35 from the apex is represented accurately. This may seem to be a very poor approximation indeed but, if one recalls that the equation of motion (Eq. 4.82) is dependent on the fourth power of the temperature, and observes from Fig. 4.22 that at $r_{\rm d} \sim 0.35$, $(T/T_c)^4 \sim 0.5^4 \approx 6 \times 10^{-2}$ it can be appreciated that, on account of the relative importance of those regions where $\Delta T/T > 1$ during the bullets *initial* stages of motion, Eq. (4.82) represents a fair approximation to the true equation of motion. I have stressed the word initial since in the later stages of the bullet's motion when it is moving relativistically, aberrated, blue-shifted radiation from these same regions is of importance and acts to reduce the speed of the bullet. Fortunately though, when $r_{\rm d} \sim 1$ the ratio $\Delta T/T \sim 0.1$, except for those regions essentially on the funnel limb ($r_{\rm d} \approx 1$) where $\Delta T/T$ rises dramatically for the reasons already given above, and the approximation is again fair.

To summarise, Eq. (4.82) is a reasonable approximation to the equation of motion for a bullet with a dimensionless radius $r_{b_d} \sim 10^{-3}$ and improves as r_{b_d} decreases. There is, however, clearly scope for a more complete treatment of the problem which does not involve the assumption that $\Delta T/T = 0$ but I will consider this topic no further in the present work.

I shall now investigate the solutions to Eq. (4.82). In Fig. 4.30 the (truncated) terminal speed, β_{15}, is shown as a function of the parameter X_{ad} for motion within a funnel of semi-angle 1° and for selected initial dimensionless heights. The upper line, in fact, consists of the superposition of the data for $z_{0_{\rm d}} = 0.01$ and 0.1 from which it can immediately be concluded that the terminal speed is insensitive to the initial bullet height from $z_{0_{\rm d}} = 0.01$ to at least 0.1.

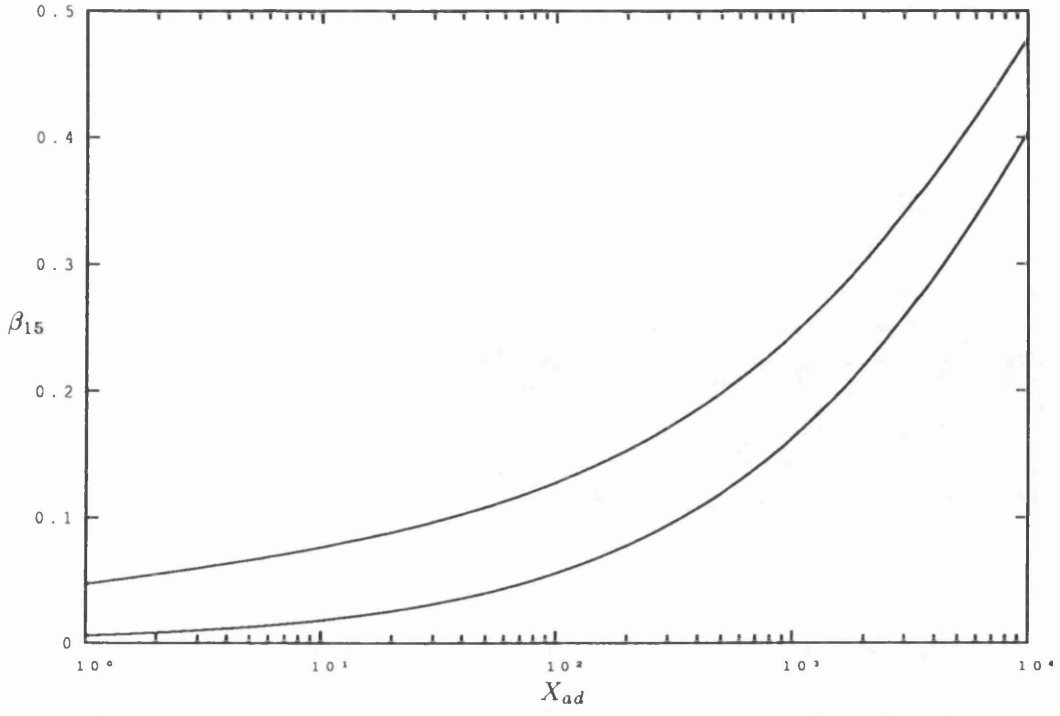

Fig. 4.30. The (truncated) terminal speed, β_{15}, versus the parameter X_{ad} for axial motion within a finite funnel of semi-angle 1° for which the run of temperature with radius is given by the standard model. The upper line consists of the superposition of the data for a bullet released at an initial, dimensionless height $z_{o_d}=0.01$ and 0.1 whilst the lower line represents a bullet for which $z_{o_d}=1$.

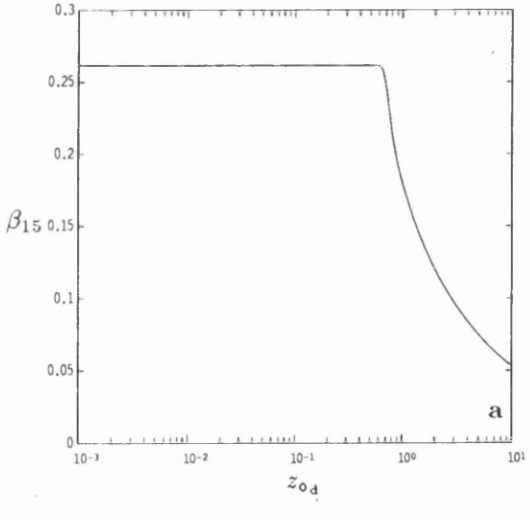

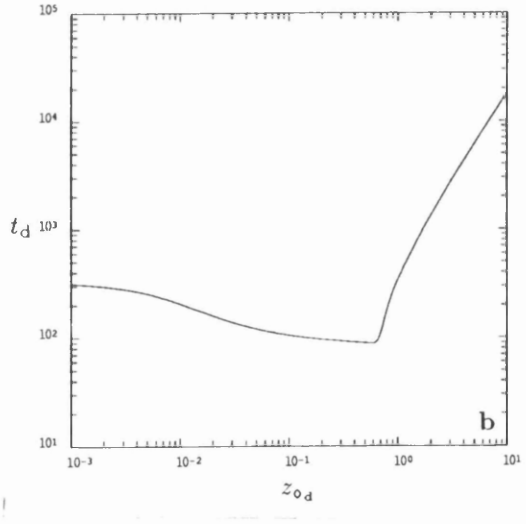

Figs. 4.31a,b,c. Numerical solutions to Eq. (4.82) for axial motion within a finite accretion funnel of semi-angle 1° for which with the run of temperature with radius is given by the standard model with the parameter $X_{ad}=1255$. In **a** the (truncated) terminal speed β_{15} is plotted as a function of the initial dimensionless height, z_{o_d}; in **b** the dimensionless time, t_d, taken by the bullet to attain 99.5% of its (truncated) terminal speed is plotted as a function of the initial dimensionless height whilst in **c**, the dimensionless distance z_d over which the bullet achieves 99.5% of β_{15} is plotted as a function of z_{o_d}.

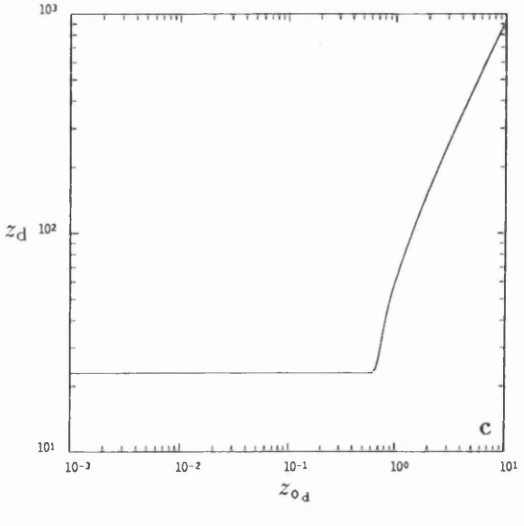

For the attainment of a terminal speed of 0.2602c, interpolation of the data for $z_{0_d} = 0.01$ and 0.1 reveals that $X_{ad} = 1235$ is a necessary condition whilst for a speed of 0.2602c to represent 99.5% of the terminal speed requires that $X_{ad} = 1255$. Integrating Eq. (4.82) with the latter value of X_{ad} yields the results displayed in Figs. 4.31a,b,c. The terminal speed (Fig. 4.31a) is constant for all release heights less than $0.55R_{ad}$ whilst the minimum time for the attainment of a speed of 0.2602c is 89 units (Fig. 4.31b) and occurs for a bullet released at a dimensionless height of 0.55 units above the apex. By Eq. (4.59*a*) this represents a real time of approximately $3000R_{ad_{10}}$ seconds which, for an accretion disc of radius 10^9 m, is in rough agreement with the observations in SS433. The attainment distance (Fig. 4.31b), however, lies well beyond the funnel mouth and is typically $23R_{ad}$ for bullets formed at a distance less than $0.5R_{ad}$ from the funnel base. On the basis of this fact alone the polytropic temperature profile can probably be regarded as inappropriate to SS433.

By Eq. 4.59*d* it is simple to show, with T_1 replaced by T_c, that

$$T_{c_8} = \left(\frac{X_{ad}}{6.61 \times 10^2}\right)^{\frac{1}{4}} \mathrm{m}_{0_{21}}^{\frac{1}{4}} r_{b_{d_{-3}}}^{-\frac{1}{2}} R_{ad_{10}}^{-\frac{3}{4}} \tag{4.89}$$

which for a bullet mass of 10^{21} kg and dimensionless radius 10^{-3} units implies that, for the attainment of a terminal speed of 0.2602c ($X_{ad} = 1235$), the temperature at the funnel base needs be $\sim 1.17 \times 10^8$ K for an accretion disc of radius 10^{10} m and $\sim 6.58 \times 10^8$ K for an accretion disc of radius 10^9 metres. These are perfectly reasonable base temperatures but, from inspection of Fig. 4.23, they are only possible within the polytropic model for accretion disc masses in excess of $100M_\odot$ which is well above the likely upper bound to the disc mass.

For the simple polytropic model considered above it is clear that the disc masses necessary for the required funnel base temperatures are absurdly high. These base temperatures can, however, be achieved for much smaller disc masses if allowance is made for the presence of a compact object at the disc centre. Recalling Eq. (3.20) which gives the temperature at the surface of a neutron star for a disc of uniform density to be supported solely by radiation pressure, it is easy to show that for a typical neutron star mass of $1.4M_\odot$ and radius of 10 km that the temperature close to the neutron star surface must be approximately

$$T_{c_8} \sim 1.4 \left[\frac{M_{ad}/10M_\odot}{R_{ad_{10}}^3}\right]^{\frac{1}{4}} . \tag{4.90}$$

Thus, funnel base temperatures of $\sim 1.17 \times^8$ K and $\sim 6.58 \times 10^8$ K can be achieved within accretion discs of radii 10^{10} m and 10^9 m respectively for disc masses (excluding the mass of the neutron star) of $\sim 5M_\odot$. Indeed, since in the derivation of Eq. (3.20) the assumption that the density of the accretion disc is uniform was used, the temperature given by Eq. (4.90) is a rough estimate of the lower bound on the temperature at the neutron star surface. Consequently, a disc mass of less than $\sim 5M_\odot$ would probably be sufficient to ensure the requisite funnel base temperatures. This value, though much lower than those demanded by the simple polytropic

model considered above, is still too high for self-gravity to be neglected as is common in accretion disc theory. The scenario is, on account of the substantial envelope mass, similar to that proposed by Collins, Brown and Casinelli (1990) in which the jets originate from polar holes in a precessing giant star at the centre of which is located a compact object. Such an anomaly could arise through the rapid transfer of matter from an evolved giant star onto an already supercricical accreting compact object with an existing pair of well established, oppositely aligned jets.

The large discrepancy between the central temperature predicted by the polytropic model (Eq. 4.78) and that given by Eq. (4.90) arises from the failure of the single polytropic model to account for the existence of a neutron star at the core of the spherical envelope. A better and more representative model would consist of two distinct polytropes: a polytrope of index $n_p = 3$ for the radiative envelope and a polytrope perhaps of index $n_p = 0$, for which the density of the polytrope is uniform, for the neutron star. I will, however, leave this as a topic for future consideration.

A polytrope of index $n_p = 3$, amongst other things, provides a means of deducing the rough form of the run of temperature with radius throughout a gaseous sphere in radiative equilibrium. If the run of normalised temperature with dimensionless radius for the single polytropic model (Eq. 4.80*b*, Fig. 4.22) is, as would seem reasonable, similar to that in the radiative portion of a composite polytropic model, then the equation of motion (Eq. 4.82) remains valid (and so too, therefore, do the results) though with the funnel base temperature now given by Eq. (4.90) rather than by Eq. (4.78).

§4.7 Conclusions

For the motion of a bullet above an infinite, planar radiator for which the emergent, frequency integrated specific intensity is given by the Eddington limb darkening approximation, the terminal speed is 0.5144c. This is marginally higher than the figure of 0.4514c for motion above an infinite, isothermal plane. If the emergent, frequency integrated specific intensity is given by a generalisation to the Eddington limb darkening approximation then the terminal speed is lowest, with a value of 0.3139c, in the extreme limb brightening limit and highest, with a value of 0.6096c, in the extreme limb darkening limit. This trend results from the action of aberrated, blue-shifted photons emanating from the radiator limb which for the limb brightened radiator account for a greater proportion of the total energy flux than do photons arising from a similar location on the limb darkened plane and, therefore, for a given energy flux emergent from the plane and a particular bullet velocity, provide a greater decelerative force. Regardless of whether the plane is limb brightened or darkened, motion parallel to its surface is always attenuated with the degree of attenuation being greatest for the most limb brightened radiator. Also, for a given degree of limb brightening or darkening and a particular speed parallel to the z-axis the degree of damping of the velocity component parallel to the plane surface is greatest

when the direction of motion is downwards towards the radiator.

If the accretion funnels of SS433 are modelled as infinite cones for which the blackbody surface temperature decreases exponentially with radial distance from the apex and the scale heights are chosen such that the effective surface temperature is in agreement with the observations then, assuming a funnel base temperature of 8×10^8 K, appropriate scale heights are $\sim 0.1 R_{ad}$. Since the terminal speed is strictly attained in the limit where $t \rightarrow \infty$ it cannot be determined precisely but only to a high degree of accuracy if a suitably long time interval is employed; in this work a period of 10^{15} dimensionless time units was used. The terminal speed is dependent on the parameter $\tilde{X}$ which is given by the ratio of the power intercepted by the bullet to its rest mass energy all times the light crossing time across one scale height. For a given value of the parameter $\tilde{X}$ the terminal speed is found to be remarkably independent of the height above the funnel apex at which the bullet is formed *if* this height is less than roughly one scale height or equivalently one tenth of the accretion disc radius. If the release point exceeds this rough limit then the terminal speed which can be achieved greatly decreases.

Observational uncertainty on the jet speed is about 0.5% and therefore any relative deviation in the bullet's speed once it has attained 99.5% of its terminal speed will be comparable to this observational uncertainty. The minimum time taken by the bullet to attain 99.5% of the terminal speed occurs at a height of approximately one scale height above the apex. This same limit also marks the boundary beyond which the distance taken by the bullet to attain 99.5% of its terminal speed greatly increases. For release heights less than about one scale height the attainment distance is, like the terminal speed, remarkably independent of the initial height. The value of the parameter $\tilde{X}$ required for the attainment of a specific terminal speed is particularly insensitive to the release height for narrow cones with semi-angles less than about 4°. This insensitivity is a very important feature and may partially explain why the observed speed of the jets in SS433 is so constant. The attainment of a terminal speed of 0.2602c within a funnel semi-angle 1° necessitates that the value of the parameter $\tilde{X}$ be 2052. For the accepted values of the funnel semi-angle, the speed of the jets in SS433 is very close to, if not at, the highest that can possibly be achieved.

The minimum attainment time taken by a bullet to achieve a speed of 0.2602c, which represents 99.5% of the terminal speed, within a funnel of semi-angle 1° with a base temperature 8×10^8 K is ~ 80 s for an accretion disc of radius 10^9 m and ~ 614 s for an accretion disc of radius 10^{10} m. The former value is in particularly good agreement with the observations which indicate that the acceleration time-scale is ~ 100 seconds. The corresponding attainment distance is $\sim 6 R_{ad}$ for a disc of radius 10^9 m and $\sim 5 R_{ad}$ for an accretion disc of $\sim 10^{10}$ metres. Therefore, if the attainment distance is to be comparable to the 10^{10} m indicated by observations then the disc radius needs to be less than $\sim 1.7 \times 10^9$ metres. However, if $R_{ad} \sim 10^9$ m then, for a funnel base temperature of 8×10^8 K, the funnel semi-angle must exceed $\sim 0.8°$ if a terminal speed of 0.2602c is to be possible even for a likely minimum bullet mass of 5×10^{20} kg. Funnel semi-angles in the upper part of the range of accepted values and accretion disc radii less than

$\sim 1.7 \times 10^9$ m are, therefore, preferable.

Unlike that for motion above an infinite, isothermal planar radiator the terminal speed of matter moving axially above a finite, isothermal radiating plane is not restricted to one universal value. Instead, the terminal speed is dependent on the parameter X which is identical to the parameter $\tilde{X}$ mentioned above excepting that the characteristic time scale is given by the light crossing time across one plane radius. The initial height of $\sim 0.1R_p$ denotes the rough limit before which, for a given value of the parameter X, the terminal speed is quite independent of the release height and beyond which the terminal speed falls sharply and the attainment distance rises quickly. This dependence of the terminal speed on the parameter X permits the attainment of highly relativistic terminal speeds e.g. terminal speeds in excess of 0.99c are possible for motion above a thin accretion disc with model parameters suitable for neutron star accretion. The marked increase in the terminal speeds that can be achieved is attributable to a considerable decrease in the effectiveness of photons emitted from the limb of a finite, planar radiator to provide a decelerative force compared to those emitted from the limb of an infinite, planar radiator.

A cursory, relativistic treatment of motion above a spherical, isotropic radiator showed that there is a typical reduction of $\sim 2\%$ in the continuum radiation pressure for wind speeds ~ 3000 km/s relative to that derived in the Newtonian limit. Although the discrepancy is negligibe for the range of wind speeds known to date, a relativistic treatment should be adopted for wind speeds much in excess of 3000 km/s which are most likely to occur as a result of black hole accretion in AGN.

Obvious similarities exist between the exponentially decaying temperature profile model and that for the finite, isothermal plane as regards the behaviour of the terminal speed and attainment distance both before and beyond a model dependent release height. Motion within the radiation field of a finite, isothermal funnel is no different: the terminal speed is, for a given value of the parameter X_{ad} and the funnel semi-angle, constant if the release point is located anywhere between the funnel apex and a point just below the funnel mouth. Motion within a narrow funnel is characterised by a period of very rapid acceleration on the immediate approach to the funnel mouth. For all funnel semi-angles the maximum *exit* speed is identical to the terminal speed above an infinite, isothermal plane.

For model parameters appropriate to SS433 the contribution made by the exterior, spherical surface of the accretion disc in enhancing the terminal speed is completely negligible. A terminal speed of 0.2602c can be achieved with a funnel of semi-angle 0.01 rads if the parameter X_{ad} has the value 2.36. For a bullet of minimum cross-section and a mass of 10^{21} kg this corresponds to a temperature of 2.4×10^8 K. On account of the inverse proportionality of the temperature to the square root of the bullet radius this quoted funnel temperature represents a rough upper bound on that required for the attainment of a terminal speed of 0.2602c. The minimum attainment time occurs for an initial height given by $0.98R_{ad}$. For an accretion disc of radius 10^{10} m the attainment time and distance are ~ 63 s and $\sim 1.37R_{ad}$ respectively. These results

are in excellent agreement with the observations of SS433.

A terminal speed of 0.2602c can be achieved above a finite, polytropic funnel of semi-angle 1° for which the run of temperature with radius is appropriate for a system in radiative equilibrium if the parameter X_{ad} has the value 1235. For a bullet of mass 10^{21} kg and dimensionless radius $r_{b_d} = 10^{-3}$ and a disc of radius 10^9 m this represents an acceptable base temperature of 1.17×10^8 K. However, for the simple polytropic model considered this central temperature requires that the mass of the disc be in excess of $100M_\odot$ which is far greater than any realistic upper bound to the disc mass unless adequate account is taken of the compact object located at the disc centre. The terminal speed is independent of the height of bullet formation up to a distance $0.55R_{ad}$ from the funnel apex. The minimum attainment time taken to reach a speed of 0.2602c, which corresponds to 99.5%, of the terminal speed, is $\sim$ 300 s for an accretion disc of radius 10^9 m whilst the minimum attainment distance, which is independent of the accretion disc radius, is $\sim 23R_{ad}$. This large attainment distance indicates that the polytropic temperature profile utilised in the model is inappropriate for SS433.

To summarise, the best match to the observations, particularly the attainment of a terminal speed close to the funnel mouth, is obtained from the model in which the accretion disc funnels of SS433 are represented as finite, conical isothermal radiators. As I have previously mentioned, it is inconceivable that the accretion funnels are truly isothermal over their entire length though it may be that the temperature gradient along the length of the funnels is much smaller than anticipated. A lowering of the temperature gradient may result if radiation from the hottest regions near the funnel base is absorbed then re-radiated by those further from the apex thereby directly raising their temperature above that for material equally distant from the funnel apex but located *within* the accretion disc. This is analagous to what has been termed the 'reflection effect' which occurs in binary systems. Possible observational evidence to support this suggestion is provided by the periodic variation in the optical continuum spectrum (Wagner, 1986) which may be due to high temperature radiation being scattered or re-radiated from regions near the funnel mouth.

Chapter 5

Future Work

§5.1 Introduction

In this concluding chapter I will present topics related to the work in this thesis which could be considered in any future investigation. The first, and principle topic, involves what has been termed the Compton rocket effect (O'Dell, 1981). The term 'rocket' refers to the increase in the radiation pressure experienced by a hot plasma over that experienced by a cold plasma in the presence of an anisotropic radiation field due to Compton scattering of the incident photon flux. A hot plasma is driven away from the radiation source by both the incident photon flux and by an anisotropic loss in internal energy. The significance of the latter contribution to the total driving force increases with the internal energy of the plasma. In §5.2 below I will derive the Compton rocket equation of motion and highlight its similarity with the bullet equation of motion derived in §2.6 and, in addition, present the equation of motion in a form which ultimately permits a fluid treatment of the plasma. The solution of the fluid dynamical equations of motion for a plasma confined within a conical radiator will be left as a topic for future research. An expression for the radiation force per unit volume acting on a plasma at rest within the radiation field produced by an infinite, conical radiator of uniform brightness will be derived and the magnitude of the enhancement in the radiation force attributable to the Compton rocket effect in the context of SS433 will be considered. The remaining topics, presented in the final section, represent a series of worthwhile improvements and extensions which are related specifically to the 'bullet model' outlined in the previous research chapters.

§5.2 The Compton Rocket Effect

§5.2.1 Derivation of the Fundamental Equations

Consider a volume element of plasma moving with a flow velocity $c\underline{\beta}_{(1)f}$ in $\angle S_{(1)}$, the rest frame of the radiation source. Let the instantaneous inertial rest frame of the plasma element be denoted by $\angle S_{(2)}$. Consider one particular electron in the plasma element that is observed in $\angle S_{(2)}$ to have a thermal velocity $c\underline{\beta}_{(2)t}$. Since the number of Compton scatterings is a countable quantity it is a Lorentz invariant. By Eq. (2.8) it is evident that $dt_{(2)} = \gamma_{(2)t} dt_{(3)}$ and therefore the scattering rate of this particular electron, as observed in $\angle S_{(2)}$, is

$$\frac{dN_{(2)}}{dt_{(2)}} = \frac{1}{\gamma_{(2)t}} \frac{dN}{dt_{(3)}} \tag{5.1}$$

where

$$\gamma_{(2)t} = \frac{1}{\sqrt{1-\beta_{(2)t}^2}} \,. \tag{5.2}$$

In the instantaneous rest frame of the electron ($\angle S_{(3)}$) the scattering rate is given by

$$\frac{dN}{dt_{(3)}} = \iint c\sigma dn_{(3)} \tag{5.3}$$

where σ is the Compton cross-section and $dn_{(3)}$ is the differential photon number density in $\angle S_{(3)}$ which is defined as the number of photons per unit volume within the frequency range $\nu_{(3)}$ to $\nu_{(3)} + d\nu_{(3)}$ moving within the solid angle $d\Omega_{(3)i}$ about the direction $\hat{\underline{k}}_{(3)i}$. The subscript '$i$' indicates that the parameter corresponds to that of the *incident* photons. The next step makes use of the fact that

$$\frac{dn}{\nu} = \text{Lorentz invariant} \,. \tag{5.4}$$

This can readily be deduced as follows: From the definition of the photon differential number density given above and by the definition of the differential number of photons given by Eq. (2.57) it is clear that

$$dn = \frac{dN}{d^3\underline{x}} = f(\underline{x},\underline{k},t)d^3\underline{k} = \left(\frac{2\pi}{c}\right)^3 f(\underline{x},\frac{2\pi\nu}{c}\hat{\underline{k}},t)\,\nu^2\,d\nu\,d\Omega \,. \tag{5.5}$$

By Eq. (2.58) the distribution function $f(\underline{x},\underline{k},t)$ is a Lorentz invariant whilst by Eqs. (2.67) and (2.69) $\nu^2 d\Omega$ is also a Lorentz invariant. Since $\nu d\nu$ must transform in the same manner as ν^2 the quantity $\nu d\nu d\Omega$ is a Lorentz invariant too and, therefore, dn/ν satisfies Eq. (5.4). Utilising this invariance and the Doppler shift relation given by Eq. (2.63) the scattering rate, as determined in the instantaneous rest frame of the electron, can be written as

$$\frac{dN}{dt_{(3)}} = \iint c\sigma\gamma_{(2)t}\left(1-\underline{\beta}_{(2)t}\cdot\hat{\underline{k}}_{(2)i}\right) dn_{(2)} \,. \tag{5.6}$$

According to Eq. (2.59) the energy attributable to the passage of photons in the frequency range ν to $\nu + d\nu$ within a solid angle $d\Omega$ about $\hat{\underline{k}}$ across a differential surface element of area dA and unit normal $\hat{\underline{n}}$ in a time interval dt is

$$dE_\nu = \left(\frac{2\pi}{c}\right)^3 h\, f(\underline{x},\frac{2\pi\nu}{c}\hat{\underline{k}},t)\,\nu^3\,d\nu\,d\Omega\,c dt\,(\hat{\underline{k}}\cdot\hat{\underline{n}})\,dA \,. \tag{5.7}$$

Equating this expression with the definition of the specific intensity given by Eq. (2.23) results in the identification

$$f(\underline{x},\frac{2\pi\nu}{c}\hat{\underline{k}},t) = \frac{I_\nu(\underline{x},\hat{\underline{k}},t)}{\left(\frac{2\pi}{c}\right)^3 hc\nu^3} \tag{5.8}$$

which upon substitution into Eq. (5.5) yields

$$\mathrm{d}n = \frac{I_\nu(\underline{x}, \hat{\underline{k}}, t)}{ch\nu}\,\mathrm{d}\nu\mathrm{d}\Omega\,. \tag{5.9}$$

Thus, Eq. (5.6) can be expressed as

$$\frac{\mathrm{d}N}{\mathrm{d}t_{(3)}} = \iint \sigma\gamma_{(2)t}\frac{I_{\nu_{(2)i}}(\underline{x}_{(2)}, \hat{\underline{k}}_{(2)i}, t_{(2)})}{h\nu_{(2)i}}\left(1 - \underline{\beta}_{(2)t}\cdot\hat{\underline{k}}_{(2)i}\right)\mathrm{d}\nu_{(2)i}\,\mathrm{d}\Omega_{(2)i}\,. \tag{5.10}$$

In the instantaneous rest frame of the electron the frequency of a photon prior to scattering, $\nu_{(3)i}$, is related to that after Compton scattering, $\nu_{(3)s}$, according to the relation

$$\nu_{(3)s} = \frac{\nu_{(3)i}}{1 + \frac{h\nu_{(3)i}}{m_e c^2}\left(1 - \hat{\underline{k}}_{(3)i}\cdot\hat{\underline{k}}_{(3)s}\right)} \tag{5.11}$$

where m_e is the electron rest mass (Blumenthal and Gould, 1970). The Thomson limit corresponds to the regime in which

$$h\nu_{(3)i} \ll m_e c^2 \tag{5.12}$$

or equivalently, by Eq. (5.11), to that in which

$$\nu_{(3)s} \approx \nu_{(3)i}\,. \tag{5.13}$$

By the Doppler shift formula, Eq. (5.13) can be written as

$$\nu_{(2)s} \approx \frac{1 - \underline{\beta}_{(2)t}\cdot\hat{\underline{k}}_{(2)i}}{1 - \underline{\beta}_{(2)t}\cdot\hat{\underline{k}}_{(2)s}}\,\nu_{(2)i} \tag{5.14}$$

and, upon inclusion of Eq. (5.14) into Eq. (5.10) as the argument of a delta function, permits the scattering rate in the electron rest frame (Eq. 5.10) to be expressed as

$$\frac{\mathrm{d}N}{\mathrm{d}t_{(3)}} = \iiint \left\{\sigma\gamma_{(2)t}\frac{I_{\nu_{(2)i}}(\underline{x}_{(2)}, \hat{\underline{k}}_{(2)i}, t_{(2)})}{h\nu_{(2)i}}\left(1 - \underline{\beta}_{(2)t}\cdot\hat{\underline{k}}_{(2)i}\right)\right.$$
$$\left.\times\,\delta\left[\nu_{(2)s} - \left(\frac{1 - \underline{\beta}_{(2)t}\cdot\hat{\underline{k}}_{(2)i}}{1 - \underline{\beta}_{(2)t}\cdot\hat{\underline{k}}_{(2)s}}\right)\nu_{(2)i}\right]\right\}\mathrm{d}\nu_{(2)i}\,\mathrm{d}\nu_{(2)s}\,\mathrm{d}\Omega_{(2)i}\,. \tag{5.15}$$

In the instantaneous rest frame of the electron the Thomson differential cross-section (Blumenthal and Gould, 1970) is

$$\frac{\mathrm{d}\sigma}{\mathrm{d}\Omega_{(3)s}} = \frac{3}{16\pi}\sigma_{\mathrm{T}}\left\{1 + \left(\hat{\underline{k}}_{(3)i}\cdot\hat{\underline{k}}_{(3)s}\right)^2\right\} \tag{5.16}$$

from which it can readily be shown that in the flow frame ($\angle S_{(2)}$) the Thomson differential cross-section is

$$\frac{\mathrm{d}\sigma}{\mathrm{d}\Omega_{(3)s}} = \frac{3}{16\pi}\sigma_{\mathrm{T}}\left\{1+\left[1-\frac{1-\underline{\hat{k}}_{(2)i}\cdot\underline{\hat{k}}_{(2)s}}{\gamma_{(2)t}^2\left(1-\underline{\beta}_{(2)t}\cdot\underline{\hat{k}}_{(2)i}\right)\left(1-\underline{\beta}_{(2)t}\cdot\underline{\hat{k}}_{(2)s}\right)}\right]^2\right\} \times \frac{1}{\left[\gamma_{(2)t}\left(1-\underline{\beta}_{(2)t}\cdot\underline{\hat{k}}_{(2)s}\right)\right]^2}\,. \tag{5.17}$$

With reference to Eqs. (5.1) and (5.15), the scattering rate in the flow frame can then be written as

$$\frac{\mathrm{d}N}{\mathrm{d}t_{(2)}} = \iiiint\left\{\frac{I_{\nu_{(2)i}}(\underline{x}_{(2)},\underline{\hat{k}}_{(2)i},t_{(2)})}{h\nu_{(2)i}}\left(1-\underline{\beta}_{(2)t}\cdot\underline{\hat{k}}_{(2)i}\right) \times\delta\left[\nu_{(2)s}-\left(\frac{1-\underline{\beta}_{(2)t}\cdot\underline{\hat{k}}_{(2)i}}{1-\underline{\beta}_{(2)t}\cdot\underline{\hat{k}}_{(2)s}}\right)\nu_{(2)i}\right]\left(\frac{\mathrm{d}\sigma}{\mathrm{d}\Omega_{(2)s}}\right)\right\}\mathrm{d}\nu_{(2)i}\,\mathrm{d}\nu_{(2)s}\,\mathrm{d}\Omega_{(2)i}\,\mathrm{d}\Omega_{(2)s}\,. \tag{5.18}$$

For a relativistic electron gas $\gamma_{(2)t} \gg 1$ and in this limit

$$\beta_{(2)t} \approx 1-\frac{1}{2\gamma_{(2)t}^2}\,. \tag{5.19}$$

Therefore, according to the Doppler shift formula, Eq. (2.63), the maximum and minimum frequencies of the incident photons, as observed in the electron rest frame, are respectively

$$\nu_{(3)i}^{max} = \gamma_{(2)t}(1+\beta_{(2)t})\nu_{(2)i} \approx 2\gamma_{(2)t}\nu_{(2)i} \quad\text{and}\quad \nu_{(3)i}^{min} = \gamma_{(2)t}(1-\beta_{(2)t})\nu_{(2)i} \approx \frac{\nu_{(2)i}}{2\gamma_{(2)t}}\,. \tag{5.20a,b}$$

The frequency of the scattered radiation as observed in the plasma flow frame is related to that in the electron rest frame according to the relation

$$\nu_{(2)s} = \gamma_{(2)t}\left(1+\beta_{(2)t}\cdot\underline{\hat{k}}_{(3)s}\right)\nu_{(3)s} \tag{5.21}$$

and, therefore, in the Thomson limit the maximum frequency of the scattered radiation observed in $\angle S_{(2)}$ is, by Eqs. (5.13) and (5.20a),

$$\nu_{(2)s}^{max} = 2\gamma_{(2)t}\nu_{(3)s}^{max} \approx 2\gamma_{(2)t}\nu_{(3)i}^{max} \approx 4\gamma_{(2)t}^2\nu_{(2)i}\,. \tag{5.22}$$

Thus, the maximum energy of a scattered photon observed in the rest frame of the plasma is a factor $4\gamma_{(2)t}^2$ greater than that of the incident photon. The characteristic frequency of a Thomson

scattered photon is, therefore, $\sim \gamma^2_{(2)i}\nu_{(2)i}$. Though the corresponding energy of this photon is large it is small in comparison to the rest mass energy of the electron if $h\nu_{(2)i} \ll m_e c^2/\gamma^2_{(2)i}$ which, therefore, loses a small fraction of its total energy as a result of each scattering. In the Klein-Nishina limit this is not so and the scattered photon carries away a considerable fraction of the electron's energy. In either case the relativistic electrons undergo Compton cooling, a process which is commonly referred to as the inverse Compton effect. In the reverse situation, where the incident photons are more energetic than the scattering electrons, the photons will in general lose energy due to the Compton recoil of the electrons which, in turn, become Compton heated. Before proceeding further with derivation of the fundamental equations I will briefly consider the applicability of Thomson scattering in the context of SS433.

A likely upper bound on the temperature at the base of the accretion funnels is 8×10^8 K. For a plasma at such a temperature the most likely thermal speed of the constituent electrons is ~ 0.575c (see below) and, consequently, the typical maximum frequency of any radiation as observed in the rest frame of an electron is $\sim 2\nu_{(2)i}$. For a jet speed of 0.26c the maximum frequency of any incident radiation observed in the flow frame is $\sim 1.3\nu_{(1)i}$ and therefore $\nu^{max}_{(3)i} \sim 2.6\nu_{(1)i}$. If the funnel walls radiate as a blackbody at a temperature T then according to the Wien displacement law the frequency at which the maximum in $B_\nu(T)$ occurs is

$$\nu = 5.88 \times 10^8 T \,\mathrm{Hz}\ . \tag{5.23}$$

Therefore the typical maximum frequency of the incident radiation as observed in the electron rest frame is $\nu^{max}_{(3)i} \approx 1.22 \times 10^{20}$ Hz which corresponds to a ratio $h\nu^{max}_{(3)i}/m_e c^2 \approx 1$. This ratio is the greatest that can possibly be achieved in SS433 for a photon with a frequency given by the Wein displacement law and, since the brightness of a blackbody drops very steeply with frequency beyond the maximum, it is also a very good indicator of the absolute maximum ratio. Evidently the problem should ideally be formulated with the incorporation of Klein-Nishina scattering. I will, however, leave such an analysis as a topic for future work and continue in the Thomson limit, but now aware of its limited applicability.

As mentioned above, in the Thomson limit, a distribution of electrons undergoing Compton cooling lose a small fraction of their energy as a result of each scattering. In the flow frame the energy gained by the photon is simply

$$\Delta\mathcal{E}_{(2)ph} = h\nu_{(2)s} - h\nu_{(2)i} \tag{5.24a}$$

for which the corresponding change in momentum is

$$\Delta\underline{p}_{(2)ph} = \frac{h\nu_{(2)s}}{c}\,\underline{\hat{k}}_{(2)s} - \frac{h\nu_{(2)i}}{c}\,\underline{\hat{k}}_{(2)i}\ . \tag{5.24b}$$

The rate at which the electron loses energy in the flow frame is given by the product of the

scattering rate in the flow frame (Eq. 5.18) with the energy lost at each scattering (Eq. 5.24a) leading to the mathematical expression

$$\frac{\mathrm{d}\mathcal{E}_{(2)e}}{\mathrm{d}t_{(2)}} = -\iiiint \left\{ \frac{I_{\nu_{(2)i}}(\underline{x}_{(2)}, \hat{\underline{k}}_{(2)i}, t_{(2)})}{h\nu_{(2)i}} \left(1 - \underline{\beta}_{(2)t} \cdot \hat{\underline{k}}_{(2)i}\right) \left(h\nu_{(2)s} - h\nu_{(2)i}\right) \right.$$
$$\left. \times\, \delta\left[\nu_{(2)s} - \left(\frac{1 - \underline{\beta}_{(2)t} \cdot \hat{\underline{k}}_{(2)i}}{1 - \underline{\beta}_{(2)t} \cdot \hat{\underline{k}}_{(2)s}}\right)\nu_{(2)i}\right] \left(\frac{\mathrm{d}\sigma}{\mathrm{d}\Omega_{(2)s}}\right) \right\} \mathrm{d}\nu_{(2)i}\, \mathrm{d}\nu_{(2)s}\, \mathrm{d}\Omega_{(2)i}\, \mathrm{d}\Omega_{(2)s}. \quad (5.25a)$$

Similarly, the rate at which momentum is transferred to the electron by the radiation field is

$$\frac{\mathrm{d}\underline{p}_{(2)e}}{\mathrm{d}t_{(2)}} = -\iiiint \left\{ \frac{I_{\nu_{(2)i}}(\underline{x}_{(2)}, \hat{\underline{k}}_{(2)i}, t_{(2)})}{h\nu_{(2)i}} \left(1 - \underline{\beta}_{(2)t} \cdot \hat{\underline{k}}_{(2)i}\right) \left(\frac{h\nu_{(2)s}}{\mathrm{c}}\, \hat{\underline{k}}_{(2)s} - \frac{h\nu_{(2)i}}{\mathrm{c}}\, \hat{\underline{k}}_{(2)i}\right) \right.$$
$$\left. \times\, \delta\left[\nu_{(2)s} - \left(\frac{1 - \underline{\beta}_{(2)t} \cdot \hat{\underline{k}}_{(2)i}}{1 - \underline{\beta}_{(2)t} \cdot \hat{\underline{k}}_{(2)s}}\right)\nu_{(2)i}\right] \left(\frac{\mathrm{d}\sigma}{\mathrm{d}\Omega_{(2)s}}\right) \right\} \mathrm{d}\nu_{(2)i}\, \mathrm{d}\nu_{(2)s}\, \mathrm{d}\Omega_{(2)i}\, \mathrm{d}\Omega_{(2)s}. \quad (5.25b)$$

The procedure for evaluating these integrals is lengthy but, on account of their similar form, is much the same for each. For this reason the approach to integrating Eq. (5.25a) will be outlined and the integrated form of the rate of change of momentum equation merely stated, the remaining manipulation being left to the reader.

The integration over $\nu_{(2)s}$ is trivial and requires no explanation whilst the integration over $\nu_{(2)i}$ can be performed by appealing to the Lorentz invariance of I_ν/ν^3 (Eq. 2.60) and the Doppler shift formula (Eq. 2.63). The rate of energy loss equation then has the form

$$\frac{\mathrm{d}\mathcal{E}_{(2)e}}{\mathrm{d}t_{(2)}} = -\iint \left\{ I_{(1)}(\underline{x}_{(1)}, \hat{\underline{k}}_{(1)i}, t_{(1)})\, \gamma^4_{(1)f} \left(1 - \underline{\beta}_{(1)f} \cdot \hat{\underline{k}}_{(1)i}\right)^4 \left(1 - \underline{\beta}_{(2)t} \cdot \hat{\underline{k}}_{(2)i}\right) \right.$$
$$\left. \times \left[\left(\frac{1 - \underline{\beta}_{(2)t} \cdot \hat{\underline{k}}_{(2)i}}{1 - \underline{\beta}_{(2)t} \cdot \hat{\underline{k}}_{(2)s}}\right) - 1\right] \left(\frac{\mathrm{d}\sigma}{\mathrm{d}\Omega_{(2)s}}\right) \right\} \mathrm{d}\Omega_{(2)i}\, \mathrm{d}\Omega_{(2)s} \quad (5.26)$$

where $I_{(1)}$ is the frequency integrated specific intensity as observed in the rest frame of the radiator. The integral over $\Omega_{(2)s}$ is best performed by transforming to the instantaneous rest frame of the electron. Using the equation for the transformation of the raypath vector (Eq. 2.62) it can readily be shown that

$$\left(\frac{1 - \underline{\beta}_{(2)t} \cdot \hat{\underline{k}}_{(2)i}}{1 - \underline{\beta}_{(2)t} \cdot \hat{\underline{k}}_{(2)s}}\right) - 1 = \gamma^2_{(2)t} \left(1 + \underline{\beta}_{(2)t} \cdot \hat{\underline{k}}_{(3)s}\right) \left(1 + \underline{\beta}_{(2)t} \cdot \hat{\underline{k}}_{(2)i}\right) - 1 \quad (5.27)$$

which upon substitution into Eq. (5.26), and with reference to the differential Thomson cross-

section given by Eq. (5.16), yields

$$\frac{\mathrm{d}\mathcal{E}_{(2)e}}{\mathrm{d}t_{(2)}} = -\frac{3}{16\pi}\sigma_{\mathrm{T}} \iint \left\{ I_{(1)}(\underline{x}_{(1)}, \hat{\underline{k}}_{(1)i}, t_{(1)})\, \gamma_{(1)f}^4 \left(1 - \underline{\beta}_{(1)f} \cdot \hat{\underline{k}}_{(1)i}\right)^4 \left(1 - \underline{\beta}_{(2)t} \cdot \hat{\underline{k}}_{(2)i}\right) \right.$$
$$\times \left. \left[\gamma_{(2)t}^2 \left(1 + \underline{\beta}_{(2)t} \cdot \hat{\underline{k}}_{(3)s}\right) \left(1 - \underline{\beta}_{(2)t} \cdot \hat{\underline{k}}_{(2)i}\right) - 1\right] \left[1 + \left(\hat{\underline{k}}_{(3)i} \cdot \hat{\underline{k}}_{(3)s}\right)^2\right] \right\} \mathrm{d}\Omega_{(2)i}\, \mathrm{d}\Omega_{(2)s}$$
$$= -\sigma_{\mathrm{T}} \int \left\{ I_{(1)}(\underline{x}_{(1)}, \hat{\underline{k}}_{(1)i}, t_{(1)})\, \gamma_{(1)f}^4 \left(1 - \underline{\beta}_{(1)f} \cdot \hat{\underline{k}}_{(1)i}\right)^4 \left(1 - \underline{\beta}_{(2)t} \cdot \hat{\underline{k}}_{(2)i}\right) \right.$$
$$\times \left. \left[\gamma_{(2)t}^2 \left(1 - \underline{\beta}_{(2)t} \cdot \hat{\underline{k}}_{(2)i}\right) - 1\right] \right\} \mathrm{d}\Omega_{(2)i} \,. \tag{5.28a}$$

Upon integration over the frequency of the incident radiation, the frequency of the scattered radiation and the solid angle into which it is scattered, the rate of change of momentum equation (Eq. 5.25*b*) reduces to

$$\frac{\mathrm{d}\underline{p}_{(2)e}}{\mathrm{d}t_{(2)}} = -\frac{\sigma_{\mathrm{T}}}{\mathrm{c}} \int \left\{ I_{(1)}(\underline{x}_{(1)}, \hat{\underline{k}}_{(1)i}, t_{(1)})\, \gamma_{(1)f}^4 \left(1 - \underline{\beta}_{(1)f} \cdot \hat{\underline{k}}_{(1)i}\right)^4 \left(1 - \underline{\beta}_{(2)t} \cdot \hat{\underline{k}}_{(2)i}\right) \right.$$
$$\times \left. \left[\gamma_{(2)t}^2 \left(1 - \underline{\beta}_{(2)t} \cdot \hat{\underline{k}}_{(2)i}\right) \underline{\beta}_{(2)t} - \hat{\underline{k}}_{(2)i}\right] \right\} \mathrm{d}\Omega_{(2)i} \,. \tag{5.28b}$$

For the particular case in which the flow velocity is zero, the inertial frames $\angle \mathrm{S}_{(1)}$ and $\angle \mathrm{S}_{(2)}$ are identical and Eq. (5.28b) simplifies to

$$\frac{\mathrm{d}\underline{p}_{(1)e}}{\mathrm{d}t_{(1)}} = -\frac{\sigma_{\mathrm{T}}}{\mathrm{c}} \int \left\{ I_{(1)}(\underline{x}_{(1)}, \hat{\underline{k}}_{(1)i}, t_{(1)}) \left(1 - \underline{\beta}_{(1)t} \cdot \hat{\underline{k}}_{(1)i}\right) \right.$$
$$\times \left. \left[\gamma_{(1)t}^2 \left(1 - \underline{\beta}_{(1)t} \cdot \hat{\underline{k}}_{(1)i}\right) \underline{\beta}_{(1)t} - \hat{\underline{k}}_{(1)i}\right] \right\} \mathrm{d}\Omega_{(1)i} \,. \tag{5.29}$$

In the limit where the frequency integrated specific intensity is replaced by the frequency integrated Planckian (Eq. 2.47) and the Thomson cross-section is replaced by the radiation cross-section of the bullet this is identical to Eq. (2.85) derived earlier, through a largely macroscopic approach, to describe the three-force experienced by a grey, massive bullet moving within a blackbody radiation field. Since an electron has no physical size, Eq. (5.29) gives a very accurate representation of the equation of motion in the Thomson limit regardless of the physical form of the radiation field. This same degree of authenticity applies to the motion of a massive bullet only within the radiation field created by an infinite, isothermal radiator. For other radiator configurations the problem is blighted with finite size effects which, although considered in previous chapters in order to ascertain the degree of validity of the various equations of motion, ought to be quantified properly in any future analysis.

From inspection of Eqs. (5.28*a*, *b*) it is obvious that both integrands are functions of the incident raypath three-vector as determined in both frames $\angle \mathrm{S}_{(1)}$ and $\angle \mathrm{S}_{(2)}$. To make further

progress in the integration of these equations it is necessary to select one specific inertial frame and to perform all calculations in that frame. Since the frequency integrated specific intensity is expressed in terms of the coordinates of the rest frame of the radiation source, it is the natural frame to choose.

To transform the integrand of Eq. (5.28*a*) to $\angle S_{(1)}$ both the transformation properties of $d\Omega_{(2)i}$ and the quantity $(1-\underline{\beta}_{(2)t}\cdot\hat{\underline{k}}_{(2)i})$ need to be known. The transformation of an element of solid angle is described by Eq. (2.70) whilst the transformation equation for the latter quantity can readily be deduced as below.

In the flow frame the four-velocity of an electron is $V^{\mu}_{(2)} = \gamma_{(2)t}c\,(1,\underline{\beta}_{(2)t})$ whilst the propagation four-vector of an incident photon is given by $K^{\mu}_{(2)i} = (K^{0}_{(2)i}, \underline{k}_{(2)i})$. In $\angle S_{(1)}$ these same four-vectors are given by $V^{\mu}_{(1)} = \gamma_{(1)r}c\,(1,\underline{\beta}_{(1)r})$ and $K^{\mu}_{(1)i} = (K^{0}_{(1)i}, \underline{k}_{(1)i})$ respectively where the subscript 'r' indicates that the velocity of the electron as observed in the radiation source rest frame, $\underline{\beta}_{(1)r}$, consists of the relativistic *resultant* of the velocities $\underline{\beta}_{(1)f}$ and $\underline{\beta}_{(2)t}$. Both $\underline{\beta}_{(1)r}$ and $\gamma_{(1)r}$ will be determined shortly. Utilising the fact that any four-vector product is a world scalar it follows that

$$1-\underline{\beta}_{(2)t}\cdot\hat{\underline{k}}_{(2)i} = \frac{1}{\gamma_{(2)t}cK^{0}_{(2)i}}V^{\mu}_{(1)}K_{(1)i\mu} = \frac{\gamma_{(1)r}K^{0}_{(1)i}}{\gamma_{(2)t}K^{0}_{(2)i}}\left(1-\beta_{(1)r}\cdot\hat{\underline{k}}_{(1)i}\right). \tag{5.30}$$

Then, by the definition of the propagation four-vector given by Eq. (2.21) and the Doppler shift expression given by Eq. (2.63), it is obvious that

$$1-\underline{\beta}_{(2)t}\cdot\hat{\underline{k}}_{(2)i} = \frac{\gamma_{(1)r}}{\gamma_{(2)t}\gamma_{(1)f}}\left(\frac{1-\underline{\beta}_{(1)r}\cdot\hat{\underline{k}}_{(1)i}}{1-\underline{\beta}_{(1)f}\cdot\hat{\underline{k}}_{(1)i}}\right) \tag{5.31}$$

which upon substitution into the rate of energy loss equation (Eq. 5.28*a*), along with the equation for the transformation for an element of solid angle (Eq. 2.70), yields

$$\frac{d\mathcal{E}_{(2)e}}{dt_{(2)}} = -\sigma_T\frac{\gamma_{(1)r}}{\gamma_{(2)t}}\int\left\{I_{(1)}(\underline{x}_{(1)},\hat{\underline{k}}_{(1)i},t_{(1)})\left(1-\beta_{(1)r}\cdot\hat{\underline{k}}_{(1)i}\right)\right.$$
$$\left.\times\left[\gamma_{(2)t}\gamma_{(1)r}\left(1-\beta_{(1)r}\cdot\hat{\underline{k}}\right)-\gamma_{(1)f}\left(1-\underline{\beta}_{(1)f}\cdot\hat{\underline{k}}_{(1)i}\right)\right]\right\}d\Omega_{(1)i}\,. \tag{5.32a}$$

Substituting these same expressions into the equation for the rate of momentum transfer (Eq. 5.28*b*), along with the equation for the transformation of a raypath vector (Eq. 2.62), gives

$$\frac{d\underline{p}_{(2)e}}{dt_{(2)}} = -\frac{\sigma_T}{c}\frac{\gamma_{(1)r}}{\gamma_{(2)t}}\int\left\{I_{(1)}(\underline{x}_{(1)},\hat{\underline{k}}_{(1)i},t_{(1)})\left(1-\beta_{(1)r}\cdot\hat{\underline{k}}_{(1)i}\right)\left[\gamma_{(2)t}\gamma_{(1)r}\left(1-\underline{\beta}_{(1)r}\cdot\hat{\underline{k}}_{(1)i}\right)\underline{\beta}_{(2)t}\right.\right.$$
$$\left.\left.-\hat{\underline{k}}_{(1)i}-\left\{(\gamma_{(1)f}-1)\frac{\hat{\underline{k}}_{(1)i}\cdot\underline{\beta}_{(1)f}}{\beta^{2}_{(1)f}}-\gamma_{(1)f}\right\}\beta_{(1)f}\right]\right\}d\Omega_{(1)i}\,. \tag{5.32b}$$

All that is now required for Eqs. (5.32a, b) to be fully specified are expressions for the functional dependence of both $\underline{\beta}_{(1)r}$ and $\gamma_{(1)r}$ on $\underline{\beta}_{(1)f}$ and $\underline{\beta}_{(2)t}$. These can readily be derived: the relevant four-velocities have been stated above and the appropriate transformation is

$$V^{\mu}_{(1)} = \Lambda^{\mu}{}_{\nu}(-\underline{\beta}_{(1)f})V^{\nu}_{(2)} \tag{5.33}$$

where the general boost matrix, $\Lambda(\underline{\beta})$, is given in Eq. (2.4). The time-component and three-vector component of Eq. (5.33) respectively yield

$$\gamma_{(1)r} = \gamma_{(2)t}\gamma_{(1)f}\left(1 + \underline{\beta}_{(1)f} \cdot \underline{\beta}_{(2)t}\right) \tag{5.34a}$$

and

$$\underline{\beta}_{(1)r} = \frac{\underline{\beta}_{(2)t} + \left\{\gamma_{(1)f} - [\gamma_{(1)f} - 1]\frac{\underline{\beta}_{(1)f}\cdot\underline{\beta}_{(2)t}}{\beta^2_{(1)f}}\right\}\underline{\beta}_{(1)f}}{\gamma_{(1)f}\left(1 + \underline{\beta}_{(1)f} \cdot \underline{\beta}_{(2)t}\right)} . \tag{5.34b}$$

Thus far, equations describing the rate at which a single electron moving with a thermal velocity $\underline{\beta}_{(2)t}$ in a flow frame which itself moves with respect to the radiation source with a flow velocity $\underline{\beta}_{(1)f}$ have been derived. I shall now extend the analysis applying the equations expressed above to an ensemble of electrons, or equivalently to a volume element of plasma. For this to be possible it is essential that the distribution of thermal velocities of the electrons be known.

For a relativistic gas in local thermodynamic equilibrium (or at least collisional equilibrium) consisting of material particles of rest mass m_0, the distribution function is (Synge, 1957)

$$g(\varphi, P^{\mu}V_{\mu}, \underline{x}) = \frac{n(\underline{x})\,\varphi}{4\pi m_0^2 c^3 K_2(m_0\varphi)} \exp\left\{-\varphi\frac{P^{\mu}V_{\mu}}{c^2}\right\} \qquad \text{with} \qquad \varphi = \frac{c^2}{kT} \tag{5.35a, b}$$

where T is the absolute temperature of the gas, $n(\underline{x})$ is the particle number density at $\underline{x}$, P^{μ} is the particle four-momentum, V^{μ} is the *flow* four-velocity and K_2 is a modified Bessel function of order 2. The number of particles within a phase space cell $\mathrm{d}^3\underline{x}\,\mathrm{d}^3\underline{p}$ is then given by

$$\mathrm{d}N = g(\varphi, P^{\mu}V_{\mu}, \underline{x})\,\mathrm{d}^3\underline{x}\,\mathrm{d}^3\underline{p} . \tag{5.36}$$

Having expressed the rate of energy loss equation (Eq. 5.32a) and the rate of momentum transfer equation (Eq. 5.32b) as functions of the electron thermal velocity, $\underline{\beta}_{(2)t}$, rather than momentum it is preferable, for my purposes to have Eq. (5.36) expressed in terms of 'beta-space' rather than three-momentum space. This requires that the relation between an element of beta-space, $\mathrm{d}^3\underline{\beta}$, and three-momentum space, $\mathrm{d}^3\underline{p}$, be found.

In spherical polar coordinates an element of 'beta-space' and three-momentum space can be respectively written as

$$\mathrm{d}^3\underline{\beta} = \beta^2 \sin\theta \, \mathrm{d}\beta \, \mathrm{d}\theta \, \mathrm{d}\phi \qquad \text{and} \qquad \mathrm{d}^3\underline{p} = p^2 \sin\theta \, \mathrm{d}p \, \mathrm{d}\theta \, \mathrm{d}\phi \tag{5.37a, b}$$

which together imply that

$$\frac{\mathrm{d}^3\underline{p}}{\mathrm{d}^3\underline{\beta}} = \frac{p^2 \mathrm{d}p}{\beta^2 \mathrm{d}\beta} \, . \tag{5.38}$$

From the definition of four-momentum given by Eq. (2.12) it is obvious that

$$p^2 = \underline{p} \cdot \underline{p} = m_0 \gamma^2 \mathrm{c}^2 \beta^2 = m_0^2 \mathrm{c}^2 (\gamma^2 - 1) \tag{5.39}$$

and it therefore follows that

$$p\mathrm{d}p = m_0^2 \mathrm{c}^2 \gamma \mathrm{d}\gamma \tag{5.40}$$

which upon substitution into Eq. (5.38), by Eq. (5.39), yields

$$\frac{\mathrm{d}^3\underline{p}}{\mathrm{d}^3\underline{\beta}} = \frac{m_0^3 \mathrm{c}^3 \gamma (\gamma^2 - 1)^{\frac{1}{2}}}{\beta^2} \frac{\mathrm{d}\gamma}{\mathrm{d}\beta} = m_0^3 \mathrm{c}^3 \gamma^5 \, . \tag{5.41}$$

Hence, the number of particles within an element of phase space $\mathrm{d}^3\underline{\beta} \, \mathrm{d}^3\underline{x}$ is

$$\mathrm{d}N = g(\varphi, P^\mu V_\mu, \underline{x}) \, m_0^3 \mathrm{c}^3 \gamma^5 \mathrm{d}^3\underline{\beta} \, \mathrm{d}^3\underline{x} \tag{5.42}$$

which, for a spatially isotropic distribution, can, by Eqs. (5.35a, b), be expressed as

$$\mathrm{d}N = \frac{n m_0 \varphi}{4\pi K_2(m_0\varphi)} \exp\left\{-\varphi \frac{P^\mu V_\mu}{\mathrm{c}^2}\right\} \gamma^5 \, \mathrm{d}^3\underline{\beta} \, \mathrm{d}^3\underline{x} \, . \tag{5.43}$$

In the plasma flow frame ($\angle S_{(2)}$) the four vector product $P^\mu_{(2)} V_{(2)\mu} = \gamma_{(2)t} m_0 \mathrm{c}^2$ and therefore the number of electrons within the comoving phase space cell $\mathrm{d}^3\underline{\beta}_{(2)t} \, \mathrm{d}^3\underline{x}_{(2)}$ is given by

$$\mathrm{d}N_e = \frac{n_{e(2)} m_e \varphi}{4\pi K_2(m_e\varphi)} \exp\left\{-\gamma_{(2)t} m_e \varphi\right\} \gamma^5_{(2)t} \, \mathrm{d}^3\underline{\beta}_{(2)t} \, \mathrm{d}^3\underline{x}_{(2)} \, . \tag{5.44}$$

The distribution of electron thermal velocities, $\underline{\beta}_{(2)t}$, for various temperatures is illustrated in Fig. 5.1. The most probable thermal velocity, $\underline{\beta}^*_{(2)t}$, is, by Eq. (5.44), such that

$$\frac{\mathrm{d}}{\mathrm{d}\beta_{(2)t}} \left\{\exp\left(-\gamma_{(t)t} m_e \varphi\right) \gamma^5_{(2)t} \beta^2_{(2)t}\right\} = 0 \tag{5.45}$$

the solution to which satisfies

$$(m_e\varphi)\gamma^{*3}_{(2)t} - 5\gamma^{*2}_{(2)t} - (m_e\varphi)\gamma^{*}_{(2)t} + 3 = 0\ . \tag{5.46}$$

For temperatures of 10^8, 4×10^8 and 8×10^8 K the most probable electron thermal velocities are 0.187c, 0.391c and 0.575c respectively.

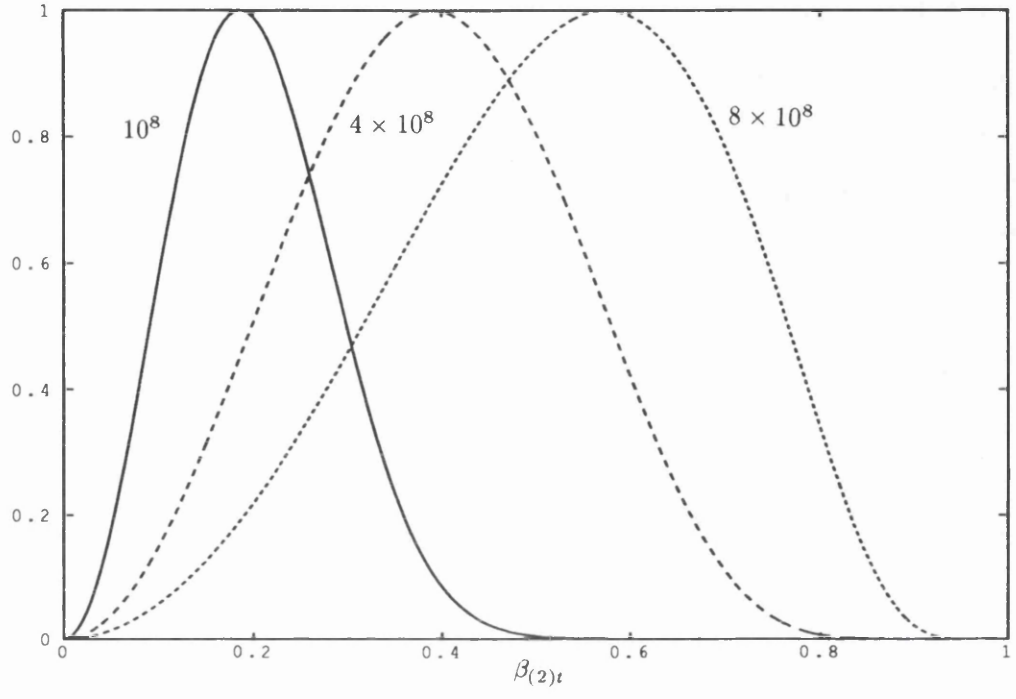

Fig. 5.1. The distribution in speed for an electron gas at the temperatures indicated. The ordinate is proportional to the number of electrons with speeds in the range $\beta_{(2)t}$ to $\beta_{(2)t}+\mathrm{d}\beta_{(2)t}$. Each graph has been normalised so as to have a maximum of unity.

As an aside, consider the behaviour of Eq. (5.44) for large values of φ or equivalently for low absolute temperatures. For large x the modified Bessel function $K_n(x)$ is given by the asymptotic expansion (Abramowitz and Stegun, 1970)

$$K_n(x) \sim \sqrt{\frac{\pi}{2x}}\, e^{-x} \left\{1 + \frac{m-1}{8x} + \frac{(m-1)(m-9)}{2!(8x)^2} + \ldots\right\} \qquad \text{where} \qquad m = 4n^2 \quad (5.47a, b)$$

and therefore for $\beta \ll 1$, Eq. (5.44) is approximately

$$\begin{aligned} \mathrm{d}N_e &\approx n_{e(2)} \left(\frac{m_e}{2\pi kT}\right)^{\frac{3}{2}} \exp\left\{-\left(\gamma_{(2)t} - 1\right)\frac{m_e c^2}{kT}\right\} \mathrm{d}^3\underline{v}_{(2)t}\, \mathrm{d}^3\underline{x}_{(2)} \\ &\approx n_{e(2)} \left(\frac{m_e}{2\pi kT}\right)^{\frac{3}{2}} \exp\left\{-\frac{m_e v^2_{(2)t}}{2kT}\right\} \mathrm{d}^3\underline{v}_{(2)t}\, \mathrm{d}^3\underline{x}_{(2)} \end{aligned} \tag{5.48}$$

which is the familiar Maxwellian distribution. The temperature T in Eq. (5.35b) is then identical to the kinetic temperature.

Before entering into the analysis for an ensemble of electrons I will briefly define the mean of a quantity x. For any spatially isotropic distribution this takes the form

$$\langle x \rangle = \frac{\int x(\beta)\, g(\beta)\, \mathrm{d}^3\underline{\beta}}{\int g(\beta)\, \mathrm{d}^3\underline{\beta}} = \frac{1}{n}\int x(\beta)\, g(\beta)\, \mathrm{d}^3\underline{\beta} \tag{5.49}$$

which for a relativistic distribution function can, by Eq. (5.44), be expressed as

$$\begin{aligned}\langle x \rangle &= \frac{m_0\varphi}{K_2(m_0\varphi)}\int_0^1 x(\beta)\exp\{-m_0\varphi\gamma\}\,\gamma^5\beta^2\mathrm{d}\beta \\ &= \frac{m_0\varphi}{K_2(m_0\varphi)}\int_0^\infty x(y)\exp\{-m_0\varphi\cosh y\}\cosh y\,\sinh^2 y\,\mathrm{d}y\,.\end{aligned} \tag{5.50a}$$

where

$$y = \cosh^{-1}\gamma\,. \tag{5.50b}$$

Returning now to the task of expressing the equation of motion in a form more suitable for a fluid treatment. By Eq. (5.49) the expected rate of energy loss per electron and the expected rate of momentum transfer per electron in the flow frame are respectively

$$\left\langle \frac{\mathrm{d}\mathcal{E}_{(2)e}}{\mathrm{d}t_{(2)}} \right\rangle = \frac{1}{n_{(2)e}}\int \frac{\mathrm{d}\mathcal{E}_{(2)e}}{\mathrm{d}t_{(2)}}\, g(\beta_{(2)t})\, \mathrm{d}^3\underline{\beta} \tag{5.51a}$$

where $\mathrm{d}\mathcal{E}_{(2)e}/\mathrm{d}t_{(2)}$ is given by Eq. (5.32a) and

$$\left\langle \frac{\mathrm{d}\underline{p}_{(2)e}}{\mathrm{d}t_{(2)}} \right\rangle = \frac{1}{n_{(2)e}}\int \frac{\mathrm{d}\underline{p}_{(2)e}}{\mathrm{d}t_{(2)}}\, g(\beta_{(2)t})\, \mathrm{d}^3\underline{\beta} \tag{5.51b}$$

where $\mathrm{d}\underline{p}_{(2)e}/\mathrm{d}t_{(2)}$ is given by Eq. (5.32b). Hence the rate of energy loss per unit volume and the rate at which energy is transferred to the plasma per unit volume are

$$\left\langle \frac{\mathrm{d}\mathcal{E}_{(2)}}{\mathrm{d}t_{(2)}} \right\rangle_V = \int \frac{\mathrm{d}\mathcal{E}_{(2)e}}{\mathrm{d}t_{(2)}}\, g(\beta_{(2)t})\, \mathrm{d}^3\underline{\beta} \tag{5.52a}$$

and

$$\left\langle \frac{\mathrm{d}\underline{p}_{(2)}}{\mathrm{d}t_{(2)}} \right\rangle_V = \int \frac{\mathrm{d}\underline{p}_{(2)e}}{\mathrm{d}t_{(2)}}\, g(\beta_{(2)t})\, \mathrm{d}^3\underline{\beta} \tag{5.52b}$$

respectively.

At this stage it is relevant to introduce the four-force density $\tilde{F}^\mu$. As the name suggests it is a slight variant on the four-force, F^μ, which, for a particle of constant rest mass, is given by Eq. (2.20). The four-force density is defined to be

$$\tilde{F}^\mu \equiv \frac{F^\mu}{\Delta V_0} = \frac{\gamma}{\Delta V_0}\left(\frac{\underline{f}\cdot\underline{v}}{\mathrm{c}}, \underline{f}\right) \tag{5.53}$$

where ΔV_0 is a proper volume element. Since F^μ is a four-vector and ΔV_0 is a world scalar, the four-force density is a genuine four-vector. If the ordinary force density is defined to be $\underline{\tilde{f}} = \underline{f}/\Delta V$ it then follows that

$$\tilde{F}^\mu = \left(\frac{\underline{\tilde{f}} \cdot \underline{v}}{c}, \underline{\tilde{f}} \right) . \tag{5.54}$$

The rate of change of momentum per unit volume given by Eq. (5.52*b*) obviously comprises the three-vector component to the four-force density in $\angle S_{(2)}$ whilst it can easily be shown that the rate of energy loss per unit volume given by Eq. (5.52*a*) comprises the time-component of the four-force density in $\angle S_{(2)}$. Therefore, since

$$\tilde{F}^\mu_{(1)} = \Lambda^\mu{}_\nu(-\underline{\beta}_{(1)f})\tilde{F}^\nu_{(2)} \tag{5.55}$$

the rate of energy loss per unit volume and the rate of change of momentum per unit volume in the rest frame of the radiator are given respectively by

$$\left\langle \frac{d\mathcal{E}_{(1)}}{dt_{(1)}} \right\rangle_V = \gamma_{(1)f} \left\{ \left\langle \frac{d\mathcal{E}_{(2)}}{dt_{(2)}} \right\rangle_V + \left[\underline{\beta}_{(1)f} \cdot \left\langle \frac{d\underline{p}_{(2)}}{dt_{(2)}} \right\rangle_V \right] \right\} \tag{5.56a}$$

and

$$\left\langle \frac{d\underline{p}_{(1)}}{dt_{(1)}} \right\rangle_V = \left\langle \frac{d\underline{p}_{(2)}}{dt_{(2)}} \right\rangle_V + \left\{ \gamma_{(1)f} \left\langle \frac{d\mathcal{E}_{(2)}}{dt_{(2)}} \right\rangle_V + \frac{\gamma_{(1)f} - 1}{\beta^2_{(1)f}} \left[\underline{\beta}_{(1)f} \cdot \left\langle \frac{d\underline{p}_{(2)}}{dt_{(2)}} \right\rangle_V \right] \right\} \underline{\beta}_{(1)f} . \tag{5.56b}$$

If the plasma is treated as a relativistic fluid it is then possible to determine the fluid-dynamical equations which can be expressed in the form (Mihalas and Mihalas, 1984)

$$M^{\mu\nu}_{;\nu} = \tilde{F}^\mu \tag{5.57}$$

where $M^{\mu\nu}$ is the material stress-energy tensor and the semi-colon, as is conventional, signifies the covariant derivative. I will not, in this work, attempt to solve the fluid-dynamical equations but do intend at a later stage to investigate their solution with particular emphasis on configurations in which the plasma is constrained to move within the confines of a conical radiator. **This represents a major future research topic.** In the meantime consideration will be restricted to the case where the plasma flow velocity $\underline{\beta}_{(1)f} = 0$. I will determine the radiation force exerted on the plasma per unit volume and the rate of energy loss per unit volume. Though this reveals nothing about the terminal flow speed of the plasma it will provide an indication of the typical enhancement to the initial driving force, due to the finite temperature of the bullet, which can be expected.

§5.2.2 A Simple Solution of the Fundamental Equations

If the plasma is at rest with respect to the radiation source such that $\underline{\beta}_{(1)f} = 0$ then the reference frames $\angle S_{(1)}$ and $\angle S_{(2)}$ are identical and the rate of energy loss per electron is, by Eq. (5.28*a*), given by

$$\frac{d\mathcal{E}_{(1)e}}{dt_{(1)}} = -\sigma_T \int \left\{ I_{(1)}(\underline{x}_{(1)}, \hat{\underline{k}}_{(1)i}, t_{(1)}) \left(1 - \underline{\beta}_{(1)t} \cdot \hat{\underline{k}}_{(1)i}\right) \left[\gamma^2_{(1)t} \left(1 - \underline{\beta}_{(1)t} \cdot \hat{\underline{k}}_{(1)i}\right) - 1\right] \right\} d\Omega_{(1)i} \tag{5.58}$$

whilst the rate of transfer of momentum to the plasma per electron is given by Eq. (5.29). For motion within an infinite conical radiator of uniform brightness $I_{(1)0}$ and semi-angle α these equations, upon integration over all directions of the incident raypath vector $\hat{\underline{k}}_{(1)i}$, become

$$\frac{d\mathcal{E}_{(1)e}}{dt_{(1)}} = -\frac{1}{3}\pi\sigma_T I_{(1)0}\gamma^2_{(1)t}\left\{6\left(\beta^2_{(1)t_x} + \beta^2_{(1)t_y} + \beta^2_{(1)t_z}\right)(\cos\alpha + 1) - \left(\beta^2_{(1)t_x} + \beta^2_{(1)t_y}\right)(\cos^3\alpha - 3\cos\alpha - 2) + 2\beta^2_{(1)t_z}(\cos^3\alpha + 1) - 2\beta_{(1)t_z}\sin^2\alpha\right\} \tag{5.59a}$$

and

$$\frac{d\underline{p}_{(1)e}}{dt_{(1)}} = -\frac{1}{3}\frac{\pi\sigma_T}{c} I_{(1)0}\left\{\gamma^2_{(1)t}\left[6(\cos\alpha + 1) - \left(\beta^2_{(1)t_x} + \beta^2_{(1)t_y}\right)(\cos^3\alpha - 3\cos\alpha - 2) + 2\beta^2_{(1)t_z}(\cos^3\alpha + 1) - 6\beta_{(1)t_z}\sin^2\alpha\right]\begin{pmatrix}\beta_{(1)t_x}\\ \beta_{(1)t_y}\\ \beta_{(1)t_z}\end{pmatrix} - \begin{pmatrix}\beta_{(1)t_x}\left[\cos^2\alpha - 3\cos\alpha - 2\right]\\ \beta_{(1)t_y}\left[\cos^2\alpha - 3\cos\alpha - 2\right]\\ 3\sin^2\alpha - 2\beta_{(1)t_z}\left[\cos^3\alpha + 1\right]\end{pmatrix}\right\}. \tag{5.59b}$$

For a spatially isotropic distribution, the differential number density of electrons in $\angle S_{(1)}$ can, by Eq. (5.44), be expressed as

$$dn_{(1)e} = dn_{(1)e}(\beta_{(1)t})\frac{d\Omega_{\beta_{(1)t}}}{4\pi} \tag{5.60a}$$

where

$$dn_{(1)e}(\beta_{(1)t}) = \frac{n_{e(1)}m_e\varphi}{K_2(m_e\varphi)}\exp\left\{-\gamma_{(1)t}m_e\varphi\right\}\gamma^5_{(1)t}\beta^2_{(1)t}\,d\beta_{(1)t}\,. \tag{5.60b}$$

Therefore, with reference to Eq. (5.49) and denoting any of the three cartesian coordinate axes by the subscript 'j', the following identities hold true:

$$\left\langle \beta_{(1)t_j} \right\rangle = \frac{\int \beta_{(1)t_z} dn_{(1)e}}{n_{(1)e}} = \frac{\int \beta_{(1)t} dn_{(1)e}(\beta_{(1)t})}{n_{(1)e}} \frac{\int_0^{2\pi}\int_0^{\pi} \sin\theta\cos\theta\, d\theta\, d\phi}{4\pi} = 0 \tag{5.61a}$$

$$\left\langle \gamma^2_{(1)t}\beta_{(1)t_j} \right\rangle = \frac{\int \gamma^2_{(1)t}\beta_{(1)t_z} dn_{(1)e}}{n_{(1)e}} = \frac{\int \gamma^2_{(1)t}\beta_{(1)t} dn_{(1)e}(\beta_{(1)t})}{n_{(1)e}} \frac{\int_0^{2\pi}\int_0^{\pi} \sin\theta\cos\theta\, d\theta\, d\phi}{4\pi} = 0 \tag{5.61b}$$

$$\left\langle \gamma^2_{(1)t}\beta^2_{(1)t_j} \right\rangle = \frac{\int \gamma^2_{(1)t}\beta^2_{(1)t_*}\,\mathrm{d}n_{(1)e}}{n_{(1)e}} = \frac{\int \gamma^2_{(1)t}\beta^2_{(1)t}\mathrm{d}n_{(1)e}(\beta_{(1)t})}{n_{(1)e}} \frac{\int_0^{2\pi}\int_0^{\pi} \sin\theta\cos^2\theta\,\mathrm{d}\theta\,\mathrm{d}\phi}{4\pi}$$

$$= \frac{\int \gamma^2_{(1)t}\beta^2_{(1)t}\mathrm{d}n_{(1)e}}{3n_{(1)e}} = \frac{1}{3}\left\langle \gamma^2_{(1)t}\beta^2_{(1)t} \right\rangle . \qquad (5.61c)$$

Hence, by Eq. (5.59*a*), the expected rate of energy loss in a unit volume of the plasma due to the incident photon flux originating from the funnel walls is

$$\left\langle \frac{\mathrm{d}\mathcal{E}_{(1)}}{\mathrm{d}t_{(1)}} \right\rangle_V = -\frac{8\pi}{3}\sigma_{\mathrm{T}} I_{(1)0}\,(\cos\alpha + 1)\left\langle \gamma^2_{(1)t}\beta^2_{(1)t} \right\rangle \qquad (5.62a)$$

whilst the expected rate of momentum transfer to a unit volume of the plasma by the radiation field is, by Eq. (5.59*b*),

$$\left\langle \frac{\mathrm{d}\underline{p}_{(1)}}{\mathrm{d}t_{(1)}} \right\rangle_V = \frac{\pi\sigma_{\mathrm{T}}}{\mathrm{c}} I_{(1)0}\left\{1 + \frac{2}{3}\left\langle \gamma^2_{(1)t}\beta^2_{(1)t} \right\rangle\right\} \sin^2\alpha \begin{pmatrix} 0 \\ 0 \\ 1 \end{pmatrix} . \qquad (5.62b)$$

These results are similar to those derived by O'Dell (1981) for a plasma located in the vicinity of a point source of radiation with respect to which it is at rest. The important feature of Eq. (5.62*b*) is that for a relativistic plasma, the radiation force experienced per unit volume is a factor $1 + 2/3\langle\gamma^2_{(1)t}\beta^2_{(1)t}\rangle$ above that for a cold plasma. This enhancement is due to anisotropic Compton losses in the plasma which are a direct consequence of the anisotropy in the radiation field to which the plasma is subjected. The initial rate of acceleration of a relativistic plasma moving within a conical radiator will, therefore, be greater than that for a cold plasma; a feature which should reduce the typical timescale for the attainment of a given fraction of the terminal speed. This is significant in SS433 where the acceleration timescale is $\sim$ 100 seconds. Equation (5.62*a*) indicates that the hotter the plasma the more rapid is its rate of cooling and consequently the enhanced acceleration rate may only be realised in the initial stages of the plasma's motion. However, in a future treatment consideration should be given to heat transfer from the bullet's interior to its surface. (An analogous situation arises in the sun where rapid heat loss from the surface is offset by heat supplied from the interior.) The full implications of the rate of energy loss equation on the rate of bulk acceleration can only be determined accurately within the context of a full fluid treatment of the plasma. Such an approach has previously been undertaken by Cheng and O'Dell (1981) and Phinney (1982). The former authors considered the motion of a plasma moving above a point source of radiation and found that the Compton rocket effect can accelerate the plasma to relativistic bulk speeds on a time scale comparable to that for energy loss. Phinney (1982) concluded that relativistic bulk speeds can be achieved though with seemingly unreasonable heating rates and, further, that the Compton rocket effect can significantly alter the structure of thick, radiation supported accretion discs if some of the electrons are relativistic.

The importance of the Compton rocket effect is essentially governed by the magnitude of the parameter $\langle \gamma^2_{(1)t}\beta^2_{(1)t}\rangle$ which, by Eqs. (5.50a, b), is

$$\begin{aligned}\left\langle \gamma^2_{(1)t}\beta^2_{(1)t}\right\rangle &= \frac{m_e\varphi}{K_2(m_e\varphi)}\int_0^\infty \exp\{-m_e\varphi\cosh y\}\cosh\,\sinh^4 y\,\mathrm{d}y \\ &= \frac{m_e\varphi}{16K_2(m_e\varphi)}\int_0^\infty \exp\{-m_e\varphi\cosh y\}\{\cosh 5y - 3\cosh 3y + 2\cosh y\}\,\mathrm{d}y \\ &= \frac{1}{16}\frac{m_e\varphi}{K_2(m_e\varphi)}\{K_5(m_e\varphi) - 3K_3(m_e\varphi) + 2K_1(m_e\varphi)\} \qquad (5.63)\end{aligned}$$

A plot $\langle \gamma^2_{(1)t}\beta^2_{(1)t}\rangle$ as a function of T for an isotropic distribution of electrons is illustrated in Fig. 5.2. For a temperature $T = 8\times 10^8$ K, the likely upper bound on the temperature at the base of the jets in SS433, $\langle \gamma^2_{(1)t}\beta^2_{(1)t}\rangle = 0.553$. Thus the maximal initial acceleration that can be expected in SS433 is a factor ~ 1.37 greater than that possible if the Compton rocket effect is neglected, as in the analysis of chapters 3 and 4.

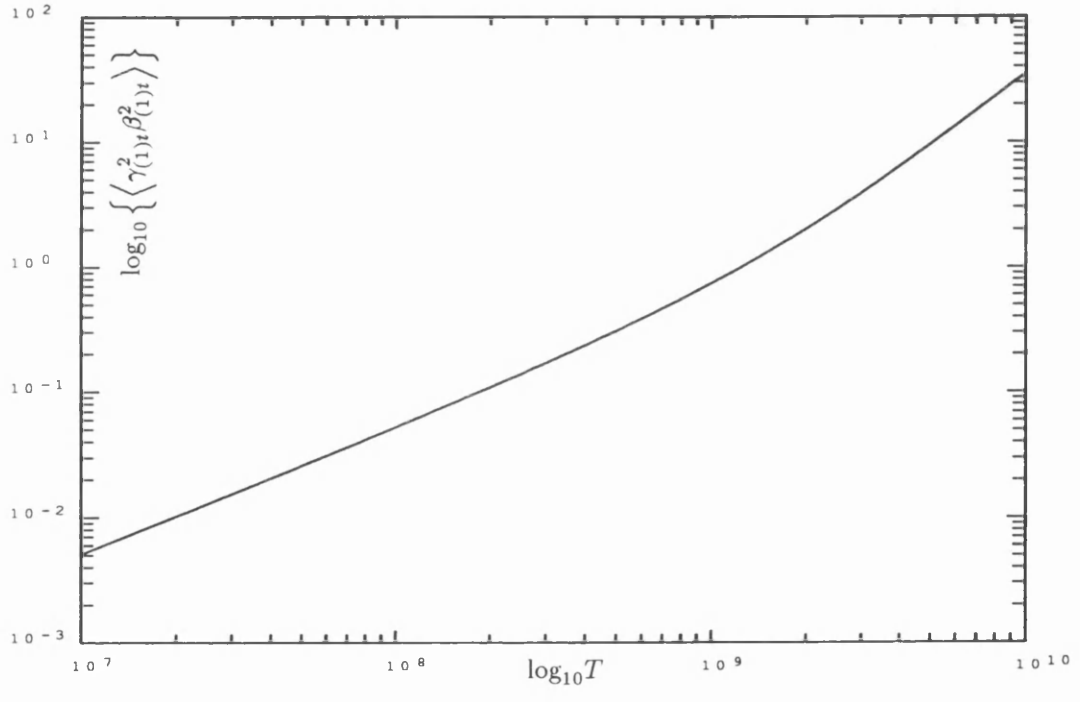

Fig. 5.2. The expected value of $\gamma^2_{(1)t}\beta^2_{(1)t}$ versus temperature (Kelvin) for an isotropic distribution of electrons.

In the treatment above it has been assumed that the plasma is dilute and therefore that each electron in the plasma is subjected to the radiation field attributable to the funnel walls. This is unlikely to be so, particularly in the initial stages of the bullet's motion. A better treatment should, therefore, include a realistic description of the passage of the radiation through the plasma which can, theoretically, be accomplished by solving the equation of radiative transfer (Eq. 2.38). It was further assumed that the electron distribution is isotropic in the plasma flow frame which, according to Phinney (1982), can only be achieved through collective plasma instabilities. This isotropy in the electron distribution can be expected, principally through Compton scattering, to lead to a progressive isotropisation of the radiation field with increasing

optical depth within the plasma. Since the Compton rocket is fuelled by anisotropic Compton losses resulting from an inherent anisotropy in the illuminating radiation field, this progressive isotropisation will tend to diminish the effectiveness of the Compton rocket mechanism.

§5.3 Further Considerations

The most pressing problem associated with the analysis in the previous chapters has been the intrusion of finite size effects. Their result is to restrict the validity of the equations of motion for a massive bullet to instances where, in essence, the typical bullet length scale is much smaller than that over which any changes in the brightness of the radiator occur. The exception to this is the specific case where the radiator is both infinite and of uniform brightness. The most readily achievable improvement to the model would, therefore, be the full incorporation of finite size effects into the derivation of the fundamental equations of motion. This should be possible by extending the derivation described in §2.6.

Throughout the work presented here, the bullets have been assumed to have a constant cross-section. This will, almost certainly, not be so since the tendency of any hot plasma is to cool by expansion, converting thermal energy into bulk kinetic energy as it does so. A simple, preliminary investigation of the effect of bullet expansion on, for example, the rate of bulk acceleration could be performed by assuming that the bullet expands spherically within an infinite conical radiator of uniform brightness such that it always fills the funnel. The bullet cross-section will then be defined in terms of the location of its centre above the apex and the funnel semi-angle, except for locations beyond a certain height when the bullet becomes optically thin and the cross-section remains constant.

Attention should also be directed towards the bullet geometry. The form of the bullet will evolve with the radiation pressure acting over its surface which will change as both the bullet location within the radiation field, and its velocity, change. An initial step in this investigation would be to consider the motion of a spheroidal bullet, varying selected geometrical parameters to determine the effect each has on the rate of acceleration and the terminal speed of the bullet.

In chapter 3 I considered the off-axis motion of a bullet moving above or within an infinite plane or cone. A worthwhile extension to this work would be an investigation of the off-axis motion within a finite conical radiator. Such an analysis should yield information on the degree of jet collimation that can be achieved and, given the observed degree of collimation, could indicate the region within the funnel in which the bullets are formed.

Further work could also involve the determination of more realistic temperature profiles for the radiation field within the accretion funnel. One approach is to solve the equations of stellar structure whilst another possibility could involve the twin polytropic model outlined in §4.6.2.

References

Abell G.O., Margon B.: 1979, *Nature*, **279**, 701.

Abramowicz M.A., Calvani M., Madau P.: 1987, *Comments Astrophys.*, **12**, 67.

Abramowicz M.A., Calvani M., Nobili L.: 1980, *Astrophys. J.*, **242**, 772.

Abramowitz M., Stegun I.A.: 1972, *Handbook of Mathematical Functions*, Dover Publications, Inc., New York.

Amitai-Milchgrub A., Piran T., Shaham J.: 1979, *Nature*, **280**, 473.

Anderson S.F., Margon B., Grandi S.A.: 1983a, *Astrophys. J.*, **269**, 605.

Anderson S.F., Margon B., Grandi S.A.: 1983b, *Astrophys. J.*, **273**, 697.

Antokhina A.A., Cherpashchuk A.M.: 1987, *Sov. Astron.*, **31**, 295.

Asadullaev S.S., Cherepashchuk A.M.: 1987, *Soviet Astron.*, **30**, 57.

Band D.L.: 1989, *Astrophys. J.*, **336**, 937.

Bedogni A., Braccesi A., Marano B., Messina A.: 1980, *Astron. Astrophys.*, **84**, L4.

Begelman M.C., Blandford R.D., Rees M.J.: 1984, *Rev. Mod. Phys.*, **56**, 255.

Begelman M.C., Rees M.J.: 1984, *MNRAS*, **206**, 209.

Begelman M.C., Sarazin C.L., Hatchett S.P., McKee C.F., Arons J.: 1980, *Astrophys. J.*, **238**, 722.

Benford G.: 1978, *MNRAS*, **183**, 29.

Blumenthal G.R., Gould R.J.: 1970, *Reviews of Modern Physics*, **42**, 237.

Bodo G., Ferrari A., Massaglia S., Tsinganos K.: 1985, *Astron. Astrophys.*, **149**, 246.

Bonsignori-Facondi S.R., Padrielli L., Montebugnoli S., Barbieri R.: 1986, *Astron. Astrophys.*, **166**, 157.

Borisov N.V., Fabrika S.N.: 1987, *Soviet Astron. Lett.*, **13**, 487.

Boyd R.N., Wiescher M., Newsom G.H., Collins G.W.: 1984, *Astrophys. J. Lett.*, **276**, L9.

Bradt H.V.D., McClintock J.E.: 1983, *Ann. Rev. Astron. Astrophys.*, **21**, 33.

Brinkmann W., Kawai N., Matsuoka M.: 1989, *Astron. Astrophys.*, **218**, L13.

Brinkmann W., Kawai N., Matsuoka M., Fink H.H.: 1991, *Astron. Astrophys.*, **241**, 112.

Brown J.C., Cassinelli J.P., Collins G.W.: 1991, *Astrophys. J.*, **378**, 307.

Calvani M., Nobili L.: 1980, *Vistas Astron.*, **25**, 173.

Calvani M., Nobili L.: 1981, *Astrophys. Space Sci.*, **79**, 387.

Caswell J.L., Lerche I.: 1979, *MNRAS*, **187**, 201.

Chandrasekhar S.: 1939, *An Introduction to the Study of Stellar Structure*, The University of Chicago Press, Chicago, Illinois.

Cheng A.Y.S., O'Dell S.L.: 1981, *Astrophys. J. Lett.*, **251**, L49.

Cherepaschuk A.M.: 1981, *MNRAS*, **194**, 761.

Cherepashchuk A.M.: 1988, *Sov. Sci. Rev. E. Astrophys. Space Phys.*, **7**, 183.

Ciatti F., Mammano A., Iijima T., Vittone A.: 1983, *Astron. Astrophys. Suppl. Ser.*, **52**, 443.

Ciatti F., Mammano A., Vittone A.: 1981, *Astron. Astrophys.*, **94**, 251.

Clark D.H.: 1984, *The Quest for SS433*, Viking Penguin Inc.

Clark D.H., Green A.J., Caswell J.L.: 1975, *Aust. J. Phys. Astrophys. Suppl.*, **37**, 75.

Clark D.H., Murdin P.: 1978, *Nature*, **276**, 45.

Clark D.H., Parkinson J.H., Caswell J.L.: 1975, *Nature*, **254**, 674.

Clayton D.D.: 1968, *Principles of Stellar Evolution*, McGraw-Hill, New York, pp. 155-165.

Collins G.W.: 1985, *MNRAS*, **213**, 279.

Collins G.W.: 1989, *The Fundamentals of Stellar Astrophysics*, W.H. Freeman and Company, New York, pp. 42-53.

Collins G.W., Brown J.C., Casinelli J.P.: 1990, *Nature*, **347**, 433.

Collins G.W., Newsom G.H.: 1986, *Astrophys. J.*, **308**, 144.

Collins G.W., Newsom G.H., Boyd R.N.: 1981, *Astrophys. Space Sci.*, **76**, 417.

Conti P.S., Underhill A.B.: 1988, *O Stars and Wolf-Rayet Stars*, Monograph Series on Non-thermal Phenomena in Stellar Atmospheres (NASA SP-497), Washington, D.C., p184.

Cowley A.P., Crampton D., Hutchings J.B.: 1979, *Astrophys. J.*, **231**, 539.

Crampton D., Cowley A.P., Hutchings J.B.: 1980, *Astrophys. J. Lett.*, **235**, L131.

Crampton D., Hutchings J.B.: 1981, *Astrophys. J.*, **251**, 604.

Davidson K., McCray R.: 1980, *Astrophys. J.*, **241**, 1082.

Davidson K., Pacini F., Salpeter E.E.: 1971, *Astrophys. J.*, **168**, 45.

DeCampli W.M.: 1980, *Astrophys. J.*, **242**, 306.

De Cuyper J.P.: 1981, *IAU Symp.: 'Fundamental Problems in the Theory of Stellar Evolution'*, **93**, 184.

deVeght Chr., Gehlich U.K.: 1979, *Astron. Astrophys.*, **79**, L16.

D'Odorico, Oosterloo T., Zwitter T., Calvani M.: 1991, *Nature*, **353**, 329.

Dopita M.A., Cherespaschuk A.M.: 1981, *Vistas Astron.*, **25**, 51.

Downes A.B.J., Pauls T., Salter C.J.: 1981, *Astron. Astrophys.*, **103**, 277.

Eggum G.E., Coroniti F.V., Katz J.I.: 1985, *Astrophys. J. Lett.*, **298**, L41.

Eichler D.: 1983, *Astrophys. J.*, **172**, 48.

Fabian A.C., Eggleton P.P., Hut P., Pringle J.E.: 1986, *Astrophys. J.*, **305**, 333.

Fabian A.C., Rees M.J.: 1979, *MNRAS*, **187**, 13p.

Fejes I.: 1986, *Astron. Astrophys.*, **168**, 69.

Ferrari A., Habbal S., Rosner R., Tsinganos K.: 1984, *Astrophys. J. Lett.*, **277**, L35.

Ferrari A., Habbal S., Rosner R., Tsinganos K.: 1985, *Astrophys. J.*, **294**, 397.

Fielder R.L., Johnston K.J., Spencer J.H., Waltman E.B., Florkowski D.R., Matsakis D.N., Josties F.J., Angerhofer P.E., Klepczynski W.J., McCarthy D.D.: 1987, *Astron. J.*, **94**, 1244.

Fillipenko A.V., Romani R.W., Sargent W.L.W., Blandford R.D.: 1988, *Astron. J.*, **96**, 242.

Forman W., Jones. C., Cominsky L., Julien P., Murray S., Peters G., Tanabaum H. , Giacconi

R.: 1978, *Astrophys. J. Suppl.*, **38**, 357.

Forman W., Jones C., Tanbaum H.: 1976, *Astrophys. J. Lett.*, **206**, L29.

Frank J., King A.R., Raine D.J.: 1985, *Accretion Power in Astrophysics*, Cambridge University Press.

Geldzahler B.J., Downes A.J.B., Shaffer D.B.: 1981, *Astron. Astrophys.*, **98**, 205.

Geldzahler B.J., Pauls T., Salter C.J.: 1980, *Astron. Astrophys.*, **84**, 237.

Geldzahler B.J., Share G.H., Kinzer R.L., Magura J., Chupp E.L., Rieger E.: 1988, *Astrophys. J.*, **342**, 1123.

Gilmore W.S., Seaquist E.R., Stocke J.T., Crane P.C.: 1980, *Astron. J.*, **86**, 864.

Gilmore W.S., Seaquist E.R., Stocke J.T., Crane P.C.: 1981, *Astron. J.*, **86**, 864.

Gradshteyn I.S., Ryzhik I.M.: 1980, *Table of Integrals, Series and Products*, Academic Press Inc., 111 Fifth Avenue, New York 10003.

Grindlay J.E., Band D., Seward F., Leahy D., Weisskopf M.C, Marshall F.E.: 1984, *Astrophys. J.*, **277**, 286.

Harrison E.: 1990, *Observatory*, **110**, 122.

Helfer H.L., Savedoff M.P.: 1984, *Astrophys J. Lett.*, **283**, L49.

Henson G.D., Kemp J.C., Barbour M.S., Kraus D.J., Leibowitz E.M.: 1983, *Astrophys. J.*, **275**, 247.

Hjellming R.M., Johnston K.J.: 1981a, *Nature*, **290**, 100.

Hjellming R.M., Johnston K.J.: 1981b, *Astrophys. J. Lett.*, **246**, L141.

Hjellming R.M., Johnstom K.J.: 1986, in *The Physics of Accretion onto Compact Objects*, ed. K.O. Mason, M.G. Watson and N.E. White (Berlin: Springer-Verlag), p287.

Icke V.: 1989, *Astron. Astrophys.*, **216**, 294.

Johnston K.J., Geldzahler B.J., Spencer J.H., Waltman E.B., Klepczynski W.J., Josties R.J., Angerhofer P.E., Florkowski D.R., McCarthy D.D., Matsakis D.: 1984, *Astron. J.*, **89**, 509.

Johnston K.J., Santini N.J., Spencer J.H., Klepczynski W.J., Kaplan G.H., Josities R.J., Angerhofer P.E., Florkowski D.R., Matsakis D.: 1981, *Astron. J.*, **86**, 1377.

Kaplan G.H., Kallarakal V.V., Harrington R.S., Johnston K.J., Spencer J.H.: 1980, *Astron. J.*, **85**, 64.

Katz J.I.: 1980, *Astrophys. J. Lett.*, **236**, L127.

Katz J.I.: 1981, *Astron. Astrophys.*, **95**, L15.

Katz J.I.: 1986, *Comments Ap.*, **11**, 201.

Katz J.I.: 1987, *Astron. Astrophys.*, **317**, 264.

Katz J.I., Anderson S.F., Margon B., Grandi S.A.: 1982, *Astrophys. J.*, **260**, 780.

Katz J.I., Piran T.: 1982, *Astrophys. Lett.*, **23**, 11.

Kawai N., Matsuaka M., Pan H.C., Stewart G.C.: 1989, *Publ. Astron. Soc. Jpn.*, **41**, 491.

Kemp J.C., Henson G.D., Kraus D.J., Carrol L.C., Beardsley I.S., Takagishi K., Jugaku J., Matsuoka M., Leibowitz E.M., Mazeh T., Mendelson H.: 1986, *Astrophys. J.*, **305**, 805.

Kirshner R.P., Chevalier R.A.: 1980, *Astrophys. J. Lett.*, **242**, L77.

Kochanek C.S.: 1991, *Astrophys. J.*, **371**, 289.

Königl A.: 1983, *MNRAS*, **205**, 471.

Kopylov I.M., Kumaigorodskaya R.N., Somov N.N., Somova T.A., Fabrika S.N.: 1986, *Soviet Astron.*, **30**, 408.

Krautter A., Henrikson R.N., Lake K.: 1983, *Astrophys. J.*, **269**, 81.

Kundt W.: 1985, *Astron. Astrophys.*, **150**, 276.

Kundt W.: 1987, *Astrophys. Space Sci.*, **134**, 407.

Lamb R.C., Ling J.C., Mahoney W.A., Riegler G.R., Wheaton W.A., Jacobson A.S.: 1983, *Nature*, **305**, 37.

Lebedev V.S., Pimonov A.A.: 1981, *Soviet Astron. Lett.*, **7**, 333.

Liebert J., Angel J.R.P., Hege E.K., Martin P.G., Blair W.P.: 1979, *Nature*, **279**, 384.

Leibowitz E.M.: 1984, *MNRAS*, **210**, 279.

Leibowitz E.M., Mazeh T., Mendelson H.: 1984, *Nature*, **307**, 34.

Lu J.F., Pinault S.: 1988, *Astrophys. Lett. and Commun.*, **27**, 13.

MacCallum C.J., Huters C.J., Stang P.D., Leventhal M.: 1985, *Astrophys. J.*, **291**, 486.

Mammano A., Ciatti F., Vittone A.: 1980, *Astron. Astrophys.*, **85**, 14.

Mammano A., Margoni R., Ciatti F., Cristiani S.: 1983, *Astron. Astrophys.*, **119**, 153.

Manka R., Bednárek I.: 1991, *Astrophys. Space Sci.*, **176**, 325.

Margon B.: 1984, *Ann. Rev. Astron. Astrophys.*, **22**, 507.

Margon B., Anderson S.F.: 1989, *Astrophys. J.*, **347**, 448.

Margon B., Anderson S.F., Aller L.H., Downes R.A., Keyes C.D.: 1984, *Astrophys. J.*, **281**, 313.

Margon B., Downes R.A., Gunn J.E.: 1981, *Astrophys. J.*, **249**, L1.

Margon B., Grandi S.A., Downes R.A.: 1980, *Astrophys J.*, **241**, 306.

Margon B., Ford H.C., Grandi S.A., Stone R.P.S.: 1979b , *Astrophys. J. Lett.*, **233**, L63.

Margon B., Ford H.C., Katz J.I., Kwitter K.B., Ulrich R.K., Stone R.P.S., Klemola A.: 1979a, *Astrophys J. Lett.*, **230**, L41.

Marshall F.E.: 1984, *Astrophys. J.*, **277**, 286.

Marshall F.E., Swank J.H., Boldt E.A., Holt S.S., Serlemitosis P.J.: 1979, *Astrophys. J. Lett.*, **230**, L145.

Martin P.G., Rees M.J.: 1979, *MNRAS*, **189**, 19p.

Mather J.C., Cheng E.S., Eplee R.E., Isaacman R.B., Meyer S.S., Shafer R.A., Weiss R., Wright E.L., Bennett C.L., Boggess N.W., Dwek E., Gulkis S., Hauser M G., Janssen M., Kelsall T., Lubin P.M., Moseley S.H., Murdock T.L., Silverberg R.F., Smoot G.F., Wilkinson D.T.: 1990, *Astrophys. J. Lett.*, **354**, L37.

Matsuoka M., Takano S., Makishima K.: 1986, *MNRAS*, **222**, 605.

Mazeh T., Kemp J., Leibowitz E.M., Meningher H., Mendelson H.: 1987, *Astrophys. J.*, **317**, 824.

Mestel L., Takhar H.S.: 1972, *MNRAS*, **156**, 419.

Mihalas D., Mihalas B.W.: 1984, *Foundations of Radiation Hydrodynamics*, New York Oxford.

Milgrom M.: 1979a, *Astron. Astrophys.*, **76**, L3.

Milgrom M.: 1979b, *Astron. Astrophys.*, **78**, L2.

Milgrom M., Anderson S.F., Margon B.: 1982, *Astrophys. J.*, **256**, 222.

Murdin P., Clark D.H., Martin P.G.: 1980, *MNRAS*, **193**, 135.

Newsom G.H., Collins G.W.: 1981, *Astron. J.*, **86**, 1250.

Niell A.E., Lockhart T.G., Preston R.A.: 1981, *Astrophys. J.*, **250**, 248.

Nobili L., Calvani M., Turolla R.: 1985, *MNRAS*, **214**, 161.

Norman E.B., Bodansky D.: 1984, *Nature*, **308**, 212.

O'Dell S.L.: 1981, *Astrophys. J. Lett.*, **243**, L147.

Papaloizou J.C.B., Pringle J.E.: 1982, *MNRAS*, **200**, 49.

Phinney E.S.: 1982, *MNRAS*, **198**, 1109.

Ramaty R., Kozlovsky B., Lingenfelter R.E.: 1984, *Astrophys. J. Lett.*, **283**, L13.

Ricketts M.J., Hall D., Page C.G., Pounds K.A., Sims M.R.: 1981, *Vistas Astron.*, **25**, 71.

Rindler W.: 1982, *Introduction to Special Relativity*, Oxford.

Roberts W.J.: 1974, *Astrophys. J.*, **187**, 575.

Romney J.D., Schilizzi R.T., Fejes I., SpencerR.E.: 1987, *Astrophys. J.*, **321**, 822.

Rybicki G.B., Lightman A.P.: 1979, *Radiative Processes in Astrophysics*, New York.

Ryle M., Caswell J.L., Hine G., Shakeshaft J.: 1978, *Nature*, **276**, 571.

Sarazin C.L., Begelman M.C., Hatchett C.F.: 1980, *Astrophys. J. Lett.*, **238**, L129.

Seaquist E.R.: 1981a, *Vistas Astron.*, **25**, 61.

Seaquist E.R.: 1981b, *Vistas Astron.*, **25**, 79.

Seaquist E.R., Garrison R.F., Gregory P.C., Taylor A.R., Crane P.C.: 1979, *Astron. J.*, **84**, 1037.

Seaquist E.R., Gilmore W.S., Johnston K.J, Grindlay J.E: 1982, *Astrophys. J.*, **260**, 220.

Seward F.D, Grindlay J., Seaquist E., Gilmore W.: 1980, *Nature*, **287**, 806.

Seward F.D., Page C.G., Turner M.J.L., Pounds K.A.: 1976, *MNRAS*, **175**, 39.

Shakura N.I. Sunyaev R.A.: 1973, *Astron. Astrophys.*, **24**, 337.

Shapiro P.R., Milgrom M., Rees M.J.: 1986, *Astrophys. J. Suppl. Ser.*, **60**, 393.

Shu F. H.: 1991, *The Physics of Astrophysics - Volume I: Radiation*, University Science Books, 20 Edgehill Road, Mill Valley, CA 94941.

Sikora M., Wilson D.B.: 1981, *MNRAS*, **197**, 529.

Spencer R.E.: 1979, *Nature*, **282**, 483.

Spencer R.E.: 1984, *MNRAS*, **209**, 869.

Stephenson C.B., Sanduleak N.: 1977, *Astrophys. J. Suppl.*, **33**, 459.

Stewart G.C., Watson M.G., Matsuoka M., Brinkmann W., Jugaku J., Takagishi K., Omadaka T., Kemp J.C., Kenson G.D., Kraus D.J., Mazeh T., Leibowitz E.M.: 1987, *MNRAS*, **228**, 293.

Strittmatter P.A., Williams R.E.: 1976, *Ann. Rev. Astron. Astrophys.*, **14**, 307.

Swihart T.L.: 1981, *Radiation Transfer and Stellar Atmospheres*, Pachart Publishing House, Tucson.

Synge J.L.: 1957, *The Relativistic Gas*, North-Holland Publishing Company, Amsterdam.

van den Heuvel E.P.J., Ostriker J.P., Petterson J.A.: 1980, *Astron. Astrophys.*, **81**, L7.

van den Heuvel E.P.J.: 1981, *Vistas Astr.*, **25**, 95.

van Gorkom J.H., Goss W.M., Seaquist E.R., Gilmore W.S.: 1982, *MNRAS*, **198**, 757.

Vermeulen R.: 1989, *Ph.D Thesis, University of Leiden.*

Vermeulen R.C., McAdam W.B., Trushkin S.A., Facondi S.R., Fielder R.L., Hjellming R.M., Johnston K.J., Corbin J.: 1993b, *Astron. Astrophys.*, **270**, 189.

Vermeulen R.C., Murdin P.G., van den Heuvel E.P.J., Fabfika S.N., Wagner R.M., Margon B., Hutchings J.B., Schilizzi R.T., van Kerkwijk M.H., van den Hoek L.B., Ott E., Angebault L.P., Miley G.K., D'Odorico S., Borisov N.: 1993c, *Astron. Astrophys.*, **270**, 204.

Vermeulen R.C., Schilizzi R.T., Icke V., Fejes I., Spencer R.E.; 1987, *Nature*, **328**, 309.

Vermeulen R.C., Schilizzi R.T., Spencer R.E., Romney J.D., Fejes I.: 1993a, *Astron. Astrophys.*, **270**, 177.

Wagner R.M.: 1983, *Ph.D. thesis, Ohio State University.*

Wagner R.M.: 1986, *Astrophys. J.*, **308**, 152.

Walker R.C., Readhead A.C.S., Seielstad G.A., Preston R.A., Niell A.E., Resch G.M., Crane P.C., Shaffer D.B., Geldzahler D.B., Neff S.G., Shapiro I.I., Jauncey D.L., Nicolson G.D.: 1981, *Astrophys. J.*, **243**, 589.

Warwick R.S., Marshall N., Fraser G.W., Watson M.G., Lawrence A., Page C.G., Pounds K.A., Ricketts M.J., Sims M.R., Smith A.: 1981, *MNRAS*, **197**, 865.

Watson M.G., Stewart G.C., Brinkmann W., King A.R.: 1986, *MNRAS*, **222**, 261.

Watson M.G., Willingdale R., Grindlay J.E., Seward F.P.: 1983, *Astrophys. J.*, **273**, 688.

Webster A.: 1979, *MNRAS*, **189**, 33p.

Whitmire D.P., Matese J.J.: 1980, *MNRAS*, **193**, 707.

Wilkinson D.T.: 1990, *Astrophys. J. Lett.*, **354**, L37.

Zealy W.J., Dopita M.A., Malin D.F.: 1980, *MNRAS*, **192**, 731.

Zhi F.L., Ruffini R., Stella L.: 1981, *Vistas in Astronomy*, **25**, 185.

Zwitter T., Calvani M.: 1989, *MNRAS*, **236**, 581.

Zwitter T., Calvani M.: 1990, *Astro. Lett. Communications*, **27**, 385.

Zwitter T., Calvani M., Bodo G., Massaglia S.: 1989, *Fundamentals of Cosmic Physics*, **13**, 309.

Zwitter T., Calvani M., D'Odorico S.: 1991, *Astron. Astrophys.*, **251**, 92.